UC Berkeley
UC Berkeley Electronic Theses and Dissertations

Title

Terrestrial carbon fluxes and pools under a changing climate

Permalink

https://escholarship.org/uc/item/0gg1s5wz

ISBN

9798173788450

Author

Nguyen, Bao Ngoc

Publication Date

2026-07-10

Peer reviewed|Thesis/dissertation

eScholarship.org Powered by the California Digital Library
University of California

Terrestrial carbon fluxes and pools under a changing climate

By

Bao Ngoc Nguyen

A dissertation submitted in partial satisfaction of the

requirements for the degree of

Doctor of Philosophy

in

Environmental Science, Policy, and Management

in the

Graduate Division

of the

University of California, Berkeley

Committee in charge:

Professor Trevor Keenan, Co-Chair

Professor Dennis Baldocchi, Co-Chair

Professor Lau Gherardi

Summer 2026

Terrestrial carbon fluxes and pools under a changing climate

Copyright 2026

By

Bao Ngoc Nguyen

Abstract

Terrestrial carbon fluxes and pools under a changing climate

By

Bao Ngoc Nguyen

Doctor of Philosophy in Environmental Science, Policy, and Management

University of California, Berkeley

Professor Trevor Keenan, Co-Chair

Professor Dennis Baldocchi, Co-Chair

Terrestrial ecosystems have captured 21% of human-emitted CO_2 over the last decade, highlighting the importance of studying their carbon cycle dynamics under a changing climate. The terrestrial carbon cycle has two main parts: carbon fluxes and pools, which represent short-term carbon exchanges such as between biosphere-atmosphere, and long-term carbon storage such as in vegetation and soils. When climate becomes more variable with changing precipitation regimes, increasing atmospheric CO_2 concentration, and warmer temperature, how terrestrial carbon flux and pools respond to these changes determines the ecosystems' carbon storage potential.

Throughout my Ph.D. dissertation, I utilize the global network of eddy-covariance CO_2 flux tower measurements across diverse ecosystems (FLUXNET) together with tree-ring data, a geospatial foundation model, and Dynamic Global Vegetation Models (DGVMs) to answer important scientific questions about terrestrial carbon fluxes and pools under a changing climate. Specifically, my dissertation (1) models rain-induced CO_2 pulses from global drylands, the processes that have been largely ignored in dryland carbon cycle modeling, through the FluxPulse framework, (2) spatializes CO_2 fluxes at a 10-m resolution within tower measurement areas to

support carbon monitoring of lands of interest, through the FluxLens framework, and (3) demonstrates that the recently observed short-term decoupling between photosynthesis and plant growth neither implies sink limitation nor constrains long-term growth.

Firstly, climate change leads to increases in rainfall intensity and decreases in frequency, making water-limited ecosystems more vulnerable. In drylands, vegetation and soil microbes rely on intermittent rainfall to thrive and regulate ecosystem carbon dynamics, yet the carbon pulses resulting from sporadic rainfall events have been extremely understudied. In the first chapter, I utilize the FLUXNET global database of ecosystem carbon fluxes to identify a widespread underestimation of rain-induced carbon losses from global drylands. I build an unprecedented dataset of manually and machine-learning labeled rain-pulse events, including more than 1800 rain-induced carbon loss events across 323 site-years at 34 dryland eddy-covariance sites worldwide. I find that rain-induced carbon losses contribute significantly to annual net ecosystem productivity and ecosystem respiration, but existing eddy-covariance carbon flux models significantly underestimate the response of ecosystem respiration and vegetation productivity to rainfall events by up to 30%. Motivated by these results, I develop FluxPulse, a novel approach to resolve rain-induced biases in current carbon flux models.

Secondly, in an era where precise quantification of land carbon uptake and release becomes more and more important for ecosystem carbon monitoring, I extend my focus from drylands to global terrestrial ecosystems and introduce the Flux observation Local ENvironment Scaling (FluxLens), a novel framework for spatializing carbon fluxes within flux tower areas at 10-meter resolution. FluxLens uses Google AlphaEarth Foundations (AEF) annual embedding datasets and climate datasets to predict monthly estimates of gross primary productivity (*GPP*) and ecosystem respiration (R_{eco}) at 10-m spatial resolution within tower measurement areas, across 184 global eddy-covariance tower sites. Across sites, FluxLens captures well CO_2 flux magnitude, seasonal dynamics, and visible spatial nonuniformity, with the mean predictions across all pixels consistent with flux-tower *GPP* and R_{eco} estimates (Site-specific pixel-mean R^2 *GPP* = 0.65-0.94 (25^{th}-75^{th} percentile); R^2 R_{eco} = 0.58-0.88).

Finally, rising atmospheric CO_2 has increased global photosynthesis by roughly 14% in the last 40 years, but whether this increase in carbon source activity translates into lasting woody biomass gains remains uncertain. Resolving this question is central to

evaluating the potential of terrestrial ecosystems to continue slowing climate change in the coming decades. Recent studies have reported a short-term decoupling between photosynthesis and woody biomass growth and interpreted this as evidence of emerging or intensifying sink limitation. By combining tree-ring data, eddy-covariance observations, and an ensemble of global vegetation models simulating carbon fluxes and pools from annual to centennial scales, I show widespread decoupling between photosynthesis and growth. Crucially, however, this decoupling has no bearing on long-term growth outcomes under elevated CO_2. My third chapter shows that short-term decoupling arises primarily from the dominant role of processes downstream of photosynthesis, and that its magnitude is unrelated to whether ecosystems are source- or sink-limited. These findings call into question previous reports of a strengthening sink limitation, and suggest that plants may not be as constrained under elevated CO_2 variability as currently assumed.

My dissertation answers important and relevant questions about the long-term relationship between carbon fluxes and pools under a changing climate, and develops two novel frameworks: FluxPulse for modeling rain-induced CO_2 pulses from global drylands and FluxLens for spatializing tower-based carbon fluxes at 10-meter resolution. Chapter 1 provides the first global assessment of the impact and drivers of rain-induced carbon losses across global drylands since their first official documentation in the 1950s. Chapter 2 leverages an emerging geospatial foundation model to provide spatially explicit carbon flux estimates with promising applications in ecosystem monitoring, land management, high-resolution satellite product evaluation, and plot-to-tower comparisons. Chapter 3 challenges previous reports of a strengthening sink limitation, and suggests that plants may not be as constrained under elevated CO_2 variability as currently assumed. Together, these chapters contribute to the understanding of terrestrial carbon fluxes and pools under a changing climate.

To my loved ones,

"The family is the foundation of everything."

"Gia đình là nền tảng của mọi thứ"

- Robson de Souza

Content

List of figures iii
List of tables vi
Acknowledgments viii
Chapter 1: Widespread underestimation of rain-induced soil carbon pulses from global drylands 1
1.1. Introduction 4
1.2. Methods 8
1.3. Results and Discussion 18
1.4. Conclusions 27
1.5. Acknowledgment 28
1.6. Data availability 28
1.7. Bibliography 29
1.8. Extended Data 51
Chapter 2: FluxLens: A 10-meter Spatialization Framework for Eddy-Covariance CO_2 Fluxes 62
1.1. Introduction 65
1.2. Methods 68
1.3. Results 77
1.4. Discussion 93
1.5. Conclusions 98
1.6. Acknowledgment 99
1.7. Data availability 99
1.8. Bibliography 100
1.9. Extended Data 123
Chapter 3: Long-term biomass growth unimpeded by short-term photosynthetic decoupling 143
1.1. Introduction 146
1.2. Methods 149
1.3. Results and Discussion 152
1.4. Conclusions 160
1.5. Acknowledgment 161
1.6. Data availability 161
1.7. Bibliography 162
1.8. Extended Data 184

List of figures

Chapter 1: Widespread underestimation of rain-induced soil carbon pulses from global drylands

Figure 1.1. Conceptual diagram of pulse events. 5

Figure 1.2. Partitioning methods underestimate pulse event CO_2 fluxes. 19

Figure 1.3. Rain-induced CO_2 pulses decay across sites. 21

Figure 1.4. Random forest performance for detecting pulse events. 25

Extended Data Figure 1.1. Global map of sites included in this research. 51

Extended Data Figure 1.2. Percent of pulse events that have precipitation data record (P, P_F, and P_ERA columns in FLUXNET database) within ±1 day from the start day of the events in 34 sites. 51

Extended Data Figure 1.3. Comparison between soil pH obtained from Soilgrids and the BADM (Biological, Ancillary, Disturbance and Metadata) of AmeriFlux & ICOS sites. 52

Extended Data Figure 1.4. Pearson correlation between pulse characteristics (Length, intensity, and size) and hydrologic variables (rewetting intensity (ΔEF, ΔP), antecedent water availability (Pre-pulse EF)) for each site. 52

Extended Data Figure 1.5. Bias (%) of FluxPulse R_{eco} and Nighttime (NT)-method R_{eco} when comparing to nighttime NEE during two days before and after the start of pulse events at three sites that use an enclosed-path system (ES-LM1, ES-LM2, and ES-Abr). 54

Extended Data Figure 1.6. Bias (%) of FluxPulse R_{eco} and Nighttime (NT)-method R_{eco} when comparing to nighttime NEE during two days after the start of pulse events at 34 sites. 55

Extended Data Figure 1.7. Difference between half-hourly NEE during daytime and nighttime (NEE_{DT} - NEE_{NT}) for the period of two days before each pulse event. 56

Extended Data Figure 1.8. Partial Dependence Plots for the responses of site-specific decay rate (k_s) to nine predictors. 57

Extended Data Figure 1.9. Partial Dependence Plots for the responses of site-specific pulse intensity (α_s) to nine predictors. 58

Extended Data Figure 1.10. Partial Dependence Plots for the responses of pulse occurrence to temporal predictors. 59

Chapter 2: FluxLens: A 10-meter Spatialization of Global Eddy-Covariance CO_2 Fluxes

Figure 2.1. FluxLens workflow. 70
Figure 2.2. Performance of different model setups in estimating GPP (a-c) and R_{eco} (d-f) from 115 unseen datasets across runs and temporal scales. 79
Figure 2.3. Performance of different model setups in estimating GPP across IGBP vegetation classes from 115 unseen datasets across all runs. 80
Figure 2.4. Performance of different model setups in estimating R_{eco} across IGBP vegetation classes from 115 unseen datasets across all runs. 81
Figure 2.5. Performance of the XGB_Emb+Clim, XGB_GAM and pixel-mean XGB_GAM at individual sites for GPP and R_{eco} prediction. 83
Figure 2.6. 10-m pixel-wise monthly GPP estimates within the 250-m-radius around the eddy-covariance tower at the Lochristi poplar-planted site (BE-Lcr) (unseen site) from 2019-2022. 86
Figure 2.7. 10-m pixel-wise monthly R_{eco} estimates within the 250-m-radius around the eddy-covariance tower at the Lochristi poplar-planted site (BE-Lcr) (unseen site) from 2019-2022. 87
Figure 2.8. 10-m pixel-wise monthly GPP estimates within the 250-m-radius around the eddy-covariance tower at the Majadas del Tietar North savanna (ES-LM1) (unseen site) from 2017-2024. 88
Figure 2.9. 10-m pixel-wise monthly R_{eco} estimates within the 250-m-radius around the eddy-covariance tower at the Majadas del Tietar North savanna (ES-LM1) (unseen site) from 2017-2024. 89
Figure 2.10. 10-m pixel-wise monthly GPP estimates within the 250-m-radius around the eddy-covariance tower at the Mayberry wetland (US-Myb) (unseen site) from 2017-2021. 90
Figure 2.11. 10-m pixel-wise monthly R_{eco} estimates within the 250-m-radius around the eddy-covariance tower at the Mayberry wetland (US-Myb) (unseen site) from 2017-2021. 91
Extended Data Figure 2.1. Global distribution of 184 eddy-covariance flux sites (blue dots) used in this study. 140
Extended Data Figure 2.2. Comparison between ERA-Interim reanalysis and flux-based meteorological variables 141
Extended Data Figure 2.3. Performance of different model setups in terms of RMSE in estimating GPP (a-c) and R_{eco} (d-f) from 115 unseen datasets across runs and temporal scales. 142

Chapter 3: Long-term biomass growth unimpeded by short-term photosynthetic decoupling

Figure 3.1. Short-term correlations between annual gross primary production (GPP) and annual woody carbon increment (ΔcWood). 153
Figure 3.2. Relationship between $\beta_{cWood,GPP}$ and $r_{\Delta cWood,GPP}$. 155
Figure 3.3. Net allocation and trends in plant carbon fluxes and pools. 157
Figure 3.4. Long-term changes in the allocation of gross primary production to net woody biomass growth. 159
Extended Data Figure 3.1. Global maps of 31 eddy-covariance sites with on-site tree-ring data used in this research. 187
Extended Data Figure 3.2. Relationship between $\beta_{cWood,GPP}$ and $r_{\Delta cWood,GPP}$ within individual models. 189

List of tables

Chapter 2: FluxLens: A 10-meter Spatialization of Global Eddy-Covariance CO_2 Fluxes

Table 2.1. XGBoost model setup description for predicting Gross Primary Productivity (GPP) and Ecosystem Respiration (R_{eco}) 75

Extended Data Table 2.1. List of 184 eddy-covariance flux sites and years of data used in this study. 123

Extended Data Table 2.2. Parameters for XGBoost models used in our study. 137

Extended Data Table 2.3. Pairwise t-test comparisons (reported in P values) of model performance in terms of R^2 among five model setups for GPP monthly predictions. 137

Extended Data Table 2.4. Pairwise t-test comparisons (reported in P values) of model performance in terms of R^2 among five model setups for R_{eco} monthly predictions. 137

Extended Data Table 2.5. Pairwise t-test comparisons (reported in P values) of model performance in terms of R^2 among five model setups for predicting GPP mean seasonal cycle (MSC). 138

Extended Data Table 2.6. Pairwise t-test comparisons (reported in P values) of model performance in terms of R^2 among five model setups for predicting R_{eco} mean seasonal cycle (MSC). 138

Extended Data Table 2.7. Pairwise t-test comparisons (reported in P values) of model performance in terms of R^2 among five model setups for predicting GPP monthly anomaly. 139

Extended Data Table 2.8. Pairwise t-test comparisons (reported in P values) of model performance in terms of R^2 among five model setups for predicting R_{eco} monthly anomaly. 139

Chapter 3: Long-term biomass growth unimpeded by short-term photosynthetic decoupling

Extended Data Table 3.1. List of eddy-covariance flux towers used in this study that have onsite ring width measurements. 184

Extended Data Table 3.2. Mean $r_{\Delta cWood,GPP}$ across all tower-overlapping grid cells for each model and scenario presented in Figure 3.1. 188

Extended Data Table 3.3. Pair t-test p-values for mean distribution 190

differences of $\mathbf{r}_{\Delta \mathrm{cWood,GPP}}$ between observations (obs) and scenarios (S0, S1, S2).

Acknowledgments

My 16-year-old self spent a great deal of time thinking about which career would suit me best in the future. I analyzed my strengths and weaknesses, personality, hobbies, and passions, and I finally realized that becoming a scientist was the most fulfilling career I could ever ask for. It was the perfect path for a curious teenage girl who was never afraid to bother her parents, teachers, and sister with silly questions; a girl who loved delving deeply into her own world, solving math problems, and building (mostly unsuccessful) science projects; and a girl who thirsted for intellectual freedom and aspired to push the boundaries of knowledge and do something meaningful to the world. Most importantly, that girl found herself in every moment asking and solving scientific questions.

Over the past five years, I have finally been able to live my dream. All beautiful things began when Professor Trevor Keenan took me from the waitlist and offered me a place in his lab. I was an undergraduate having no papers except for a deep passion and a strong belief in myself. And then, it was not the scientist from *"Cloudy with a Chance of Meatballs"* taught me the proper ways of doing science, it was the professors, colleagues, and peers I met during my Ph.D. at UC Berkeley and throughout my research visits taught me the best lessons about what it truly means to be a scientist.

My advisor Trevor has given the intellectual freedom and the highest level of support I could ever have hoped for. I was young, energetic, and perhaps a little out of control during my first few years of Ph.D., but you were extraordinarily patient with my development and steep learning curve. I asked for your patience, and you gave it to me generously. I love the way you give me research feedback; your comments have always felt constructive, encouraging, and more importantly, I have always felt that we were working together as friends and colleagues, rather than as a professor and a student. I have enjoyed all of our discussions; they were all pleasant and productive. I have enjoyed the freedom you gave me to become the best version of myself, and your huge support for how crazy my research ideas were. Your brilliant ideas and perspectives have leveraged my science, and brought my science into a new and higher standard. Through this journey, I have accomplished my dream of meeting and learning from the brightest minds in the world. Your unconventional, out-of-the-box thinking will continue to inspire me far beyond my Ph.D. I am lucky to have met you and received your guidance and

support during my early stage of learning how to be a good scientist.

The second person I am grateful to have met is Professor Dennis Baldocchi. I am lucky to have your guidance over the past five years, and to be inspired by your love for science. As you once said, courage is contagious. Your personality is admirable, and your consistency and strong scientific ethics are also contagious. I hope that one day I can inspire the next generations like what you have done, and keep the flame of science everywhere, all the time. Your commitment to creating positive changes in seemingly small acts like volunteering to introduce elementary school students to ecosystem and flux sciences is a powerful example of how to return kindness to the world. These things have touched my heart. I want to send my deepest respect to you, and thank you for all the science advice, the timeless and golden references, and the encouragement you have given me to pursue original science. And thank you as well for welcoming me into your lab activities.

The third person I want to thank is Professor Laureano Gherardi, who taught me some of the most important fundamental concepts in ecology, and who I always feel so empowered and inspired after meeting with. Lau patiently worked through every figure with me across three chapters of the book *Principles of Terrestrial Ecosystem Ecology* by Chapin et al. (2011), making sure that I understood not only the meaning of each figure, each axis, but more importantly, the scientific storry behind it. You taught me to transform complex scientific ideas into concise figures and how to build multiple layers of meaning into these figures to communicate with different audiences. And thank you also for teaching me how to write a scientific paper, from structuring the Introduction, developing a compelling storyline, to making the narrative and results coherent and defensible. You saved me during my most vulnerable years at UC Berkeley and helped me go from 0 to 1 as I worked to overcome a steep learning curve.

My Ph.D. experience would not be that transformative without the research visits at international institutions. I would like to express my deep appreciation to Dr. Mirco Migliavacca, whose paper and research ideas have transformed my thinking, and who generously hosted me during my research visit to Ispra, Italy. You are one of the kindest people I have ever met and I really enjoyed collaborating and working with you. It was a pleasant experience in Ispra, and I appreciated you help in even very small things such as giving me the mosquito repellent and picking me up from the airport at 6 a.m. And thank you so much for connecting me with the

scientists at the Max Planck Institute. Markus, Martin, Jake, Nick, and Sophia are truly amazing and inspiring, and I look forward to more opportunities to collaborate with them. I could truly feel the science passion in your heart as well as other European scientists I have met. I have learned so much about how to conduct good science. I left feeling very inspired. Perhaps one day, I will move to Europe, who knows!

One of the highlights of my Ph.D. experience was the once-in-a-lifetime opportunity to conduct research above the Arctic Circle in in Svalbard, Norway, and to experience 24 hours of winter darkness! I am deeply grateful to Professor Dinh Khuong at the University of Oslo for giving me this opportunity to step far beyond my comfort zone and accomplish my dream! I witnessed advanced technologies of collecting deep-ocean zooplankton under extremely challenging weather, and had the chance to work with Janne, an inspiring, enthusiastic, and hardworking scientist in Svalbard. You showed me that the world is much bigger than I had imagined and that countless fascinating things are still waiting for us to explore. I look forward to future opportunities to stay connected, and I am sure that our paths will cross again!

I also want to dedicate a paragraph for Maoya Bassiouni for all your help throughout my Ph.D. journey. You were there during a time when I was still discovering my research interests, trying to understand who I was a scientist, and struggling to learn so much new knowledge. Your encouragement helped me believe in myself, in my decision to use evaporative fraction in my first chapter, and in my decisions during the postdoctoral application process. Without your daily and immediate support, I do not know whether I could have made it through my Ph.D. It is very lucky for me to meet you and I wish you all the best in your future journey! Please remember that meeting you is a life-changing moment!

Next, I would like to thank Miao Zhang, my dear friend and colleague who has always brought so much joy and happiness into my life and often gave me a reason to go to the lab. Thank you for listening to all my trivial stories, celebrating every small scientific finding with me, and making my life at UC Berkeley so much brighter and more joyful. I was really sad when you left, and I cannot wait to see you again soon! I deeply cherish all the time we spent together. You are such an amazing science buddy!!

I would like to thank all my current and former lab members for creating such a welcoming, supportive, and collaborative place to do science and share ideas. Thank you for all the scientific feedback and the fun moments during lab socials and group lunches. Huiqi, it has been such a pleasure to have your support throughout my Ph.D. Thank you for all the moments when we shared our experiences and struggles. You always made me feel understood and reminded me that I was not alone in this journey. We definitely need to collect all the photos we took together at AGU! Kyle, I feel so lucky that we were in the same lab. You are such a kind, thoughtful, and mature person, and I am truly grateful for all the advice you gave me. I will miss you, but I am sure our paths will cross again. I wish you and your family all the best, and I want you to know how much I appreciated your support during my five years at UC Berkeley. Jackie, it has been wonderful having you as a lab mate! You are cheerful, positive, and such a great listener. You are always pleasant to talk to and work with. I wish you and your bunnies all the best, and I look forward to many more board-game matches with you!

I am also grateful to my ESPM friends—Anna, Sierra, Kat, Seb, Seth, and Shera—for their friendship and support throughout my Ph.D. Kat, Seb, and Seth, thank you especially for being my rock-climbing partners and helping me relax and de-stress along the way! I would also like to thank my conference friends—Sneha, Weiwei, Benju, Dohee, Yang Gu, Anam, and Lindsey—whom I had the joy of seeing a few times each year. You made every conference feel exciting and full of laughter! In addition, I am deeply thankful to my co-authors, Hoang Nguyen, Quang Nguyen, and Josh Nguyen, for your collaboration, thoughtful discussions, and contributions to our shared scientific work.

Ryann and Zarah, I can't appreciate how grateful I am to receive your support and encouragement during my Ph.D. at ESPM! Ryann, you were the person who encouraged me to move forward after receiving a 53 out of 100 in a statistics class and who supported me in retaking my qualifying exam after I partially failed it. Whenever I faced a problem or struggled, I turned to you because I trusted that you could help, and you always did. Your support transformed my Ph.D. experience, and I am incredibly grateful for everything you have done for me. Zarah, although we have not had as many opportunities to talk, your smile and positive energy have always brightened my day. Simply seeing you smile and warmly interact with others brought me so much happiness and positivity. Thank you both for the wonderful work you have done to support Ph.D. students like me at ESPM. We are

incredibly lucky to have you. I look forward to sharing the next chapters of my journey with you, and I want you to know how deeply thankful I am for your kindness, encouragement, and support.

I would like to extend my thanks to my friends, Mai Duong, Tri Huynh, Chau Huynh, Amber, Tina, Cindy, Son Pham, David, Jade, and Long for supporting me throughout my Ph.D. journey. A big shout-out goes to my coolest friend, Mai Duong, for being my rock-climbing partner, accompanying me through both challenging and joyful moments, and even helping revise my proposal for my Arctic research trip. I still owe you a few adventures in Europe and Africa! Thank you for understanding how demanding and overwhelming my Ph.D. journey could be, for always sympathizing with me, and for forgiving me during the times when I disappeared. You are truly a wonderful friend, and I feel incredibly grateful that our paths crossed during my adventure in California.

I would also like to thank VEF for supporting me during one of the most challenging periods of my Ph.D. A special shout-out goes to Mr. Cuong Nguyen for always being there to listen to my silly thoughts, worries, and struggles. Your support has meant so much to me.

I would also like to thank Sang Nguyen, Bao Yen, Thao Do, Trang Phan, and Ha Phuong for always welcoming me home and spending time with me. You have been an incredible source of emotional support, and I am so grateful to have you in my life. I am also deeply thankful to my large extended families on both my father's and mother's sides for always looking forward to my visits, spending time with me, and taking such wonderful care of me.

I would also like to acknowledge Joshua Schimel, even though we have never met. His book *Writing Science: How to Write Papers That Get Cited and Proposals That Get Funded* transformed the way I write, think about, and communicate science. When my sister was pursuing her Ph.D., I noticed a copy of the book in her bookshelf. I was only a high school student at the time and was curious to read it, although I could understand very little. Years later, when it was my turn to pursue a Ph.D., the book became an invaluable guide and saved me in many ways. It has deeply influenced both my sister and me, shaping how we understand and express science.

To my husband, I wish I had met you sooner so that I would not have had to face so many difficult moments alone or spend so many nights struggling with my thoughts. Your encouragement and belief in me have empowered me so much, especially your kindness and acceptance of my character. It is a beautiful feeling to be with someone who always encourages me to be my true self, embracing all my silly and awkward moments, and who continues to love and support me wherever life takes me. You have also helped me see many other beautiful aspects of life and make stressful moments seem so small compared with the life waiting ahead. You are the perfect puzzle piece in my life. I enjoy every moment with you, and I am glad to have you as a lifelong soulmate. I look forward to more happy and joyful moments with you in many adventures ahead <3

I would also like to express my deep appreciation to my parents-in-law and sister-in-law for their tremendous support. Thank you for every meal you cooked for me and every restaurant you took me to, for checking on me and being so understanding during my most stressful moments, and for genuinely celebrating every milestone I achieved. I am especially grateful for your support of our little family with my husband and our two cats, Milo and Tobi through every adventure we encounter. Your kindness and love for us will never fade, and neither will our love for you.

My sister has been a huge supporter during my years doing Ph.D. at UC Berkeley, and also the one who first inspired me to become a scientist and showed me all the exciting science projects and fun things to do in my childhood. I appreciate your time and efforts in giving me a pleasant childhood, growing my curiosity, and nurturing a warm heart. You taught me the fundamental concept in soil microbiology, you are there when I cried in the most vulnerable moments during my Ph.D. Every time I have concerns or unsure about something, I asked you and got immediate support and valuable advice. You have been the person I have looked up to since childhood, and who on Earth would not admire such a talented sister? I wish you all the best in your journeys as a professor and a mother with the cute and lovely baby! I am so happy for you and wish all the best things on Earth for you and your family. Thank you for inspiring me and nurturing my passion for science from such a young age, and I could not be prouder of you.

And finally, my deepest appreciation and respect go to my mom and dad, who are the foundation of everything I have achieved. I could not have been happy without

a loving family, nor could I have focused on science and pursued my passions without your unconditional support. My mom has always been there to offer immediate encouragement and unconditional love whenever I felt stressed or doubted myself. My dad's positivity and humor are contagious, and he makes every problem feel so small! All my worries magically disappear when I talk to you. I want to remain your little daughter forever because you are the people I can always cry with, the people I call home, and the people with whom I never fear being judged. Wherever Mom and Dad are, that is where home is. I love you so much and I wish you all the best things in this world. I love you more than I can say.

Sometimes I wanted this journey to end, but sometimes I wanted it to continue forever. It has been an overall pleasant five years doing my Ph.D. at UC Berkeley. I learned more than I could have hoped for, met extraordinary mentors, colleagues, and friends, and spend time and energy to pursuing the excellence I had always dreamed of. It was rough, it was lost, it was endless, because nothing is easy if we dream big and are ambitious. But when there is a will, there is a way. When the will is strong enough, nothing matters more than following it, because the pursuit itself allows us to become our truest selves. I am happy with what I have over the past five years at UC Berkeley. I have dreamed, but could never have imagined that I could go this far. I have the golden chance to learn how to do good science from the most supportive system and the most brilliant minds in the field.

Finally, I am really proud to have become a scientist.

July 23rd, 2026

Ngoc Nguyen

"Motivation gets you going, but discipline keeps you growing"

- John C. Maxwell

Chapter 1

Widespread underestimation of rain-induced soil carbon pulses from global drylands

Widespread underestimation of rain-induced soil carbon emissions from global drylands

Ngoc B. Nguyen [1], Mirco Migliavacca [2], Maoya Bassiouni [1], Dennis D. Baldocchi [1], Laureano A. Gherardi [1], Julia K. Green [1,3], Dario Papale [4,5], Markus Reichstein [6], Kai-Hendrik Cohrs [7], Alessandro Cescatti [2], Tuan Dung Nguyen [8], Hoang H. Nguyen [9], Quang Minh Nguyen [10], Trevor F. Keenan [1,11]

[1] *Department of Environment Science, Policy, and Management, University of California Berkeley, Berkeley, USA*

[2] *European Commission, Joint Research Centre (JRC), Ispra, Italy*

[3] *Department of Environmental Science, University of Arizona, Tucson, Arizona, USA*

[4] *National Research Council (CNR), Institute of Research on Terrestrial Ecosystems (IRET), Monterotondo Scalo (Roma), Italy*

[5] *University of Tuscia, DIBAF, Viterbo, Italy*

[6] *Max Planck Institute of Biogeochemistry, Department of Biogeochemical Integration, Jena, Germany*

7 Universitat de València, València, Spain

8 Department of Computer and Information Science, University of Pennsylvania, Philadelphia, PA, USA

9 H. Milton Stewart School of Industrial & Systems Engineering, Georgia Institute of Technology, Atlanta, GA, USA

10 Department of Electrical Engineering and Computer Science, Massachusetts Institute of Technology, Cambridge, MA, USA

11 Climate and Ecosystem Sciences Division, Lawrence Berkeley National Laboratory, Berkeley, CA, USA

An edited version of this chapter is published as:

Nguyen, N.B., Migliavacca, M., Bassiouni, M. et al. Widespread underestimation of rain-induced soil carbon emissions from global drylands. Nat. Geosci. 18, 869–876 (2025).

"It's harder to go from 0 to 1 than from 1 to 10. You can scale and multiply what's there, but zero will remain zero no matter how hard it's multiplied."

- Thomas Vato

Abstract

Dryland carbon fluxes, particularly those driven by ecosystem respiration, are highly sensitive to water availability and rain pulses. However, the magnitude of rain-induced carbon emissions remains unclear globally. Here we quantify the impact of rain-pulse events on the carbon balance of global drylands and characterize their spatiotemporal controls. Using eddy-covariance observations of carbon, water and energy fluxes from 34 dryland sites worldwide, we produce an inventory of over 1800 manually identified rain-induced CO_2 pulse events. Based on this inventory, a machine learning algorithm is developed to automatically detect rain-induced CO_2 pulse events. Our findings show that existing partitioning methods underestimate ecosystem respiration and photosynthesis by up to 30% during rain-pulse events, which annually contribute 16.9±2.8% of ecosystem respiration and 9.6±2.2% of net ecosystem productivity. We show that the carbon loss intensity correlates most strongly with annual productivity, aridity, and soil pH. Finally, we identify a universal decay rate of rain-induced CO_2 pulses and use it to bias correct respiration estimates. Our research highlights the importance of rain-induced carbon emissions for the carbon balance of global drylands and suggests that ecosystem models may largely underrepresent the influence of rain pulses on the carbon cycle of drylands.

1.1. Introduction

Drylands cover over a third of the global land surface (Reynolds et al., 2007; Whitford & Duval, 2020) and significantly influence the trend and interannual variability of the terrestrial carbon sink (Ahlström et al., 2015; Poulter et al., 2014; Sitch et al., 2024). These ecosystems are water-limited, with rainfall driving vegetation and microbial processes that impact ecosystem carbon dynamics (Noy-Meir, 1973). Sporadic rain pulses in particular play a crucial role in determining plant growth, microbial activity, soil moisture, and overall ecosystem productivity (Feldman et al., 2018; Kannenberg et al., 2023; Sala et al., 2012). Although the influence of water availability on dryland carbon dynamics is well established (Gherardi & Sala, 2019; Huxman, Cable, et al., 2004; Noy-Meir, 1973), the processes governing responses to rain pulses remained poorly understood. The amount of carbon lost due to heterotrophic respiration stimulated by rain-pulse events and the key drivers of those losses across diverse dryland ecosystems, remain open questions (Barnard, 2020; Jarvis et al., 2007; Rousk & C. Brangarí, 2022; L. Xu et al., 2004), and the underlying processes are thus typically not included in models of dryland carbon dynamics (MacBean et al., 2021; Rousk & C. Brangarí, 2022; W. K. Smith et al., 2019).

Rain pulses trigger abiotic and biotic soil CO_2 pulses, a phenomenon often termed a rain-induced CO_2 pulse event or pulse event. Abiotic CO_2 pulses occur when water displaces CO_2 from soil pores (Huxman, Snyder, et al., 2004; Maier et al., 2010) or dissolves carbonates (Inglima et al., 2009). Biotic CO_2 pulses, known as the Birch effect, result from microbial respiration surges following the sudden availability of labile carbon and nutrients (Birch, 1958; Bottner, 1985; Fierer & Schimel, 2003; Jarvis et al., 2007; Schimel, 2018). This resource pulse may arise from the release of intracellular solutes, microbial lysis, and physical breakdown of soil aggregates (Fierer & Schimel, 2003; Placella et al., 2012; Rutledge et al., 2010). While abiotic CO_2 pulses are short-lived (Inglima et al., 2009; Serrano-Ortiz et al., 2010), Birch-effect CO_2 pulses can last several days and lead to significant ecosystem carbon losses during the day and night (Jarvis et al., 2007; Lee et al., 2004; L. Xu et al., 2004; Yan et al., 2014). Microbial respiration can increase 60 to 80 fold after rainfall (L. Xu et al., 2004), then decay as the soil dries (Birch, 1958; Jarvis et al., 2007; Liu et al., 2002; Rousk &

C. Brangarí, 2022; L. Xu et al., 2004) , contributing up to 40% to total soil respiration during the growing season (Yan et al., 2014), and 5-10% to annual net ecosystem productivity (Lee et al., 2004) (Fig. 1.1). The intensity of these pulses has been linked to hydrologic dynamics such as the intensity/frequency of rewetting and antecedent soil dryness (Huxman, Snyder, et al., 2004; Jarvis et al., 2007; Rousk & C. Brangarí, 2022; L. Xu et al., 2004). In contrast, plant-microbe interactions are often neglected, mainly because previous research focused on soil-centric environments or vegetation-senescence periods (Barnard, 2020; Inglima et al., 2009). The combined effects of vegetation, soil properties, climate, and hydrologic dynamics on rain-induced carbon losses, therefore, remains poorly constrained.

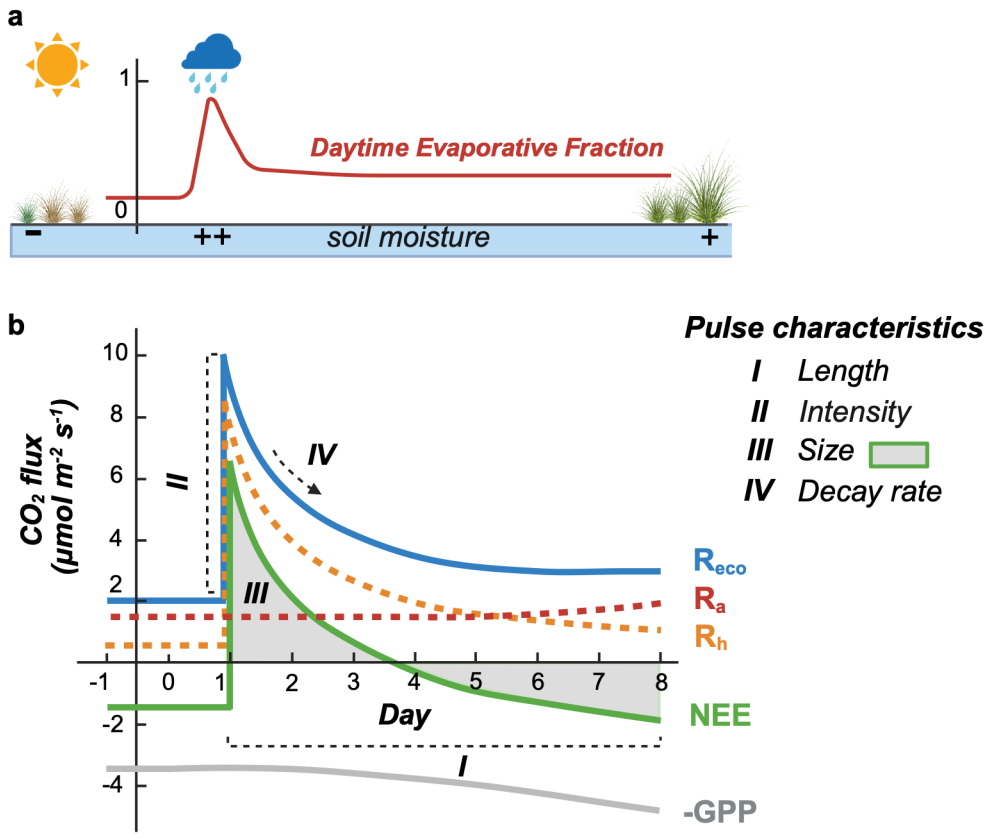


Figure 1.1. Conceptual diagram of pulse events. *Pulse events, or rain-induced CO_2 pulse events, are defined as ecological processes in which rainfall on previously dry soils triggers pulses of soil CO_2 and, consequently, pulses of net CO_2 flux (NEE).* ***(a)*** *The horizontal bar represents the soil moisture gradient, daytime evaporative fraction*

(EF), and vegetation growth before and after rain pulses. ***(b)*** *Dynamics of daily ecosystem carbon fluxes (R_a, R_h, R_{eco}, NEE, GPP) during pulse events and CO_2 pulse characteristics: (i) length, (ii) intensity, (iii) size, and (iv) decay rate (see Methods). R_{eco} is ecosystem respiration, R_a is autotrophic respiration, and R_h is heterotrophic respiration. NEE is net ecosystem exchange of CO_2 flux measured directly from eddy covariance towers. GPP is gross primary productivity; we plotted -GPP instead of GPP for visualization purposes. The first-principle relationship between carbon fluxes can be described as follow: $NEE = R_a + R_h - GPP$, $R_{eco} = R_a + R_h$.*

Modeling these pulse-driven events is particularly challenging due to the sporadic and discontinuous nature of rainfall in drylands (Noy-Meir, 1973). Most models effectively incorporate steady-state processes such as responses to temperature, long-term changes in soil moisture, and vegetation productivity. However they largely neglect non-steady-state but significant rain-induced carbon losses (Migliavacca et al., 2011; Raich & Potter, 1995; Reichstein et al., 2003, 2005; L. Xu et al., 2004; L. Xu & Baldocchi, 2004). This omission could lead to substantial underestimation of soil and ecosystem respiration, potentially resulting in inaccurate estimates of related processes such as gross primary productivity (Jung et al., 2024; Rousk & C. Brangarí, 2022). The lack of a broad characterization of dryland rain-induced CO_2 pulses has hindered the integration of these processes into existing ecosystem models.

Detecting rain-induced carbon losses across diverse dryland ecosystems is a critical first step to improving model predictions of dryland carbon fluxes. FLUXNET, which provides global eddy covariance measurements of net CO_2 flux or net ecosystem exchange (*NEE*) (D. Baldocchi et al., 2001; D. D. Baldocchi, 2020), offers a unique opportunity to analyze CO_2 pulse responses at high temporal resolution. Rainfall driven ecosystem respiration (R_{eco}) pulses manifest as net CO_2 anomalies, because microbial activity typically responds more rapidly to rainfall than vegetation (S. Chen et al., 2009; B. Huang & Nobel, 1993; Huxman, Cable, et al., 2004; Migliavacca et al., 2011; Noy-Meir, 1973; Placella et al., 2012; Roby et al., 2020) (Fig. 1.1). However, FLUXNET does not provide continuous measurements of soil and ecosystem respiration (Jung et al., 2024), making *NEE* the variable of choice for detecting rain-

induced carbon losses. Furthermore, conventional eddy covariance partitioning methods estimate R_{eco} using an Arrhenius-type temperature function (Lasslop et al., 2010; Reichstein et al., 2005) (Equation 2), which may not effectively capture rain-induced carbon losses (Jung et al., 2024; L. Xu & Baldocchi, 2004). *NEE* observations from FLUXNET thus provide a unique opportunity to both identify and characterize soil CO_2 pulses.

Here, we combine a novel manually-labeled database of 1857 pulse events with machine learning frameworks to detect rain-induced carbon losses across 34 dryland eddy-covariance sites, encompassing 323 years of half-hourly observations. Using this database, we characterize the spatiotemporal drivers of net CO_2 pulse dynamics, and bias-correct R_{eco} estimates derived from the conventional nighttime partitioning method. We refer to this integrated detection and correction approach as FluxPulse. Our results highlight widespread underestimation of carbon losses during rain-pulse events in global drylands, with significant implications for dryland carbon balance variability under climate change.

1.2. Methods

1.2.1. Data sources

We collected openly available eddy covariance data from FLUXNET2015 (Pastorello et al., 2020), AmeriFlux (www.ameriflux.lbl.gov), and ICOS (Integrated Carbon Observation System) Warm Winter 2020 (Warm Winter 2020 Team & ICOS Ecosystem Thematic Centre, 2022) (www.icos-cp.eu), all produced through ONEFlux processing under a CC-BY-4.0 license (Pastorello et al., 2020). We used only original half-hourly measurements extracted from the gapfilled versions of net ecosystem exchange of CO_2 (NEE_VUT_REF), latent heat flux (LE_F_MDS), and sensible heat flux (H_F_MDS), along with meteorological variables such as air temperature (TA_F_MDS) and incoming shortwave radiation (SW_IN_F_MDS). For precipitation, we gathered both tower-measured precipitation (P) and downscaled precipitation (P_ERA) from ERA-Interim reanalysis data products published via the above eddy covariance networks (Vuichard & Papale, 2015).

We selected eddy covariance sites that satisfied the following criteria: (1) ratio of annual precipitation to potential evapotranspiration (P/PET) < 0.65, a common definition of a dryland (Abatzoglou et al., 2018), (2) at least four years of data, and (3) short and sparse vegetation (typically height < 2 m and area < 30% of tree cover) with IGBP vegetation types belonging to Grasslands (GRA), Savannas (SAV), Open Shrublands (OSH), Closed Shrublands (CSH), and Woody Savannas (WSA). We selected ecosystems with short and sparse vegetation to minimize rain loss from vegetation interception and reduce strong vegetation interference with rain-induced CO_2 pulse signals detected in NEE measurements. In total, our data contained 34 sites across North America, Europe, and Australia, with mean annual precipitation (MAP) ranging from 245 to 1180 mm, mean annual temperature (MAT) ranging from 7 to 29°C, and record length ranging from 4 to 21 years in each site (Extended Data Fig. 1.1; Supplementary Table 1).

1.2.2. Identification of pulse events

We established a foundational database of pulse events by manually labeling the start and end dates of these events, across 323 site-years of data in 34 sites. We

then developed a machine learning algorithm to automatically detect pulse events from half-hourly eddy covariance data, which was trained on the manually labeled dataset.

Pulse event indicator. Rainfall is typically measured by the tipping bucket method in the eddy covariance network; nevertheless, this method is known to under-report rainfall due to instrument limitations, and landscape heterogeneity (Gebler, 2015; Legates & DeLiberty, 1993). We confirmed that many tower data likely under-reported precipitation by noting that precipitation downscaled from ERA (P_ERA) is more synchronous with net CO_2 pulses than the in-situ-measured precipitation (P) (Extended Data Fig. 1.2). We therefore used P_ERA as the primary rainfall record.

In addition to rainfall, we used daytime Evaporative Fraction (*EF*) as an index of soil water availability and rainfall occurrence. *EF* is the fraction of available energy allocated to evapotranspiration from the land surface, which we calculated on a daily scale as the average daytime ratio between latent heat flux and the sum of latent and sensible heat fluxes (Shuttleworth et al., 1989). Daytime *EF* varies between 0 and 1, with 1 indicating a non-water-limiting condition as all available energy is converted to latent heat, and 0 indicating a water-limited condition since all available energy is converted to sensible heat. EF range is 0.19±0.18 to 0.52±0.15 across 34 studied sites, including both growing and non-growing seasons. Rainfall after a long dry period creates a surge of *EF*, and dry ecosystems rarely get too wet for *EF* to saturate, making *EF* a potential indicator of soil water availability and rainfall occurrence. Compared to in-situ soil water content measurements, *EF* is broadly available and can be calculated consistently across eddy covariance sites.

Manual labeling of pulse events. We manually labeled the start and end dates of pulse events via observations of net CO_2 pulses, aiming to study their spatiotemporal dynamics and to develop supervised machine learning models for labeling these events (Supplementary Extended Data Fig. 1.10 for detailed criteria for labeling). We used original half-hourly time series data on net ecosystem exchange of CO_2 (*NEE*), daytime Evaporative Fraction (*EF*), and downscaled precipitation (P_ERA) from ERA-Interim reanalysis data. Across 34 sites over 323 site years, we manually labeled 1857 pulse events, with durations ranging from 2 to 26 days. The start date of the pulse event was labeled based on satisfying the following conditions: (1) *NEE* suddenly

increases sharply, (2) *NEE* gradually decays over at least two days after the peak day to distinguish the start of pulses from random noises, (3) *EF* suddenly increases sharply, and (4) Positive precipitation (Supplementary Table 2). Sometimes, condition (4) was not satisfied but we still marked the start of the pulse event because it is likely that rainfall was under-reported. The end date of the pulse event was defined as the date when nighttime *NEE* stabilizes and approximates its pre-pulse magnitude (Supplementary Extended Data Fig. 1.10).

Machine learning labeling of pulse events. We used random forests to automatically label pulse events at a half-hourly scale, since random forests, or tree-based models in general, have been shown to outperform deep learning on tabular datasets (Grinsztajn et al., 2022). Furthermore, random forest can inherently handle missing time series data and is more time-efficient compared to deep learning algorithms. Specifically, we applied the random forest binary classification algorithm using the function '*RandomForestClassifier*' in the Python '*sklearn*' package. The algorithm, trained on previously manually labeled datasets, processes FLUXNET formatted data to label measurements as pulse events or not on a half-hourly scale. To train and evaluate this model, we first selected 28 out of 34 sites that each has at least five years of data and 20 recorded pulse events. We trained one foundation model using data from all selected sites, using the last three years at each site as the testing set; the rest of the observations were randomly split into a training set and a validation set of ratio 80%:20%. This approach not only enhances the generalization capability of our model but also mitigates the risk of overfitting. The validation set was used for model selection purposes (such as tuning hyper-parameters), while the test set was used to evaluate the model's final performance. The features used by the random forest model include hydrologic and carbon flux characteristics that are important signals for the pulse events, including rewetting intensity (*ΔEF*), antecedent water availability (pre-pulse *EF*), pulse intensity (*ΔNEE*), and antecedent ecosystem productivity (pre-pulse *NEE*) (see Methods). The full list can be found in Fig. 1.4c.

We evaluate this model, again with respect to the test set, using two common metrics for classification tasks: precision and recall. Precision is the fraction of pulse events the model detected that were actually real ($\frac{\text{True Positive}}{\text{True Positive+False Positive}}$), while recall is the fraction of actual pulse events that were successfully detected by the model

($\frac{\text{True Positive}}{\text{True Positive+False } Negative}$). For example, if there are 12 pulse events in total, and the model detected 10 events with only 7 of them being actual pulse events, then precision is 7/10 and recall is 7/12.

Finally, the random forest model allowed us to investigate feature importance, that is, how relatively useful each covariate is in predicting the outcome. In particular, for each feature, we computed the normalized total reduction in the Gini impurity across decision tree leaves. Higher Gini importance indicates that the feature reduces more uncertainty in prediction on average, and hence is more important (Breiman et al., 2017). We report these scores in Fig. 1.4c.

1.2.3. Characterizing rain-induced carbon pulses

Length, Intensity, and Size. We characterized rain-induced carbon pulses within the eddy-covariance network by defining the length, intensity, and size of net ecosystem exchange (*NEE*) during each event (Equation 1; Fig. 1.1). Even though the decay rate is an important feature of pulse events (Fig. 1.1), due to the uncertainties of half-hourly data and heterogeneity in data quality across sites, it is not possible to derive the decay rate for each event. Instead, we characterized the site-specific decay rate for all pulse events within one site (see below). Regarding pulse length, we defined it as the number of days of the pulse events from the start to the end dates, which was directly calculated from the manually labeled dataset. Pulse intensity is, conceptually, the initial response of microbial respiration (R_h) to rainfall, which was calculated as the change in *NEE* (ΔNEE) between the mean of two days after and the mean of two days before rainfall (Fig. 1.1). *NEE* was used instead of R_h to calculate the pulse intensity since vegetation has a lagged response to rainfall, hence ΔNEE is equal to ΔR_h on the first few days of the pulse events, and the eddy-covariance network does not provide direct measurements of R_h (Fig. 1.1). Regarding pulse size, we defined it as the sum of the daily mean of half-hourly *NEE* during the whole period of pulse events (Fig. 1.1).

Site-specific pulse intensity and decay rate. To estimate site-specific pulse intensity and decay rate, we fitted a 1st-order kinetic equation, which aims to mimic the litter decomposition function (Chapin et al., 2011), as follows:

$$NEE_{\mathrm{i,s}} = \alpha_{\mathrm{s}} \times e^{-k_{\mathrm{s}} \times i} \quad \text{Equation 1}$$

where $NEE_{i,s}$ is the maximum of daily mean *NEE* on day *i* from all pulse events in site *s* (Equation 1). α_s and k_s are the site-specific pulse intensity and decaying rate of site *s* respectively (Equation 1). The site-specific pulse intensity α_s is obtained by fitting Equation 1 to all pulse events from one site, which is different from the pulse intensity of individual pulse events mentioned above (*ΔNEE*), even though they represent a similar concept of the initial response of the net carbon flux to rainfall.

1.2.4. Existing R_{eco}/*GPP* partitioning methods

Parametric methods. The partitioning methods we utilize partition R_{eco} and *GPP* from *NEE* based on the relationship *NEE* = R_{eco} – *GPP*, in which *NEE* is the net ecosystem exchange of CO_2 fluxes measured directly from eddy-covariance towers, R_{eco} is ecosystem respiration, and *GPP* is gross primary productivity (Fig. 1.1). We evaluated the performance of partitioning methods on estimating R_{eco} and *GPP* during pulse events and annually. The common parametric approaches that have been widely used by the flux community are the nighttime (NT) method, which derives R_{eco} from nighttime data as an Arrhenius-type function of temperature (Lloyd & Taylor, 1994; Reichstein et al., 2005), and the daytime (DT) approach, which models *GPP* and R_{eco} based on the light-response curve of *GPP* and temperature response of R_{eco} (Lasslop et al., 2010). Both approaches model R_{eco} at half-hour *j* as an exponential function of air temperature (Equation 2) (Lloyd & Taylor, 1994):

$$Reco_{\mathrm{NT_{method\ j}}} = R_{\mathrm{ref}} \times e^{E_0 \times \left(\frac{1}{T_{ref} - T_0} - \frac{1}{Tair_{\mathrm{j}} - T_0}\right)} \quad \text{Equation 2}$$

where $Reco_{\mathrm{NT_{method\ j}}}$ is R_{eco} modelled by the NT method at half-hour j, $T_{air\ j}$ is the air temperature at half-hour j, R_{ref} is reference respiration at reference temperature (T_{ref} = 288.15 °K), T_0 = 227.13 °K , and E_0 is temperature sensitivity (Fig. 1.2c).

Machine learning methods. In addition to evaluating the parametric approaches, we assessed machine learning methods to partition R_{eco} and *GPP* during pulse events, which are a hybrid model based on artificial neural networks (NN) (Tramontana et al., 2020), and a causal hybrid model based on double machine learning (DML) (Cohrs

et al., 2024). The NN approach integrates physical constraints to simultaneously estimate R_{eco} and *GPP* through two subnetworks and showed improved flux estimates during pulse events at the US-SRG site (Tramontana et al., 2020). The causal hybrid model enhances the hybrid model by incorporating principled causal knowledge and employs the Double Machine Learning (DML) approach for estimating causal effects (Cohrs et al., 2024). Each model incorporates variables such as soil water content, shortwave radiation, day of the year, wind speed, vapor pressure deficit, and air temperature as predictors. We reimplemented both approaches and ran them on our selected sites.

1.2.5. FluxPulse: Modeling rain-induced CO_2 pulses from flux data

We developed the FluxPulse algorithm to model rain-induced carbon pulses from eddy-covariance flux data in 34 studied global dryland sites. FluxPulse bias-corrects R_{eco} and *GPP* from the Nighttime (NT) method during pulse events and pre-pulse periods, in which the NT method fails to capture the temporal dynamics (Fig. 1.2c). For non-rewetting and non-pre-pulse periods, FluxPulse retains R_{eco} and *GPP* estimates from the NT method. A visualization tool for FluxPulse bias-corrected datasets can be accessed via https://ngoc-nguyen-ucberkeley.shinyapps.io/fluxpulse_visualization/.

Bias-correct carbon fluxes during pulse events. To bias-correct both R_{eco} and *GPP* during pulse events, we first bias-corrected R_{eco}, then calculated *GPP* as the difference between bias-corrected R_{eco} and *NEE*. In summary, FluxPulse re-estimates R_{eco} during pulse events by forcing R_{eco} on the first day of pulse events to approximate maximum *NEE* on the same day, then calculating R_{eco} in the following days using the decay rate *k*, which is computed empirically for each pulse event (Equation 4). A correction factor β, which was written as a decay function and calculated on a daily scale, was applied to all half-hourly NT-method R_{eco} ($Reco_{\mathrm{NT_{method}}}$) from the same day to obtain the half-hourly FluxPulse R_{eco} ($Reco_{\mathrm{FluxPulse}}$) (Equation 3).

$$Reco_{\mathrm{FluxPulse\ i,j}} = \beta_{\mathrm{i}} \times Reco_{\mathrm{NT_{method}\ i,j}} \quad \text{Equation 3}$$

Where $Reco_{\mathrm{FluxPulse\ i,j}}$ is FluxPulse bias-corrected R_{eco} on day *i* and half-hour *j*; β_i is

the correction factor applied to all $Reco_{\mathrm{NT_{method}\ i,j}}$ on day *i* and half-hour *j*, in which $Reco_{\mathrm{NT_{method}\ i,j}}$ is R_{eco} obtained from the NT method. β decays over time to represent the decaying characteristics of R_{eco} during pulse events (Equation 4, Fig. 1.1) (Jarvis et al., 2007; L. Xu et al., 2004), and is calculated as:

$$\beta_{\mathrm{i}} = \frac{NEE_{98^{\mathrm{th}}{}_1}}{Reco_{\mathrm{NT_{method}\ 98^{th}{}_1}}} \times e^{-k\times(i-1)} \qquad \text{Equation 4}$$

where $NEE_{98^{\mathrm{th}}{}_1}$ and $Reco_{\mathrm{NT_{method}\ 98^{th}{}_1}}$ are, respectively, 98th percentile of half-hourly NEE and NT-method R_{eco} on day one of the pulse event (Equation 4). 98th percentile values were chosen to select the maximum *NEE* and NT-method R_{eco} during pulse events. On day one (*i* = 1), β_{i} is equal to the ratio between 98th percentile *NEE* and 98th percentile NT-method R_{eco} (Equation 4), hence for $Reco_{\mathrm{NT_{method}\ i,j}}$ equals to $Reco_{\mathrm{NT_{method}\ 98^{th}{}_1}}$, $Reco_{\mathrm{FluxPulse\ i,j}}$ is equal to 98th percentile *NEE.* This bias-correction method reduces the bias of the NT-method R_{eco} and forces the maximum of FluxPulse R_{eco} to approximate maximum *NEE* during pulse events, given R_{eco} should be theoretically larger or equal to *NEE* (Equation 3).

In Equation 4, *k* is theoretically the decay rate of each pulse event. Since the half-hourly data is often noisy, and we do not have direct, continuous measurements of R_{eco} or R_h, the decay rate *k* was estimated empirically as follows (Extended Data Fig. 1.5, 1.6). Firstly, we fitted a 1st-order kinetic equation similar to Equation 1 to the array $NEE_{68^{\mathrm{th}}{}_1}$, $NEE_{68^{\mathrm{th}}{}_2}$, $NEE_{68^{\mathrm{th}}{}_3}$⋯, $NEE_{68^{\mathrm{th}}{}_{\mathrm{i}}}$ in which $NEE_{\mathrm{p^{th}{}_i}}$ is the p^{th} percentile of all half-hourly *NEE* on day *i*. 68th percentile was chosen to reflect values within ±1 standard deviation from the mean on each day. If the non-linear fit is statistically significant ($p < 0.1$), then the estimate of *k* is accepted. If the non-linear fit is not statistically significant, we fitted a 1st-order kinetic equation to an alternative array: $\overline{NEE_1}$, $\overline{NEE_2}$, $\overline{NEE_3}$, ⋯, $\overline{NEE_t}$, in which $\overline{NEE_t}$ is the mean of all half-hourly *NEE* in day *i* from all pulse events in a specific site. We validated FluxPulse R_{eco} against *NEE* at night, which was assumed to approximate R_{eco} due to the lack of photosynthesis at night (Extended Data Fig. 1.5, 1.6). We only selected pulse events that lasted longer than three days for validation in order to minimize the effect of random error and the potential introduction of uncertainties due to low-turbulence

conditions.

It is worth noting that in Equation 4, by using *NEE* to set FluxPulse R_{eco} during pulse events, we implicitly assume that *GPP* during the first day of rainfall is minimal due to the pre-pulse dry periods. Even though this is not the case in most sites (Extended Data Fig. 1.7), the assumption is necessary as there are no direct measurements of *GPP* and the partitioning methods available cannot provide reliable *GPP* estimates during pulse events. Importantly, this assumption is conservative and does not inflate the magnitude or importance of the main results. If *GPP* is positive on the first day of the pulse event, the bias in R_{eco} is expected to be even larger since $R_{eco} = NEE + GPP$. Our reported bias values therefore likely underestimate the true bias associated with the partitioning methods assessed during pulse events (Fig. 1.2a, b).

Bias-correct carbon fluxes during pre-pulse periods. In addition to being biased during pulse events, the NT partitioning method is biased in the days leading up to pulse events (Fig. 1.2c; Extended Data Fig. 1.5). This is due to the fact that the NT method uses a moving window to estimate R_{ref} (Equation 2), and this window overlaps with the pulse event periods in the days prior to the pulse event. We therefore bias-corrected R_{eco} and *GPP* before the pulse events to reduce the pre-pulse biases (Fig. 1.2c; Extended Data Fig. 1.5; see Methods). We selected the pre-pulse period as *n* days before the pulse events (*n* being the event length) and used a 2-day window to estimate R_{ref} instead of a 4-day window used in the NT Method (Reichstein et al., 2005) (Equation 2). Only pre-pulse periods that do not overlap with previous pulse events were selected for correction.

FluxPulse technical assessment. Validation against the *NEE* measurements at night is complicated by the fact that rain events greatly reduce data quality for eddy-covariance measurements, particularly for open-path sensors. The three sites in the database use enclosed CO_2 sensors (ES-LM1, ES-LM2, and ES-Abr), however, which are robust under rainfall conditions (Burba, 2022). Evaluation against night-time observations for those three sites shows that FluxPulse reduces the median R_{eco} bias from 27.0% to 0.7% (Extended Data Fig. 1.5). Across 82% of all studied sites, FluxPulse reduces biases significantly from the NT method ($p < 0.001$, one-tailed paired t-test) and successfully captures the pulse temporal dynamics (Extended Data Fig. 1.5, 1.6).

1.2.6. Hydrologic characteristics

Carbon flux characteristics during pulse events are strongly affected by the level of soil dryness and rainfall rewetting intensities (Rousk & C. Brangarí, 2022; L. Xu et al., 2004). We tested two different indices for rewetting intensity: the Evaporative Fraction (*EF*) and precipitation (*P*) (Extended Data Fig. 1.4). The rewetting intensity (*ΔEF* or *ΔP*) is the difference in either *EF* or *P* between two days after and two days before the rainfall. We calculated the antecedent water availability, denoted as pre-pulse *EF*, as the mean of *EF* 15 days before rainfall. A lower pre-pulse *EF* indicates a drier antecedent period. We took the average *EF* in 15 days before the pulse events happened but not a longer or shorter period because a longer time window could include a mix of growing season and non-growing season, and a shorter period does not fully represent the history of water stress.

1.2.7. Soil characteristics

Microbial response to rewetting is influenced not only by water dynamics, but also by soil properties (Singh, 2023; L. Xu et al., 2004). We extracted soil chemical and physical properties such as soil pH, texture, and soil organic carbon from SoilGrids (www.soilgrids.org), which is a 250-m resolution interpolated global map of soil properties (Poggio et al., 2021).

1.2.8. Analysis of spatiotemporal drivers of rain-induced carbon losses

We used the LMG method in the R package 'relaimpo' to assess the importance of spatial drivers such as soil characteristics, vegetation uptake, and climatic conditions on the intensity and decay rate of *NEE* during pulse events (Fig. 1.3). The LMG method is robust to multicollinearity between variables and provides confidence interval estimation via bootstrapping (Lindeman et al., 1980). Regarding the temporal drivers of rain-induced carbon losses, we used the feature importance scores obtained from using random forests to label pulse events (see Method Section 2).

To analyze the directional relationship between site-specific pulse intensity/decay rate and each predictor, we used Partial Dependence Plot (PDP), which effectively considers confounding effects between multiple predictors and the

target variable, without assuming a linear relationship like the Pearson correlation (Extended Data Fig. 1.8, 1.10).

1.3. Results and Discussion

1.3.1. Widespread underestimation of pulse event carbon fluxes

We found that pulse events significantly impact the dryland carbon balance, contributing 16.9±2.8% (mean ± the margin of error) to annual ecosystem respiration (R_{eco}) and 9.6±2.2% to net ecosystem productivity (*NEP*) across sites (Fig. 1.2a). These findings align with previous research showing that soil CO_2 pulses contribute 5-10% of annual *NEP* in a midlatitude forest, with carbon losses during pulse events being comparable to the annual *NEP* of many ecosystems (Lee et al., 2004; L. Xu et al., 2004).

Despite this substantial contribution, we found that all four existing eddy-covariance partitioning methods significantly underestimate R_{eco} and *GPP* during the pulse events when compared our FluxPulse bias-corrected fluxes (Fig. 1.2b). Underestimation for R_{eco} ranged from 13.4±9.4% to 26.7±9.0%, while *GPP* ranged from 17.8±11.7% to 33.8±14.2% (Fig. 1.2b, c). Since *GPP* is estimated as the difference between R_{eco} and *NEE*, any underestimation of R_{eco} directly affects *GPP* estimates (Fig. 1.1).

The four partitioning methods examined include parametric approaches (Nighttime method (NT) (Reichstein et al., 2005) and Daytime method (DT) (Lasslop et al., 2010)) and machine learning methods (Double machine learning (DML) (Cohrs et al., 2024) and artificial neural networks (NN) (Tramontana et al., 2020)) (see Methods). We performed a one-tailed paired t-test to compare partitioning methods, which revealed a clear ranking of R_{eco} underestimation during pulse events, with: NN (13.4±9.4%) < DML (17.9±9.7%) < NT (22.9±10.7%), DT (26.7±9.0%) ($p < 0.01$) (Fig. 1.2b). The NN approach underestimates R_{eco} the least, followed by the DML approach, while the NT and DT methods exhibit similar underestimations. Regarding *GPP* during pulse events, the NT method shows the largest bias ($p < 0.01$): NT (33.8±14.2%), DT (17.8±11.7%), DML (20.9±12.4%), NN (18.2±11.2%) (Fig. 1.2b).

Among the four partitioning methods assessed, machine learning approaches (Neural Network (NN), Double Machine Learning (DML)) underestimate R_{eco} the least, highlighting their improved performance at capturing non-steady-state events compared to the parametric approaches assessed (Tramontana et al., 2020). The underestimation of R_{eco} also leads to underestimation of *GPP*, particularly in methods where *GPP* is calculated as R_{eco} minus *NEE*. The Nighttime method (NT) shows the

largest GPP underestimations (Fig. 1.2b), often leading to systematic negative half-hourly *GPP* during the first few days of pulse events (Jung et al., 2024).

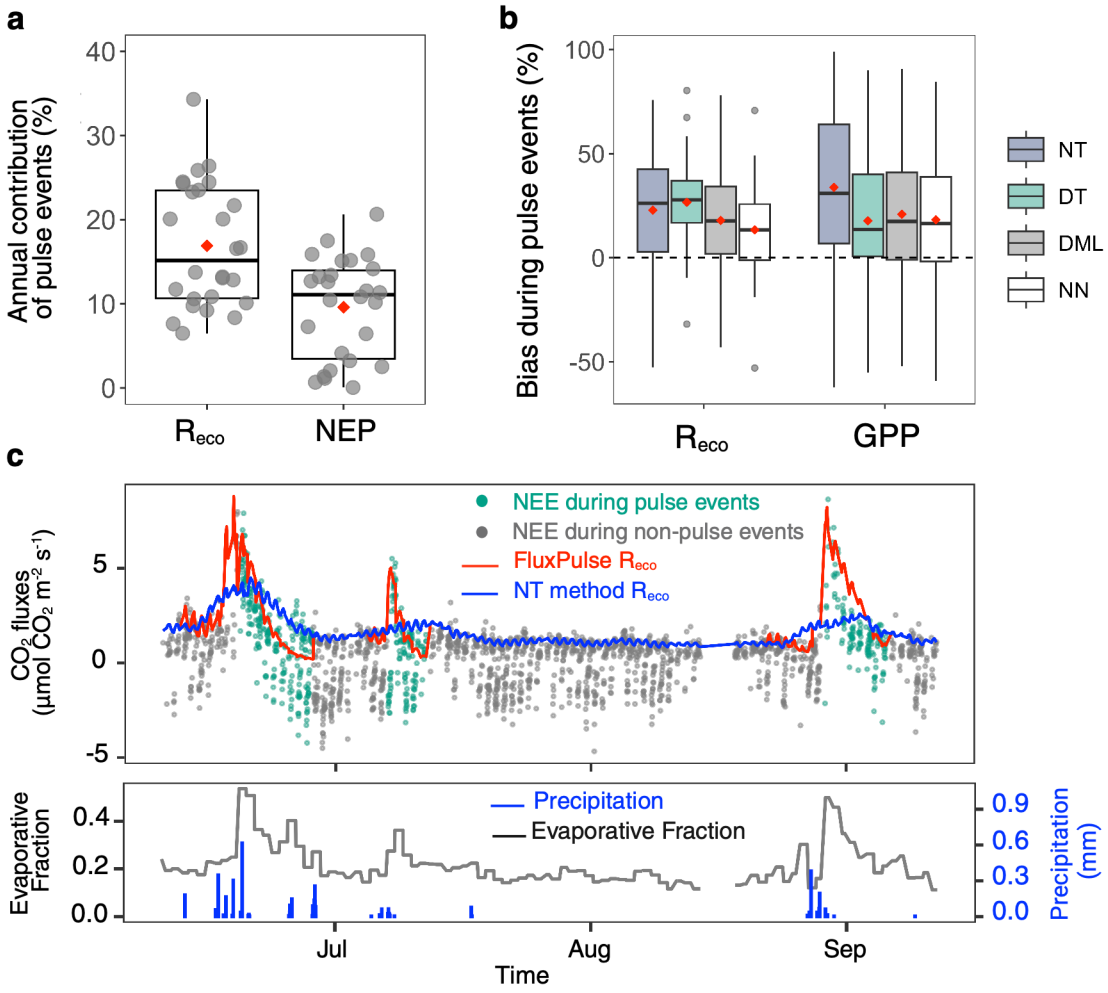


Figure 1.2. Partitioning methods underestimate pulse event CO_2 fluxes. *(a) Contributions of ecosystem respiration (R_{eco}) and net ecosystem productivity (NEP) during pulse events to annual R_{eco} and NEP. Pulse event contribution (%) at each individual site is calculated as* $\frac{sum(x)}{sum(y)} \times 100$*, in which x is FluxPulse bias-corrected half-hourly R_{eco} or NEP during pulse events and y is all available half-hourly bias-corrected R_{eco} or NEP (Two sites whose NEP contribution values greater than three times of standard deviation were removed in the boxplots for visualization purposes).*

(b) Performance of partitioning methods on estimating ecosystem respiration (R_{eco}) and gross primary productivity (GPP) during pulse events. Fluxes estimated from four methods were compared to the FluxPulse bias-corrected R_{eco} and GPP, which are the Nighttime method (NT), the Daytime method (DT), Double Machine Learning (DML), and Neural Network (NN) (see Methods). The flux underestimation is calculated as $\frac{sum(x)-sum(y)}{sum(x)} \times 100$*, in which x is the FluxPulse half-hourly R_{eco} or GPP and y is the partitioned half-hourly R_{eco} or GPP from different partitioning methods. Thus, positive y values indicate flux underestimations, while negative y values indicate flux overestimations. In Fig. 1.2(a) and (b), 28/34 sites whose FluxPulse significantly reduces biases ($p < 0.001$, Extended Data Fig. 1.6) are included. The boxes represent interquartile range (IQR) marked with 25th, 50th, 75th percentile and whiskers extending to 1.5 times the IQR. The red diamonds represent the mean of the boxplots. In Fig. 1.2(b), all boxplots have the mean of distribution statistically greater than 0 (one-tailed paired t-test, $p < 0.01$). (c) Half-hourly time series visualization of Net Ecosystem Exchange (NEE), Ecosystem Respiration estimated by the FluxPulse bias-corrected algorithm (FluxPulse R_{eco}) and by the Nighttime method (NT method R_{eco}) at the Albuera site, Spain (ES-Abr) in 2017. NEE points corresponding to pulse events are manually labeled in green, while others are labeled in black. The red line represents FluxPulse bias-corrected R_{eco}, and the blue line represents R_{eco} estimated by the nighttime (NT) method. In the lower graph, the black line shows the daytime evaporative fraction (EF), calculated daily. The blue bars are precipitation downscaled from ERA-Interim reanalysis data products, with half-hourly resolution. A sharp rise in EF and increased precipitation indicates the occurrence of pulse events and net CO_2 pulses.*

Actual biases in existing methods for estimating R_{eco} and *GPP* during pulse events could be much higher than those reported here. Our approach assumes minimal *GPP* during the first day of pulse events, using maximum *NEE* to estimate maximum R_{eco}, given that *GPP* estimates are not reliable during pulse events (see Methods). Minimal *GPP* at the beginning of pulse events could happen in some sites due to the intensive pre-pulse dryness; however, we demonstrate that this is not the case in most sites

(Extended Data Fig. 1.7). Even though the underestimates we quantified are conservative, our FluxPulse bias-correction method significantly reduces biases compared to existing partitioning methods, providing more reliable estimates of carbon fluxes during pulse events.

1.3.2. Convergence in decay rate of rain-induced carbon pulses

Analyzing more than 1800 pulse events, we found that rain-induced carbon pulses decay exponentially after rain events in 85% of sites, following a universal exponential decay pattern (Fig. 1.3a). The intensity and decay rates of these pulses are primarily governed by environmental factors related to vegetation growth, climate, and soil properties (Fig. 1.3b, c). We calculated site-specific pulse intensity (α_s) and decay rate (k_s) by fitting a 1st-order kinetic reaction function to the daily maximum *NEE* across all pulse events at each site (Fig. 1.3a). The site-specific pulse intensity represents the maximum magnitude of rain-induced carbon losses at a site, and the site-specific decay rate represents how fast the carbon losses decay over time (Equation 1).

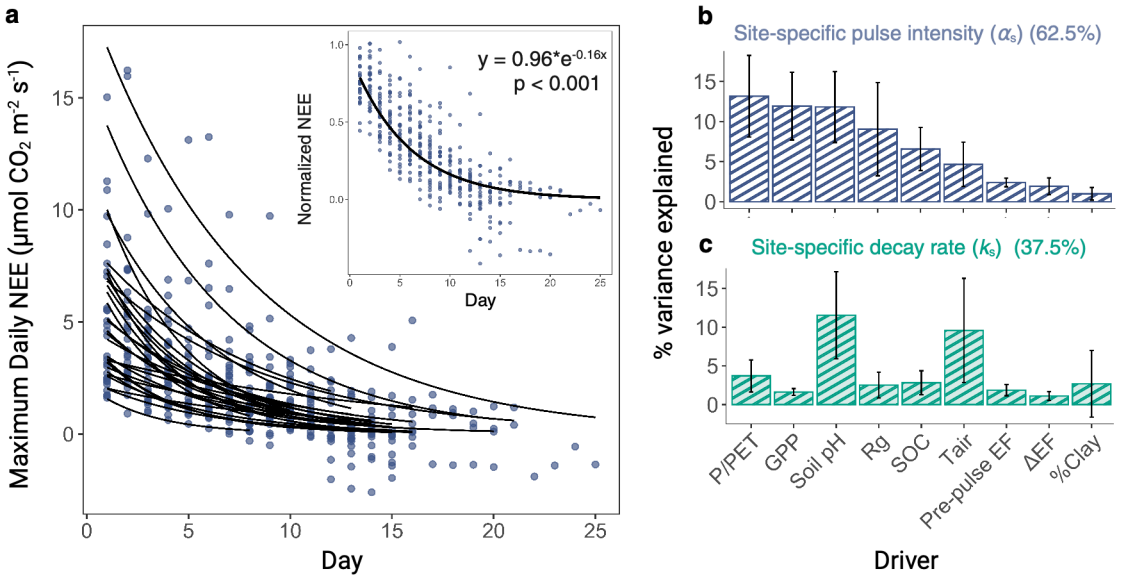


Figure 1.3. Rain-induced CO_2 pulses decay across sites. *(a) Net ecosystem exchange (NEE) declines over time during pulse events across 29/34 sites with statistically significant site-specific decay rate ($p < 0.05$; the p value is derived from*

the statistical test for parameter estimates when fitting the decay function to the data). The y-axis of the outer graph is the maximum of daily mean NEE from all pulse events from one site, the x-axis is the number of days after the pulse event starts, assuming that rainfall starts on day 1. The 1st-order kinetic reaction function is fitted for each site and displayed as black lines (Equation 1). The inset presents the same data but normalized by site-specific pulse intensity (α_s)*, and reveals a convergent decay rate across sites (k_s = 0.16 ± 0.01, $p < 0.001$). (b, c) Relative importance analysis of nine predictors for site-specific pulse intensity (α_s) (b) and decay rate (k_s) (c) across 29/34 sites. Predictors related to soil characteristics are clay percentage (%Clay), soil organic carbon from 0-5 cm (SOC) (g kg^{-1}), and soil pH. The predictor representing vegetation productivity is annual GPP obtained from the Nighttime (NT) partitioning method (μmol CO_2 m^{-2} s^{-1}). Predictors representing hydrologic conditions are aridity index (P/PET), rewetting intensity (ΔEF), and antecedent water availability (Pre-pulse EF). Predictors representing climatic conditions are global shortwave radiation (R_g) (W m^{-2}), and air temperature (T_{air}) (°C). Data in the bar plots are presented as mean value ± standard deviation. The standard deviation of the bars is calculated by bootstrap sampling (100 times resampling with replacement). All predictors explain 62.5% and 37.5% of the variance in the site-specific pulse intensity and decay rate respectively.*

When normalizing the *NEE* rain-pulse response curves by site-specific pulse intensity, the response curves across sites converge to a universal decaying function ($y = 0.96 \times e^{-0.16x}$) (Fig. 1.3a). This indicates a consistent response of soil microbes to rain pulses, likely due to the strong relationship between soil microbes, soil water potential and evaporation (Orchard & Cook, 1983). Prior studies have shown that cumulative soil evaporation follows a square root of time as the soil dries (Gardner, 1959), further supporting this convergence. Our finding of the convergent decay rate could facilitate the future incorporation of the rain-pulse effect into large-scale ecosystem models. The decaying pattern of net CO_2 flux over time likely results from resource depletion (labile carbon, nitrogen, water availability, etc.), changes in microbial community composition (Placella et al., 2012), and vegetation growth triggered by pulse events which off-sets CO_2 release. The widespread decay pattern highlights the biological influence of rainfall on ecosystem processes beyond abiotic

influences, reinforcing the importance of the Birch effect in dryland carbon cycling. Our findings align with previous regional and laboratory studies (Birch, 1958; Jarvis et al., 2007; Jenerette et al., 2008; L. Xu et al., 2004), confirming the widespread occurrence of the Birch effect in global drylands.

Multiple environmental factors influence the spatial dynamics of net carbon fluxes during pulse events. The three strongest predictors for the site-specific pulse intensity (α_s) across sites are aridity index (*P/PET*), *GPP*, and soil *pH*, together with other factors explaining 62.5% variance (Fig. 1.3b). α_s increases with Aridity index (*P/PET*) and *GPP* but decreases with soil pH (Extended Data Fig. 1.9). For the site-specific decay rate (k_s), soil *pH* and air temperature were important predictors, with k_s increasing with soil pH and temperature (Extended Data Fig. 1.8). However, compared to α_s, environmental factors explain only 37.5% of variance in k_s (Fig. 1.3b, c). Regarding hydrologic factors, we used Evaporative Fraction (*EF*), the fraction of available energy allocated to evapotranspiration, as a proxy of soil water availability and rainfall occurrence (see Methods). Despite exhibiting a strong temporal correlation with pulse intensity and size, pre-pulse *EF* (the 14-day average EF before a pulse event) and *ΔEF* (a measure of the rewetting intensity) do not significantly explain the spatial variability of net CO_2 pulses during pulse events, (Fig. 1.3b, c; Fig. 1.4c; Extended Data Fig. 1.1.4).

Our results show that vegetation productivity is key to initial rewetting responses, as more productive sites supply more labile carbon through root exudation and plant litter, enhancing microbial decomposition (Fig. 1.3b, c) (Barnard, 2020; Tang et al., 2005; L. Xu et al., 2004). This also explains why soil organic carbon (*SOC*) shows little explanatory power for the spatial distribution of pulse characteristics (Fig. 1.3b, c), since *SOC* composition (e.g., labile vs. recalcitrant *SOC*) is likely more important than total *SOC* in sustaining the Birch effect (Fig. 1.3b, c) (Deng et al., 2017; Fierer & Schimel, 2003). Besides *GPP*, aridity index (*P/PET*) is a major predictor of pulse intensity across sites (Fig. 1.3b). Among all dry sites, wetter sites have higher pulse intensity (Extended Data Fig. 1.9). This suggests that wetter dryland sites have sufficient moisture to enhance vegetation growth, supplying substrates for microbial decomposition, while they are still dry enough for the Birch effect to occur.

Among all environmental factors, soil *pH* is a top predictor of both site-

specific pulse intensity and decay rate (Fig. 1.3b, c). Previous studies have highlighted the influence of soil *pH* on microbial composition (Chapin et al., 2011; Dacal et al., 2019; Fierer et al., 2009; Lauber et al., 2009; Schneider et al., 2012; Sinsabaugh et al., 2008; Tripathi et al., 2018), with soil microbial diversity peaks at near-neutral soil pH at a continental scale (Lauber et al., 2009). In our study, we also observe that the site-specific pulse intensity peaks at a pH of 6 and gradually declines as the pH increases to 8 (Extended Data Fig. 1.9). This could be attributed to various soil characteristics associated with soil pH, as well as physiological constraints on soil bacteria under extremely acidic or alkaline conditions (Lauber et al., 2009). Our validation of SoilGrids *pH* against site-specific measurements confirms soil *pH* measurement robustness (Extended Data Fig. 1.3). Our study shows that soil *pH* is an important spatial driver of rain-induced carbon pulses, potentially due to its influence on soil microbial dynamics.

1.3.3. Detecting and characterizing rain-induced carbon pulses

Rain-induced CO_2 pulse events are non-steady-state ecological processes, making them challenging to detect and model across sites. Nevertheless, automated pulse detection is now possible, given the large amount of data and a better understanding of the complexity of rain-pulse responses. We developed an automated detection framework using a random forest binary classification algorithm, in addition to manually labeling pulse events (see Methods). Our results demonstrate that although performance varies across sites, which is possibly due to data quality and site-specific measurement uncertainties, such automated detection is applicable across diverse ecosystems. We successfully detected at least 60% of pulse events in 15/28 sites (Fig. 1.4a). Detection is most effective for major pulse events—those with net positive CO_2 emissions, with 76% of pulses whose size between 10 to 15 μmol CO_2 m^{-2} s^{-1} being correctly detected across sites (Fig. 1.4b).

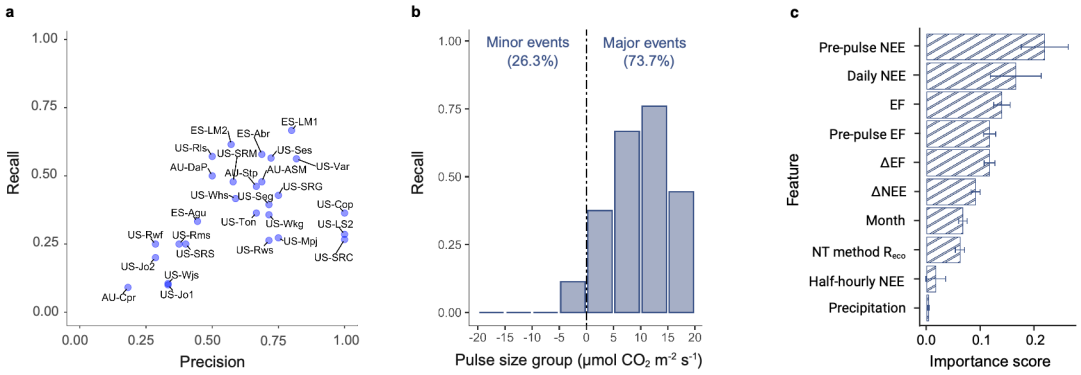


Figure 1.4. Random forest performance for detecting pulse events. *(a) Performance for detecting the start date of pulse events (within ±2 days error) across 28 qualified sites (Supplementary Table 1 for more details). Precision is the fraction of pulse events the model detected that were real, while recall is the fraction of actual pulse events that were successfully detected by the model. (b) Recall rate for different pulse size groups (divided into equal intervals of 5 μmol CO_2 m^{-2} s^{-1}, ranging from -20 to 20 μmol CO_2 m^{-2} s^{-1}). The dashed line x = 0 defines major (x > 0) and minor (x < 0) pulse events based on the size of net CO_2 pulses. Major pulse events (73.7% of the testing set) are defined as carbon sources, while minor pulse events (26.3%) are carbon sinks. (c) Feature importance score for all variables used in the random forest model to detect pulse events across 28 sites. Data are presented as mean value ± standard deviation of accumulation of the impurity decrease for each feature within each decision tree.*

We used two common classification metrics to evaluate model performance: precision and recall. Precision is the fraction of detected pulse events that are actual pulse events, while recall is the fraction of actual pulse events correctly detected by the model. Actual pulse events, in this case, are manually labelled pulse events. For example, if 12 pulse events occur, and the model detects 10 events with only 7 of them being real, then precision is 7/10 (70%) and recall is 7/12 (58%) (see Methods). Across sites, the model achieves a precision greater than 0.60 at 15/28 sites (Fig. 1.4a). Recall rates are generally lower than precision, with the highest recall rate (0.67) observed at the ES-LM1 site (Fig. 1.4a; Supplementary Table 1). Recall improves with the net CO_2 pulse size, reaching 0.76 for pulses ranging from 10-15 μmol CO_2 m^{-2} s^{-1}

(Fig. 1.4b). Although the model did not effectively capture pulse events with negative pulse sizes, it performed well on most pulse events (73.7% of the pulse events in the testing set), particularly those with positive pulse sizes (Fig. 1.4b).

Among the features used for classification (see Methods), pre-pulse *NEE* and daily mean *NEE* are the two most important predictors of the forest detection algorithm (Fig. 1.4c), meaning that ecosystem status before pulse events is crucial to detecting them. Pulse occurrence is more likely with positive pre-pulse *NEE*, and less likely with negative pre-pulse *NEE* values when vegetation is active (Extended Data Fig. 1.10). In a woody savanna, the magnitude of CO_2 pulses has also been shown to be inversely correlated with pre-pulse R_{eco} (L. Xu et al., 2004).

Additionally, *EF*-derived indices (*EF*, antecedent water availability (Pre-pulse *EF*), and rewetting intensity (*ΔEF*)) accurately describe temporal variability in pulse characteristics and improve machine learning detection performance (Fig. 1.3b, c; Fig. 1.4c; Extended Data Fig. 1.4). Lower pre-pulse *EF* and higher *EF* associate with a higher chance of pulse events (Extended Data Fig. 1.10). Furthermore, our analysis across multiple sites indicates that more intense rewetting events (*ΔEF*) and drier pre-pulse periods (pre-pulse *EF*) are linked with higher pulse intensity (Δ*NEE*) and greater pulse size (Extended Data Fig. 1.4). This indicates that larger pulses are more likely after prolonged dry periods followed by intense rewetting. Our findings suggest that under future scenarios of more intense precipitation and prolonged dry intervals, rain-induced carbon losses will likely intensify (Feldman et al., 2024).

Including site-static variables (e.g., soil *pH*, vegetation productivity, aridity index) does not enhance model performance, though adding month as a temporal variable enhances results (Fig. 1.4c). Interestingly, precipitation is not a significant predictor of pulse occurrence or intensity (Fig. 1.4c; Extended Data Fig. 1.4), most likely because *EF* already captures rainfall effects, and not all rainfall events trigger CO_2 pulses.

Overall, *EF* is an integrated index that captures water dynamics, including the wetting intensity and antecedent water availability. Compared to precipitation, *EF*-derived indices play an important role in the pulse detection algorithm (Fig. 1.4c) and they significantly correlate with pulse intensity and size across most sites (Extended Data Fig. 1.4). While precipitation is undoubtedly a major driver of rain-induced CO_2

pulses, its direct influence is difficult to detect due to under-report rainfall from using the tipping bucket method and landscape heterogeneity (Gebler, 2015; Legates & DeLiberty, 1993). *EF*, which integrates both wetting intensity and antecedent water availability, could thus be a promising index for water availability particularly at eddy-covariance sites where precipitation and soil moisture data are limited.

While the start date of pulse events is typically well-defined, determining the end date is more ambiguous, as the end date corresponds to the system either returning to pre-pulse conditions or reaching a stabilized state. However, since carbon emissions are greatest in the first few days of pulse events, potential misidentification of the end date is unlikely to significantly impact overall CO_2 loss estimates. Future work should further optimize detection algorithms and test whether rain-induced CO_2 pulses occur in other biomes whose high vegetation activity could mask their signals. Overall, the random forest gives insight into the drivers of pulse responses, enabling a deeper understanding of pulse responses in dryland ecosystems.

1.4. Conclusions

Drylands drive the interannual variability and trend of global land carbon sink, but the processes underlying the rain-induced carbon losses responsible for carbon flux variability have not been widely incorporated in terrestrial ecosystem carbon models (Metz et al., 2023). Our study demonstrates that rain-induced carbon losses follow a significant and consistent decay pattern across sites, and contribute significantly to the carbon balance of drylands (16.9±2.8% of annual ecosystem respiration and 9.6±2.2% of annual net ecosystem productivity). We show that existing partitioning methods substantially underestimate carbon fluxes in drylands, potentially affecting higher-level ecosystem carbon models and upscaling studies that rely on flux partitioned data. We resolve persistent biases in current eddy-covariance partitioning methods by providing FluxPulse, a bias-corrected dataset of ecosystem carbon fluxes in drylands. Our results highlight the importance of effectively incorporating rain-induced carbon losses from pulse events into models from site to global scales. This is particularly important given the projected expansion of drylands in the 21st century (J. Huang et al., 2016) and rapid changes in global

precipitation patterns favoring more intense and less frequent rainfall (Feldman et al., 2024).

1.5. Acknowledgments

This research received support through Schmidt Sciences, LLC., with a research exchange experience to the European Commission, Joint Research Centre in Ispra, Italy supported by the NSF FLUXNET AccelNet program (award #2113978). MB acknowledges support from the U.S. Department of Agriculture National Institute of Food and Agriculture (award# 2023-67012-40086). DP thanks the support of the ITINERIS project (ID IR0000032) funded by EU - Next Generation EU Mission 4 - Investment 3.1. TFK acknowledges support from a DOE Early Career Research Program award #DE-SC0021023 and NASA Awards 80NSSC21K1705 and 80NSSC20K1801. MB and TFK acknowledge support from NASA award # 80NSSC25K7327. MR and KHC acknowledge funding by the European Research Council (ERC) Synergy Grant Understanding and Modeling the Earth System with Machine Learning (USMILE) under the Horizon 2020 research and innovation programme (Grant agreement No. 855187). Thanks to Dr. David Miller from Cornell University for proof-reading the manuscript and providing the aridity index dataset based on the TerraClimate precipitation and potential evapotranspiration data. Thanks to Dr. Trang TH Nguyen, Joseph Verfaillie, Dr. Ronald Amundson, and scientists at Max Planck Institute for Biogeochemistry, Germany for valuable feedback on the mechanisms of the soil carbon pulses. The figures were created with the assistance of BioRender.com. The authors thank the AmeriFlux, ICOS and FLUXNET communities for the unique data contributions.

1.6. Data availability

Eddy covariance sites are obtained from FLUXNET (www.fluxnet.org), AmeriFlux (www.ameriflux.lbl.gov), and ICOS (Integrated Carbon Observation System) Warm Winter 2020 (www.icos-cp.eu). Soil properties are obtained from Soilgrids (www.soilgrids.org). The manual pulse labeling dataset, FluxPulse bias-corrected eddy-covariance datasets, and datasets used to generate the figures are publicly accessible at https://github.com/ngocnguyen99/FluxPulse.

1.7. Bibliography

Abatzoglou, J. T., Dobrowski, S. Z., Parks, S. A., & Hegewisch, K. C. (2018). TerraClimate, a high-resolution global dataset of monthly climate and climatic water balance from 1958–2015. *Scientific Data*, *5*(1), 170191. https://doi.org/10.1038/sdata.2017.191

Ahlström, A., Raupach, M. R., Schurgers, G., Smith, B., Arneth, A., Jung, M., Reichstein, M., Canadell, J. G., Friedlingstein, P., Jain, A. K., Kato, E., Poulter, B., Sitch, S., Stocker, B. D., Viovy, N., Wang, Y. P., Wiltshire, A., Zaehle, S., & Zeng, N. (2015). The dominant role of semi-arid ecosystems in the trend and variability of the land CO2 sink. *Science*, *348*(6237), 895–899. https://doi.org/10.1126/science.aaa1668

Babst, F., Bouriaud, O., Papale, D., Gielen, B., Janssens, I. A., Nikinmaa, E., Ibrom, A., Wu, J., Bernhofer, C., Köstner, B., Grünwald, T., Seufert, G., Ciais, P., & Frank, D. (2014). Above-ground woody carbon sequestration measured from tree rings is coherent with net ecosystem productivity at five eddy-covariance sites. *New Phytologist*, *201*(4), 1289–1303. https://doi.org/10.1111/nph.12589

Bacastow, R., & Keeling, C. K. (1973). Atmospheric carbon dioxide and radiocarbon in the natural carbon cycle: II. Changes from A. D. 1700 to 2070 as deduced from a geochemical model. *Brookhaven Symposia in Biology*, (30), 86–135.

Baldocchi, D. (2014). Measuring fluxes of trace gases and energy between ecosystems and the atmosphere – the state and future of the eddy covariance method. *Global Change Biology*, *20*(12), 3600–3609. https://doi.org/10.1111/gcb.12649

Baldocchi, D. D. (2020). How eddy covariance flux measurements have contributed to our understanding of Global Change Biology. *Global Change Biology*, *26*(1), 242–260. https://doi.org/10.1111/gcb.14807

Baldocchi, D., Falge, E., Gu, L., Olson, R., Hollinger, D., Running, S., null, Anthoni, P., Bernhofer, C., Davis, K., Evans, R., Fuentes, J., Goldstein, A., Katul, G., Law, B., Lee, X., Malhi, Y., Meyers, T., Munger, W., Oechel, W., … Wofsy, S. (2001). FLUXNET: A new tool to study the temporal and spatial variability of ecosystem-scale carbon dioxide, water vapor, and energy flux densities.

Bulletin of the American Meteorological Society, *82*(11), 2415–2434. https://doi.org/10.1175/1520-0477(2001)082%3C2415:FANTTS%3E2.3.CO;2

Barnard, R. L. (2020). Rewetting of soil: Revisiting the origin of soil CO2 emissions. *Soil Biology and Biochemistry*.

Birch, H. F. (1958). The effect of soil drying on humus decomposition and nitrogen availability. *Plant and Soil*, *10*(1), 9–31. https://doi.org/10.1007/BF01343734

Bottner, P. (1985). Response of microbial biomass to alternate moist and dry conditions in a soil incubated with 14C- and 15N-labelled plant material. *Soil Biology and Biochemistry*, *17*(3), 329–337. https://doi.org/10.1016/0038-0717(85)90070-7

Breiman, L., Friedman, J., Olshen, R. A., & Stone, C. J. (2017). *Classification and Regression Trees*. Chapman and Hall/CRC. https://doi.org/10.1201/9781315139470

Broeckx, L. S., Verlinden, M. S., Berhongaray, G., Zona, D., Fichot, R., & Ceulemans, R. (2014). The effect of a dry spring on seasonal carbon allocation and vegetation dynamics in a poplar bioenergy plantation. *GCB Bioenergy*, *6*(5), 473–487. https://doi.org/10.1111/gcbb.12087

Brown, C. F., Kazmierski, M. R., Pasquarella, V. J., Rucklidge, W. J., Samsikova, M., Zhang, C., Shelhamer, E., Lahera, E., Wiles, O., Ilyushchenko, S., Gorelick, N., Zhang, L. L., Alj, S., Schechter, E., Askay, S., Guinan, O., Moore, R., Boukouvalas, A., & Kohli, P. (2025). *AlphaEarth Foundations: An embedding field model for accurate and efficient global mapping from sparse label data* (arXiv:2507.22291). arXiv. https://doi.org/10.48550/arXiv.2507.22291

Bu, J., & Xiao, J. (2025). Upscaling eddy covariance measurements of carbon and water fluxes to the continental scale by incorporating GEDI-derived canopy structural complexity metrics. *Remote Sensing of Environment*, *329*, 114930. https://doi.org/10.1016/j.rse.2025.114930

Burba, G. (2022). *Eddy covariance method for scientific, regulatory, and commercial applications*. LI-COR Biosciences. https://books.google.com/books?hl=en&lr=&id=acKEEAAAQBAJ&oi=fnd&pg=PA1&dq=Eddy+Covariance+Method+for+Scientific,+Regulatory,+and+C

ommercial+Applications&ots=BE9CiHBLZy&sig=OVSnaD2X5VrmAkdIxvT2uuyZDpI

Cabon, A., Kannenberg, S. A., Arain, A., Babst, F., Baldocchi, D., Belmecheri, S., Delpierre, N., Guerrieri, R., Maxwell, J. T., McKenzie, S., Meinzer, F. C., Moore, D. J. P., Pappas, C., Rocha, A. V., Szejner, P., Ueyama, M., Ulrich, D., Vincke, C., Voelker, S. L., … Anderegg, W. R. L. (2022). Cross-biome synthesis of source versus sink limits to tree growth. *Science*, *376*(6594), 758–761. https://doi.org/10.1126/science.abm4875

Cabon, A., Peters, R. L., Fonti, P., Martínez-Vilalta, J., & De Cáceres, M. (2020). Temperature and water potential co-limit stem cambial activity along a steep elevational gradient. *New Phytologist*, *226*(5), 1325–1340. https://doi.org/10.1111/nph.16456

Campioli, M., Vicca, S., Luyssaert, S., Bilcke, J., Ceschia, E., Chapin III, F. S., Ciais, P., Fernández-Martínez, M., Malhi, Y., Obersteiner, M., Olefeldt, D., Papale, D., Piao, S. L., Peñuelas, J., Sullivan, P. F., Wang, X., Zenone, T., & Janssens, I. A. (2015). Biomass production efficiency controlled by management in temperate and boreal ecosystems. *Nature Geoscience*, *8*(11), 843–846. https://doi.org/10.1038/ngeo2553

Chapin, F. S., Matson, P. A., & Vitousek, P. M. (2011). *Principles of Terrestrial Ecosystem Ecology*. Springer. https://doi.org/10.1007/978-1-4419-9504-9

Chen, S., Lin, G., Huang, J., & Jenerette, G. D. (2009). Dependence of carbon sequestration on the differential responses of ecosystem photosynthesis and respiration to rain pulses in a semiarid steppe. *Global Change Biology*, *15*(10), 2450–2461. https://doi.org/10.1111/j.1365-2486.2009.01879.x

Chen, T., & Guestrin, C. (2016). XGBoost: A Scalable Tree Boosting System. *Proceedings of the 22nd ACM SIGKDD International Conference on Knowledge Discovery and Data Mining*, 785–794. https://doi.org/10.1145/2939672.2939785

Chu, H., Baldocchi, D. D., John, R., Wolf, S., & Reichstein, M. (2017). Fluxes all of the time? A primer on the temporal representativeness of FLUXNET. *Journal of Geophysical Research: Biogeosciences*, *122*(2), 289–307. https://doi.org/10.1002/2016JG003576

Chu, H., Luo, X., Ouyang, Z., Chan, W. S., Dengel, S., Biraud, S. C., Torn, M. S., Metzger, S., Kumar, J., Arain, M. A., Arkebauer, T. J., Baldocchi, D., Bernacchi, C., Billesbach, D., Black, T. A., Blanken, P. D., Bohrer, G., Bracho, R., Brown, S., … Zona, D. (2021). Representativeness of Eddy-Covariance flux footprints for areas surrounding AmeriFlux sites. *Agricultural and Forest Meteorology*, *301–302*, 108350. https://doi.org/10.1016/j.agrformet.2021.108350

Chu, H., Metzger, S., Ouyang, Z., Griebel, A., Yi, K., Durden, D., Wolf, S., Kasak, K., Rey-Sanchez, C., Hernandez Rodriguez, L. C., Oikawa, P., Falco, N., Runkle, B. R. K., Ahmadi, A., & Matthes, J. (2026). Flux Footprints: A Critical Link to Bridge Eddy-Covariance Measurements With Models, Remote Sensing, and Other Observations. *Global Change Biology*, *32*(4), e70887. https://doi.org/10.1111/gcb.70887

Cohrs, K.-H., Varando, G., Carvalhais, N., Reichstein, M., & Camps-Valls, G. (2024). Causal hybrid modeling with double machine learning—Applications in carbon flux modeling. *Machine Learning: Science and Technology*. https://doi.org/10.1088/2632-2153/ad5a60

Dacal, M., Bradford, M. A., Plaza, C., Maestre, F. T., & García-Palacios, P. (2019). Soil microbial respiration adapts to ambient temperature in global drylands. *Nature Ecology & Evolution*, *3*(2), 232–238. https://doi.org/10.1038/s41559-018-0770-5

Delire, C., Séférian, R., Decharme, B., Alkama, R., Calvet, J.-C., Carrer, D., Gibelin, A.-L., Joetzjer, E., Morel, X., Rocher, M., & Tzanos, D. (2020). The Global Land Carbon Cycle Simulated With ISBA-CTRIP: Improvements Over the Last Decade. *Journal of Advances in Modeling Earth Systems*, *12*(9), e2019MS001886. https://doi.org/10.1029/2019MS001886

Delwiche, K., Matthes, J. H., Arias-Ortiz, A., Knox, S. H., Oikawa, P., Sturtevant, C., Verfaillie, J., Szutu, D., Keenan, T. F., & Baldocchi, D. (2025). Dynamic methane emissions in a restored wetland: Decadal insights into uncertain climate outcomes and critical science needs. *Agricultural and Forest Meteorology*, *373*, 110735. https://doi.org/10.1016/j.agrformet.2025.110735

Deng, Q., Hui, D., Chu, G., Han, X., & Zhang, Q. (2017). Rain-induced changes in soil CO2 flux and microbial community composition in a tropical forest of China. *Scientific Reports*, *7*(1), 5539. https://doi.org/10.1038/s41598-017-06345-2

El-Madany, T. S., Reichstein, M., Perez-Priego, O., Carrara, A., Moreno, G., Pilar Martín, M., Pacheco-Labrador, J., Wohlfahrt, G., Nieto, H., Weber, U., Kolle, O., Luo, Y.-P., Carvalhais, N., & Migliavacca, M. (2018). Drivers of spatio-temporal variability of carbon dioxide and energy fluxes in a Mediterranean savanna ecosystem. *Agricultural and Forest Meteorology*, *262*, 258–278. https://doi.org/10.1016/j.agrformet.2018.07.010

Fatichi, S., Leuzinger, S., & Körner, C. (2014). Moving beyond photosynthesis: From carbon source to sink-driven vegetation modeling. *New Phytologist*, *201*(4), 1086–1095. https://doi.org/10.1111/nph.12614

Fatichi, S., Pappas, C., Zscheischler, J., & Leuzinger, S. (2019). Modelling carbon sources and sinks in terrestrial vegetation. *New Phytologist*, *221*(2), 652–668. https://doi.org/10.1111/nph.15451

Feldman, A. F., Feng, X., Felton, A. J., Konings, A. G., Knapp, A. K., Biederman, J. A., & Poulter, B. (2024). Plant responses to changing rainfall frequency and intensity. *Nature Reviews Earth & Environment*, *5*(4), 276–294. https://doi.org/10.1038/s43017-024-00534-0

Feldman, A. F., Short Gianotti, D. J., Konings, A. G., McColl, K. A., Akbar, R., Salvucci, G. D., & Entekhabi, D. (2018). Moisture pulse-reserve in the soil-plant continuum observed across biomes. *Nature Plants*, *4*(12), 1026–1033. https://doi.org/10.1038/s41477-018-0304-9

Fierer, N., Grandy, A. S., Six, J., & Paul, E. A. (2009). Searching for unifying principles in soil ecology. *Soil Biology and Biochemistry*, *41*(11), 2249–2256. https://doi.org/10.1016/j.soilbio.2009.06.009

Fierer, N., & Schimel, J. P. (2003). A Proposed Mechanism for the Pulse in Carbon Dioxide Production Commonly Observed Following the Rapid Rewetting of a Dry Soil. *Soil Science Society of America Journal*, *67*(3), 798–805. https://doi.org/10.2136/sssaj2003.7980

Friedlingstein, P., Jones, M. W., O'Sullivan, M., Andrew, R. M., Bakker, D. C. E., Hauck, J., Le Quéré, C., Peters, G. P., Peters, W., Pongratz, J., Sitch, S., Canadell, J. G.,

Ciais, P., Jackson, R. B., Alin, S. R., Anthoni, P., Bates, N. R., Becker, M., Bellouin, N., … Zeng, J. (2022). Global Carbon Budget 2021. *Earth System Science Data*, *14*(4), 1917–2005. https://doi.org/10.5194/essd-14-1917-2022

Friedlingstein, P., Le Quéré, C., O'Sullivan, M., Hauck, J., Landschützer, P., Luijkx, I. T., Li, H., van der Woude, A., Schwingshackl, C., Pongratz, J., Regnier, P., Andrew, R. M., Bakker, D. C. E., Canadell, J. G., Ciais, P., Gasser, T., Jones, M. W., Lan, X., Morgan, E., … Tian, H. (2026). Emerging climate impact on carbon sinks in a consolidated carbon budget. *Nature*, *649*(8095), 98–103. https://doi.org/10.1038/s41586-025-09802-5

Friedlingstein, P., O'Sullivan, M., Jones, M. W., Andrew, R. M., Bakker, D. C. E., Hauck, J., Landschützer, P., Le Quéré, C., Li, H., Luijkx, I. T., Peters, G. P., Peters, W., Pongratz, J., Schwingshackl, C., Sitch, S., Canadell, J. G., Ciais, P., Aas, K., Alin, S. R., … Zeng, J. (2025). *Global Carbon Budget 2025*. ESSD – Anthroposphere/Energy and anthropogenic emissions. https://doi.org/10.5194/essd-2025-659

Friend, A. D., Chen, Y., Eckes-Shephard, A. H., Fonti, P., Hellmann, E., Rademacher, T., Richardson, A. D., & Thomas, P. R. (2025). *Implications of source-sink feedbacks for modelling tree carbon assimilation and growth* (p. 2024.09.27.615358). bioRxiv. https://doi.org/10.1101/2024.09.27.615358

Friend, A. D., Eckes-Shephard, A. H., Fonti, P., Rademacher, T. T., Rathgeber, C. B. K., Richardson, A. D., & Turton, R. H. (2019). On the need to consider wood formation processes in global vegetation models and a suggested approach. *Annals of Forest Science*, *76*(2), Article 2. https://doi.org/10.1007/s13595-019-0819-x

Gaber, M., Kang, Y., Schurgers, G., & Keenan, T. (2024). Using automated machine learning for the upscaling of gross primary productivity. *Biogeosciences*, *21*(10), 2447–2472. https://doi.org/10.5194/bg-21-2447-2024

Gardner, W. R. (1959). Solutions of the Flow Equation for the Drying of Soils and Other Porous Media. *Soil Science Society of America Journal*, *23*(3), 183–187. https://doi.org/10.2136/sssaj1959.03615995002300030010x

Gebler, S. (2015). Actual evapotranspiration and precipitation measured by lysimeters: A comparison with eddy covariance and tipping bucket. *Hydrol. Earth Syst. Sci.*

Gessler, A., & Zweifel, R. (2024). Beyond source and sink control – toward an integrated approach to understand the carbon balance in plants. *New Phytologist*, *242*(3), 858–869. https://doi.org/10.1111/nph.19611

Gherardi, L. A., & Sala, O. E. (2019). Effect of interannual precipitation variability on dryland productivity: A global synthesis. *Global Change Biology*, *25*(1), 269–276. https://doi.org/10.1111/gcb.14480

Green, J. K., & Keenan, T. F. (2022). The limits of forest carbon sequestration. *Science (New York, N.Y.)*, *376*(6594), 692–693. https://doi.org/10.1126/science.abo6547

Grinsztajn, L., Oyallon, E., & Varoquaux, G. (2022). *Why do tree-based models still outperform deep learning on tabular data?* (arXiv:2207.08815). arXiv. http://arxiv.org/abs/2207.08815

Griscom, B. W., Adams, J., Ellis, P. W., Houghton, R. A., Lomax, G., Miteva, D. A., Schlesinger, W. H., Shoch, D., Siikamäki, J. V., Smith, P., Woodbury, P., Zganjar, C., Blackman, A., Campari, J., Conant, R. T., Delgado, C., Elias, P., Gopalakrishna, T., Hamsik, M. R., … Fargione, J. (2017). Natural climate solutions. *Proceedings of the National Academy of Sciences*, *114*(44), 11645–11650. https://doi.org/10.1073/pnas.1710465114

Haverd, V., Smith, B., Nieradzik, L., Briggs, P. R., Woodgate, W., Trudinger, C. M., Canadell, J. G., & Cuntz, M. (2018). A new version of the CABLE land surface model (Subversion revision r4601) incorporating land use and land cover change, woody vegetation demography, and a novel optimisation-based approach to plant coordination of photosynthesis. *Geoscientific Model Development*, *11*(7), 2995–3026. https://doi.org/10.5194/gmd-11-2995-2018

Hsiao, T. C. (1973). Plant Responses to Water Stress. *Annual Review of Plant Biology*, *24*(Volume 24, 1973), 519–570. https://doi.org/10.1146/annurev.pp.24.060173.002511

Huang, B., & Nobel, P. S. (1993). Hydraulic conductivity and anatomy along lateral roots of cacti: Changes with soil water status. *New Phytologist*, *123*(3), 499–507. https://doi.org/10.1111/j.1469-8137.1993.tb03762.x

Huang, J., Yu, H., Guan, X., Wang, G., & Guo, R. (2016). Accelerated dryland expansion under climate change. *Nature Climate Change*, *6*(2), 166–171. https://doi.org/10.1038/nclimate2837

Huxman, T. E., Cable, J. M., Ignace, D. D., Eilts, J. A., English, N. B., Weltzin, J., & Williams, D. G. (2004). Response of net ecosystem gas exchange to a simulated precipitation pulse in a semi-arid grassland: The role of native versus non-native grasses and soil texture. *Oecologia*, *141*(2), 295–305. https://doi.org/10.1007/s00442-003-1389-y

Huxman, T. E., Snyder, K. A., Tissue, D., Leffler, A. J., Ogle, K., Pockman, W. T., Sandquist, D. R., Potts, D. L., & Schwinning, S. (2004). Precipitation pulses and carbon fluxes in semiarid and arid ecosystems. *Oecologia*, *141*(2), 254–268. https://doi.org/10.1007/s00442-004-1682-4

Inglima, I., Alberti, G., Bertolini, T., Vaccari, F. P., Gioli, B., Miglietta, F., Cotrufo, M. F., & Peressotti, A. (2009). Precipitation pulses enhance respiration of Mediterranean ecosystems: The balance between organic and inorganic components of increased soil CO2 efflux. *Global Change Biology*, *15*(5), 1289–1301. https://doi.org/10.1111/j.1365-2486.2008.01793.x

Jarvis, P., Rey, A., Petsikos, C., Wingate, L., Rayment, M., Pereira, J., Banza, J., David, J., Miglietta, F., Borghetti, M., Manca, G., & Valentini, R. (2007). Drying and wetting of Mediterranean soils stimulates decomposition and carbon dioxide emission: The "Birch effect"†. *Tree Physiology*, *27*(7), 929–940. https://doi.org/10.1093/treephys/27.7.929

Jenerette, G. D., Scott, R. L., & Huxman, T. E. (2008). Whole ecosystem metabolic pulses following precipitation events. *Functional Ecology*, *22*(5), 924–930. https://doi.org/10.1111/j.1365-2435.2008.01450.x

Jiang, M., Medlyn, B. E., Drake, J. E., Duursma, R. A., Anderson, I. C., Barton, C. V. M., Boer, M. M., Carrillo, Y., Castañeda-Gómez, L., Collins, L., Crous, K. Y., De Kauwe, M. G., dos Santos, B. M., Emmerson, K. M., Facey, S. L., Gherlenda, A. N., Gimeno, T. E., Hasegawa, S., Johnson, S. N., … Ellsworth, D. S. (2020). The fate of carbon in a mature forest under carbon dioxide enrichment. *Nature*, *580*(7802), 227–231. https://doi.org/10.1038/s41586-020-2128-9

Joiner, J., & Yoshida, Y. (2020). Satellite-based reflectances capture large fraction of variability in global gross primary production (GPP) at weekly time scales. *Agricultural and Forest Meteorology*, *291*, 108092. https://doi.org/10.1016/j.agrformet.2020.108092

Jung, M., Koirala, S., Weber, U., Ichii, K., Gans, F., Camps-Valls, G., Papale, D., Schwalm, C., Tramontana, G., & Reichstein, M. (2019). The FLUXCOM ensemble of global land-atmosphere energy fluxes. *Scientific Data*, *6*(1), 74. https://doi.org/10.1038/s41597-019-0076-8

Jung, M., Nelson, J., Migliavacca, M., El-Madany, T., Papale, D., Reichstein, M., Walther, S., & Wutzler, T. (2024). *Technical note: Flagging inconsistencies in flux tower data*.

Jung, M., Reichstein, M., & Bondeau, A. (2009). Towards global empirical upscaling of FLUXNET eddy covariance observations: Validation of a model tree ensemble approach using a biosphere model. *Biogeosciences*, *6*(10), 2001–2013. https://doi.org/10.5194/bg-6-2001-2009

Jung, M., Reichstein, M., Ciais, P., Seneviratne, S. I., Sheffield, J., Goulden, M. L., Bonan, G., Cescatti, A., Chen, J., de Jeu, R., Dolman, A. J., Eugster, W., Gerten, D., Gianelle, D., Gobron, N., Heinke, J., Kimball, J., Law, B. E., Montagnani, L., … Zhang, K. (2010). Recent decline in the global land evapotranspiration trend due to limited moisture supply. *Nature*, *467*(7318), 951–954. https://doi.org/10.1038/nature09396

Kang, Y., Bassiouni, M., Gaber, M., Lu, X., & Keenan, T. F. (2025). CEDAR-GPP: Spatiotemporally upscaled estimates of gross primary productivity incorporating CO_2 fertilization. *Earth System Science Data*, *17*(6), 3009–3046. https://doi.org/10.5194/essd-17-3009-2025

Kannenberg, S. A., Babst, F., Barnes, M. L., Cabon, A., Dannenberg, M. P., Johnston, M. R., & Anderegg, W. R. L. (2025). Stand density and local climate drive allocation of GPP to aboveground woody biomass. *New Phytologist*, *246*(2), 543–553. https://doi.org/10.1111/nph.20414

Kannenberg, S. A., Barnes, M. L., Bowling, D. R., Driscoll, A. W., Guo, J. S., & Anderegg, W. R. L. (2023). Quantifying the drivers of ecosystem fluxes and water potential across the soil-plant-atmosphere continuum in an arid woodland. *Agricultural*

and Forest Meteorology, *329*, 109269. https://doi.org/10.1016/j.agrformet.2022.109269

Kannenberg, S. A., Cabon, A., Babst, F., Belmecheri, S., Delpierre, N., Guerrieri, R., Maxwell, J. T., Meinzer, F. C., Moore, D. J. P., Pappas, C., Ueyama, M., Ulrich, D. E. M., Voelker, S. L., Woodruff, D. R., & Anderegg, W. R. L. (2022). Drought-induced decoupling between carbon uptake and tree growth impacts forest carbon turnover time. *Agricultural and Forest Meteorology*, *322*, 108996. https://doi.org/10.1016/j.agrformet.2022.108996

Keenan, T. F. (2026). *FLUXNET Data Explorer* [Computer software]. Zenodo. https://doi.org/10.5281/zenodo.20331228

Keenan, T. F., Luo, X., Stocker, B. D., De Kauwe, M. G., Medlyn, B. E., Prentice, I. C., Smith, N. G., Terrer, C., Wang, H., Zhang, Y., & Zhou, S. (2023). A constraint on historic growth in global photosynthesis due to rising CO2. *Nature Climate Change*, *13*(12), 1376–1381. https://doi.org/10.1038/s41558-023-01867-2

Keenan, T. F., Prentice, I. C., Canadell, J. G., Williams, C. A., Wang, H., Raupach, M., & Collatz, G. J. (2016). Recent pause in the growth rate of atmospheric CO2 due to enhanced terrestrial carbon uptake. *Nature Communications*, *7*(1), 13428. https://doi.org/10.1038/ncomms13428

Kim, J., Guo, Q., Baldocchi, D. D., Leclerc, M. Y., Xu, L., & Schmid, H. P. (2006). Upscaling fluxes from tower to landscape: Overlaying flux footprints on high-resolution (IKONOS) images of vegetation cover. *Agricultural and Forest Meteorology, Advances in Surface-Atmosphere Exchange - A Tribute to Marv Wesely*, *136*(3), 132–146. https://doi.org/10.1016/j.agrformet.2004.11.015

Kljun, N., Calanca, P., Rotach, M. W., & Schmid, H. P. (2015). A simple two-dimensional parameterisation for Flux Footprint Prediction (FFP). *Geoscientific Model Development*, *8*(11), 3695–3713. https://doi.org/10.5194/gmd-8-3695-2015

Körner, C. (2022). The forest's nutrient cycle drives its carbon cycle. *Tree Physiology*, *42*(3), 425–427. https://doi.org/10.1093/treephys/tpab170

Lasslop, G., Reichstein, M., Papale, D., Richardson, A. D., Arneth, A., Barr, A., Stoy, P., & Wohlfahrt, G. (2010). Separation of net ecosystem exchange into assimilation and respiration using a light response curve approach: Critical

issues and global evaluation. *Global Change Biology*, *16*(1), 187–208. https://doi.org/10.1111/j.1365-2486.2009.02041.x

Lauber, C. L., Hamady, M., Knight, R., & Fierer, N. (2009). Pyrosequencing-Based Assessment of Soil pH as a Predictor of Soil Bacterial Community Structure at the Continental Scale. *Applied and Environmental Microbiology*, *75*(15), 5111–5120. https://doi.org/10.1128/AEM.00335-09

Lawrence, D. M., Fisher, R. A., Koven, C. D., Oleson, K. W., Swenson, S. C., Bonan, G., Collier, N., Ghimire, B., van Kampenhout, L., Kennedy, D., Kluzek, E., Lawrence, P. J., Li, F., Li, H., Lombardozzi, D., Riley, W. J., Sacks, W. J., Shi, M., Vertenstein, M., … Zeng, X. (2019). The Community Land Model Version 5: Description of New Features, Benchmarking, and Impact of Forcing Uncertainty. *Journal of Advances in Modeling Earth Systems*, *11*(12), 4245–4287. https://doi.org/10.1029/2018MS001583

Lee, X., Wu, H.-J., Sigler, J., Oishi, C., & Siccama, T. (2004). Rapid and transient response of soil respiration to rain. *Global Change Biology*, *10*(6), 1017–1026. https://doi.org/10.1111/j.1529-8817.2003.00787.x

Legates, D. R., & DeLiberty, T. L. (1993). Precipitation Measurement Biases in the United States. *JAWRA Journal of the American Water Resources Association*, *29*(5), 855–861. https://doi.org/10.1111/j.1752-1688.1993.tb03245.x

Lempereur, M., Martin-StPaul, N. K., Damesin, C., Joffre, R., Ourcival, J.-M., Rocheteau, A., & Rambal, S. (2015). Growth duration is a better predictor of stem increment than carbon supply in a Mediterranean oak forest: Implications for assessing forest productivity under climate change. *New Phytologist*, *207*(3), 579–590. https://doi.org/10.1111/nph.13400

Lienert, S., & Joos, F. (2018). A Bayesian ensemble data assimilation to constrain model parameters and land-use carbon emissions. *Biogeosciences*, *15*(9), 2909–2930. https://doi.org/10.5194/bg-15-2909-2018

Lim, H., Medvigy, D., Mäkelä, A., Kim, D., Albaugh, T. J., Knier, A., Blaško, R., C Campoe, O., Deshar, R., Franklin, O., Henriksson, N., Littke, K., Lutter, R., Maier, C. A., Palmroth, S., Rosenvald, K., Slesak, R. A., Tullus, A., & Oren, R. (2024). Overlooked branch turnover creates a widespread bias in forest carbon accounting. *Proceedings of the National Academy of Sciences of the United*

States of America, *121*(42), e2401035121. https://doi.org/10.1073/pnas.2401035121

Lindeman, R. H., Merenda, P. F., & Gold, R. Z. (1980). *Introduction to bivariate and multivariate analysis* (Vol. 4). Scott, Foresman Glenview, IL. https://library.wur.nl/WebQuery/titel/1714678

Litton, C. M., Raich, J. W., & Ryan, M. G. (2007). Carbon allocation in forest ecosystems. *Global Change Biology*, *13*(10), 2089–2109. https://doi.org/10.1111/j.1365-2486.2007.01420.x

Liu, X., Wan, S., Su, B., Hui, D., & Luo, Y. (2002). Response of soil CO2 efflux to water manipulation in a tallgrass prairie ecosystem. *Plant and Soil*, *240*(2), 213–223. https://doi.org/10.1023/A:1015744126533

Lloyd, J., & Taylor, J. A. (1994). On the Temperature Dependence of Soil Respiration. *Functional Ecology*, *8*(3), 315–323. https://doi.org/10.2307/2389824

Luo, Y., El-Madany, T. S., Filippa, G., Ma, X., Ahrens, B., Carrara, A., Gonzalez-Cascon, R., Cremonese, E., Galvagno, M., Hammer, T. W., Pacheco-Labrador, J., Martín, M. P., Moreno, G., Perez-Priego, O., Reichstein, M., Richardson, A. D., Römermann, C., & Migliavacca, M. (2018). Using Near-Infrared-Enabled Digital Repeat Photography to Track Structural and Physiological Phenology in Mediterranean Tree–Grass Ecosystems. *Remote Sensing*, *10*(8), 1293. https://doi.org/10.3390/rs10081293

MacBean, N., Scott, R. L., Biederman, J. A., Peylin, P., Kolb, T., Litvak, M. E., Krishnan, P., Meyers, T. P., Arora, V. K., Bastrikov, V., Goll, D., Lombardozzi, D. L., Nabel, J. E. M. S., Pongratz, J., Sitch, S., Walker, A. P., Zaehle, S., & Moore, D. J. P. (2021). Dynamic global vegetation models underestimate net CO2 flux mean and inter-annual variability in dryland ecosystems. *Environmental Research Letters*, *16*(9), 094023. https://doi.org/10.1088/1748-9326/ac1a38

Maier, M., Schack-Kirchner, H., Hildebrand, E. E., & Holst, J. (2010). Pore-space CO2 dynamics in a deep, well-aerated soil. *European Journal of Soil Science*, *61*(6), 877–887. https://doi.org/10.1111/j.1365-2389.2010.01287.x

Mcshane, E. J. (1937). *JENSEN'S INEQUALITY*.

Melton, J. R., Arora, V. K., Wisernig-Cojoc, E., Seiler, C., Fortier, M., Chan, E., & Teckentrup, L. (2020). CLASSIC v1.0: The open-source community successor

to the Canadian Land Surface Scheme (CLASS) and the Canadian Terrestrial Ecosystem Model (CTEM) – Part 1: Model framework and site-level performance. *Geoscientific Model Development*, *13*(6), 2825–2850. https://doi.org/10.5194/gmd-13-2825-2020

Metz, E.-M., Vardag, S. N., Basu, S., Jung, M., Ahrens, B., El-Madany, T., Sitch, S., Arora, V. K., Briggs, P. R., Friedlingstein, P., Goll, D. S., Jain, A. K., Kato, E., Lombardozzi, D., Nabel, J. E. M. S., Poulter, B., Séférian, R., Tian, H., Wiltshire, A., … Butz, A. (2023). Soil respiration–driven CO2 pulses dominate Australia's flux variability. *Science*, *379*(6639), 1332–1335. https://doi.org/10.1126/science.add7833

Metzger, S., Junkermann, W., Mauder, M., Butterbach-Bahl, K., Trancón y Widemann, B., Neidl, F., Schäfer, K., Wieneke, S., Zheng, X. H., Schmid, H. P., & Foken, T. (2013). Spatially explicit regionalization of airborne flux measurements using environmental response functions. *Biogeosciences*, *10*(4), 2193–2217. https://doi.org/10.5194/bg-10-2193-2013

Migliavacca, M., Reichstein, M., Richardson, A. D., Colombo, R., Sutton, M. A., Lasslop, G., Tomelleri, E., Wohlfahrt, G., Carvalhais, N., Cescatti, A., Mahecha, M. D., Montagnani, L., Papale, D., Zaehle, S., Arain, A., Arneth, A., Black, T. A., Carrara, A., Dore, S., … Van Der MOLEN, M. K. (2011). Semiempirical modeling of abiotic and biotic factors controlling ecosystem respiration across eddy covariance sites. *Global Change Biology*, *17*(1), 390–409. https://doi.org/10.1111/j.1365-2486.2010.02243.x

Muller, B., Pantin, F., Génard, M., Turc, O., Freixes, S., Piques, M., & Gibon, Y. (2011). Water deficits uncouple growth from photosynthesis, increase C content, and modify the relationships between C and growth in sink organs. *Journal of Experimental Botany*, *62*(6), 1715–1729. https://doi.org/10.1093/jxb/erq438

Nelson, J. A., Walther, S., Gans, F., Kraft, B., Weber, U., Novick, K., Buchmann, N., Migliavacca, M., Wohlfahrt, G., Šigut, L., Ibrom, A., Papale, D., Göckede, M., Duveiller, G., Knohl, A., Hörtnagl, L., Scott, R. L., Dušek, J., Zhang, W., … Jung, M. (2024). X-BASE: The first terrestrial carbon and water flux products from an extended data-driven scaling framework, FLUXCOM-X. *Biogeosciences*, *21*(22), 5079–5115. https://doi.org/10.5194/bg-21-5079-2024

Nguyen, N. B., Migliavacca, M., Bassiouni, M., Baldocchi, D. D., Gherardi, L. A., Green, J. K., Papale, D., Reichstein, M., Cohrs, K.-H., Cescatti, A., Nguyen, T. D., Nguyen, H. H., Nguyen, Q. M., & Keenan, T. F. (2025). Widespread underestimation of rain-induced soil carbon emissions from global drylands. *Nature Geoscience*, 1–8. https://doi.org/10.1038/s41561-025-01754-9

Norby, R. J. (2025). Forest productivity response to elevated CO2 in free-air CO2 enrichment experiments: The 23 percent solution, revisited. *New Phytologist*, *246*(5), 1952–1959. https://doi.org/10.1111/nph.70162

Novick, K. A., Metzger, S., Anderegg, W. R. L., Barnes, M., Cala, D. S., Guan, K., Hemes, K. S., Hollinger, D. Y., Kumar, J., Litvak, M., Lombardozzi, D., Normile, C. P., Oikawa, P., Runkle, B. R. K., Torn, M., & Wiesner, S. (2022). Informing Nature-based Climate Solutions for the United States with the best-available science. *Global Change Biology*, *28*(12), 3778–3794. https://doi.org/10.1111/gcb.16156

Noy-Meir, I. (1973). Desert Ecosystems: Environment and Producers. *Annual Review of Ecology and Systematics*, 25–51. http://www.jstor.org/stable/2096803

Oikawa, P. Y., Jenerette, G. D., Knox, S. H., Sturtevant, C., Verfaillie, J., Dronova, I., Poindexter, C. M., Eichelmann, E., & Baldocchi, D. D. (2017). Evaluation of a hierarchy of models reveals importance of substrate limitation for predicting carbon dioxide and methane exchange in restored wetlands. *Journal of Geophysical Research: Biogeosciences*, *122*(1), 145–167. https://doi.org/10.1002/2016JG003438

Orchard, V. A., & Cook, F. J. (1983). Relationship between soil respiration and soil moisture. *Soil Biology and Biochemistry*, *15*(4), 447–453. https://doi.org/10.1016/0038-0717(83)90010-X

Papale, D., & Valentini, R. (2003). A new assessment of European forests carbon exchanges by eddy fluxes and artificial neural network spatialization. *Global Change Biology*, *9*(4), 525–535. https://doi.org/10.1046/j.1365-2486.2003.00609.x

Pastorello, G., Trotta, C., Canfora, E., Chu, H., Christianson, D., Cheah, Y.-W., Poindexter, C., Chen, J., Elbashandy, A., Humphrey, M., Isaac, P., Polidori, D., Reichstein, M., Ribeca, A., van Ingen, C., Vuichard, N., Zhang, L., Amiro, B.,

Ammann, C., ⋯ Papale, D. (2020). The FLUXNET2015 dataset and the ONEFlux processing pipeline for eddy covariance data. *Scientific Data*, *7*(1), 225. https://doi.org/10.1038/s41597-020-0534-3

Placella, S. A., Brodie, E. L., & Firestone, M. K. (2012). Rainfall-induced carbon dioxide pulses result from sequential resuscitation of phylogenetically clustered microbial groups. *Proceedings of the National Academy of Sciences*, *109*(27), 10931–10936. https://doi.org/10.1073/pnas.1204306109

Poggio, L., de Sousa, L. M., Batjes, N. H., Heuvelink, G. B. M., Kempen, B., Ribeiro, E., & Rossiter, D. (2021). SoilGrids 2.0: Producing soil information for the globe with quantified spatial uncertainty. *SOIL*, *7*(1), 217–240. https://doi.org/10.5194/soil-7-217-2021

Poulter, B., Frank, D., Ciais, P., Myneni, R. B., Andela, N., Bi, J., Broquet, G., Canadell, J. G., Chevallier, F., Liu, Y. Y., Running, S. W., Sitch, S., & van der Werf, G. R. (2014). Contribution of semi-arid ecosystems to interannual variability of the global carbon cycle. *Nature*, *509*(7502), 600–603. https://doi.org/10.1038/nature13376

Rahman, M. (2026). Physically interpretable AlphaEarth foundation model embeddings enable LLM-based land surface intelligence. *Remote Sensing Applications: Society and Environment*, *42*, 102045. https://doi.org/10.1016/j.rsase.2026.102045

Raich, J. W., & Potter, C. S. (1995). Global patterns of carbon dioxide emissions from soils. *Global Biogeochemical Cycles*, *9*(1), 23–36. https://doi.org/10.1029/94GB02723

Rao, M. P., Pacheco-Solana, A., Li, R., Oryan, B., Jensen, J. E., Rodriguez-Caton, M., Klinek, L., Pierrat, Z. A., Ruehr, S., Oelkers, R., Boeschoten, L. E., Griffin, K. L., McCormack, M. L., Yang, X., Verfaillie, J., Baldocchi, D., Hise, J., Turner, A. J., Scanlon, T. M., ⋯ Magney, T. S. (2026). Decoupled carbon assimilation and growth responses to aridity in temperate deciduous oaks. *Science Advances*, *12*(24), eady7139. https://doi.org/10.1126/sciadv.ady7139

Reichstein, M., Falge, E., Baldocchi, D., Papale, D., Aubinet, M., Berbigier, P., Bernhofer, C., Buchmann, N., Gilmanov, T., Granier, A., Grünwald, T., Havránková, K., Ilvesniemi, H., Janous, D., Knohl, A., Laurila, T., Lohila, A., Loustau, D., Matteucci,

G., ⋯ Valentini, R. (2005). On the separation of net ecosystem exchange into assimilation and ecosystem respiration: Review and improved algorithm. *Global Change Biology*, *11*(9), 1424–1439. https://doi.org/10.1111/j.1365-2486.2005.001002.x

Reichstein, M., Rey, A., Freibauer, A., Tenhunen, J., Valentini, R., Banza, J., Casals, P., Cheng, Y., Grünzweig, J. M., Irvine, J., Joffre, R., Law, B. E., Loustau, D., Miglietta, F., Oechel, W., Ourcival, J.-M., Pereira, J. S., Peressotti, A., Ponti, F., ⋯ Yakir, D. (2003). Modeling temporal and large-scale spatial variability of soil respiration from soil water availability, temperature and vegetation productivity indices. *Global Biogeochemical Cycles*, *17*(4). https://doi.org/10.1029/2003GB002035

Reynolds, J. F., Smith, D. M. S., Lambin, E. F., Turner, B. L., Mortimore, M., Batterbury, S. P. J., Downing, T. E., Dowlatabadi, H., Fernández, R. J., Herrick, J. E., Huber-Sannwald, E., Jiang, H., Leemans, R., Lynam, T., Maestre, F. T., Ayarza, M., & Walker, B. (2007). Global Desertification: Building a Science for Dryland Development. *Science*, *316*(5826), 847–851. https://doi.org/10.1126/science.1131634

Richardson, A. D., Carbone, M. S., Keenan, T. F., Czimczik, C. I., Hollinger, D. Y., Murakami, P., Schaberg, P. G., & Xu, X. (2013). Seasonal dynamics and age of stemwood nonstructural carbohydrates in temperate forest trees. *The New Phytologist*, *197*(3), 850–861. https://www.jstor.org/stable/newphytologist.197.3.850

Roby, M. C., Scott, R. L., & Moore, D. J. P. (2020). High Vapor Pressure Deficit Decreases the Productivity and Water Use Efficiency of Rain-Induced Pulses in Semiarid Ecosystems. *Journal of Geophysical Research: Biogeosciences*, *125*(10), e2020JG005665. https://doi.org/10.1029/2020JG005665

Romero, E., Rey-Sanchez, C., Gerlein-Safdi, C., Baldocchi, D. D., Lee, P., & Dronova, I. (2026). Photosynthesis, heat, and structure: An evident hierarchy of environmental conditions driving wetland carbon assimilation. *Remote Sensing of Environment*, *338*, 115339. https://doi.org/10.1016/j.rse.2026.115339

Rousk, J., & C. Brangarí, A. (2022). Do the respiration pulses induced by drying–rewetting matter for the soil–atmosphere carbon balance? *Global Change Biology*, *28*(11), 3486–3488. https://doi.org/10.1111/gcb.16163

Rutledge, S., Campbell, D. I., Baldocchi, D., & Schipper, L. A. (2010). Photodegradation leads to increased carbon dioxide losses from terrestrial organic matter. *Global Change Biology*, *16*(11), 3065–3074. https://doi.org/10.1111/j.1365-2486.2009.02149.x

Sala, O. E., Gherardi, L. A., Reichmann, L., Jobbágy, E., & Peters, D. (2012). Legacies of precipitation fluctuations on primary production: Theory and data synthesis. *Philosophical Transactions of the Royal Society B: Biological Sciences*, *367*(1606), 3135–3144. https://doi.org/10.1098/rstb.2011.0347

Schimel, J. P. (2018). *Life in Dry Soils: Effects of Drought on Soil Microbial Communities and Processes*.

Schmid, H. P., & Lloyd, C. R. (1999). Spatial representativeness and the location bias of flux footprints over inhomogeneous areas. *Agricultural and Forest Meteorology*, *93*(3), 195–209. https://doi.org/10.1016/S0168-1923(98)00119-1

Schneider, T., Keiblinger, K. M., Schmid, E., Sterflinger-Gleixner, K., Ellersdorfer, G., Roschitzki, B., Richter, A., Eberl, L., Zechmeister-Boltenstern, S., & Riedel, K. (2012). Who is who in litter decomposition? Metaproteomics reveals major microbial players and their biogeochemical functions. *The ISME Journal*, *6*(9), 1749–1762. https://doi.org/10.1038/ismej.2012.11

Serrano-Ortiz, P., Roland, M., Sanchez-Moral, S., Janssens, I. A., Domingo, F., Goddéris, Y., & Kowalski, A. S. (2010). Hidden, abiotic CO2 flows and gaseous reservoirs in the terrestrial carbon cycle: Review and perspectives. *Agricultural and Forest Meteorology*, *150*(3), 321–329. https://doi.org/10.1016/j.agrformet.2010.01.002

Shuttleworth, J., Gurney R, J., Hsu A., Y., & Ormsby J., P. (1989). FIFE: The variation in energy partition at surface flux sites. *IAHS Publication (International Association of Hydrological Sciences)*, (186), 67–74. https://jglobal.jst.go.jp/en/detail?JGLOBAL_ID=200902011991788720

Singh, S. (2023). How the Birch effect differs in mechanisms and magnitudes due to soil texture. *Soil Biology and Biochemistry*.

Sinsabaugh, R. L., Lauber, C. L., Weintraub, M. N., Ahmed, B., Allison, S. D., Crenshaw, C., Contosta, A. R., Cusack, D., Frey, S., Gallo, M. E., Gartner, T. B., Hobbie, S. E., Holland, K., Keeler, B. L., Powers, J. S., Stursova, M., Takacs-Vesbach, C., Waldrop, M. P., Wallenstein, M. D., … Zeglin, L. H. (2008). Stoichiometry of soil enzyme activity at global scale. *Ecology Letters*, *11*(11), 1252–1264. https://doi.org/10.1111/j.1461-0248.2008.01245.x

Sitch, S., O'Sullivan, M., Robertson, E., Friedlingstein, P., Albergel, C., Anthoni, P., Arneth, A., Arora, V. K., Bastos, A., Bastrikov, V., Bellouin, N., Canadell, J. G., Chini, L., Ciais, P., Falk, S., Harris, I., Hurtt, G., Ito, A., Jain, A. K., … Zaehle, S. (2024). Trends and Drivers of Terrestrial Sources and Sinks of Carbon Dioxide: An Overview of the TRENDY Project. *Global Biogeochemical Cycles*, *38*(7), e2024GB008102. https://doi.org/10.1029/2024GB008102

Smith, B., Wårlind, D., Arneth, A., Hickler, T., Leadley, P., Siltberg, J., & Zaehle, S. (2014). Implications of incorporating N cycling and N limitations on primary production in an individual-based dynamic vegetation model. *Biogeosciences*, *11*(7), 2027–2054. https://doi.org/10.5194/bg-11-2027-2014

Smith, W. K., Dannenberg, M. P., Yan, D., Herrmann, S., Barnes, M. L., Barron-Gafford, G. A., Biederman, J. A., Ferrenberg, S., Fox, A. M., Hudson, A., Knowles, J. F., MacBean, N., Moore, D. J. P., Nagler, P. L., Reed, S. C., Rutherford, W. A., Scott, R. L., Wang, X., & Yang, J. (2019). Remote sensing of dryland ecosystem structure and function: Progress, challenges, and opportunities. *Remote Sensing of Environment*, *233*, 111401. https://doi.org/10.1016/j.rse.2019.111401

Tang, J., Baldocchi, D. D., & Xu, L. (2005). Tree photosynthesis modulates soil respiration on a diurnal time scale. *Global Change Biology*, *11*(8), 1298–1304. https://doi.org/10.1111/j.1365-2486.2005.00978.x

Teets, A., Fraver, S., Hollinger, D. Y., Weiskittel, A. R., Seymour, R. S., & Richardson, A. D. (2018). Linking annual tree growth with eddy-flux measures of net ecosystem productivity across twenty years of observation in a mixed conifer

forest. *Agricultural and Forest Meteorology*, *249*, 479–487. https://doi.org/10.1016/j.agrformet.2017.08.007

Teets, A., Moore, D. J. P., Alexander, M. R., Blanken, P. D., Bohrer, G., Burns, S. P., Carbone, M. S., Ducey, M. J., Fraver, S., Gough, C. M., Hollinger, D. Y., Koch, G., Kolb, T., Munger, J. W., Novick, K. A., Ollinger, S. V., Ouimette, A. P., Pederson, N., Ricciuto, D. M., … Richardson, A. D. (2022). Coupling of Tree Growth and Photosynthetic Carbon Uptake Across Six North American Forests. *Journal of Geophysical Research: Biogeosciences*, *127*(4), e2021JG006690. https://doi.org/10.1029/2021JG006690

Terrer, C., Jackson, R. B., Prentice, I. C., Keenan, T. F., Kaiser, C., Vicca, S., Fisher, J. B., Reich, P. B., Stocker, B. D., Hungate, B. A., Peñuelas, J., McCallum, I., Soudzilovskaia, N. A., Cernusak, L. A., Talhelm, A. F., Van Sundert, K., Piao, S., Newton, P. C. D., Hovenden, M. J., … Franklin, O. (2019). Nitrogen and phosphorus constrain the CO2 fertilization of global plant biomass. *Nature Climate Change*, *9*(9), 684–689. https://doi.org/10.1038/s41558-019-0545-2

Tramontana, G., Ichii, K., Camps-Valls, G., Tomelleri, E., & Papale, D. (2015). Uncertainty analysis of gross primary production upscaling using Random Forests, remote sensing and eddy covariance data. *Remote Sensing of Environment*, *168*, 360–373. https://doi.org/10.1016/j.rse.2015.07.015

Tramontana, G., Migliavacca, M., Jung, M., Reichstein, M., Keenan, T. F., Camps-Valls, G., Ogee, J., Verrelst, J., & Papale, D. (2020). Partitioning net carbon dioxide fluxes into photosynthesis and respiration using neural networks. *Global Change Biology*, *26*(9), 5235–5253. https://doi.org/10.1111/gcb.15203

Tripathi, B. M., Stegen, J. C., Kim, M., Dong, K., Adams, J. M., & Lee, Y. K. (2018). Soil pH mediates the balance between stochastic and deterministic assembly of bacteria. *The ISME Journal*, *12*(4), 1072–1083. https://doi.org/10.1038/s41396-018-0082-4

Trugman, A. T., & Anderegg, L. D. L. (2025). Source vs sink limitations on tree growth: From physiological mechanisms to evolutionary constraints and terrestrial carbon cycle implications. *New Phytologist*, *245*(3), 966–981. https://doi.org/10.1111/nph.20294

Vicca, S., Luyssaert, S., Peñuelas, J., Campioli, M., Chapin III, F. S., Ciais, P., Heinemeyer, A., Högberg, P., Kutsch, W. L., Law, B. E., Malhi, Y., Papale, D., Piao, S. L., Reichstein, M., Schulze, E. D., & Janssens, I. A. (2012). Fertile forests produce biomass more efficiently. *Ecology Letters*, *15*(6), 520–526. https://doi.org/10.1111/j.1461-0248.2012.01775.x

Vuichard, N., Messina, P., Luyssaert, S., Guenet, B., Zaehle, S., Ghattas, J., Bastrikov, V., & Peylin, P. (2019). Accounting for carbon and nitrogen interactions in the global terrestrial ecosystem model ORCHIDEE (trunk version, rev 4999): Multi-scale evaluation of gross primary production. *Geoscientific Model Development*, *12*(11), 4751–4779. https://doi.org/10.5194/gmd-12-4751-2019

Vuichard, N., & Papale, D. (2015). Filling the gaps in meteorological continuous data measured at FLUXNET sites with ERA-Interim reanalysis. *Earth System Science Data*, *7*(2), 157–171. https://doi.org/10.5194/essd-7-157-2015

Walker, A. P., De Kauwe, M. G., Bastos, A., Belmecheri, S., Georgiou, K., Keeling, R. F., McMahon, S. M., Medlyn, B. E., Moore, D. J. P., Norby, R. J., Zaehle, S., Anderson-Teixeira, K. J., Battipaglia, G., Brienen, R. J. W., Cabugao, K. G., Cailleret, M., Campbell, E., Canadell, J. G., Ciais, P., … Zuidema, P. A. (2021). Integrating the evidence for a terrestrial carbon sink caused by increasing atmospheric CO2. *New Phytologist*, *229*(5), 2413–2445. https://doi.org/10.1111/nph.16866

Waring, R. H., Landsberg, J. J., & Williams, M. (1998). Net primary production of forests: A constant fraction of gross primary production? *Tree Physiology*, *18*(2), 129–134. https://doi.org/10.1093/treephys/18.2.129

Warm Winter 2020 Team, & ICOS Ecosystem Thematic Centre. (2022). *Warm Winter 2020 ecosystem eddy covariance flux product for 73 stations in FLUXNET-Archive format—Release 2022-1 (Version 1.0).* https://doi.org/10.18160/2G60-ZHAK

White, A. C., Rogers, A., Rees, M., & Osborne, C. P. (2016). How can we make plants grow faster? A source-sink perspective on growth rate. *Journal of Experimental Botany*, *67*(1), 31–45. https://doi.org/10.1093/jxb/erv447

Whitford, W. G., & Duval, B. D. (2020). Chapter 3—Characterization of Desert Climates. In W. G. Whitford & B. D. Duval (Eds.), *Ecology of Desert Systems (Second Edition)* (pp. 47–72). Academic Press. https://doi.org/10.1016/B978-0-12-815055-9.00003-5

Xiao, J., Baldocchi, D., Ichii, K., Li, F., & Papale, D. (2025). Insights into terrestrial carbon and water cycling from the global eddy covariance network. *Nature Reviews Earth & Environment*, 1–20. https://doi.org/10.1038/s43017-025-00743-1

Xiao, J., Ollinger, S. V., Frolking, S., Hurtt, G. C., Hollinger, D. Y., Davis, K. J., Pan, Y., Zhang, X., Deng, F., Chen, J., Baldocchi, D. D., Law, B. E., Arain, M. A., Desai, A. R., Richardson, A. D., Sun, G., Amiro, B., Margolis, H., Gu, L., … Suyker, A. E. (2014). Data-driven diagnostics of terrestrial carbon dynamics over North America. *Agricultural and Forest Meteorology*, *197*, 142–157. https://doi.org/10.1016/j.agrformet.2014.06.013

Xiao, J., Zhuang, Q., Baldocchi, D. D., Law, B. E., Richardson, A. D., Chen, J., Oren, R., Starr, G., Noormets, A., Ma, S., Verma, S. B., Wharton, S., Wofsy, S. C., Bolstad, P. V., Burns, S. P., Cook, D. R., Curtis, P. S., Drake, B. G., Falk, M., … Torn, M. S. (2008). Estimation of net ecosystem carbon exchange for the conterminous United States by combining MODIS and AmeriFlux data. *Agricultural and Forest Meteorology*, *148*(11), 1827–1847. https://doi.org/10.1016/j.agrformet.2008.06.015

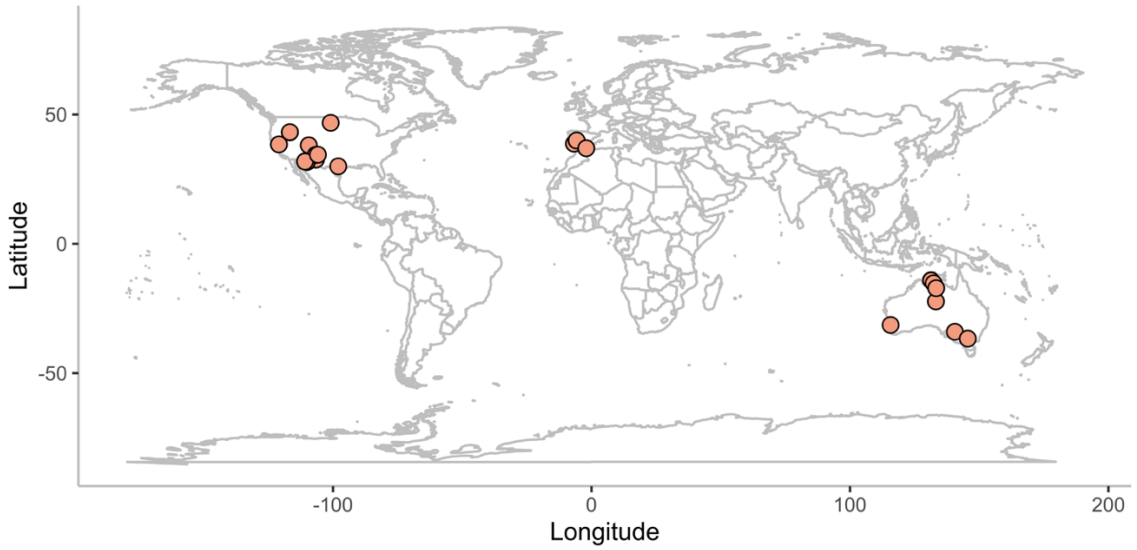
Xu, K., Metzger, S., & Desai, A. R. (2017). Upscaling tower-observed turbulent exchange at fine spatio-temporal resolution using environmental response functions. *Agricultural and Forest Meteorology*, *232*, 10–22. https://doi.org/10.1016/j.agrformet.2016.07.019

Xu, L., & Baldocchi, D. D. (2004). Seasonal variation in carbon dioxide exchange over a Mediterranean annual grassland in California. *Agricultural and Forest Meteorology*, *123*(1), 79–96. https://doi.org/10.1016/j.agrformet.2003.10.004

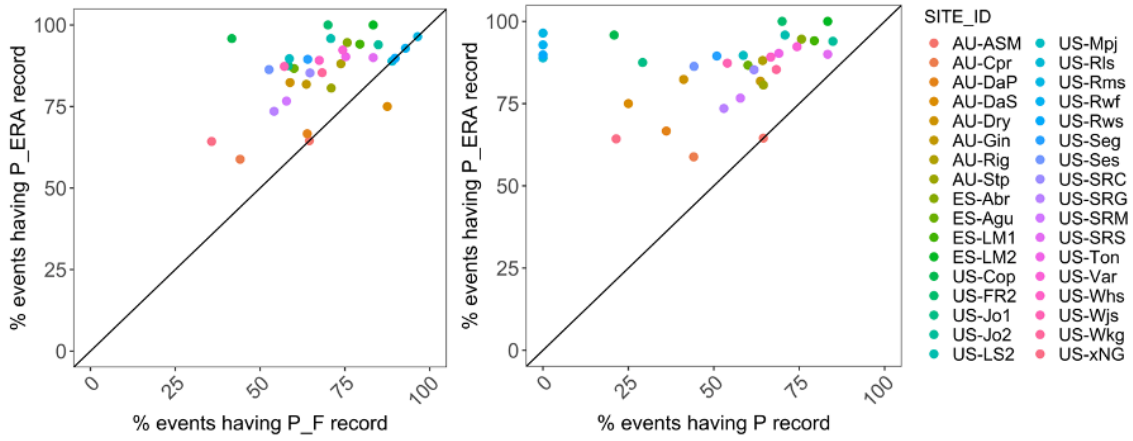
Xu, L., Baldocchi, D. D., & Tang, J. (2004). How soil moisture, rain pulses, and growth alter the response of ecosystem respiration to temperature. *Global Biogeochemical Cycles*, *18*(4). https://doi.org/10.1029/2004GB002281

Yan, L., Chen, S., Xia, J., & Luo, Y. (2014). Precipitation Regime Shift Enhanced the Rain Pulse Effect on Soil Respiration in a Semi-Arid Steppe. *PLOS ONE*, *9*(8), e104217. https://doi.org/10.1371/journal.pone.0104217

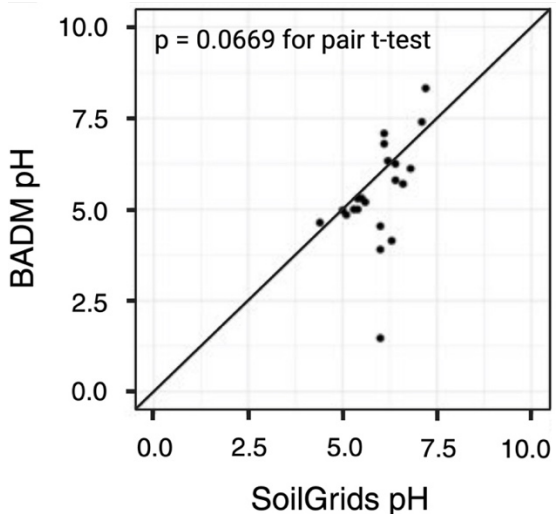
1.8. Extended Data



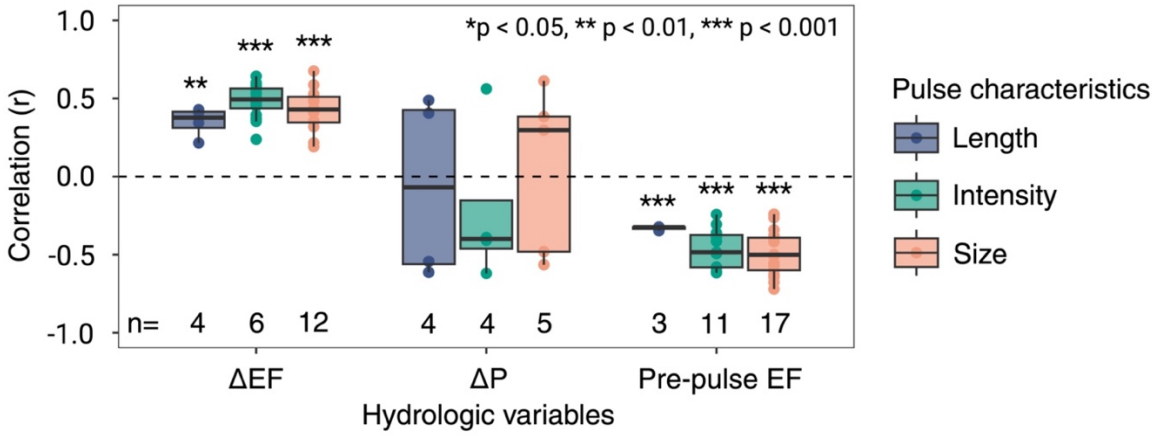
Extended Data Figure 8.1. *Global map of sites included in this research.*



Extended Data Figure 1.9. *Percent of pulse events that have precipitation data record (P, P_F, and P_ERA columns in FLUXNET database) within ±1 day from the start day of the events in 34 sites (0.001 mm was set as the threshold for precipitation occurrence). P_ERA aligned most accurately with the occurrence of pulse events, whereas P_F and P records were absent for several of these events.*

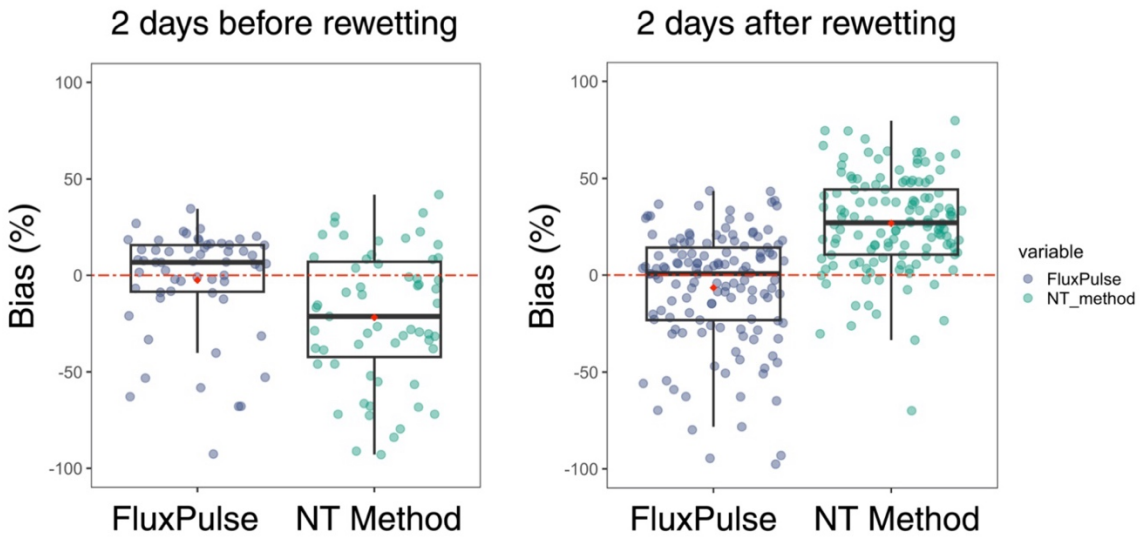


Extended Data Figure 1.10. *Comparison between soil pH obtained from Soilgrids and the BADM (Biological, Ancillary, Disturbance and Metadata) of AmeriFlux & ICOS sites.*



Extended Data Figure 1.11. *Pearson correlation between pulse characteristics (Length, intensity, and size) and hydrologic variables (rewetting intensity (ΔEF, ΔP), antecedent water availability (Pre-pulse EF)) for each site. Only sites with a significant linear relationship with climatic drivers are shown as points (p < 0.05). Asterisks indicate the level of two-tailed t-test significance for whether the mean of the distribution is different than 0. The boxes represent interquartile range (IQR) marked*

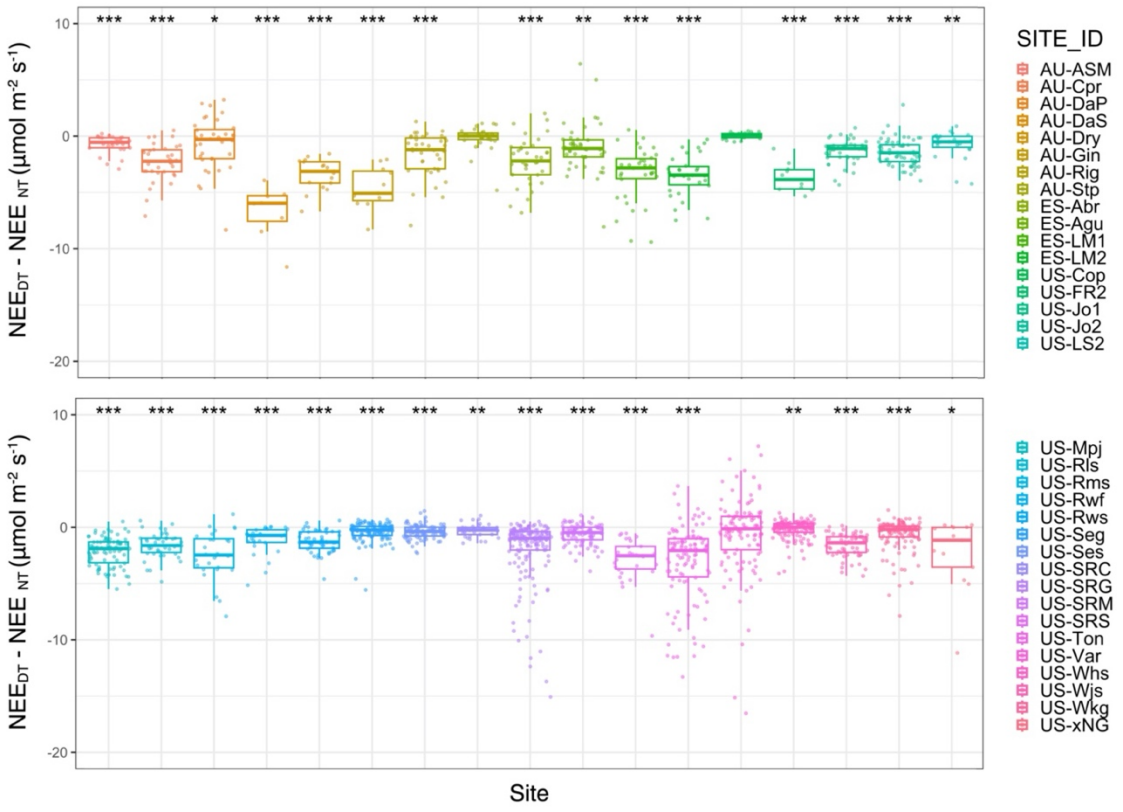
with 25th, 50th, 75th percentile and whiskers extending to 1.5 times the IQR. n indicates the number of points in each boxplot.



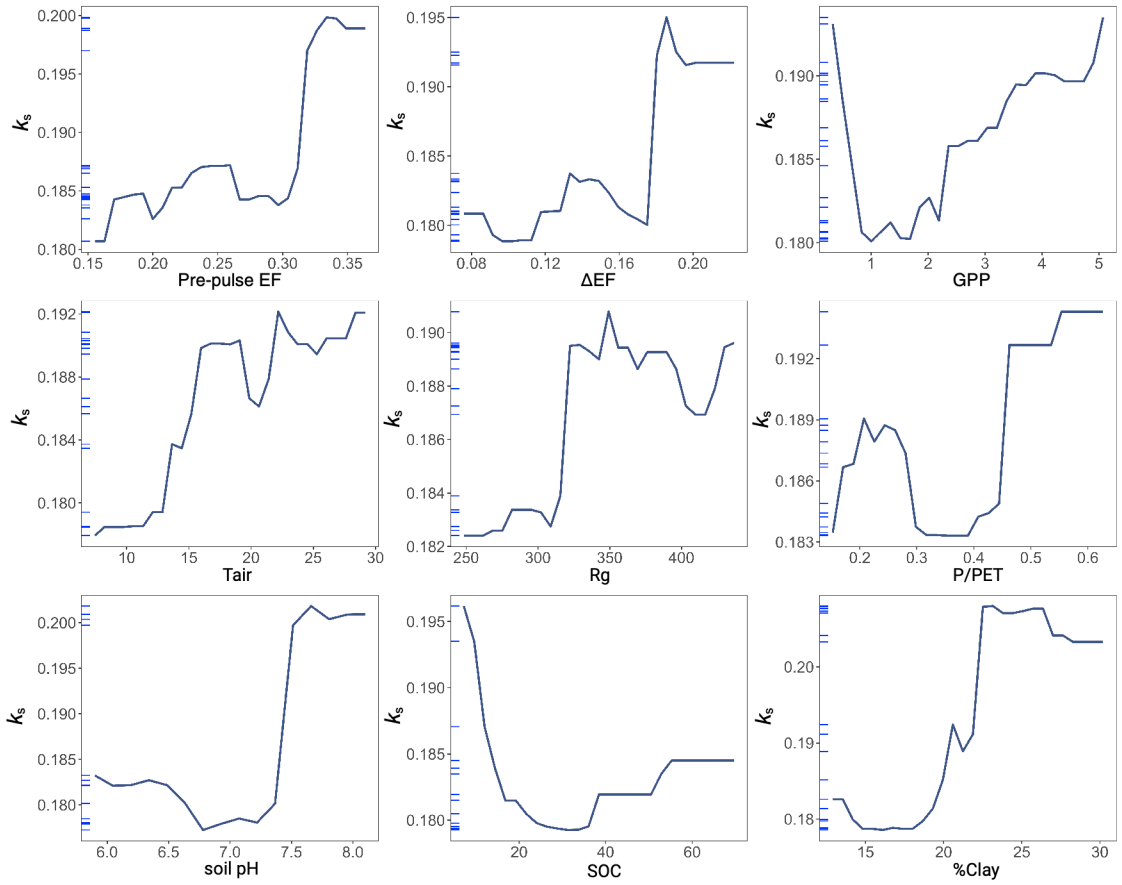
Extended Data Figure 1.12. *Bias (%) of FluxPulse R_{eco} and Nighttime (NT)-method R_{eco} when comparing to nighttime NEE during two days before and after the start of pulse events at three sites that use an enclosed-path system (ES-LM1, ES-LM2, and ES-Abr). Bias (%) is calculated as (x-y)/x*100%, in which x is the 68th percentile (1 standard deviation) of half-hourly Nighttime NEE, and y is the 68th percentile of half-hourly modelled R_{eco} (either FluxPulse or NT-method R_{eco}) during two days before and after the start of pulse events. Note that there are fewer points before pulse events than after because we only bias-corrected the pre-pulse periods that are not overlapped with previous pulse events. The pre-pulse period covers n days before each pulse event, in which n is the length of that pulse event. The boxes represent interquartile range (IQR) marked with 25th, 50th, 75th percentile and whiskers extending to 1.5 times the IQR. The red diamonds represent the mean of the boxplots.*



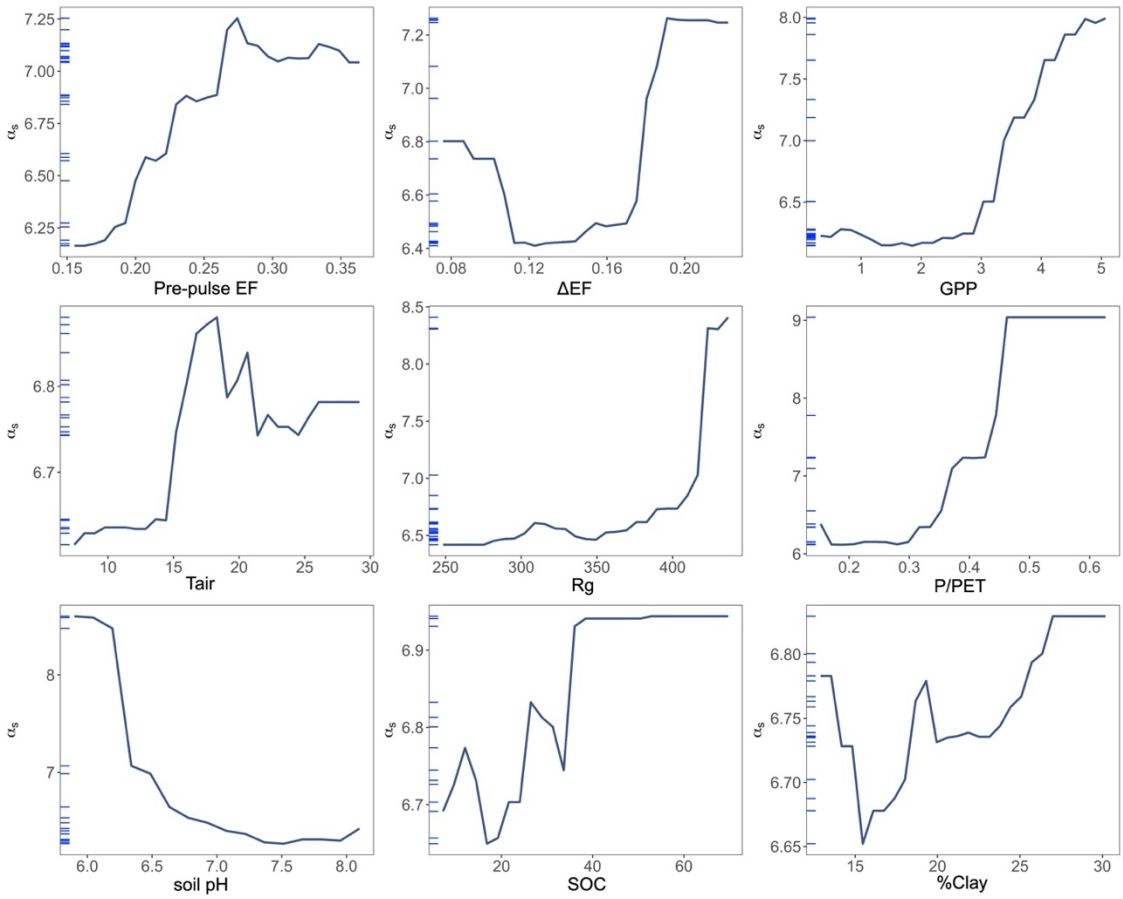
Extended Data Figure 1.13. *Bias (%) of FluxPulse R_{eco} and Nighttime (NT)-method R_{eco} when comparing to nighttime NEE during two days after the start of pulse events at 34 sites. Bias (%) is calculated as (x-y)/x*100, in which x is the 68th percentile (1 standard deviation) of half-hourly Nighttime NEE, and y is the 68th percentile of half-hourly modelled R_{eco} (either FluxPulse or NT-method R_{eco}) during two days after the start of pulse events. The boxes represent interquartile range (IQR) marked with 25th, 50th, 75th percentile and whiskers extending to 1.5 times the IQR. The red diamonds represent the mean of the boxplots.*



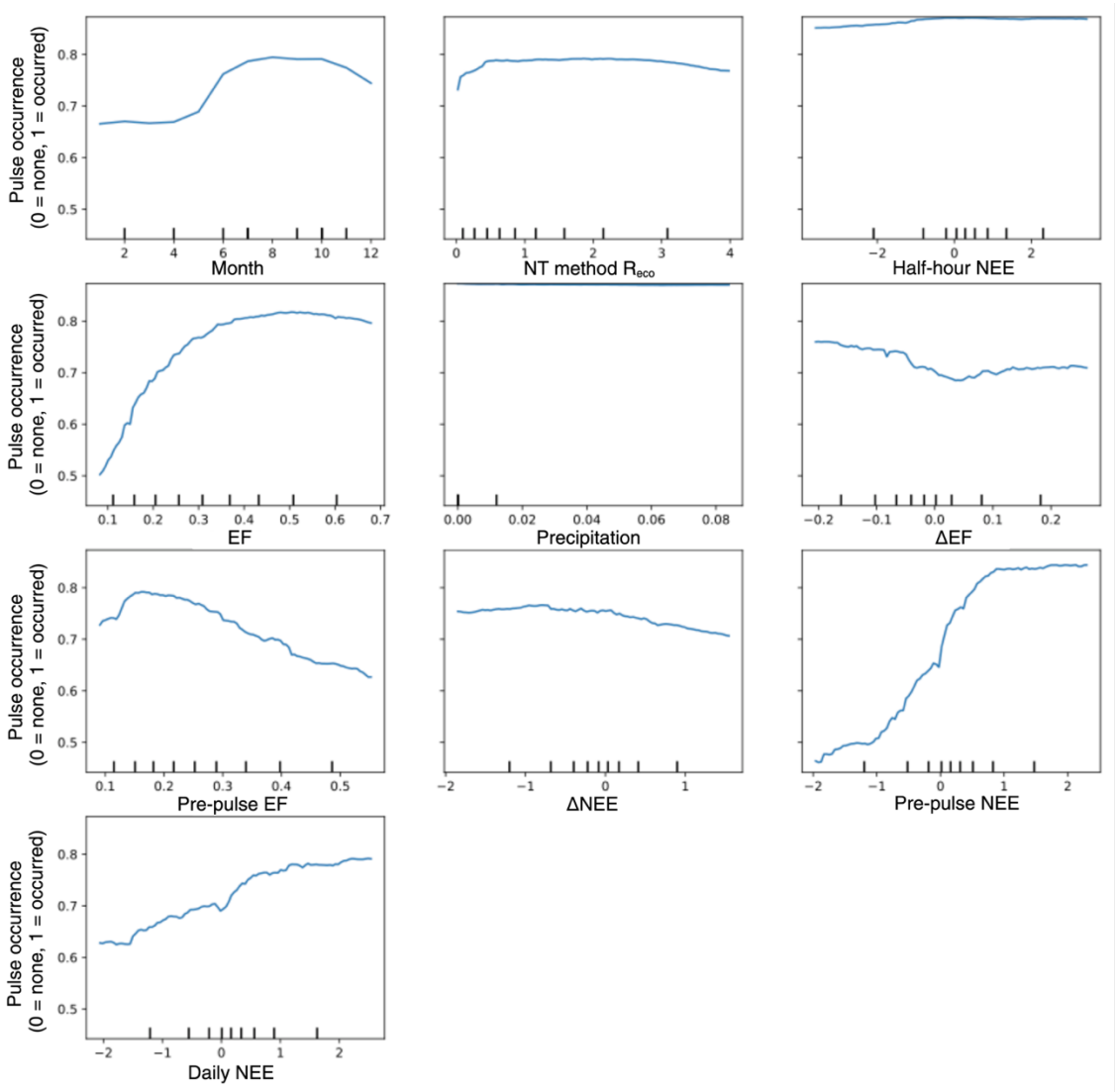
Extended Data Figure 1.14. *Difference between half-hourly NEE during daytime and nighttime (NEE_{DT} - NEE_{NT}) for the period of two days before each pulse event. NEE_{DT} - NEE_{NT} could indicate the presence of vegetation activity before pulse events, since the more negative is $NEE_{DT} – NEE_{NT}$, the more likely vegetation is active (NEE_{DT} - NEE_{NT} = ($R_{eco\ DT}$ – GPP) – $R_{eco\ NT}$ = ($R_{eco\ DT}$ – $R_{eco\ NT}$) – GPP). Assuming that $R_{eco\ DT} – R_{eco\ NT}$ is positive since R_{eco} increases with temperature, then the observed negative NEE_{DT} - NEE_{NT} must be due to positive GPP. Asterisks indicate the level of one-tailed t-test significance for whether the mean of the distribution is greater than 0 (*p < 0.05, **p< 0.01, ***p<0.001). The boxes represent interquartile range (IQR) marked with 25th, 50th, 75th percentile and whiskers extending to 1.5 times the IQR.*



Extended Data Figure 1.8. *Partial Dependence Plots for the responses of site-specific decay rate (k_s) to nine predictors. Predictors related to soil characteristics are clay percentage (%Clay), soil organic carbon from 0-5 cm (SOC) (g kg^{-1}), and soil pH. The predictor representing vegetation productivity is annual GPP obtained from the Nighttime (NT) partitioning method (μmol CO_2 m^{-2} s^{-1}). Predictors representing hydrologic conditions are aridity index (P/PET), rewetting intensity (ΔEF), and antecedent water availability (Pre-pulse EF). Predictors representing climatic conditions are global shortwave radiation (R_g) (W m^{-2}), and air temperature (T_{air}) (°C).*



Extended Data Figure 1.9. *Partial Dependence Plots for the responses of site-specific pulse intensity (α_s) to nine predictors. Predictors related to soil characteristics are clay percentage (%Clay), soil organic carbon from 0-5 cm (SOC) (g kg^{-1}), and soil pH. The predictor representing vegetation productivity is annual GPP obtained from the Nighttime (NT) partitioning method (μmol CO_2 m^{-2} s^{-1}). Predictors representing hydrologic conditions are aridity index (P/PET), rewetting intensity (ΔEF), and antecedent water availability (Pre-pulse EF). Predictors representing climatic conditions are global shortwave radiation (R_g) (W m^{-2}), and air temperature (T_{air}) (^{o}C).*



Extended Data Figure 1.10. *Partial Dependence Plots for the responses of pulse occurrence (value of 1 indicates that a pulse event occurred, while 0 represents no likelihood of a pulse event) to temporal predictors (see Methods and Figure 1.4c).*

Chapter 2

FluxLens: A 10-meter Spatialization Framework for Eddy-Covariance CO_2 Fluxes

FluxLens: A 10-meter Spatialization Framework for Eddy-Covariance CO_2 Fluxes

Ngoc B. Nguyen [1], Mirco Migliavacca [2], Yanghui Kang [3], Youngryel Ryu [4], Trevor F. Keenan [1,5]

[1] *Department of Environment Science, Policy, and Management, University of California, Berkeley, CA, USA*

[2] *European Commission - Joint Research Centre Via Enrico Fermi, Ispra (VA), 21027, Italy*

[3] *Department of Biological Systems Engineering, Virginia Tech, Blacksburg, VA, USA*

[4] *Department of Landscape Architecture and Rural Systems Engineering, Seoul National University, Seoul, Korea*

[5] *Climate and Ecosystem Sciences Division, Lawrence Berkeley National Laboratory, Berkeley, CA, USA*

An edited version of this chapter is currently under preparation for submission.

Abstract

Eddy-covariance towers provide valuable continuous and long-term measurements of biosphere–atmosphere CO_2 exchange across global ecosystems, contributing to our understanding of global ecosystem carbon balance and functioning. However, these measurements typically represent spatially aggregated fluxes across the tower area, limiting our ability to examine how carbon uptake and release vary within heterogeneous landscapes. Here, we introduce the Flux observation Local ENvironment Scaling (FluxLens), a novel framework for spatializing carbon fluxes within the tower areas. FluxLens combines climate variables and the Google AlphaEarth Foundations (AEF) annual embedding datasets to predict monthly estimates of gross primary productivity (*GPP*) and ecosystem respiration (R_{eco}) at 10-m spatial resolution. FluxLens first uses AEF embeddings combined with climatic features across 184 global eddy-covariance sites to improve monthly *GPP* and R_{eco} predictions compared with climate-only models (All-site R^2 *GPP* = 0.75±0.05 (mean±se); R^2 R_{eco} = 0.64±0.03). We then fine-tuned the globally trained model for each site using generalized additive models (GAMs) to incorporate site-specific information, and applied the fine-tuned models for pixel-level spatialization. Across sites, FluxLens captures well CO_2 flux magnitude, seasonal dynamics, and spatial nonuniformity within tower areas, with the mean predictions across all pixels consistent with flux-tower *GPP* and R_{eco} estimates (Site-specific pixel-mean R^2 *GPP* = 0.65-0.94 (25^{th}-75^{th} percentile); R^2 R_{eco} = 0.58-0.88). By moving beyond spatially aggregated tower-area averages, FluxLens leverages an emerging geospatial foundation model to provide spatially explicit carbon flux estimates with promising applications in ecosystem monitoring, land management, high-resolution satellite product evaluation, and plot-to-tower comparisons.

2.1. Introduction

Terrestrial ecosystems have sequestered 21% of anthropogenic CO_2 emissions in the last decade (Friedlingstein et al., 2025). Carbon stocks in terrestrial ecosystems are determined mainly by the balance between the two largest natural carbon fluxes, photosynthesis and respiration, which are carbon uptake by plants and release through ecosystem respiration to the atmosphere (Chapin et al., 2011). Knowing how much CO_2 the ecosystems breathe in and out everywhere, all the time has significant applications in efforts to evaluate carbon storage potential, inform ecosystem management, and understand ecosystem functioning (Griscom et al., 2017; Novick et al., 2022).

Eddy-covariance towers are among the most robust methods for measuring biosphere-atmosphere carbon, water, and energy exchange, leading to their rapid growth worldwide over the past 35 years (D. Baldocchi, 2014; Chu et al., 2017; Xiao et al., 2025). These towers continuously measure high-frequency CO_2 fluxes over periods ranging from half-hours to decades, providing powerful datasets for benchmarking terrestrial biosphere models, upscaling carbon fluxes from sites to regions, and understanding ecosystem processes across biomes (Xiao et al., 2025). Until now, more than 1800 towers have been operated globally (The Quantitative Ecosystem Dynamics Lab, 2026), with over a thousand sites providing publicly available half-hourly flux observations, through FLUXNET and regional flux networks (FLUXNET, 2025).

Eddy-covariance towers measure fluxes for a certain area around the towers, whose the majority of flux contribution typically comes from footprints spanning from a few hundred meters to several kilometers (Chu et al., 2021; Kljun et al., 2015; Schmid & Lloyd, 1999; Xiao et al., 2025), which are both temporally and spatially dynamic, depending on factors such as measurement height, wind direction, surface roughness, and atmospheric stability (Kim et al., 2006). Historically, flux estimates at scales of several hundred meters were often sufficient for upscaling tasks to understand regional/global carbon sources and sinks, matching with moderate-resolution remote sensing products, and studying whole-ecosystem function (Xiao et al., 2025). While substantial efforts have been made in scaling up eddy-covariance

measurements to regional and global flux products (Jung et al., 2009, 2010, 2019; Bu & Xiao, 2025; Kang et al., 2025; Nelson et al., 2024; Xiao et al., 2008, 2014; Papale & Valentini, 2003), little attention has been given to scaling down fluxes to finer spatial resolutions (Metzger et al., 2013; Romero et al., 2026; K. Xu et al., 2017). This gap may be due to the historical lack of high-resolution remote-sensing products that capture fine-scale spatial heterogeneity within tower areas. However, recent advances in Earth observations and geospatial foundation models, such as Google AlphaEarth Foundations (AEF), now provide global, high-spatial-resolution landscape characterizations down to only a few meters, which are trained on massive Earth observation datasets that represent comprehensive aspects of the ecosystems (Brown et al., 2025). AEF embeddings integrate diverse Earth observation datasets, including optical, radar, LiDAR, environmental, and annotated data, into a compact 64-dimensional representation of ecosystem state and structure (Brown et al., 2025). Their temporally continuous and high-spatial-resolution design also reduces the need for extensive preprocessing, making them readily applicable to ecosystem research. Recent studies have demonstrated the strong potential of AEF embeddings as a standalone and efficient solution for tasks such as tree species mapping (Wang et al., 2026) and irrigated cropland mapping (Yang et al., 2026). Hence, this creates opportunities to move beyond tower-area averages and spatialize carbon fluxes to precise locations at finer spatial scales.

Spatialized CO_2 flux maps provide information not only about how much CO_2 an ecosystem takes up or releases, but also where these exchanges occur within heterogeneous landscapes. Applications include but not limit to (1) estimating Gross Primary Productivity (*GPP*) and Ecosystem Respiration (R_{eco}) from specific crop fields to support agricultural management efforts, (2) comparing between plot-scale measurements and ecosystem-scale eddy-covariance observations, (3) evaluating high-resolution satellite retrievals by using the spatially explicit ground-based estimates, and (4) supporting carbon monitoring, reporting, and verification for specific lands of interests.

Here, we use the newly released Google AlphaEarth Foundations (AEF) embedding datasets to develop a machine learning framework to downscale eddy-covariance CO_2 fluxes to 10-m spatial resolution within 250-m-radius areas around

the towers. These embedding datasets compress multiple sources of Earth observation information ranging from optical, radar, LiDAR, environmental, and annotated datasets into a 64-dimensional vector for each 10-m pixel, providing a compact representation of land-surface characteristics and spatial heterogeneity (Brown et al., 2025). We use these embeddings with climatic variables and site-level information to estimate monthly *GPP* and R_{eco} across eddy-covariance sites and generate spatially explicit flux maps within tower areas. We aim to evaluate the applications of AlphaEarth Foundations embedding datasets in modeling and spatializing *GPP* and R_{eco} across sites and plant functional types (PFTs), and develop the Flux observation Local ENvironment Scaling (FluxLens), a framework for spatializing CO_2 fluxes at 10-m resolution within eddy-covariance tower areas. By spatializing fluxes to finer resolution, the FluxLens framework can support broader efforts in land management, ecosystem monitoring, plot-to-tower and satellite-to-tower comparisons, and carbon monitoring, reporting, and verification.

2.2. Methods

2.2.1. Datasets

Eddy-covariance carbon fluxes. Eddy-covariance datasets were collected from FLUXNET2015 (Pastorello et al., 2020), AmeriFlux (https://ameriflux.lbl.gov/), ICOS (https://www.icos-etc.eu/icos/), and TERN (https://www.tern.org.au/). All data are publicly available and under a CC-BY-4.0 license. We used monthly-aggregated data for Gross Primary Productivity (variable GPP_NT_VUT_REF) and Ecosystem Respiration (variable *R*ECO_NT_VUT_REF), which are partitioned using the Nighttime method (Reichstein et al., 2005) and filtered based on Variable USTAR Threshold (VUT) (Pastorello et al., 2020). A total of 184 eddy-covariance flux sites globally were included in this study, whose IGBP including CRO, GRA, SAV, EBF, CSH, MF, ENF, WET, OSH, WSA, CVM (Extended Data Table 2.1, Extended Data Fig. 2.1). We selected sites that meet the following criteria: (1) have more than three continuous years of data between 2017-2024, which is the period for which Google AlphaEarth Foundations embedding datasets are available, (2) have at least eight monthly data points for both *GPP* and R_{eco} for each year after quality control (QC > 0.7).

Climatic datasets. To obtain climatic features to predict carbon fluxes, we obtained monthly downscaled variables from ERA-Interim reanalysis provided by the eddy-covariance networks, including incoming shortwave radiation (SW_IN) (W m^{-2}), air temperature (Tair) (^{o}C), Vapor Pressure Deficit (VPD) (hPa), precipitation (P) (mm d^{-1}), and wind speed (WS) (m s^{-1}) (Table 2.1, Fig. 2.1). Overall, ERA-Interim reanalysis variables agree well with flux tower measurements except for precipitation (Extended Data Fig. 2.2). However, we still used ERA-Interim precipitation since it has been shown to capture rain-pulse events in drylands more effectively than tower-measured precipitation (Nguyen et al., 2025). ERA-Interim reanalysis variables also contain fewer data gaps than tower-based meteorological variables. For site-specific aridity index (P/PET), we derived from the TerraClimate precipitation and potential evapotranspiration data (Abatzoglou et al., 2018). A full list of climatic variables for different model setups could be found in Table 2.1.

AlphaEarth Foundations (AEF) satellite embedding datasets. AlphaEarth Foundations (AEF) version 1, released by Google DeepMind in June 2025, provides

annual global geospatial embeddings at 10-meter resolution from 2017-2024 (Fig. 2.1b) (Brown et al., 2025). These embeddings compress spatial, temporal, and measurement information from multiple Earth observation (EO) sources into 64-dimensional vectors although the physical interpretation of individual dimensions remains poorly understood since they are derived from a black-box deep learning model (Fig. 2.1b) (Brown et al., 2025; Rahman, 2026). The EO data used to train AEF include optical sensors (Sentinel-2, Landsat 8/9), radar sensors (Sentinel-1, PALSAR-2), LiDAR data (GEDI), environmental datasets (GLO-30, ERA5-Land, GRACE), and annotated datasets (National Land Cover Database, Wikipedia, etc.) (Brown et al., 2025).

The benefits of using AEF embeddings are that they provide harmonized, time-continuous, and high spatial resolution of landscape characteristics across diverse and massive EO datasets. Compared with traditional approaches that involve complex data preprocessing and combining satellite products with different spatial and temporal resolutions (Bu & Xiao, 2025; Gaber et al., 2024; Kang et al., 2025; Nelson et al., 2024), using AEF embedding datasets reduces inconsistencies among data sources while retaining crucial information about ecosystem and landscape heterogeneity in a compact embedding format. We downloaded the original AEF embeddings from Google Earth Engine for 2017-2024 at both the native 10-m resolution and as spatially aggregated values within a fixed 250-m radius centered at flux tower locations (Google, 2025). For each year, AEF provides 64 embedding values for every 10-m pixel, representing the spatial and ecological variation in the measurement area around the tower.

2.2.2. FluxLens Workflow

In this study, we developed FluxLens, a framework for spatializing CO_2 fluxes at 10-m resolution within the tower's measurement areas (Fig. 2.1). FluxLens first trains an XGBoost model across all sites using spatially-aggregated climatic and AEF embedding variables to predict monthly *GPP* and R_{eco}. The model is then fine-tuned using site-specific observations and applied to each pixel to generate pixel-wise flux predictions (Fig. 2.1).

Data splitting. To train and evaluate model predictive performance, we randomly

held out 10% of sites as an independent test (unseen) set. These held-out sites were stratified by IGBP to ensure proportional distribution across PFTs. The remaining 90% of sites were used for model training and validation. To obtain the training set, we split each remaining site temporally, using the earlier 80% of observations for training and the later 20% for validation. This splitting setup was designed to ensure that the final FluxLens model could effectively capture both spatial and temporal flux variations. After model training, predictions were generated for the held-out test sites. We ran this procedure 10 times to account for variability in the selection of test sites, resulting in 115 unique held-out sites across all runs for model evaluation, spanning eight IGBP classes (DBF, ENF, MF, WET, GRA, CRO, OSH, and SAV).

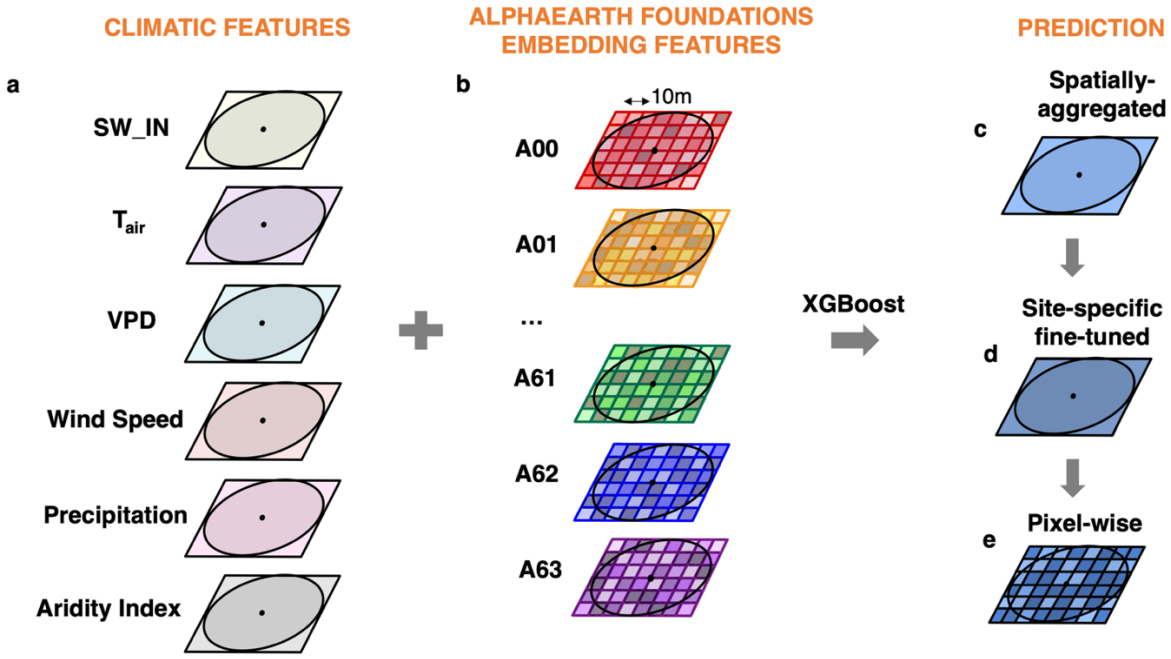


Figure 2.1. FluxLens workflow. *FluxLens uses the XGB_Emb+Clim model setup to predict GPP and R_{eco} (Table 1).* ***(a)*** *Climatic features include incoming shortwave radiation (SW_IN), air temperature (Tair), aridity index, Vapor Pressure Deficit (VPD), precipitation (P), and wind speed (WS).* ***(b)*** *Satellite embedding features include 64 dimensions (A00 to A63) from Google AlphaEarth Foundations (AEF), redrawn from (Brown et al., 2025).* ***(c)*** *An XGBoost model was used to predict flux-tower GPP and R_{eco} from the spatially-aggregated embedding and climatic features. The circle in each*

layer represents the measured area around the tower with a 250-m radius. ***(d)*** *The spatially-aggregated predictions were then fine-tuned for each site using generalized additive models (GAMs).* ***(e)*** *After fine-tuning, the XGBoost model was applied to each 10-m pixel to generate pixel-wise maps of GPP and* R_{eco}.

Model setups. We used the XGBoost (eXtreme Gradient Boosting) machine learning model to predict monthly Gross Primary Productivity (*GPP*) and Ecosystem Respiration (R_{eco}). XGBoost is a tree ensemble model that builds decision trees sequentially, with each tree correcting errors made by the previous trees (T. Chen & Guestrin, 2016). We chose the XGBoost model since tree-based models have shown robust performance on tabular datasets compared with deep-learning models, while maintaining a simpler model structure and higher computational efficiency (Grinsztajn et al., 2022). XGBoost is also robust to high-dimensional and missing datasets (T. Chen & Guestrin, 2016). Parameters for the XGBoost model can be found in Extended Data Table 2.2.

For each target variable, we designed five different model setups to test the effectiveness of adding AEF embedding features (Table 2.1). These five model setups represent simple to complex feature sets, ranging from using only one primary climatic driver for each target variable, to all climatic drivers, only embedding features, and a combination of climatic drivers with embedding features.

In the 1st model setup, which is the simplest model, we used the primary climatic driver for *GPP* and R_{eco}, which are incoming shortwave radiation (SW_IN) and air temperature (Tair) respectively (*XGB_SWin* model setup for *GPP* and *XGB_Tair* setup for R_{eco}) (Table 2.1).

In the 2nd model setup (*XGB_Clim*), we used a broader set of climatic variables including the primary drivers to predict *GPP* and R_{eco}, which are monthly air temperature (Tair), site-specific aridity index, monthly Vapor Pressure Deficit (VPD), monthly precipitation (P), monthly wind speed (WS), and monthly incoming shortwave radiation (SW_IN).

For the 3rd, 4th, and 5th model setups, we used 64 AEF embedding features alone (*XGB_Emb* setup for both *GPP* and R_{eco}), 64 AEF embedding features combined with the primary driver (*XGB_Emb+SWin* setup for *GPP* and *XGB_Emb+Tair* setup for

R_{eco}), and 64 AEF embedding features combined with all climatic variables (*XGB_Emb+Clim* setup for both *GPP* and R_{eco}), respectively (Table 2.1). The model setup with the best overall predictive performance was selected as the final FluxLens model configuration (Figure 2.1).

In addition to climatic and embedding features, all model setups include biome classification (IGBP) encoded as numeric values, and sine and cosine transformations of month to represent seasonal variation.

Model fine-tuning. Since one general XGBoost model was trained across all sites, site-specific fine-tuning is necessary to incorporate site-specific information. We used Generalized Additive Models (GAMs) to empirically bias-correct systematic biases at each site by modeling the target variables as a smooth function of the XGBoost predictions (*XGB_GAM*) (Fig. 2.1d). GAMs provide flexible nonlinear bias correction, while giving options to penalize overfitting estimations. The same GAM parameters were applied across all sites.

Generating 10-m pixel-wise predictions. The fine-tuned model was then applied to each individual 10-m pixel, using annual pixel-level embeddings and spatially-aggregated monthly climatic variables as features to predict pixel-level monthly *GPP* and R_{eco} (Fig. 2.1e).

Performance evaluation. Here we conducted three types of evaluations: (1) XGBoost performance evaluation, (2) fine-tuning evaluation, and (3) pixel-level evaluation. For XGBoost evaluation, we evaluated the XGBoost model predictive performance across all runs for each model setup at 115 unseen sites. Model performance was evaluated using the co-efficient of determination (R^2) and root mean square error (RMSE) for monthly predictions, mean seasonal cycles, and monthly anomalies. The formulas used to calculate R^2 and RMSE are provided in Equation 2.1 and Equation 2.2. Note that under this definition, R^2 can be negative if the model predictions perform worse than the observed mean, which is different from calculating R^2 as the square of Pearson correlation co-efficient (r).

$$R^2 = 1 - \frac{\sum_{i=1}^{n}(y_i - \hat{y}_i)^2}{\sum_{i=1}^{n}(y_i - \bar{y}_i)^2} \qquad \text{Equation 2.1}$$

$$RMSE = \sqrt{\frac{\sum_{i=1}^{n}(\hat{y}_i - y_i)^2}{n}} \quad \text{Equation 2.2}$$

, in which y_i, $\bar{y}_i$, and $\hat{y}_i$ are the observed, mean observed and predicted values respectively, and n is the number of observed values. The mean seasonal cycle of predictions and observations was calculated by aggregating values from the same month across all years, and monthly anomalies were calculated as the differences between predictions/observations and the mean seasonal cycle (Kang et al., 2025). In addition, we evaluated XGBoost model performance across different PFTs by calculating R^2 for monthly predictions across all runs for each model setup for each IGBP class. For the fine-tuning evaluation, we calculated R^2 of *XGB_GAM* predictions at each of the 115 unseen test sites, and compared them with the R^2 of monthly predictions from the *XGB_Emb+Clim* model setup. For the pixel-level evaluation, we aggregated predictions from all pixels within the 250-m-radius buffers around the towers and calculated their R^2 against the tower-based flux estimates. All evaluations were performed for both target variables *GPP* and R_{eco}.

2.2.3. FluxLens case studies

Here we presented three case studies to generate 10-m-pixel-level predictions of *GPP* and R_{eco} within 250-m-radius measurement areas around the towers. We chose the Lochristi poplar-planted site (BE-Lcr) in Belgium (Meulder et al., 2025), the Majadas del Tietar North nitrogen-added savanna (ES-LM1) in Spain (Carrara et al., 2026), and the Mayberry wetland (US-Myb) in California, United States (Matthes et al., 2026). These sites represent a deciduous broadleaf forest/rotational crop, a Mediterranean tree-grass savanna, and a wetland respectively. These three sites span two continents and include both water-limited and energy-limited ecosystems. They also capture diverse forms of landscape heterogeneity, including heterogeneous crop fields (BE-Lcr), scattered landscapes of oak trees and grasses (ES-LM1), and a wetland with open water (US-Myb).

Lochristi poplar-planted site (BE-Lcr). The first case study presented here is the Lochristi poplar-planted site (BE-Lcr) in Lochristi, East Flanders, Belgium (Latitude: 51.11218, Longitude: 3.85043). This site is a short-rotation bio-energy plantation of poplar (*Populus spp.*) and willow (*Salix spp.*), and is the only bio-rotation flux site in

the world (Broeckx et al., 2014). The tree density is 800 trees per hectare. The site mean annual temperature is 10.6°C and mean annual precipitation is 861.3 mm. However, the bio-energy plantation was stopped in 2023 and replaced by traditional crop lands. The site year range that overlaps with embedding datasets is 2019-2022.

Majadas del Tietar North savanna (ES-LM1). The second case-study site is the Majadas del Tietar North savanna (ES-LM1) in Spain. The site mean annual temperature and precipitation is 16.7°C and 650 mm respectively (Latitude: 39.94269, Longitude: -5.778683) (El-Madany et al., 2018). ES-LM1 is the tower located in the Nitrogen-added experiment. The canopy fraction is approximately 20%, covered mostly by oak trees (Quercus ilex) (El-Madany et al., 2018). For the grass layers, various annual herbaceous plants are present (El-Madany et al., 2018).As a result, the ES-LM1 Mediterranean savanna site has two distinct growing seasons: oak trees (spring) and herbaceous plants (late autumn) (Luo et al., 2018). Site data overlapping with embedding datasets are from 2017-2024.

Mayberry wetland (US-Myb). The final case study we examine is the Mayberry restored wetland in Sherman Island, Sacramento-San Joaquin River Delta, California, United States (Latitude: 38.0499, Longitude: -121.7650). Mayberry wetland consists of open water (depth ranging from 2 cm to 2 m) with covered vegetation dominated by tules (*Schoenoplectus acutus*) and cattails (*Typha spp.*) (Delwiche et al., 2025; Oikawa et al., 2017) (Fig. 6, 7). The site has a mean annual temperature of 15.9°C and mean annual precipitation of 338 mm, with 5 continuous years of data overlapping with the embedding datasets (2017-2021).

Table 2.1. XGBoost model setup description for predicting Gross Primary Productivity (GPP) and Ecosystem Respiration (R_{eco})

Target	Model setup	Features
Gross Primary Productivity (*GPP*) (gC m^{-2} d^{-1})	*XGB_SWin*	monthly incoming shortwave radiation (SW_IN), sin(month), cos(month), encoded site-specific IGBP
	XGB_Clim	monthly air temperature (Tair), site-specific aridity index, monthly Vapor Pressure Deficit (VPD), monthly precipitation (P), monthly wind speed (WS), monthly incoming shortwave radiation (SW_IN), sin(month), cos(month), encoded site-specific IGBP
	XGB_Emb	64 annual embedding features, sin(month), cos(month), encoded site-specific IGBP
	XGB_Emb+ SWin	64 annual embedding features, monthly incoming shortwave radiation (SW_IN), sin(month), cos(month), encoded site-specific IGBP
	XGB_Emb+ Clim	64 annual embedding features, monthly air temperature (Tair), site-specific aridity index, monthly Vapor Pressure Deficit (VPD), monthly precipitation (P), monthly wind speed (WS), monthly incoming shortwave radiation (SW_IN), sin(month), cos(month), encoded site-specific IGBP
Ecosystem Respiration (R_{eco}) (gC m^{-2} d^{-1})	*XGB_Tair*	monthly air temperature (Tair), sin(month), cos(month), encoded site-specific IGBP
	XGB_Clim	monthly incoming shortwave radiation (SW_IN), monthly air temperature (Tair), site-specific aridity index, monthly Vapor Pressure Deficit (VPD), monthly precipitation (P), monthly wind speed (WS), sin(month), cos(month), encoded site-specific IGBP
	XGB_Emb	64 annual embedding features, sin(month), cos(month), encoded site-specific IGBP
	XGB_Emb+	64 annual embedding features, monthly air

	Tair	temperature (Tair), sin(month), cos(month), encoded site-specific IGBP
	XGB_Emb+ Clim	64 annual embedding features, monthly air temperature (Tair), site-specific aridity index, monthly Vapor Pressure Deficit (VPD), monthly precipitation (P), monthly wind speed (WS), monthly incoming shortwave radiation (SW_IN), sin(month), cos(month), encoded site-specific IGBP

2.3. Results

2.3.1. Overall XGBoost model performance

We found that using embedding features significantly improves predictive performance compared with using climatic drivers alone for *GPP* and R_{eco} ($P < 0.05$; Fig. 2.2; Extended Data Table 3, 4). The only exception is for R_{eco} prediction, where *XGB_Emb* and *XGB_Clim* performance is not statistically different *(*$P = 0.08$*).* For monthly *GPP* predictions, all-site R^2 across the three embedding model setups ranges from 0.74±0.05 to 0.75±0.05 (mean±se), while R^2 is only 0.54±0.09 and 0.64±0.07 for the non-embedding *XGB_SWin* and *XGB_Clim* setups, respectively (Fig. 2.2a). Similarly, for monthly R_{eco} predictions, R^2 ranges from 0.62±0.03 to 0.64±0.03 for the embedding-based setups, compared with 0.41±0.04 and 0.50±0.05 for the non-embedding *XGB_Tair* and *XGB_Clim* setups respectively (Fig. 2.2d). There are no statistically significant differences between the three embedding setups for both *GPP* and R_{eco} monthly predictions; however, on average, *XGB_Emb+Clim* has the highest overall R^2 ($P > 0.05$; Fig. 2.2; Extended Data Table 2.3-2.8).

In addition, using embedding features substantially improves the mean seasonal cycle and anomaly predictions for *GPP* ($P < 0.05$; Fig. 2.2b, c; Extended Data Table 2.5, 2.7), while for R_{eco}, improves the mean seasonal cycle ($P < 0.05$; Fig. 2.2e; Extended Data Table 2.6) but does not significantly improve anomaly predictions comparing with *XGB_Clim* model setup (Fig. 2.2f; Extended Data Table 2.8). When comparing with the *XGB_Tair* setup, *XGB_Emb+Tair* and *XGB_Emb+Clim* show statistically higher R_{eco} anomaly predictive performance ($P < 0.05$; Fig. 2.2f; Extended Data Table 2.8). Overall, increasing model complexity leads to improved anomaly predictive performance for *GPP*, but is not always the case for R_{eco} (Fig. 2.2c, f). All embedding-based setups are not significantly different in terms of predicting MSC and anomaly for both *GPP* and R_{eco} (Fig. 2.2b, c, e, f; Extended Data Table 2.5-2.8). In general, R_{eco} estimates have lower mean R^2 across runs and model setups than *GPP* estimates in terms of monthly predictions, mean seasonal cycle, and anomaly. Among all model setups, the *XGB_Emb+Clim* setup shows the highest mean predictive performance for both *GPP* and R_{eco} across temporal scales (Fig. 2.2). We also found that embedding-based model setups have lower mean RMSE than non-embedding-

based setups for both *GPP* and R_{eco} across temporal scales, except for predicting R_{eco} monthly anomalies. However, among embedding-based setups, RMSE does not differ significantly (Extended Data Fig. 2.3).

Using embedding features achieves predictive performance comparable to previous global carbon flux modeling efforts. For *GPP* estimates, in general, the *XGB_Emb+Clim* setup R^2 reaches 0.75±0.05 across all runs (Fig. 2.2a). This performance is comparable to previous studies of monthly *GPP* modeling across global flux towers, including (Kang et al., 2025) mean R^2 = 0.72) and (Nelson et al., 2024; median R^2 ~ 0.7). Although the number of sites, data-splitting strategies, and the temporal resolution of training datasets differ slightly among studies, those studies used a comparable machine learning algorithm and evaluated model performance using comparable metrics on unseen monthly datasets.

Regarding different temporal scales, estimating the mean seasonal cycle yields higher overall R^2 than estimating monthly values for both *GPP* (MSC R^2 ranges from 0.64±0.03 to 0.82±0.01) and R_{eco} (MSC R^2 ranges from 0.51±0.03 to 0.71±0.03) across all model setups (Fig. 2.2b, e), whereas estimating anomalies is the most challenging task as indicated by much lower R^2 for both *GPP* and R_{eco} (Fig. 2.2c, f). This pattern is consistent with findings from previous studies for estimating *GPP* (Kang et al., 2025; Nelson et al., 2024).

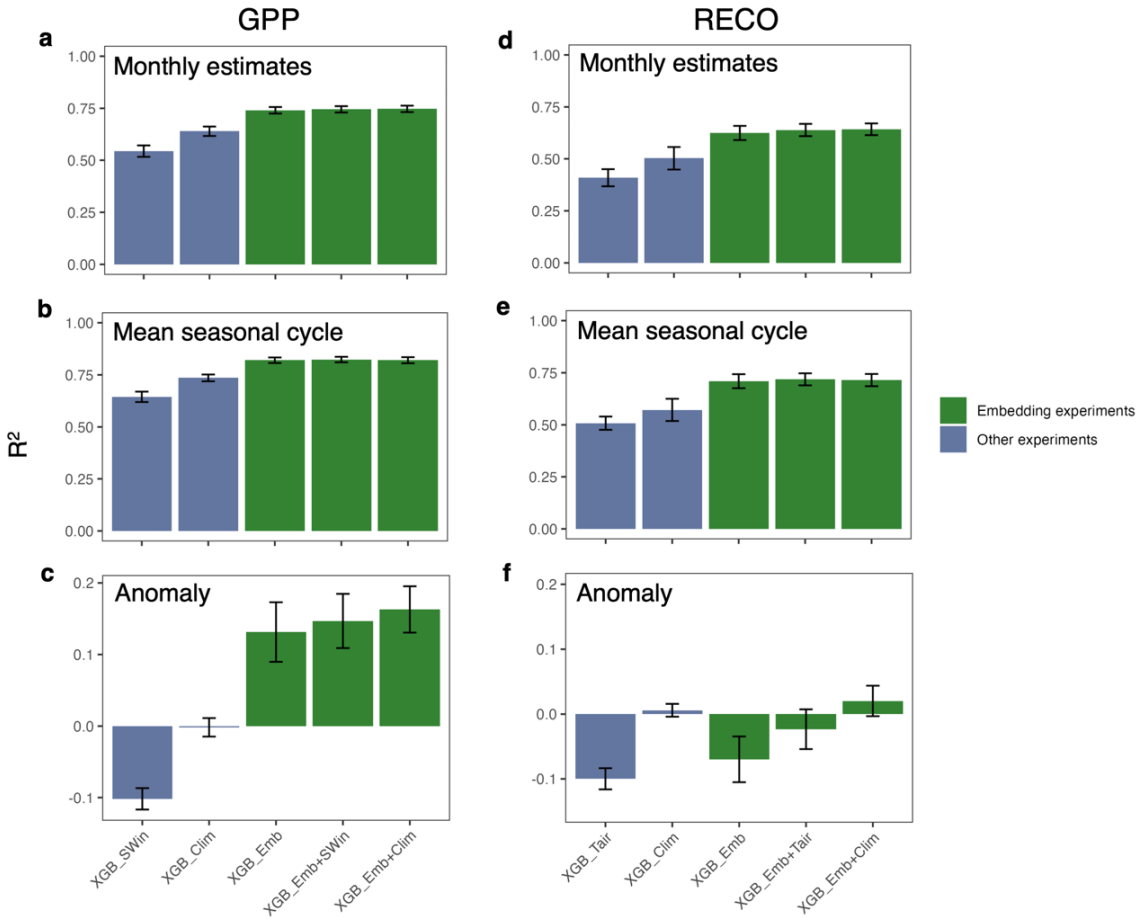


Figure 2.2. Performance of different model setups in estimating GPP (a-c) and R_{eco} (d-f) from 115 unseen datasets across runs and temporal scales. *Five model setups are evaluated for each variable and grouped into two categories: models using Google AlphaEarth Foundations (AEF) embedding features (green bars), and models without embedding features (blue bars). Details on the feature sets used in each setup are provided in Table 1. Model performance was evaluated based on R^2 of predicting monthly estimates (a, d), mean season cycles (MSC; b, e), and monthly anomalies (c, f). Bars represent averages across all runs, and error bars indicate standard errors.*

2.3.2. XGBoost model performance for *GPP* by PFTs

In general, using embedding features improves model performance for *GPP* predictions across PFTs, except for open shrubland (OSH) and savanna (SAV) ecosystems (Fig. 2.3). The most noticeable improvement is for CRO, GRA, MF, and

WET (Fig. 2.3a, d, e, h). The embedding-based setups achieve high R^2 for forest sites DBF, ENF, MF (0.7-0.9), moderate R^2 for WET, CRO, GRA (0.5-0.7), and very low R^2 for SAV and OSH (< 0) (Fig. 2.3). In contrast, the *XGB_SWin* setup achieves high R^2 only for DBF (0.84±0.02), and low R^2 across other PFTs (< 0.4). *XGB_Clim* shares similar R^2 for DBF (0.84±0.02), but consistently outperforms *XGB_SWin* across other PFTs, including ENF (0.67±0.05), MF (0.44±0.18), GRA (0.41±0.09), WET (0.28±0.26), CRO (0.35±0.05), SAV (0.21±0.15), and OSH (-0.41±0.32). Model performance is lowest for OSH and SAV across all models, with R^2 ranging from -2.26±2.47 to -0.41±0.32, and -1.76±0.55 to 0.21±0.15 respectively (Fig. 2.3f, g).

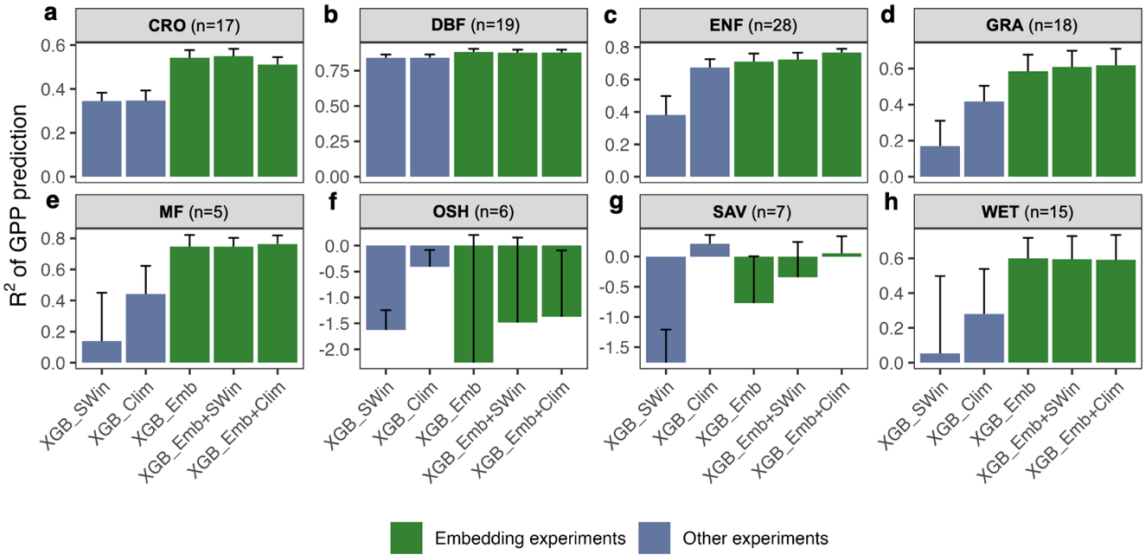


Figure 2.3. Performance of different model setups in estimating GPP across IGBP vegetation classes from 115 unseen datasets across all runs*. Five model setups are evaluated for GPP prediction and grouped into two categories: models using Google AlphaEarth embedding features (green bars), and models without embedding features (blue bars). Details on the feature sets used in each setup are provided in Table 1. Model performance was evaluated based on R-squared of predicting monthly estimates across (a) Cropland (CRO), (b) Deciduous Broadleaf Forest (DBF), (c) Evergreen Needleleaf Forest (ENF), (d) Grassland (GRA), (e) Mixed Forest (MF), (f) Open Shrubland (OSH), (g) Savanna (SAV), and (h) Wetland (WET).*

Bars represent averages across all runs, and error bars indicate standard errors. n represents the number of unseen sites in each PFT across all runs.

2.3.3. XGBoost model performance for R_{eco} by PFTs

Using embedding features results in clear improvements for R_{eco} predictions compared with non-embedding models for CRO, ENF, GRA, and WET (Fig. 2.4a, c, d, h). The R^2 values for the embedding-based setups for these PFTs are as follows: CRO (0.57±0.05 to 0.61± 0.03), ENF (0.56±0.06 to 0.59±0.06), GRA (0.53±0.10 to 0.63±0.07), and WET (0.29±0.20 to 0.39±0.15). For other PFTs including MF, OSH, and SAV, *XGB_Clim* achieves higher mean predictive performance than the three embedding-based setups, with R^2 values being 0.44±0.16, -0.18±0.14, and 0.32±0.14 respectively (Fig. 2.4e, f, g). For DBF, *XGB_Tair* with only air temperature as a climatic feature achieves the highest performance (0.60±0.08) (Fig. 2.4b). Interestingly, in DBF and WET, adding climatic variables in addition to air temperature reduces model performance (Fig. 2.4b, h). Across all model setups, OSH and SAV have the lowest performance, similar to the pattern observed for *GPP* predictions (Fig. 2.4f, g). MF, OSH, and SAV have the fewest sites in both the training and testing sets.

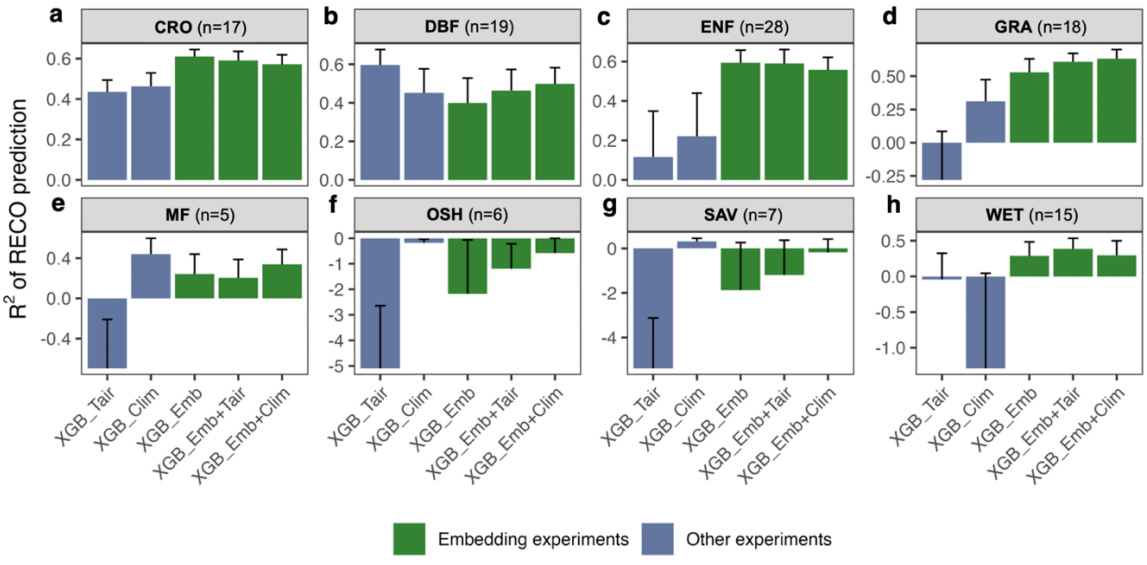


Figure 2.4. Performance of different model setups in estimating R_{eco} across IGBP vegetation classes from 115 unseen datasets across all runs*. Five model setups*

are evaluated for GPP prediction and grouped into two categories: models using Google AlphaEarth embedding features (green bars), and models without embedding features (blue bars). Details on the feature sets used in each setup are provided in Table 1. Model performance was evaluated based on R-squared of predicting monthly estimates across (a) Cropland (CRO), (b) Deciduous Broadleaf Forest (DBF), (c) Evergreen Needleleaf Forest (ENF), (d) Grassland (GRA), (e) Mixed Forest (MF), (f) Open Shrubland (OSH), (g) Savanna (SAV), and (h) Wetland (WET). Bars represent averages across all runs, and error bars indicate standard errors. n represents the number of unseen sites in each PFT across all runs.

2.3.4. Fine-tuned model performance by sites

To fine-tune the general trained model with site-specific information, we bias-corrected model predictions at each site using generalized additive models (GAMs; see Methods). We chose to fine-tune the *XGB_Emb+Clim* model setup because it achieves the highest overall mean performance for monthly, seasonality, and anomaly predictions for both *GPP* and R_{eco} (Fig. 2.2). *XGB_Emb+Clim* performance varies across sites for both *GPP* and R_{eco} with site-level R^2 interquartile ranges (25^{th}- 75^{th} percentile) of 0.43-0.88 for *GPP* (Fig. 2.5a) and 0.09-0.77 for R_{eco} (Fig. 2.5c). This means that 25% of sites achieve high predictive performance even before fine-tuning, with R^2 values of at least 0.88 for *GPP* and 0.77 for R_{eco}. GAM bias-correction improves model performance across most sites for *GPP* and R_{eco} (Fig. 2.5a, c), and the improvement was more pronounced for R_{eco} than *GPP*. The interquartile R^2 ranges for *XGB_GAM* predictions are 0.65-0.95 for *GPP* (Fig. 2.5a) and 0.64-0.90 for R_{eco} (Fig. 2.5c).

We applied the fine-tuned *XGB_GAM* model to individual pixels to predict pixel-level *GPP* and R_{eco}, and verified these pixel-level predictions by comparing their means to the tower-based estimates (Fig. 2.5b, d). The predictive performance of pixel-mean *XGB_GAM* evaluated against tower-based estimates shows interquartile ranges of 0.65-0.94 for *GPP* (Fig. 2.5b) and 0.58-0.88 for R_{eco} (Fig. 2.5d). These values are largely consistent with the predictive performance of *XGB_GAM* (Fig. 2.5b, d), although pixel-mean *XGB_GAM* shows slightly lower R^2 for R_{eco} at some sites, including some wetland sites (orange points, Fig. 2.5d).

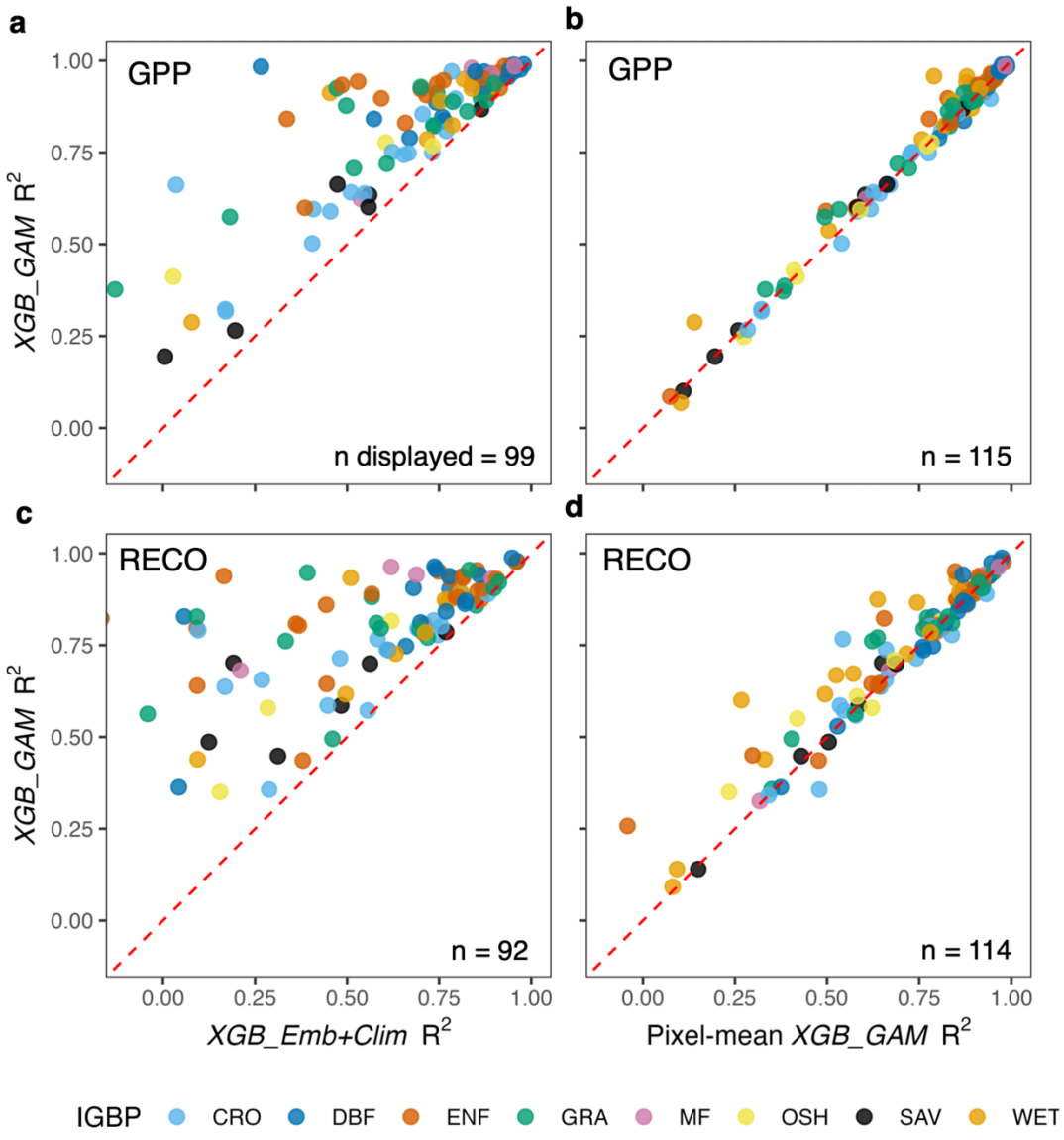


Figure 2.5. Performance of the XGB_Emb+Clim, XGB_GAM and pixel-mean XGB_GAM at individual sites for GPP and R_{eco} prediction. *XGB_Emb+Clim is the XGBoost model using embedding and climatic features as predictors (Table 1), while XGB_GAM refers to the GAM-bias-corrected or fine-tuned model of XGB_Emb+Clim (see Methods). Pixel-mean XGB_GAM represents the spatial aggregation of all pixel-level predictions within the measurement areas around the towers, after applying*

XGB_GAM to individual pixels. n represents the number of displayed sites in each panel, and sites with negative R^2 were removed for visualization purposes. Each point represents an individual site, and colors indicate the IGBP class of each site. The red diagonal line indicates the 1:1 line.

2.3.5. Generating 10m-pixel-level predictions of *GPP* and R_{eco}

We applied FluxLens using the fine-tuned *XGB_GAM* model to 10-m pixels within the 250-meter-radius measurement areas around the towers to generate high-spatial resolution maps of *GPP* and R_{eco}. At three case-study sites, our results show that FluxLens not only could capture the visible spatial nonuniformity, flux magnitude and seasonality, but also the mean aggregations across all pixels achieve high agreement with tower-based *GPP* and R_{eco} estimates (Fig. 2.5b, d; Fig. 2.6-2.11g). FluxLens maps could capture the clearly visible spatial nonuniformities such as the crop boundaries at BE-Lcr (Fig. 2.6a-f, 2.7a-f), the scattered vegetation patterns at ES-LM1 savanna (Fig. 2.8a-f, 2.9a-f), and the lower carbon fluxes over open water areas at Mayberry wetland (Fig. 2.10a-f, 2.11a-f). For BE-Lcr and ES-LM1, R^2 values between pixel-mean predictions and tower-based flux estimates reach approximately 0.87 for *GPP* (Fig. 2.6g, 2.8g) and 0.8 for R_{eco} (Fig. 2.7g, 2.9g).

Overall, at the Lochristi poplar-planted site (BE-Lcr), the *XGB_GAM* fine-tuned model improves model performance for both *GPP* and R_{eco}, increasing R^2 from 0.76 to 0.84 for *GPP* (Fig. 2.6g) and from 0.66 to 0.74 for R_{eco} (Fig. 2.7g). In particular, *XGB_GAM* reduces the growing-season underestimation of *GPP* (Fig. 2.6g).

We then applied the fine-tuned models to individual pixels to generate pixel-wise predictions for *GPP* and R_{eco}. Across pixels and years, the magnitude of *GPP* estimates ranges from -0.40 to 15.5 gC m^{-2} d^{-1} (Fig. 2.6) while for R_{eco} estimates are from 1.00 to 7.67 gC m^{-2} d^{-1} (Fig. 2.7). Spatially, the maps show clear crop-field boundaries and differences in crop phenology across the landscape (Fig. 2.6a-f, 2.7a-f). The maps also capture the seasonality of fluxes, which is consistent with that of the eddy-covariance tower-based estimates (Fig. 2.6g, 2.7g).

To evaluate these pixel-wise predictions at BE-Lcr, we took the monthly mean across all predicted pixels. R^2 value of the pixel-mean predictions is approximately equal to that of the *XGB_GAM* predictions for both *GPP* and R_{eco} (Fig. 2.6g, 2.7g). The

XGB_GAM pixel-mean predictions also correct the systematic growing-season underestimation of *GPP* from the *XGB_Emb+Clim* model (Fig. 2.6g).

For ES-LM1, clear spatial clustering patterns emerge in both *GPP* and R_{eco} pixel-wise predictions, with higher productivity and respiration in tree-covered areas (Fig. 2.8a-f, 2.9a-f). Pixel-wise *GPP* and R_{eco} range from 0.48 to 7.60 gC m^{-2} d^{-1} and 0.99 to 6.90 gC m^{-2} d^{-1}, respectively. Even though ES-LM1 is a held-out site from the model training process, it shows the highest model performance among all three case-study sites, with R^2 ranging from 0.86 – 0.87 for *GPP* and 0.77 – 0.79 for R_{eco} across the *XGB_Emb+Clim*, *XGB_GAM*, and pixel-mean *XGB_GAM* predictions (Fig. 2.8g, 2.9g). Similar to BE-Lcr, the fine-tuned and pixel-mean R^2 values are almost equal for both *GPP* and R_{eco} (Fig. 2.8g, 2.9g). All modes successfully capture the growing seasons of trees and grasses at the site (Fig. 2.8g, 2.9g).

Lastly, for Mayberry wetland, fine-tuning model *XGB_GAM* improves model performance for both *GPP* and R_{eco} (Fig. 2.10g, 2.11g). The improvement is clear for R_{eco} predictions, where fine-tuning corrects systematic underestimation during the growing season and overestimation during the non-growing season, increasing R^2 from 0.50 to 0.62 (Fig. 2.11g). For *GPP*, the fine-tuned model increases R^2 from 0.75 to 0.89 (Fig. 2.10g). Regarding the pixel-level predictions, *GPP* ranges from -0.34 to 10.0 gC m^{-2} d^{-1} (Fig. 2.10g) while R_{eco} ranges from 0.69 to 5.10 gC m^{-2} d^{-1} (Fig. 2.11g). Spatially, the maps show that open-water areas consistently have lower *GPP* and R_{eco} than vegetated areas, while areas near open water exhibit higher *GPP* and R_{eco} (Fig. 2.10a-f, 2.11-a-f). Applying the fine-tuned model to estimate pixel-level predictions, the pixel-mean *GPP* achieves an R^2 of 0.84 against tower-based estimates, slightly lower than the *XGB_GAM* R^2 of 0.89 (Fig. 2.10g). For R_{eco}, the pixel-mean R^2 is much lower than the *XGB_GAM* R^2, decreasing from 0.62 to 0.49 (Fig. 2.11g).

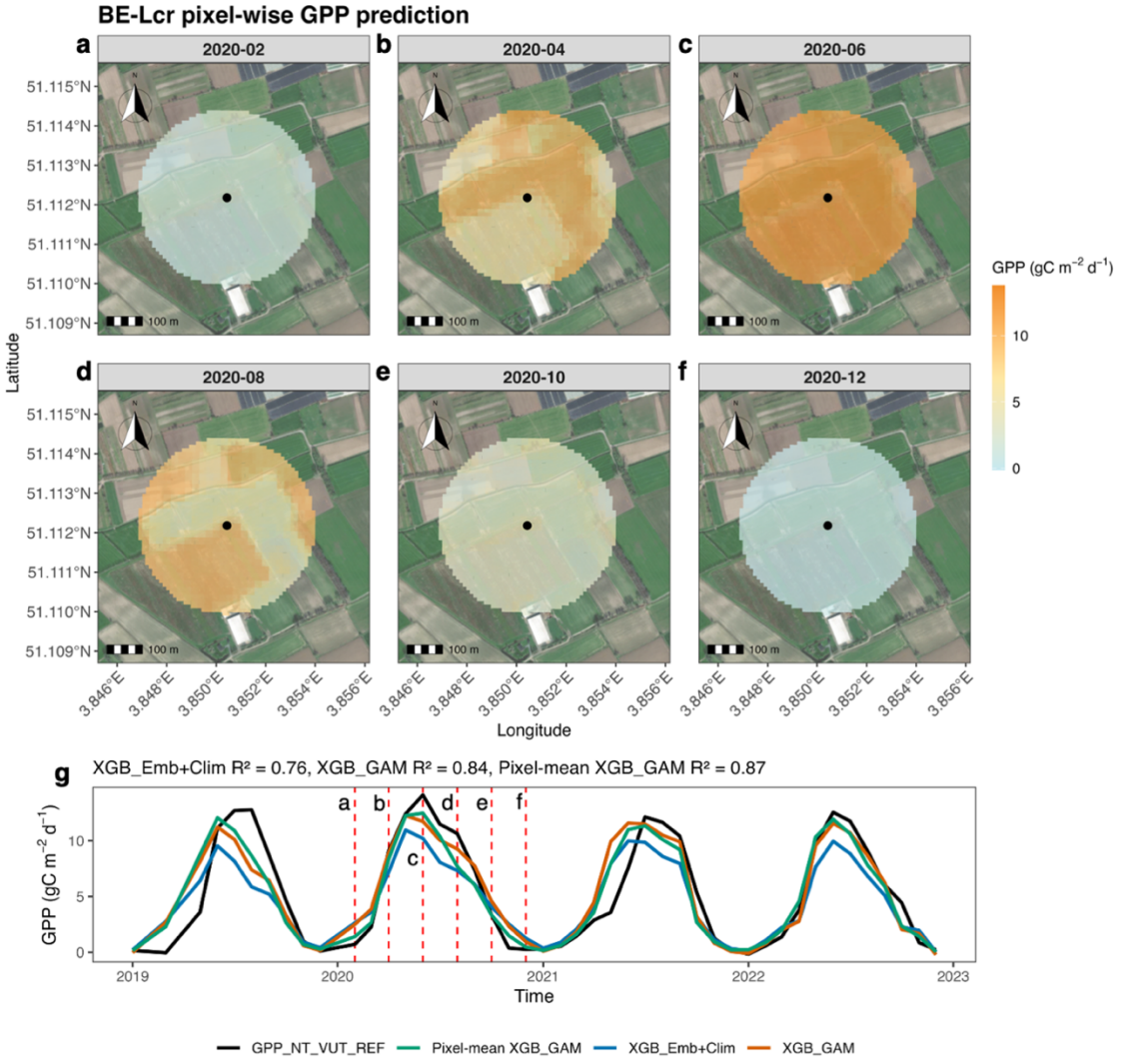


Figure 2.6. 10-m pixel-wise monthly GPP estimates within the 250-m-radius around the eddy-covariance tower at the Lochristi poplar-planted site (BE-Lcr) (unseen site) from 2019-2022. *Panels (a)-(f) show static maps of pixel-level GPP estimates for February, April, June, August, October, and December 2020 respectively, with lower values shown in blue and higher values shown in orange. Panel (g) shows the time series of tower-based GPP estimates (GPP_NT_VUT_REF) (black line), XGB_Emb+Clim predictions (blue line), XGB_GAM predictions (orange line), and pixel-mean XGB_GAM predictions after spatialization (green color). R^2 values of models before and after fine-tuning and spatialization are displayed at the top of panel (g). The red dashed lines in panel (g) indicate the time points corresponding to panels (a)-(f) respectively. The background base map is taken from Esri World*

Imagery.

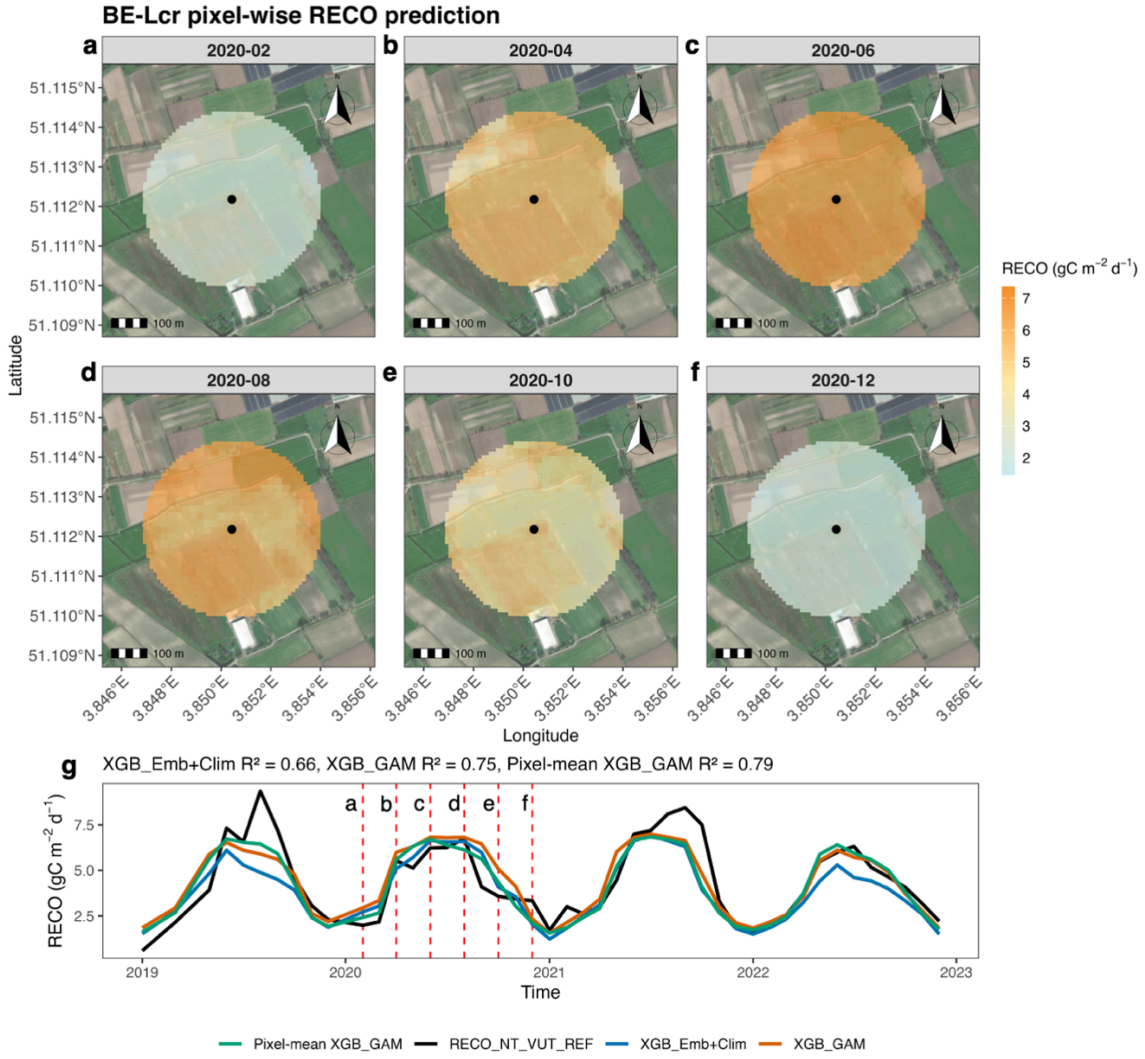


Figure 2.7. 10-m pixel-wise monthly R_{eco} estimates within the 250-m-radius around the eddy-covariance tower at the Lochristi poplar-planted site (BE-Lcr) (unseen site) from 2019-2022. *Panels (a)-(f) show static maps of pixel-level R_{eco} estimates for February, April, June, August, October, and December 2020 respectively, with lower values shown in blue and higher values shown in orange. Panel (g) shows the time series of tower-based R_{eco} estimates (RECO_NT_VUT_REF) (black line), XGB_Emb+Clim predictions (blue line), XGB_GAM predictions (orange line), and pixel-mean XGB_GAM predictions after spatialization (green color). R^2 values of models before and after fine-tuning and spatialization are displayed at the top of panel (g). The red dashed lines in panel (g) indicate the time points corresponding to*

panels (a)-(f) respectively. The background base map is taken from Esri World Imagery.

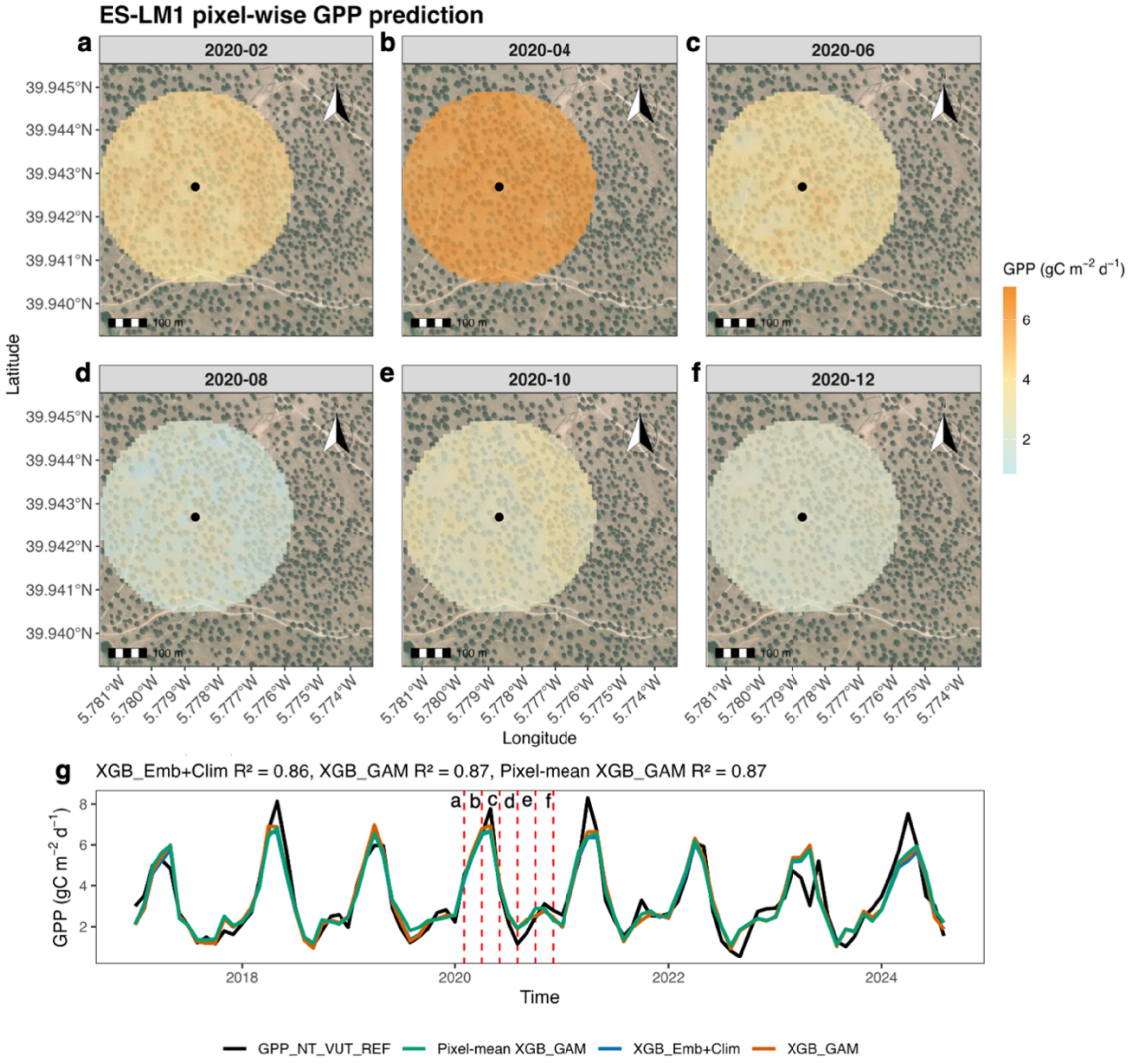


Figure 2.8. 10-m pixel-wise monthly GPP estimates within the 250-m-radius around the eddy-covariance tower at the Majadas del Tietar North savanna (ES-LM1) (unseen site) from 2017-2024. *Panels (a)-(f) show static maps of pixel-level GPP estimates for February, April, June, August, October, and December 2020 respectively, with lower values shown in blue and higher values shown in orange. Panel (g) shows the time series of tower-based GPP estimates (GPP_NT_VUT_REF) (black line), XGB_Emb+Clim predictions (blue line), XGB_GAM predictions (orange*

line), and pixel-mean XGB_GAM predictions after spatialization (green color). R^2 values of models before and after fine-tuning and spatialization are displayed at the top of panel (g). The red dashed lines in panel (g) indicate the time points corresponding to panels (a)-(f) respectively. The background base map is taken from Esri World Imagery.

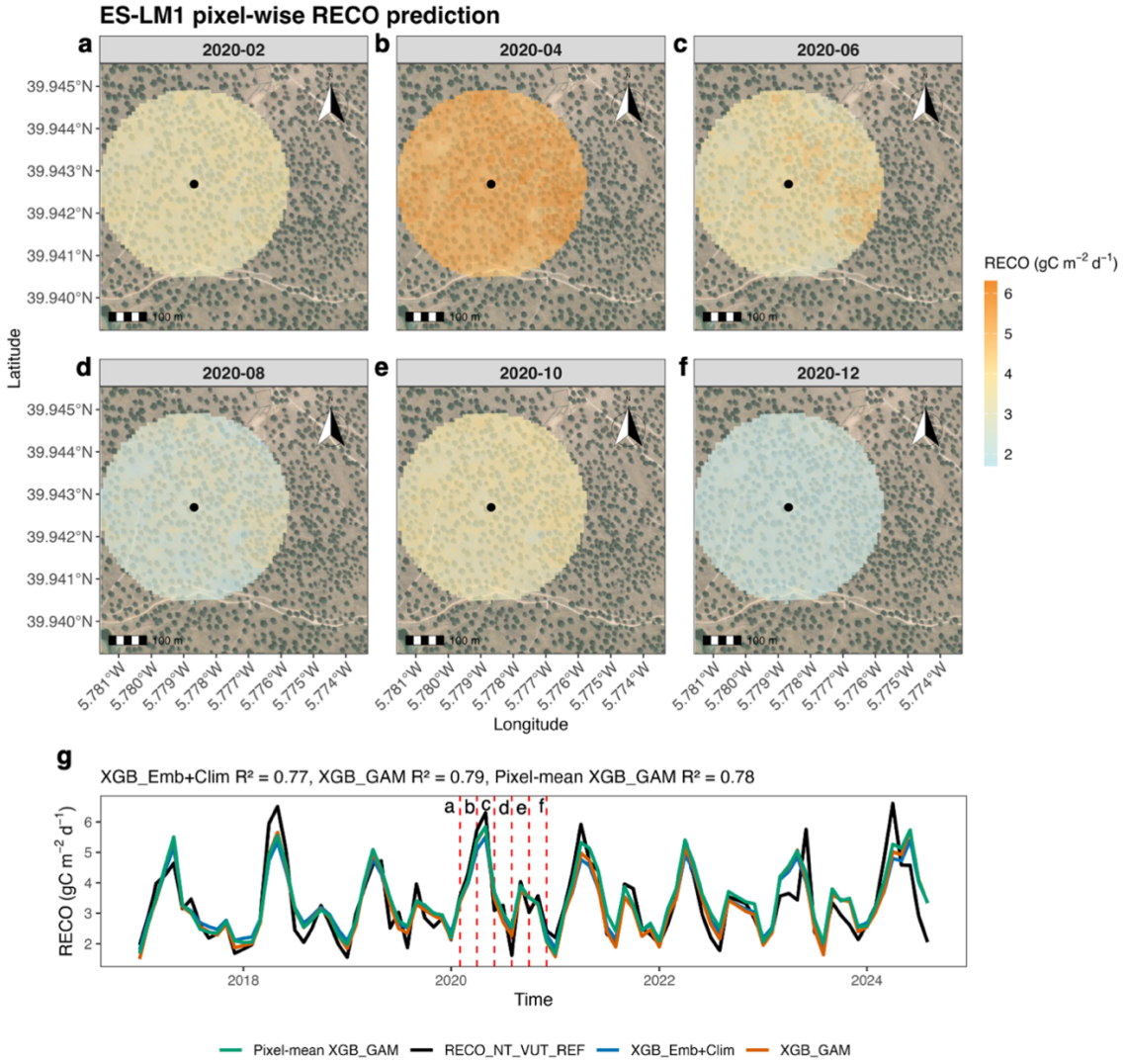


Figure 2.9. 10-m pixel-wise monthly R_{eco} estimates within the 250-m-radius around the eddy-covariance tower at the Majadas del Tietar North savanna (ES-LM1) (unseen site) from 2017-2024. *Panels (a)-(f) show static maps of pixel-level R_{eco} estimates for February, April, June, August, October, and December 2020 respectively, with lower values shown in blue and higher values shown in orange.*

Panel (g) shows the time series of tower-based R_{eco} estimates (RECO_NT_VUT_REF) (black line), XGB_Emb+Clim predictions (blue line), XGB_GAM predictions (orange line), and pixel-mean XGB_GAM predictions after spatialization (green color). R^2 values of models before and after fine-tuning and spatialization are displayed at the top of panel (g). The red dashed lines in panel (g) indicate the time points corresponding to panels (a)-(f) respectively. The background base map is taken from Esri World Imagery.

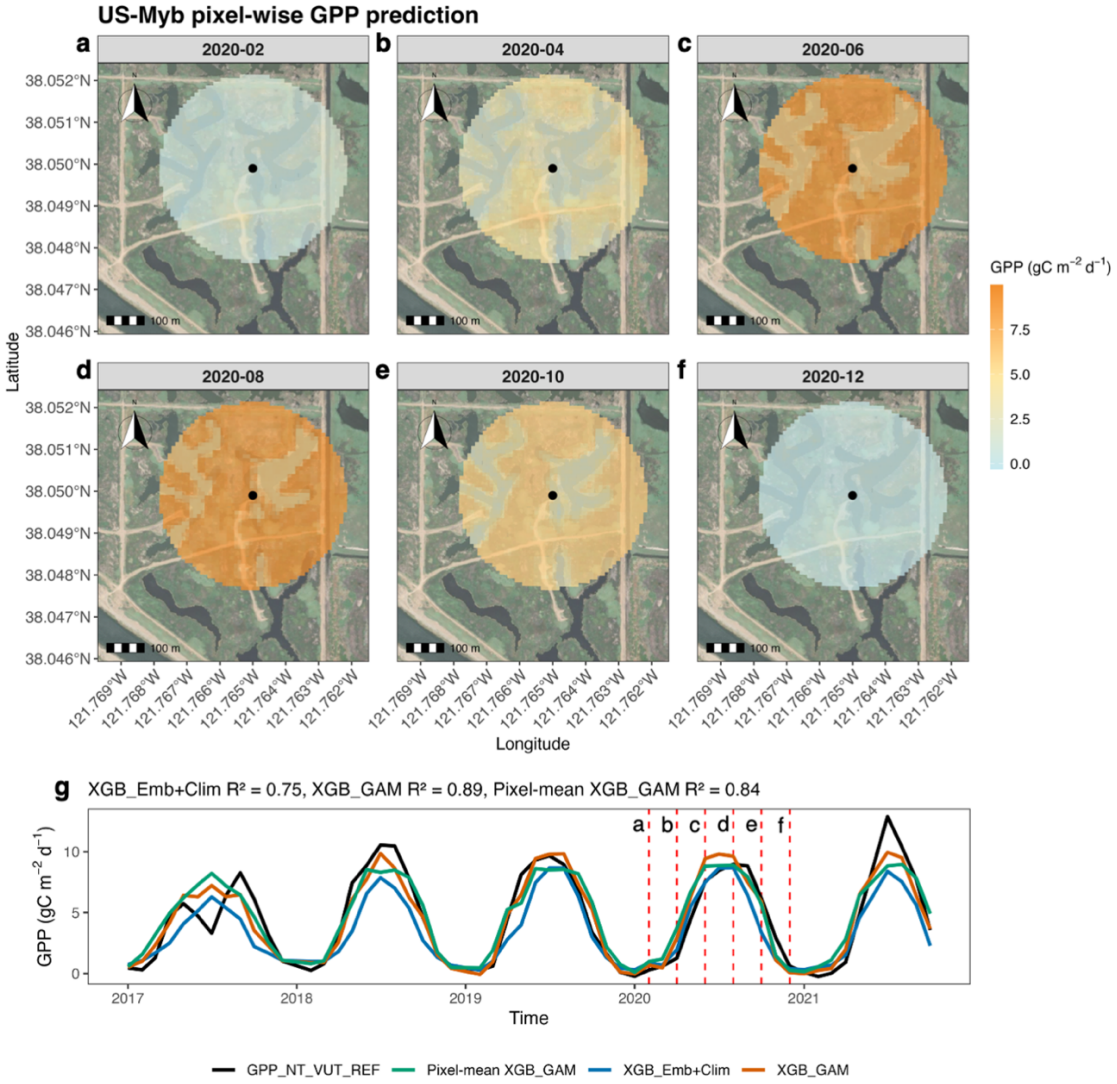


Figure 2.10. 10-m pixel-wise monthly GPP estimates within the 250-m-radius around the eddy-covariance tower at the Mayberry wetland (US-Myb) (unseen

site) from 2017-2021. *Panels (a)-(f) show static maps of pixel-level GPP estimates for February, April, June, August, October, and December 2020 respectively, with lower values shown in blue and higher values shown in orange. Panel (g) shows the time series of tower-based GPP estimates (GPP_NT_VUT_REF) (black line), XGB_Emb+Clim predictions (blue line), XGB_GAM predictions (orange line), and pixel-mean XGB_GAM predictions after spatialization (green color). R^2 values of models before and after fine-tuning and spatialization are displayed at the top of panel (g). The red dashed lines in panel (g) indicate the time points corresponding to panels (a)-(f) respectively. The background base map is taken from Esri World Imagery.*

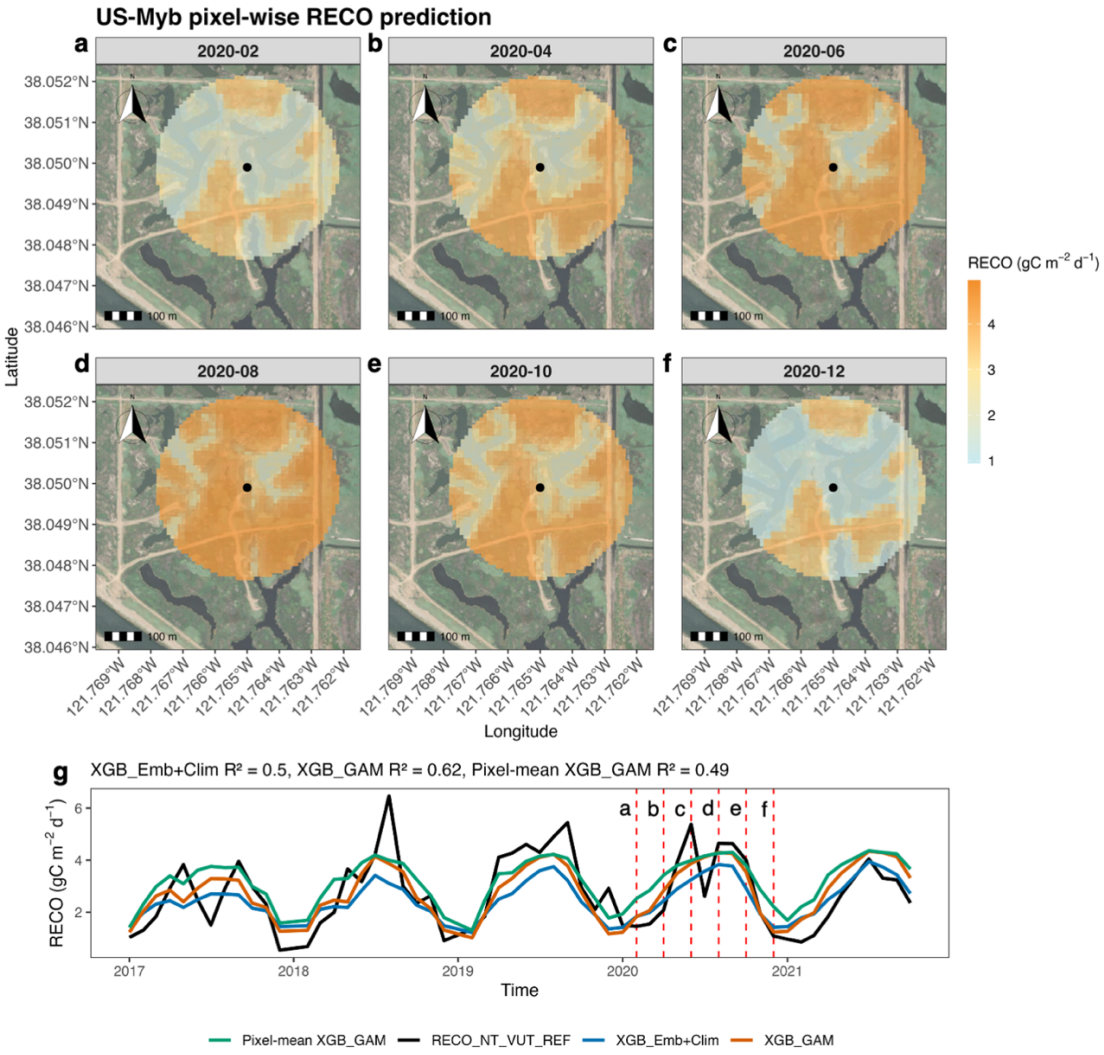


Figure 2.11. 10-m pixel-wise monthly R_{eco} estimates within the 250-m-radius around the eddy-covariance tower at the Mayberry wetland (US-Myb) (unseen site) from 2017-2021. *Panels (a)-(f) show static maps of pixel-level R_{eco} estimates for February, April, June, August, October, and December 2020 respectively, with lower values shown in blue and higher values shown in orange. Panel (g) shows the time series of tower-based R_{eco} estimates (RECO_NT_VUT_REF) (black line), XGB_Emb+Clim predictions (blue line), XGB_GAM predictions (orange line), and pixel-mean XGB_GAM predictions after spatialization (green color). R^2 values of models before and after fine-tuning and spatialization are displayed at the top of panel (g). The red dashed lines in panel (g) indicate the time points corresponding to panels (a)-(f) respectively. The background base map is taken from Esri World Imagery.*

2.4. Discussion

2.4.1. XGBoost model evaluation

Adding embedding features, either as standalone predictors or in combination with climatic variables, generally improves the mean model performance compared with only using climatic variables (Fig. 2.2). Embedding-based models also achieve comparable performance to previous studies in estimating *GPP* and R_{eco}, highlighting the potential of AEF embedding datasets for carbon flux modeling (Kang et al., 2025; Nelson et al., 2024). It is likely because embedding features contain compressed information from massive and diverse Earth observation (EO) datasets, including optical, radar, LiDAR, and environmental datasets, that represent comprehensive aspects of ecosystems and landscapes (Brown et al., 2025). The results are promising because first, embedding datasets facilitate the harmonization across different EO products and second, they highlight the opportunity to apply geospatial foundation models such as AlphaEarth Foundation to spatialize eddy-covariance measurements.

Notably, models using embedding features as standalone or in combination with climatic variables yield no significant differences in terms of overall performance ($P > 0.05$) (Fig. 2.2) (Extended Data Table 2.3, 2.4). This suggests that AEF embeddings may already contain important information about ecosystem structure and environmental conditions, and adding climatic variables does not significantly improve the embedding-based model setups. Similar findings have been reported for remote sensing-driven models, where adding meteorological variables did not significantly improve over models informed exclusively by remotely sensed data (Joiner & Yoshida, 2020; Tramontana et al., 2015). Interestingly, the embedding-only model setup (*XGB_Emb*), which only has annual embeddings and month-of-year as temporal dynamic features, achieves performance comparable to other embedding-based models that combine embeddings with monthly climatic features for both *GPP* and R_{eco} (Fig. 2.2; Extended Data Table 2.3, 2.4). This could be because, even though AEF embeddings are provided at an annual temporal resolution, their dimensions encode finer-scale temporal information from the underlying EO datasets through the Space-Time Precision (STP) encoder (Brown et al., 2025).

Across all model setups, R_{eco} mean predictive performance is lower than that of *GPP*, which could be due to R_{eco} including both autotrophic and heterotrophic respiration, which are governed by complex aboveground and belowground processes. These processes include but are not limited to plant-microbe rhizosphere interaction and soil microbial activities that are determined by not just climatic variables but also soil properties, moisture, and carbon availability that are more difficult to observe from satellites (Chapin et al., 2011; Migliavacca et al., 2011). In addition, standard flux partitioning methods may miss important R_{eco} dynamics, such as rain-induced respiration pulses in drylands (Nguyen et al., 2025). These limitations may partially explain why R_{eco} in general is more difficult to predict than *GPP* across sites and model setups. Regarding monthly anomalies for both *GPP* and R_{eco}, all models show lower predictive performance than seasonal and monthly estimates, which could be due to anomaly prediction requiring the model to capture non-steady-state and short-term processes that deviate from the seasonal patterns (Fig. 2.2).

Across half of PFTs (CRO, ENF, GRA, WET), incorporating embedding features leads to clear improvements in R_{eco} predictions compared with non-embedding models (Fig. 2.4). In other PFTs including MF, OSH, and SAV, *XGB_Clim* achieves higher mean predictive performance than three embedding-based setups, even though its predictive performance remains relatively low for these PFTs (0.44±0.16, -0.18±0.14, and 0.32±0.14 respectively) (Fig. 2.4). However, it is worth noting that there are much fewer unseen sites for these PFTs across all runs (MF: n = 5, OSH: n = 6, SAV: n = 7) than CRO (n = 17), DBF (n = 19), ENF (n = 28), GRA (n = 18), and WET (n = 15) and also fewer training sites. These smaller sample sizes could contribute to higher variability in the predictive performance for these sites and a more skewed distribution of the training datasets. In the case of DBF (n = 19), *XGB_Tair* and *XGB_Climatic* have higher performance than *XGB_Emb*, and *XGB_Tair* has the highest performance among five model setups (Fig. 2.4b). One possible explanation is that air temperature is the dominant driver of R_{eco} in energy-limited biomes like DBF, so adding additional features could lead to unnecessary complexity. Another possible explanation is related to how R_{eco} is derived from flux tower net ecosystem exchange measurements. The nighttime partitioning method estimates

R_{eco} as an exponential function of temperature, with reference respiration accounting for environmental variability within a short temporal window (Reichstein et al., 2005). Therefore, when data are aggregated to monthly averages, air temperature alone might be sufficient to predict R_{eco} in energy-limited biomes. Furthermore, when we investigate more closely into DBF sites, we found that the lower mean performance of *XGB_Climatic* was strongly influenced by site CA-TPD, where R_{eco} predictive performance was very low for *XGB_Climatic* (R^2 = -1.5) but high for *XGB_Tair* (R^2 = 0.86). This suggests that the model performance could be influenced by site-specific factors, such as site history, management practices, and data quality, which may explain why some model setups outperform others at particular sites.

Finally, among all PFTs, all models seem to be unable to capture *GPP* and R_{eco} fluxes in OSH and SAV (Fig. 2.3, 2.4). This is likely because there are fewer sites represented by these PFTs in both training and testing sets, and mechanistically, CO_2 fluxes in these ecosystems are strongly controlled by soil water availability rather than climatic variables alone. In drylands, intermittent rain pulses can trigger pulses of plant growth and soil microbial respiration that contribute substantially to annual net ecosystem productivity (Nguyen et al., 2025; Noy-Meir, 1973), which are still not captured well by both eddy-covariance carbon flux models and satellite products.

2.4.2. Fine-tuned model evaluation by sites

GAM-based fine-tuning is a simple, empirical approach for bias-correcting FluxLens predictions, making it an initial step for further model refinement at the individual site scale. Our results show that the model predictive performance varies widely across sites, and after fine-tuning, there are much fewer sites with negative R^2 and the overall R^2 range improves for both *GPP* and R_{eco}. *XGB_GAM* increases the interquartile range of R^2 from 0.43-0.88 to 0.65-0.95 for *GPP* (Fig. 2.5a), and from 0.09-0.77 to 0.64-0.90 for R_{eco} (Fig. 2.5c).

However, this correction remains empirical since it models the target variable as a non-linear function of the predictions, rather than explicitly incorporating ecological processes or site-specific mechanisms into the model. As a result, further improvements could include discussions with site-specific principal investigators to better understand site-specific conditions and measurement uncertainties, retraining

the model with more measurements, and using FluxPulse bias-corrected CO_2 fluxes during pulse events in drylands as the training datasets, since conventional eddy-covariance partitioning methods underestimate up to 30% CO_2 fluxes during rain-pulse events (Nguyen et al., 2025). Training on FluxPulse datasets could be a promising approach for incorporating pulse-driven ecological processes and improving model performance at poorly performing sites in SAV and OSH.

2.4.3. FluxLens: 10-meter spatialization of eddy-covariance carbon fluxes

Given the robust performance of FluxLens across sites, our study demonstrates that embedding datasets have strong potential in spatializing eddy-covariance carbon fluxes. FluxLens well captures flux magnitude and seasonal dynamics, with the averages across all pixels showing strong agreement with tower-based *GPP* and R_{eco} estimates, with the interquartile R^2 ranges of 0.65-0.94 for *GPP* (Fig. 2.5b) and 0.58-0.88 for R_{eco} across 115 unseen sites from all runs (Fig. 2.5d). The agreement between pixel-mean predictions and tower-based estimates provides an initial assessment of FluxLens accuracy and demonstrates its promising potential for spatializing eddy-covariance carbon fluxes. In addition, in three case-study sites, FluxLens can capture the visible spatial nonuniformities, including the crop-field boundaries at BE-Lcr (Fig. 2.6, 2.7), the scattered distribution of trees and grasses at ES-LM1 (Fig. 2.8. 2.9), and the open-water and vegetated boundaries at US-Myb (Fig. 2.10, 2.11).

Across the three case-study sites, pixel-mean predictions achieve R^2 values comparable to *XGB_GAM* predictions for *GPP* and R_{eco}, except for R_{eco} estimation at US-Myb (Fig. 2.11g). This lower performance at US-Myb could be due to the highly heterogeneous landscape which consists of both open-water and vegetated areas. It is worth acknowledging that we trained the XGBoost model using predictors calculated as the mean across all pixels within the measurement areas around the towers. Therefore, according to Jensen's inequality, assuming the landscape is never 100% homogeneous and carbon fluxes responding non-linearly to environmental predictors, the model prediction for the whole area is never equal to the mean of model predictions at individual pixels (Mcshane, 1937).

Notably, FluxLens achieves the highest performance at ES-LM1 among all

case-study sites, with R^2 values ranging from 0.85-0.87 across all *GPP* models and 0.78-0.80 across all R_{eco} models. This strong performance is likely because its paired site with similar ecosystems, ES-LM2, was included in the training set.

Our study provides a novel framework for mapping tower-based *GPP* and R_{eco} estimates at 10-m spatial resolution across diverse biomes. In contrast with previous flux-spatialization approaches focusing on individual sites (Metzger et al., 2013; Romero et al., 2026; K. Xu et al., 2017), our FluxLens framework is trained using flux towers globally, which allows us to capture cross-site variabilities and improve model generalization across biomes. In addition, FluxLens explicitly evaluates the spatialization accuracy across sites by comparing pixel-mean predictions against tower-based estimates for both *GPP* and R_{eco}. A further contribution is the production of spatially explicit R_{eco} maps, since R_{eco} has received much less attention than *GPP* in previous spatialization and upscaling efforts. Moreover, using AEF embeddings also does not require extensive data preprocessing to harmonize the spatiotemporal resolution of remote sensing products and tower carbon flux estimates, which could significantly reduce computational and manual efforts, while still producing temporally continuous and high-spatial resolution features.

Although FluxLens has limitations such as our models (1) are trained at a monthly scale rather than at a high-frequency (Metzger et al., 2013; K. Xu et al., 2017) or a biweekly temporal resolution (Romero et al., 2026), (2) do not yet incorporate dynamic footprint climatology, (3) do not yet incorporate land cover masks to mask out unreasonable predictions over non-vegetated areas, such as positive *GPP* over open-water areas at some time steps at the Mayberry wetland (Fig. 10c, d), and (4) are temporally limited to the availability of AEF embeddings from 2017 to 2024 (version 1), this framework represents a scalable and practical approach for spatializing ecosystem carbon fluxes. These maps can support applications such as estimating *GPP* and R_{eco} for specific crop fields, comparing plot-scale measurements with ecosystem-scale eddy-covariance observations, evaluating high-resolution satellite products, and supporting carbon monitoring and verification of nature-based climate solutions projects.

Further development and validation of FluxLens will require (1) independent pixel-level or sub-footprint carbon flux measurements such as from chamber-based

vegetation and soil flux measurements and from adjacent flux towers, (2) land-cover masks for non-vegetated areas, (3) metrics of landscape heterogeneity, and (4) incorporation of tower footprint climatology. It is worth noting that although we examine a fixed circular area with a 250-m radius around the towers, the true tower footprint is dynamic over time and covers an area depending on wind speed and direction, surface roughness and instrument height (Chu et al., 2021, 2026; Kljun et al., 2015). We, however, still chose to use a fixed 250-m radius area because it serves as a proof of concept for future development and applications. In general, a 250-m-radius area introduces the least bias in representing land surface characteristics among fixed-radius buffers ranging from 250 to 3000 m around the tower across diverse PFTs (Chu et al., 2021). Incorporating tower footprint climatology is necessary as future steps to account for the temporal variation in the measurement areas, which will further improve the model and the accuracy of the predictions of carbon fluxes.

2.5. Conclusions

Our study found that using embedding features achieves predictive performance comparable to previous studies and generally improves the mean model performance compared with using only climatic features for *GPP* and R_{eco}, suggesting that AEF embeddings have promising applications in predicting ecosystem carbon fluxes. However, the performance varies across flux components, temporal scales, and plant functional types. Regarding flux components, R_{eco} remains more difficult to model than *GPP* since it depends on complex interactions between above- and belowground processes that are not fully captured by the current predictors. Regarding temporal scales, monthly anomalies remain more challenging to model than seasonal patterns and monthly values. Regarding PFTs, both fluxes remain challenging to model in OSH and SAV which could be due to short-term soil moisture dynamics and ecosystem responses to rain-pulse events not being well captured by satellite datasets. Our results also suggest that adding more predictors does not always improve the model performance. In DBF, air temperature alone captures much of the R_{eco} variability, and adding more variables may introduce unnecessary complexity.

We also found that generalized additive model (GAM) correction is an

empirical, simple, and efficient approach for fine-tuning model predictions based only on site-specific eddy-covariance flux observations. Combining embedding-based XGBoost models and the GAM fine-tuned approach, our FluxLens framework could capture the visible landscape nonuniformities, flux magnitude, and seasonal dynamics at high spatial resolution within tower areas. The strong agreement between pixel-mean predictions and tower-based *GPP* and R_{eco} estimates suggests that FluxLens has strong potential in spatializing eddy-covariance fluxes. Future work should incorporate dynamic footprint climatology to model and extrapolate fluxes more accurately, and take into account carbon flux responses to rain pulses and soil water dynamics in dryland sites to better capture carbon fluxes in water-limited regions.

2.6. Acknowledgment

FLUXNET data products were produced and harmonized by eddy covariance regional networks and data processing centers, including AmeriFlux, ChinaFlux, European Fluxes Database, ICOS, JapanFlux, KoFlux, OzFlux, SAEON, and TERN. These products also include a modified version of ERA5 hourly data provided by the Copernicus Climate Change Service. Funding for the AmeriFlux data service was provided by the U.S. Department of Energy Office of Science. TERN data are from the TERN Data Discovery Portal https://portal.tern.org.au/browse/theme.

2.7. Data availability

The FLUXNET data products and citations used in this work were downloaded from the FLUXNET Data Explorer (v1.0.0) toolkit (Keenan, 2026), on March 11, 2026. Eddy covariance sites are publicly available and can also be downloaded from the official website FLUXNET Shuttle (https://data.fluxnet.org/).

2.8. Bibliography

Abatzoglou, J. T., Dobrowski, S. Z., Parks, S. A., & Hegewisch, K. C. (2018). TerraClimate, a high-resolution global dataset of monthly climate and climatic water balance from 1958–2015. *Scientific Data*, *5*(1), 170191. https://doi.org/10.1038/sdata.2017.191

Ahlström, A., Raupach, M. R., Schurgers, G., Smith, B., Arneth, A., Jung, M., Reichstein, M., Canadell, J. G., Friedlingstein, P., Jain, A. K., Kato, E., Poulter, B., Sitch, S., Stocker, B. D., Viovy, N., Wang, Y. P., Wiltshire, A., Zaehle, S., & Zeng, N. (2015). The dominant role of semi-arid ecosystems in the trend and variability of the land CO2 sink. *Science*, *348*(6237), 895–899. https://doi.org/10.1126/science.aaa1668

Babst, F., Bouriaud, O., Papale, D., Gielen, B., Janssens, I. A., Nikinmaa, E., Ibrom, A., Wu, J., Bernhofer, C., Köstner, B., Grünwald, T., Seufert, G., Ciais, P., & Frank, D. (2014). Above-ground woody carbon sequestration measured from tree rings is coherent with net ecosystem productivity at five eddy-covariance sites. *New Phytologist*, *201*(4), 1289–1303. https://doi.org/10.1111/nph.12589

Bacastow, R., & Keeling, C. K. (1973). Atmospheric carbon dioxide and radiocarbon in the natural carbon cycle: II. Changes from A. D. 1700 to 2070 as deduced from a geochemical model. *Brookhaven Symposia in Biology*, (30), 86–135.

Baldocchi, D. (2014). Measuring fluxes of trace gases and energy between ecosystems and the atmosphere – the state and future of the eddy covariance method. *Global Change Biology*, *20*(12), 3600–3609. https://doi.org/10.1111/gcb.12649

Baldocchi, D. D. (2020). How eddy covariance flux measurements have contributed to our understanding of Global Change Biology. *Global Change Biology*, *26*(1), 242–260. https://doi.org/10.1111/gcb.14807

Baldocchi, D., Falge, E., Gu, L., Olson, R., Hollinger, D., Running, S., null, Anthoni, P., Bernhofer, C., Davis, K., Evans, R., Fuentes, J., Goldstein, A., Katul, G., Law, B., Lee, X., Malhi, Y., Meyers, T., Munger, W., Oechel, W., … Wofsy, S. (2001). FLUXNET: A new tool to study the temporal and spatial variability of ecosystem-scale carbon dioxide, water vapor, and energy flux densities.

Bulletin of the American Meteorological Society, *82*(11), 2415–2434. https://doi.org/10.1175/1520-0477(2001)082%3C2415:FANTTS%3E2.3.CO;2

Barnard, R. L. (2020). Rewetting of soil: Revisiting the origin of soil CO2 emissions. *Soil Biology and Biochemistry*.

Birch, H. F. (1958). The effect of soil drying on humus decomposition and nitrogen availability. *Plant and Soil*, *10*(1), 9–31. https://doi.org/10.1007/BF01343734

Bottner, P. (1985). Response of microbial biomass to alternate moist and dry conditions in a soil incubated with 14C- and 15N-labelled plant material. *Soil Biology and Biochemistry*, *17*(3), 329–337. https://doi.org/10.1016/0038-0717(85)90070-7

Breiman, L., Friedman, J., Olshen, R. A., & Stone, C. J. (2017). *Classification and Regression Trees*. Chapman and Hall/CRC. https://doi.org/10.1201/9781315139470

Broeckx, L. S., Verlinden, M. S., Berhongaray, G., Zona, D., Fichot, R., & Ceulemans, R. (2014). The effect of a dry spring on seasonal carbon allocation and vegetation dynamics in a poplar bioenergy plantation. *GCB Bioenergy*, *6*(5), 473–487. https://doi.org/10.1111/gcbb.12087

Brown, C. F., Kazmierski, M. R., Pasquarella, V. J., Rucklidge, W. J., Samsikova, M., Zhang, C., Shelhamer, E., Lahera, E., Wiles, O., Ilyushchenko, S., Gorelick, N., Zhang, L. L., Alj, S., Schechter, E., Askay, S., Guinan, O., Moore, R., Boukouvalas, A., & Kohli, P. (2025). *AlphaEarth Foundations: An embedding field model for accurate and efficient global mapping from sparse label data* (arXiv:2507.22291). arXiv. https://doi.org/10.48550/arXiv.2507.22291

Bu, J., & Xiao, J. (2025). Upscaling eddy covariance measurements of carbon and water fluxes to the continental scale by incorporating GEDI-derived canopy structural complexity metrics. *Remote Sensing of Environment*, *329*, 114930. https://doi.org/10.1016/j.rse.2025.114930

Burba, G. (2022). *Eddy covariance method for scientific, regulatory, and commercial applications*. LI-COR Biosciences. https://books.google.com/books?hl=en&lr=&id=acKEEAAAQBAJ&oi=fnd&pg=PA1&dq=Eddy+Covariance+Method+for+Scientific,+Regulatory,+and+C

ommercial+Applications&ots=BE9CiHBLZy&sig=OVSnaD2X5VrmAkdIxvT2uuyZDpI

Cabon, A., Kannenberg, S. A., Arain, A., Babst, F., Baldocchi, D., Belmecheri, S., Delpierre, N., Guerrieri, R., Maxwell, J. T., McKenzie, S., Meinzer, F. C., Moore, D. J. P., Pappas, C., Rocha, A. V., Szejner, P., Ueyama, M., Ulrich, D., Vincke, C., Voelker, S. L., … Anderegg, W. R. L. (2022). Cross-biome synthesis of source versus sink limits to tree growth. *Science*, *376*(6594), 758–761. https://doi.org/10.1126/science.abm4875

Cabon, A., Peters, R. L., Fonti, P., Martínez-Vilalta, J., & De Cáceres, M. (2020). Temperature and water potential co-limit stem cambial activity along a steep elevational gradient. *New Phytologist*, *226*(5), 1325–1340. https://doi.org/10.1111/nph.16456

Campioli, M., Vicca, S., Luyssaert, S., Bilcke, J., Ceschia, E., Chapin III, F. S., Ciais, P., Fernández-Martínez, M., Malhi, Y., Obersteiner, M., Olefeldt, D., Papale, D., Piao, S. L., Peñuelas, J., Sullivan, P. F., Wang, X., Zenone, T., & Janssens, I. A. (2015). Biomass production efficiency controlled by management in temperate and boreal ecosystems. *Nature Geoscience*, *8*(11), 843–846. https://doi.org/10.1038/ngeo2553

Chapin, F. S., Matson, P. A., & Vitousek, P. M. (2011). *Principles of Terrestrial Ecosystem Ecology*. Springer. https://doi.org/10.1007/978-1-4419-9504-9

Chen, S., Lin, G., Huang, J., & Jenerette, G. D. (2009). Dependence of carbon sequestration on the differential responses of ecosystem photosynthesis and respiration to rain pulses in a semiarid steppe. *Global Change Biology*, *15*(10), 2450–2461. https://doi.org/10.1111/j.1365-2486.2009.01879.x

Chen, T., & Guestrin, C. (2016). XGBoost: A Scalable Tree Boosting System. *Proceedings of the 22nd ACM SIGKDD International Conference on Knowledge Discovery and Data Mining*, 785–794. https://doi.org/10.1145/2939672.2939785

Chu, H., Baldocchi, D. D., John, R., Wolf, S., & Reichstein, M. (2017). Fluxes all of the time? A primer on the temporal representativeness of FLUXNET. *Journal of Geophysical Research: Biogeosciences*, *122*(2), 289–307. https://doi.org/10.1002/2016JG003576

Chu, H., Luo, X., Ouyang, Z., Chan, W. S., Dengel, S., Biraud, S. C., Torn, M. S., Metzger, S., Kumar, J., Arain, M. A., Arkebauer, T. J., Baldocchi, D., Bernacchi, C., Billesbach, D., Black, T. A., Blanken, P. D., Bohrer, G., Bracho, R., Brown, S., … Zona, D. (2021). Representativeness of Eddy-Covariance flux footprints for areas surrounding AmeriFlux sites. *Agricultural and Forest Meteorology*, *301–302*, 108350. https://doi.org/10.1016/j.agrformet.2021.108350

Chu, H., Metzger, S., Ouyang, Z., Griebel, A., Yi, K., Durden, D., Wolf, S., Kasak, K., Rey-Sanchez, C., Hernandez Rodriguez, L. C., Oikawa, P., Falco, N., Runkle, B. R. K., Ahmadi, A., & Matthes, J. (2026). Flux Footprints: A Critical Link to Bridge Eddy-Covariance Measurements With Models, Remote Sensing, and Other Observations. *Global Change Biology*, *32*(4), e70887. https://doi.org/10.1111/gcb.70887

Cohrs, K.-H., Varando, G., Carvalhais, N., Reichstein, M., & Camps-Valls, G. (2024). Causal hybrid modeling with double machine learning—Applications in carbon flux modeling. *Machine Learning: Science and Technology*. https://doi.org/10.1088/2632-2153/ad5a60

Dacal, M., Bradford, M. A., Plaza, C., Maestre, F. T., & García-Palacios, P. (2019). Soil microbial respiration adapts to ambient temperature in global drylands. *Nature Ecology & Evolution*, *3*(2), 232–238. https://doi.org/10.1038/s41559-018-0770-5

Delire, C., Séférian, R., Decharme, B., Alkama, R., Calvet, J.-C., Carrer, D., Gibelin, A.-L., Joetzjer, E., Morel, X., Rocher, M., & Tzanos, D. (2020). The Global Land Carbon Cycle Simulated With ISBA-CTRIP: Improvements Over the Last Decade. *Journal of Advances in Modeling Earth Systems*, *12*(9), e2019MS001886. https://doi.org/10.1029/2019MS001886

Delwiche, K., Matthes, J. H., Arias-Ortiz, A., Knox, S. H., Oikawa, P., Sturtevant, C., Verfaillie, J., Szutu, D., Keenan, T. F., & Baldocchi, D. (2025). Dynamic methane emissions in a restored wetland: Decadal insights into uncertain climate outcomes and critical science needs. *Agricultural and Forest Meteorology*, *373*, 110735. https://doi.org/10.1016/j.agrformet.2025.110735

Deng, Q., Hui, D., Chu, G., Han, X., & Zhang, Q. (2017). Rain-induced changes in soil CO2 flux and microbial community composition in a tropical forest of China. *Scientific Reports*, *7*(1), 5539. https://doi.org/10.1038/s41598-017-06345-2

El-Madany, T. S., Reichstein, M., Perez-Priego, O., Carrara, A., Moreno, G., Pilar Martín, M., Pacheco-Labrador, J., Wohlfahrt, G., Nieto, H., Weber, U., Kolle, O., Luo, Y.-P., Carvalhais, N., & Migliavacca, M. (2018). Drivers of spatio-temporal variability of carbon dioxide and energy fluxes in a Mediterranean savanna ecosystem. *Agricultural and Forest Meteorology*, *262*, 258–278. https://doi.org/10.1016/j.agrformet.2018.07.010

Fatichi, S., Leuzinger, S., & Körner, C. (2014). Moving beyond photosynthesis: From carbon source to sink-driven vegetation modeling. *New Phytologist*, *201*(4), 1086–1095. https://doi.org/10.1111/nph.12614

Fatichi, S., Pappas, C., Zscheischler, J., & Leuzinger, S. (2019). Modelling carbon sources and sinks in terrestrial vegetation. *New Phytologist*, *221*(2), 652–668. https://doi.org/10.1111/nph.15451

Feldman, A. F., Feng, X., Felton, A. J., Konings, A. G., Knapp, A. K., Biederman, J. A., & Poulter, B. (2024). Plant responses to changing rainfall frequency and intensity. *Nature Reviews Earth & Environment*, *5*(4), 276–294. https://doi.org/10.1038/s43017-024-00534-0

Feldman, A. F., Short Gianotti, D. J., Konings, A. G., McColl, K. A., Akbar, R., Salvucci, G. D., & Entekhabi, D. (2018). Moisture pulse-reserve in the soil-plant continuum observed across biomes. *Nature Plants*, *4*(12), 1026–1033. https://doi.org/10.1038/s41477-018-0304-9

Fierer, N., Grandy, A. S., Six, J., & Paul, E. A. (2009). Searching for unifying principles in soil ecology. *Soil Biology and Biochemistry*, *41*(11), 2249–2256. https://doi.org/10.1016/j.soilbio.2009.06.009

Fierer, N., & Schimel, J. P. (2003). A Proposed Mechanism for the Pulse in Carbon Dioxide Production Commonly Observed Following the Rapid Rewetting of a Dry Soil. *Soil Science Society of America Journal*, *67*(3), 798–805. https://doi.org/10.2136/sssaj2003.7980

Friedlingstein, P., Jones, M. W., O'Sullivan, M., Andrew, R. M., Bakker, D. C. E., Hauck, J., Le Quéré, C., Peters, G. P., Peters, W., Pongratz, J., Sitch, S., Canadell, J. G.,

Ciais, P., Jackson, R. B., Alin, S. R., Anthoni, P., Bates, N. R., Becker, M., Bellouin, N., … Zeng, J. (2022). Global Carbon Budget 2021. *Earth System Science Data*, *14*(4), 1917–2005. https://doi.org/10.5194/essd-14-1917-2022

Friedlingstein, P., Le Quéré, C., O'Sullivan, M., Hauck, J., Landschützer, P., Luijkx, I. T., Li, H., van der Woude, A., Schwingshackl, C., Pongratz, J., Regnier, P., Andrew, R. M., Bakker, D. C. E., Canadell, J. G., Ciais, P., Gasser, T., Jones, M. W., Lan, X., Morgan, E., … Tian, H. (2026). Emerging climate impact on carbon sinks in a consolidated carbon budget. *Nature*, *649*(8095), 98–103. https://doi.org/10.1038/s41586-025-09802-5

Friedlingstein, P., O'Sullivan, M., Jones, M. W., Andrew, R. M., Bakker, D. C. E., Hauck, J., Landschützer, P., Le Quéré, C., Li, H., Luijkx, I. T., Peters, G. P., Peters, W., Pongratz, J., Schwingshackl, C., Sitch, S., Canadell, J. G., Ciais, P., Aas, K., Alin, S. R., … Zeng, J. (2025). *Global Carbon Budget 2025*. ESSD – Anthroposphere/Energy and anthropogenic emissions. https://doi.org/10.5194/essd-2025-659

Friend, A. D., Chen, Y., Eckes-Shephard, A. H., Fonti, P., Hellmann, E., Rademacher, T., Richardson, A. D., & Thomas, P. R. (2025). *Implications of source-sink feedbacks for modelling tree carbon assimilation and growth* (p. 2024.09.27.615358). bioRxiv. https://doi.org/10.1101/2024.09.27.615358

Friend, A. D., Eckes-Shephard, A. H., Fonti, P., Rademacher, T. T., Rathgeber, C. B. K., Richardson, A. D., & Turton, R. H. (2019). On the need to consider wood formation processes in global vegetation models and a suggested approach. *Annals of Forest Science*, *76*(2), Article 2. https://doi.org/10.1007/s13595-019-0819-x

Gaber, M., Kang, Y., Schurgers, G., & Keenan, T. (2024). Using automated machine learning for the upscaling of gross primary productivity. *Biogeosciences*, *21*(10), 2447–2472. https://doi.org/10.5194/bg-21-2447-2024

Gardner, W. R. (1959). Solutions of the Flow Equation for the Drying of Soils and Other Porous Media. *Soil Science Society of America Journal*, *23*(3), 183–187. https://doi.org/10.2136/sssaj1959.03615995002300030010x

Gebler, S. (2015). Actual evapotranspiration and precipitation measured by lysimeters: A comparison with eddy covariance and tipping bucket. *Hydrol. Earth Syst. Sci.*

Gessler, A., & Zweifel, R. (2024). Beyond source and sink control – toward an integrated approach to understand the carbon balance in plants. *New Phytologist*, *242*(3), 858–869. https://doi.org/10.1111/nph.19611

Gherardi, L. A., & Sala, O. E. (2019). Effect of interannual precipitation variability on dryland productivity: A global synthesis. *Global Change Biology*, *25*(1), 269–276. https://doi.org/10.1111/gcb.14480

Green, J. K., & Keenan, T. F. (2022). The limits of forest carbon sequestration. *Science (New York, N.Y.)*, *376*(6594), 692–693. https://doi.org/10.1126/science.abo6547

Grinsztajn, L., Oyallon, E., & Varoquaux, G. (2022). *Why do tree-based models still outperform deep learning on tabular data?* (arXiv:2207.08815). arXiv. http://arxiv.org/abs/2207.08815

Griscom, B. W., Adams, J., Ellis, P. W., Houghton, R. A., Lomax, G., Miteva, D. A., Schlesinger, W. H., Shoch, D., Siikamäki, J. V., Smith, P., Woodbury, P., Zganjar, C., Blackman, A., Campari, J., Conant, R. T., Delgado, C., Elias, P., Gopalakrishna, T., Hamsik, M. R., … Fargione, J. (2017). Natural climate solutions. *Proceedings of the National Academy of Sciences*, *114*(44), 11645–11650. https://doi.org/10.1073/pnas.1710465114

Haverd, V., Smith, B., Nieradzik, L., Briggs, P. R., Woodgate, W., Trudinger, C. M., Canadell, J. G., & Cuntz, M. (2018). A new version of the CABLE land surface model (Subversion revision r4601) incorporating land use and land cover change, woody vegetation demography, and a novel optimisation-based approach to plant coordination of photosynthesis. *Geoscientific Model Development*, *11*(7), 2995–3026. https://doi.org/10.5194/gmd-11-2995-2018

Hsiao, T. C. (1973). Plant Responses to Water Stress. *Annual Review of Plant Biology*, *24*(Volume 24, 1973), 519–570. https://doi.org/10.1146/annurev.pp.24.060173.002511

Huang, B., & Nobel, P. S. (1993). Hydraulic conductivity and anatomy along lateral roots of cacti: Changes with soil water status. *New Phytologist*, *123*(3), 499–507. https://doi.org/10.1111/j.1469-8137.1993.tb03762.x

Huang, J., Yu, H., Guan, X., Wang, G., & Guo, R. (2016). Accelerated dryland expansion under climate change. *Nature Climate Change*, *6*(2), 166–171. https://doi.org/10.1038/nclimate2837

Huxman, T. E., Cable, J. M., Ignace, D. D., Eilts, J. A., English, N. B., Weltzin, J., & Williams, D. G. (2004). Response of net ecosystem gas exchange to a simulated precipitation pulse in a semi-arid grassland: The role of native versus non-native grasses and soil texture. *Oecologia*, *141*(2), 295–305. https://doi.org/10.1007/s00442-003-1389-y

Huxman, T. E., Snyder, K. A., Tissue, D., Leffler, A. J., Ogle, K., Pockman, W. T., Sandquist, D. R., Potts, D. L., & Schwinning, S. (2004). Precipitation pulses and carbon fluxes in semiarid and arid ecosystems. *Oecologia*, *141*(2), 254–268. https://doi.org/10.1007/s00442-004-1682-4

Inglima, I., Alberti, G., Bertolini, T., Vaccari, F. P., Gioli, B., Miglietta, F., Cotrufo, M. F., & Peressotti, A. (2009). Precipitation pulses enhance respiration of Mediterranean ecosystems: The balance between organic and inorganic components of increased soil CO2 efflux. *Global Change Biology*, *15*(5), 1289–1301. https://doi.org/10.1111/j.1365-2486.2008.01793.x

Jarvis, P., Rey, A., Petsikos, C., Wingate, L., Rayment, M., Pereira, J., Banza, J., David, J., Miglietta, F., Borghetti, M., Manca, G., & Valentini, R. (2007). Drying and wetting of Mediterranean soils stimulates decomposition and carbon dioxide emission: The "Birch effect"†. *Tree Physiology*, *27*(7), 929–940. https://doi.org/10.1093/treephys/27.7.929

Jenerette, G. D., Scott, R. L., & Huxman, T. E. (2008). Whole ecosystem metabolic pulses following precipitation events. *Functional Ecology*, *22*(5), 924–930. https://doi.org/10.1111/j.1365-2435.2008.01450.x

Jiang, M., Medlyn, B. E., Drake, J. E., Duursma, R. A., Anderson, I. C., Barton, C. V. M., Boer, M. M., Carrillo, Y., Castañeda-Gómez, L., Collins, L., Crous, K. Y., De Kauwe, M. G., dos Santos, B. M., Emmerson, K. M., Facey, S. L., Gherlenda, A. N., Gimeno, T. E., Hasegawa, S., Johnson, S. N., … Ellsworth, D. S. (2020). The fate of carbon in a mature forest under carbon dioxide enrichment. *Nature*, *580*(7802), 227–231. https://doi.org/10.1038/s41586-020-2128-9

Joiner, J., & Yoshida, Y. (2020). Satellite-based reflectances capture large fraction of variability in global gross primary production (GPP) at weekly time scales. *Agricultural and Forest Meteorology*, *291*, 108092. https://doi.org/10.1016/j.agrformet.2020.108092

Jung, M., Koirala, S., Weber, U., Ichii, K., Gans, F., Camps-Valls, G., Papale, D., Schwalm, C., Tramontana, G., & Reichstein, M. (2019). The FLUXCOM ensemble of global land-atmosphere energy fluxes. *Scientific Data*, *6*(1), 74. https://doi.org/10.1038/s41597-019-0076-8

Jung, M., Nelson, J., Migliavacca, M., El-Madany, T., Papale, D., Reichstein, M., Walther, S., & Wutzler, T. (2024). *Technical note: Flagging inconsistencies in flux tower data*.

Jung, M., Reichstein, M., & Bondeau, A. (2009). Towards global empirical upscaling of FLUXNET eddy covariance observations: Validation of a model tree ensemble approach using a biosphere model. *Biogeosciences*, *6*(10), 2001–2013. https://doi.org/10.5194/bg-6-2001-2009

Jung, M., Reichstein, M., Ciais, P., Seneviratne, S. I., Sheffield, J., Goulden, M. L., Bonan, G., Cescatti, A., Chen, J., de Jeu, R., Dolman, A. J., Eugster, W., Gerten, D., Gianelle, D., Gobron, N., Heinke, J., Kimball, J., Law, B. E., Montagnani, L., … Zhang, K. (2010). Recent decline in the global land evapotranspiration trend due to limited moisture supply. *Nature*, *467*(7318), 951–954. https://doi.org/10.1038/nature09396

Kang, Y., Bassiouni, M., Gaber, M., Lu, X., & Keenan, T. F. (2025). CEDAR-GPP: Spatiotemporally upscaled estimates of gross primary productivity incorporating CO_2 fertilization. *Earth System Science Data*, *17*(6), 3009–3046. https://doi.org/10.5194/essd-17-3009-2025

Kannenberg, S. A., Babst, F., Barnes, M. L., Cabon, A., Dannenberg, M. P., Johnston, M. R., & Anderegg, W. R. L. (2025). Stand density and local climate drive allocation of GPP to aboveground woody biomass. *New Phytologist*, *246*(2), 543–553. https://doi.org/10.1111/nph.20414

Kannenberg, S. A., Barnes, M. L., Bowling, D. R., Driscoll, A. W., Guo, J. S., & Anderegg, W. R. L. (2023). Quantifying the drivers of ecosystem fluxes and water potential across the soil-plant-atmosphere continuum in an arid woodland. *Agricultural*

and Forest Meteorology, *329*, 109269. https://doi.org/10.1016/j.agrformet.2022.109269

Kannenberg, S. A., Cabon, A., Babst, F., Belmecheri, S., Delpierre, N., Guerrieri, R., Maxwell, J. T., Meinzer, F. C., Moore, D. J. P., Pappas, C., Ueyama, M., Ulrich, D. E. M., Voelker, S. L., Woodruff, D. R., & Anderegg, W. R. L. (2022). Drought-induced decoupling between carbon uptake and tree growth impacts forest carbon turnover time. *Agricultural and Forest Meteorology*, *322*, 108996. https://doi.org/10.1016/j.agrformet.2022.108996

Keenan, T. F. (2026). *FLUXNET Data Explorer* [Computer software]. Zenodo. https://doi.org/10.5281/zenodo.20331228

Keenan, T. F., Luo, X., Stocker, B. D., De Kauwe, M. G., Medlyn, B. E., Prentice, I. C., Smith, N. G., Terrer, C., Wang, H., Zhang, Y., & Zhou, S. (2023). A constraint on historic growth in global photosynthesis due to rising CO2. *Nature Climate Change*, *13*(12), 1376–1381. https://doi.org/10.1038/s41558-023-01867-2

Keenan, T. F., Prentice, I. C., Canadell, J. G., Williams, C. A., Wang, H., Raupach, M., & Collatz, G. J. (2016). Recent pause in the growth rate of atmospheric CO2 due to enhanced terrestrial carbon uptake. *Nature Communications*, *7*(1), 13428. https://doi.org/10.1038/ncomms13428

Kim, J., Guo, Q., Baldocchi, D. D., Leclerc, M. Y., Xu, L., & Schmid, H. P. (2006). Upscaling fluxes from tower to landscape: Overlaying flux footprints on high-resolution (IKONOS) images of vegetation cover. *Agricultural and Forest Meteorology, Advances in Surface-Atmosphere Exchange - A Tribute to Marv Wesely*, *136*(3), 132–146. https://doi.org/10.1016/j.agrformet.2004.11.015

Kljun, N., Calanca, P., Rotach, M. W., & Schmid, H. P. (2015). A simple two-dimensional parameterisation for Flux Footprint Prediction (FFP). *Geoscientific Model Development*, *8*(11), 3695–3713. https://doi.org/10.5194/gmd-8-3695-2015

Körner, C. (2022). The forest's nutrient cycle drives its carbon cycle. *Tree Physiology*, *42*(3), 425–427. https://doi.org/10.1093/treephys/tpab170

Lasslop, G., Reichstein, M., Papale, D., Richardson, A. D., Arneth, A., Barr, A., Stoy, P., & Wohlfahrt, G. (2010). Separation of net ecosystem exchange into assimilation and respiration using a light response curve approach: Critical

issues and global evaluation. *Global Change Biology*, *16*(1), 187–208. https://doi.org/10.1111/j.1365-2486.2009.02041.x

Lauber, C. L., Hamady, M., Knight, R., & Fierer, N. (2009). Pyrosequencing-Based Assessment of Soil pH as a Predictor of Soil Bacterial Community Structure at the Continental Scale. *Applied and Environmental Microbiology*, *75*(15), 5111–5120. https://doi.org/10.1128/AEM.00335-09

Lawrence, D. M., Fisher, R. A., Koven, C. D., Oleson, K. W., Swenson, S. C., Bonan, G., Collier, N., Ghimire, B., van Kampenhout, L., Kennedy, D., Kluzek, E., Lawrence, P. J., Li, F., Li, H., Lombardozzi, D., Riley, W. J., Sacks, W. J., Shi, M., Vertenstein, M., … Zeng, X. (2019). The Community Land Model Version 5: Description of New Features, Benchmarking, and Impact of Forcing Uncertainty. *Journal of Advances in Modeling Earth Systems*, *11*(12), 4245–4287. https://doi.org/10.1029/2018MS001583

Lee, X., Wu, H.-J., Sigler, J., Oishi, C., & Siccama, T. (2004). Rapid and transient response of soil respiration to rain. *Global Change Biology*, *10*(6), 1017–1026. https://doi.org/10.1111/j.1529-8817.2003.00787.x

Legates, D. R., & DeLiberty, T. L. (1993). Precipitation Measurement Biases in the United States. *JAWRA Journal of the American Water Resources Association*, *29*(5), 855–861. https://doi.org/10.1111/j.1752-1688.1993.tb03245.x

Lempereur, M., Martin-StPaul, N. K., Damesin, C., Joffre, R., Ourcival, J.-M., Rocheteau, A., & Rambal, S. (2015). Growth duration is a better predictor of stem increment than carbon supply in a Mediterranean oak forest: Implications for assessing forest productivity under climate change. *New Phytologist*, *207*(3), 579–590. https://doi.org/10.1111/nph.13400

Lienert, S., & Joos, F. (2018). A Bayesian ensemble data assimilation to constrain model parameters and land-use carbon emissions. *Biogeosciences*, *15*(9), 2909–2930. https://doi.org/10.5194/bg-15-2909-2018

Lim, H., Medvigy, D., Mäkelä, A., Kim, D., Albaugh, T. J., Knier, A., Blaško, R., C Campoe, O., Deshar, R., Franklin, O., Henriksson, N., Littke, K., Lutter, R., Maier, C. A., Palmroth, S., Rosenvald, K., Slesak, R. A., Tullus, A., & Oren, R. (2024). Overlooked branch turnover creates a widespread bias in forest carbon accounting. *Proceedings of the National Academy of Sciences of the United*

States of America, *121*(42), e2401035121. https://doi.org/10.1073/pnas.2401035121

Lindeman, R. H., Merenda, P. F., & Gold, R. Z. (1980). *Introduction to bivariate and multivariate analysis* (Vol. 4). Scott, Foresman Glenview, IL. https://library.wur.nl/WebQuery/titel/1714678

Litton, C. M., Raich, J. W., & Ryan, M. G. (2007). Carbon allocation in forest ecosystems. *Global Change Biology*, *13*(10), 2089–2109. https://doi.org/10.1111/j.1365-2486.2007.01420.x

Liu, X., Wan, S., Su, B., Hui, D., & Luo, Y. (2002). Response of soil CO2 efflux to water manipulation in a tallgrass prairie ecosystem. *Plant and Soil*, *240*(2), 213–223. https://doi.org/10.1023/A:1015744126533

Lloyd, J., & Taylor, J. A. (1994). On the Temperature Dependence of Soil Respiration. *Functional Ecology*, *8*(3), 315–323. https://doi.org/10.2307/2389824

Luo, Y., El-Madany, T. S., Filippa, G., Ma, X., Ahrens, B., Carrara, A., Gonzalez-Cascon, R., Cremonese, E., Galvagno, M., Hammer, T. W., Pacheco-Labrador, J., Martín, M. P., Moreno, G., Perez-Priego, O., Reichstein, M., Richardson, A. D., Römermann, C., & Migliavacca, M. (2018). Using Near-Infrared-Enabled Digital Repeat Photography to Track Structural and Physiological Phenology in Mediterranean Tree–Grass Ecosystems. *Remote Sensing*, *10*(8), 1293. https://doi.org/10.3390/rs10081293

MacBean, N., Scott, R. L., Biederman, J. A., Peylin, P., Kolb, T., Litvak, M. E., Krishnan, P., Meyers, T. P., Arora, V. K., Bastrikov, V., Goll, D., Lombardozzi, D. L., Nabel, J. E. M. S., Pongratz, J., Sitch, S., Walker, A. P., Zaehle, S., & Moore, D. J. P. (2021). Dynamic global vegetation models underestimate net CO2 flux mean and inter-annual variability in dryland ecosystems. *Environmental Research Letters*, *16*(9), 094023. https://doi.org/10.1088/1748-9326/ac1a38

Maier, M., Schack-Kirchner, H., Hildebrand, E. E., & Holst, J. (2010). Pore-space CO2 dynamics in a deep, well-aerated soil. *European Journal of Soil Science*, *61*(6), 877–887. https://doi.org/10.1111/j.1365-2389.2010.01287.x

Mcshane, E. J. (1937). *JENSEN'S INEQUALITY*.

Melton, J. R., Arora, V. K., Wisernig-Cojoc, E., Seiler, C., Fortier, M., Chan, E., & Teckentrup, L. (2020). CLASSIC v1.0: The open-source community successor

to the Canadian Land Surface Scheme (CLASS) and the Canadian Terrestrial Ecosystem Model (CTEM) – Part 1: Model framework and site-level performance. *Geoscientific Model Development*, *13*(6), 2825–2850. https://doi.org/10.5194/gmd-13-2825-2020

Metz, E.-M., Vardag, S. N., Basu, S., Jung, M., Ahrens, B., El-Madany, T., Sitch, S., Arora, V. K., Briggs, P. R., Friedlingstein, P., Goll, D. S., Jain, A. K., Kato, E., Lombardozzi, D., Nabel, J. E. M. S., Poulter, B., Séférian, R., Tian, H., Wiltshire, A., … Butz, A. (2023). Soil respiration–driven CO2 pulses dominate Australia's flux variability. *Science*, *379*(6639), 1332–1335. https://doi.org/10.1126/science.add7833

Metzger, S., Junkermann, W., Mauder, M., Butterbach-Bahl, K., Trancón y Widemann, B., Neidl, F., Schäfer, K., Wieneke, S., Zheng, X. H., Schmid, H. P., & Foken, T. (2013). Spatially explicit regionalization of airborne flux measurements using environmental response functions. *Biogeosciences*, *10*(4), 2193–2217. https://doi.org/10.5194/bg-10-2193-2013

Migliavacca, M., Reichstein, M., Richardson, A. D., Colombo, R., Sutton, M. A., Lasslop, G., Tomelleri, E., Wohlfahrt, G., Carvalhais, N., Cescatti, A., Mahecha, M. D., Montagnani, L., Papale, D., Zaehle, S., Arain, A., Arneth, A., Black, T. A., Carrara, A., Dore, S., … Van Der MOLEN, M. K. (2011). Semiempirical modeling of abiotic and biotic factors controlling ecosystem respiration across eddy covariance sites. *Global Change Biology*, *17*(1), 390–409. https://doi.org/10.1111/j.1365-2486.2010.02243.x

Muller, B., Pantin, F., Génard, M., Turc, O., Freixes, S., Piques, M., & Gibon, Y. (2011). Water deficits uncouple growth from photosynthesis, increase C content, and modify the relationships between C and growth in sink organs. *Journal of Experimental Botany*, *62*(6), 1715–1729. https://doi.org/10.1093/jxb/erq438

Nelson, J. A., Walther, S., Gans, F., Kraft, B., Weber, U., Novick, K., Buchmann, N., Migliavacca, M., Wohlfahrt, G., Šigut, L., Ibrom, A., Papale, D., Göckede, M., Duveiller, G., Knohl, A., Hörtnagl, L., Scott, R. L., Dušek, J., Zhang, W., … Jung, M. (2024). X-BASE: The first terrestrial carbon and water flux products from an extended data-driven scaling framework, FLUXCOM-X. *Biogeosciences*, *21*(22), 5079–5115. https://doi.org/10.5194/bg-21-5079-2024

Nguyen, N. B., Migliavacca, M., Bassiouni, M., Baldocchi, D. D., Gherardi, L. A., Green, J. K., Papale, D., Reichstein, M., Cohrs, K.-H., Cescatti, A., Nguyen, T. D., Nguyen, H. H., Nguyen, Q. M., & Keenan, T. F. (2025). Widespread underestimation of rain-induced soil carbon emissions from global drylands. *Nature Geoscience*, 1–8. https://doi.org/10.1038/s41561-025-01754-9

Norby, R. J. (2025). Forest productivity response to elevated CO2 in free-air CO2 enrichment experiments: The 23 percent solution, revisited. *New Phytologist*, *246*(5), 1952–1959. https://doi.org/10.1111/nph.70162

Novick, K. A., Metzger, S., Anderegg, W. R. L., Barnes, M., Cala, D. S., Guan, K., Hemes, K. S., Hollinger, D. Y., Kumar, J., Litvak, M., Lombardozzi, D., Normile, C. P., Oikawa, P., Runkle, B. R. K., Torn, M., & Wiesner, S. (2022). Informing Nature-based Climate Solutions for the United States with the best-available science. *Global Change Biology*, *28*(12), 3778–3794. https://doi.org/10.1111/gcb.16156

Noy-Meir, I. (1973). Desert Ecosystems: Environment and Producers. *Annual Review of Ecology and Systematics*, 25–51. http://www.jstor.org/stable/2096803

Oikawa, P. Y., Jenerette, G. D., Knox, S. H., Sturtevant, C., Verfaillie, J., Dronova, I., Poindexter, C. M., Eichelmann, E., & Baldocchi, D. D. (2017). Evaluation of a hierarchy of models reveals importance of substrate limitation for predicting carbon dioxide and methane exchange in restored wetlands. *Journal of Geophysical Research: Biogeosciences*, *122*(1), 145–167. https://doi.org/10.1002/2016JG003438

Orchard, V. A., & Cook, F. J. (1983). Relationship between soil respiration and soil moisture. *Soil Biology and Biochemistry*, *15*(4), 447–453. https://doi.org/10.1016/0038-0717(83)90010-X

Papale, D., & Valentini, R. (2003). A new assessment of European forests carbon exchanges by eddy fluxes and artificial neural network spatialization. *Global Change Biology*, *9*(4), 525–535. https://doi.org/10.1046/j.1365-2486.2003.00609.x

Pastorello, G., Trotta, C., Canfora, E., Chu, H., Christianson, D., Cheah, Y.-W., Poindexter, C., Chen, J., Elbashandy, A., Humphrey, M., Isaac, P., Polidori, D., Reichstein, M., Ribeca, A., van Ingen, C., Vuichard, N., Zhang, L., Amiro, B.,

Ammann, C., ⋯ Papale, D. (2020). The FLUXNET2015 dataset and the ONEFlux processing pipeline for eddy covariance data. *Scientific Data*, *7*(1), 225. https://doi.org/10.1038/s41597-020-0534-3

Placella, S. A., Brodie, E. L., & Firestone, M. K. (2012). Rainfall-induced carbon dioxide pulses result from sequential resuscitation of phylogenetically clustered microbial groups. *Proceedings of the National Academy of Sciences*, *109*(27), 10931–10936. https://doi.org/10.1073/pnas.1204306109

Poggio, L., de Sousa, L. M., Batjes, N. H., Heuvelink, G. B. M., Kempen, B., Ribeiro, E., & Rossiter, D. (2021). SoilGrids 2.0: Producing soil information for the globe with quantified spatial uncertainty. *SOIL*, *7*(1), 217–240. https://doi.org/10.5194/soil-7-217-2021

Poulter, B., Frank, D., Ciais, P., Myneni, R. B., Andela, N., Bi, J., Broquet, G., Canadell, J. G., Chevallier, F., Liu, Y. Y., Running, S. W., Sitch, S., & van der Werf, G. R. (2014). Contribution of semi-arid ecosystems to interannual variability of the global carbon cycle. *Nature*, *509*(7502), 600–603. https://doi.org/10.1038/nature13376

Rahman, M. (2026). Physically interpretable AlphaEarth foundation model embeddings enable LLM-based land surface intelligence. *Remote Sensing Applications: Society and Environment*, *42*, 102045. https://doi.org/10.1016/j.rsase.2026.102045

Raich, J. W., & Potter, C. S. (1995). Global patterns of carbon dioxide emissions from soils. *Global Biogeochemical Cycles*, *9*(1), 23–36. https://doi.org/10.1029/94GB02723

Rao, M. P., Pacheco-Solana, A., Li, R., Oryan, B., Jensen, J. E., Rodriguez-Caton, M., Klinek, L., Pierrat, Z. A., Ruehr, S., Oelkers, R., Boeschoten, L. E., Griffin, K. L., McCormack, M. L., Yang, X., Verfaillie, J., Baldocchi, D., Hise, J., Turner, A. J., Scanlon, T. M., ⋯ Magney, T. S. (2026). Decoupled carbon assimilation and growth responses to aridity in temperate deciduous oaks. *Science Advances*, *12*(24), eady7139. https://doi.org/10.1126/sciadv.ady7139

Reichstein, M., Falge, E., Baldocchi, D., Papale, D., Aubinet, M., Berbigier, P., Bernhofer, C., Buchmann, N., Gilmanov, T., Granier, A., Grünwald, T., Havránková, K., Ilvesniemi, H., Janous, D., Knohl, A., Laurila, T., Lohila, A., Loustau, D., Matteucci,

G., ⋯ Valentini, R. (2005). On the separation of net ecosystem exchange into assimilation and ecosystem respiration: Review and improved algorithm. *Global Change Biology*, *11*(9), 1424–1439. https://doi.org/10.1111/j.1365-2486.2005.001002.x

Reichstein, M., Rey, A., Freibauer, A., Tenhunen, J., Valentini, R., Banza, J., Casals, P., Cheng, Y., Grünzweig, J. M., Irvine, J., Joffre, R., Law, B. E., Loustau, D., Miglietta, F., Oechel, W., Ourcival, J.-M., Pereira, J. S., Peressotti, A., Ponti, F., ⋯ Yakir, D. (2003). Modeling temporal and large-scale spatial variability of soil respiration from soil water availability, temperature and vegetation productivity indices. *Global Biogeochemical Cycles*, *17*(4). https://doi.org/10.1029/2003GB002035

Reynolds, J. F., Smith, D. M. S., Lambin, E. F., Turner, B. L., Mortimore, M., Batterbury, S. P. J., Downing, T. E., Dowlatabadi, H., Fernández, R. J., Herrick, J. E., Huber-Sannwald, E., Jiang, H., Leemans, R., Lynam, T., Maestre, F. T., Ayarza, M., & Walker, B. (2007). Global Desertification: Building a Science for Dryland Development. *Science*, *316*(5826), 847–851. https://doi.org/10.1126/science.1131634

Richardson, A. D., Carbone, M. S., Keenan, T. F., Czimczik, C. I., Hollinger, D. Y., Murakami, P., Schaberg, P. G., & Xu, X. (2013). Seasonal dynamics and age of stemwood nonstructural carbohydrates in temperate forest trees. *The New Phytologist*, *197*(3), 850–861. https://www.jstor.org/stable/newphytologist.197.3.850

Roby, M. C., Scott, R. L., & Moore, D. J. P. (2020). High Vapor Pressure Deficit Decreases the Productivity and Water Use Efficiency of Rain-Induced Pulses in Semiarid Ecosystems. *Journal of Geophysical Research: Biogeosciences*, *125*(10), e2020JG005665. https://doi.org/10.1029/2020JG005665

Romero, E., Rey-Sanchez, C., Gerlein-Safdi, C., Baldocchi, D. D., Lee, P., & Dronova, I. (2026). Photosynthesis, heat, and structure: An evident hierarchy of environmental conditions driving wetland carbon assimilation. *Remote Sensing of Environment*, *338*, 115339. https://doi.org/10.1016/j.rse.2026.115339

Rousk, J., & C. Brangarí, A. (2022). Do the respiration pulses induced by drying–rewetting matter for the soil–atmosphere carbon balance? *Global Change Biology*, *28*(11), 3486–3488. https://doi.org/10.1111/gcb.16163

Rutledge, S., Campbell, D. I., Baldocchi, D., & Schipper, L. A. (2010). Photodegradation leads to increased carbon dioxide losses from terrestrial organic matter. *Global Change Biology*, *16*(11), 3065–3074. https://doi.org/10.1111/j.1365-2486.2009.02149.x

Sala, O. E., Gherardi, L. A., Reichmann, L., Jobbágy, E., & Peters, D. (2012). Legacies of precipitation fluctuations on primary production: Theory and data synthesis. *Philosophical Transactions of the Royal Society B: Biological Sciences*, *367*(1606), 3135–3144. https://doi.org/10.1098/rstb.2011.0347

Schimel, J. P. (2018). *Life in Dry Soils: Effects of Drought on Soil Microbial Communities and Processes*.

Schmid, H. P., & Lloyd, C. R. (1999). Spatial representativeness and the location bias of flux footprints over inhomogeneous areas. *Agricultural and Forest Meteorology*, *93*(3), 195–209. https://doi.org/10.1016/S0168-1923(98)00119-1

Schneider, T., Keiblinger, K. M., Schmid, E., Sterflinger-Gleixner, K., Ellersdorfer, G., Roschitzki, B., Richter, A., Eberl, L., Zechmeister-Boltenstern, S., & Riedel, K. (2012). Who is who in litter decomposition? Metaproteomics reveals major microbial players and their biogeochemical functions. *The ISME Journal*, *6*(9), 1749–1762. https://doi.org/10.1038/ismej.2012.11

Serrano-Ortiz, P., Roland, M., Sanchez-Moral, S., Janssens, I. A., Domingo, F., Goddéris, Y., & Kowalski, A. S. (2010). Hidden, abiotic CO2 flows and gaseous reservoirs in the terrestrial carbon cycle: Review and perspectives. *Agricultural and Forest Meteorology*, *150*(3), 321–329. https://doi.org/10.1016/j.agrformet.2010.01.002

Shuttleworth, J., Gurney R, J., Hsu A., Y., & Ormsby J., P. (1989). FIFE: The variation in energy partition at surface flux sites. *IAHS Publication (International Association of Hydrological Sciences)*, (186), 67–74. https://jglobal.jst.go.jp/en/detail?JGLOBAL_ID=200902011991788720

Singh, S. (2023). How the Birch effect differs in mechanisms and magnitudes due to soil texture. *Soil Biology and Biochemistry*.

Sinsabaugh, R. L., Lauber, C. L., Weintraub, M. N., Ahmed, B., Allison, S. D., Crenshaw, C., Contosta, A. R., Cusack, D., Frey, S., Gallo, M. E., Gartner, T. B., Hobbie, S. E., Holland, K., Keeler, B. L., Powers, J. S., Stursova, M., Takacs-Vesbach, C., Waldrop, M. P., Wallenstein, M. D., … Zeglin, L. H. (2008). Stoichiometry of soil enzyme activity at global scale. *Ecology Letters*, *11*(11), 1252–1264. https://doi.org/10.1111/j.1461-0248.2008.01245.x

Sitch, S., O'Sullivan, M., Robertson, E., Friedlingstein, P., Albergel, C., Anthoni, P., Arneth, A., Arora, V. K., Bastos, A., Bastrikov, V., Bellouin, N., Canadell, J. G., Chini, L., Ciais, P., Falk, S., Harris, I., Hurtt, G., Ito, A., Jain, A. K., … Zaehle, S. (2024). Trends and Drivers of Terrestrial Sources and Sinks of Carbon Dioxide: An Overview of the TRENDY Project. *Global Biogeochemical Cycles*, *38*(7), e2024GB008102. https://doi.org/10.1029/2024GB008102

Smith, B., Wårlind, D., Arneth, A., Hickler, T., Leadley, P., Siltberg, J., & Zaehle, S. (2014). Implications of incorporating N cycling and N limitations on primary production in an individual-based dynamic vegetation model. *Biogeosciences*, *11*(7), 2027–2054. https://doi.org/10.5194/bg-11-2027-2014

Smith, W. K., Dannenberg, M. P., Yan, D., Herrmann, S., Barnes, M. L., Barron-Gafford, G. A., Biederman, J. A., Ferrenberg, S., Fox, A. M., Hudson, A., Knowles, J. F., MacBean, N., Moore, D. J. P., Nagler, P. L., Reed, S. C., Rutherford, W. A., Scott, R. L., Wang, X., & Yang, J. (2019). Remote sensing of dryland ecosystem structure and function: Progress, challenges, and opportunities. *Remote Sensing of Environment*, *233*, 111401. https://doi.org/10.1016/j.rse.2019.111401

Tang, J., Baldocchi, D. D., & Xu, L. (2005). Tree photosynthesis modulates soil respiration on a diurnal time scale. *Global Change Biology*, *11*(8), 1298–1304. https://doi.org/10.1111/j.1365-2486.2005.00978.x

Teets, A., Fraver, S., Hollinger, D. Y., Weiskittel, A. R., Seymour, R. S., & Richardson, A. D. (2018). Linking annual tree growth with eddy-flux measures of net ecosystem productivity across twenty years of observation in a mixed conifer

forest. *Agricultural and Forest Meteorology*, *249*, 479–487. https://doi.org/10.1016/j.agrformet.2017.08.007

Teets, A., Moore, D. J. P., Alexander, M. R., Blanken, P. D., Bohrer, G., Burns, S. P., Carbone, M. S., Ducey, M. J., Fraver, S., Gough, C. M., Hollinger, D. Y., Koch, G., Kolb, T., Munger, J. W., Novick, K. A., Ollinger, S. V., Ouimette, A. P., Pederson, N., Ricciuto, D. M., … Richardson, A. D. (2022). Coupling of Tree Growth and Photosynthetic Carbon Uptake Across Six North American Forests. *Journal of Geophysical Research: Biogeosciences*, *127*(4), e2021JG006690. https://doi.org/10.1029/2021JG006690

Terrer, C., Jackson, R. B., Prentice, I. C., Keenan, T. F., Kaiser, C., Vicca, S., Fisher, J. B., Reich, P. B., Stocker, B. D., Hungate, B. A., Peñuelas, J., McCallum, I., Soudzilovskaia, N. A., Cernusak, L. A., Talhelm, A. F., Van Sundert, K., Piao, S., Newton, P. C. D., Hovenden, M. J., … Franklin, O. (2019). Nitrogen and phosphorus constrain the CO2 fertilization of global plant biomass. *Nature Climate Change*, *9*(9), 684–689. https://doi.org/10.1038/s41558-019-0545-2

Tramontana, G., Ichii, K., Camps-Valls, G., Tomelleri, E., & Papale, D. (2015). Uncertainty analysis of gross primary production upscaling using Random Forests, remote sensing and eddy covariance data. *Remote Sensing of Environment*, *168*, 360–373. https://doi.org/10.1016/j.rse.2015.07.015

Tramontana, G., Migliavacca, M., Jung, M., Reichstein, M., Keenan, T. F., Camps-Valls, G., Ogee, J., Verrelst, J., & Papale, D. (2020). Partitioning net carbon dioxide fluxes into photosynthesis and respiration using neural networks. *Global Change Biology*, *26*(9), 5235–5253. https://doi.org/10.1111/gcb.15203

Tripathi, B. M., Stegen, J. C., Kim, M., Dong, K., Adams, J. M., & Lee, Y. K. (2018). Soil pH mediates the balance between stochastic and deterministic assembly of bacteria. *The ISME Journal*, *12*(4), 1072–1083. https://doi.org/10.1038/s41396-018-0082-4

Trugman, A. T., & Anderegg, L. D. L. (2025). Source vs sink limitations on tree growth: From physiological mechanisms to evolutionary constraints and terrestrial carbon cycle implications. *New Phytologist*, *245*(3), 966–981. https://doi.org/10.1111/nph.20294

Vicca, S., Luyssaert, S., Peñuelas, J., Campioli, M., Chapin III, F. S., Ciais, P., Heinemeyer, A., Högberg, P., Kutsch, W. L., Law, B. E., Malhi, Y., Papale, D., Piao, S. L., Reichstein, M., Schulze, E. D., & Janssens, I. A. (2012). Fertile forests produce biomass more efficiently. *Ecology Letters*, *15*(6), 520–526. https://doi.org/10.1111/j.1461-0248.2012.01775.x

Vuichard, N., Messina, P., Luyssaert, S., Guenet, B., Zaehle, S., Ghattas, J., Bastrikov, V., & Peylin, P. (2019). Accounting for carbon and nitrogen interactions in the global terrestrial ecosystem model ORCHIDEE (trunk version, rev 4999): Multi-scale evaluation of gross primary production. *Geoscientific Model Development*, *12*(11), 4751–4779. https://doi.org/10.5194/gmd-12-4751-2019

Vuichard, N., & Papale, D. (2015). Filling the gaps in meteorological continuous data measured at FLUXNET sites with ERA-Interim reanalysis. *Earth System Science Data*, *7*(2), 157–171. https://doi.org/10.5194/essd-7-157-2015

Walker, A. P., De Kauwe, M. G., Bastos, A., Belmecheri, S., Georgiou, K., Keeling, R. F., McMahon, S. M., Medlyn, B. E., Moore, D. J. P., Norby, R. J., Zaehle, S., Anderson-Teixeira, K. J., Battipaglia, G., Brienen, R. J. W., Cabugao, K. G., Cailleret, M., Campbell, E., Canadell, J. G., Ciais, P., … Zuidema, P. A. (2021). Integrating the evidence for a terrestrial carbon sink caused by increasing atmospheric CO2. *New Phytologist*, *229*(5), 2413–2445. https://doi.org/10.1111/nph.16866

Waring, R. H., Landsberg, J. J., & Williams, M. (1998). Net primary production of forests: A constant fraction of gross primary production? *Tree Physiology*, *18*(2), 129–134. https://doi.org/10.1093/treephys/18.2.129

Warm Winter 2020 Team, & ICOS Ecosystem Thematic Centre. (2022). *Warm Winter 2020 ecosystem eddy covariance flux product for 73 stations in FLUXNET-Archive format—Release 2022-1 (Version 1.0).* https://doi.org/10.18160/2G60-ZHAK

White, A. C., Rogers, A., Rees, M., & Osborne, C. P. (2016). How can we make plants grow faster? A source-sink perspective on growth rate. *Journal of Experimental Botany*, *67*(1), 31–45. https://doi.org/10.1093/jxb/erv447

Whitford, W. G., & Duval, B. D. (2020). Chapter 3—Characterization of Desert Climates. In W. G. Whitford & B. D. Duval (Eds.), *Ecology of Desert Systems (Second Edition)* (pp. 47–72). Academic Press. https://doi.org/10.1016/B978-0-12-815055-9.00003-5

Xiao, J., Baldocchi, D., Ichii, K., Li, F., & Papale, D. (2025). Insights into terrestrial carbon and water cycling from the global eddy covariance network. *Nature Reviews Earth & Environment*, 1–20. https://doi.org/10.1038/s43017-025-00743-1

Xiao, J., Ollinger, S. V., Frolking, S., Hurtt, G. C., Hollinger, D. Y., Davis, K. J., Pan, Y., Zhang, X., Deng, F., Chen, J., Baldocchi, D. D., Law, B. E., Arain, M. A., Desai, A. R., Richardson, A. D., Sun, G., Amiro, B., Margolis, H., Gu, L., … Suyker, A. E. (2014). Data-driven diagnostics of terrestrial carbon dynamics over North America. *Agricultural and Forest Meteorology*, *197*, 142–157. https://doi.org/10.1016/j.agrformet.2014.06.013

Xiao, J., Zhuang, Q., Baldocchi, D. D., Law, B. E., Richardson, A. D., Chen, J., Oren, R., Starr, G., Noormets, A., Ma, S., Verma, S. B., Wharton, S., Wofsy, S. C., Bolstad, P. V., Burns, S. P., Cook, D. R., Curtis, P. S., Drake, B. G., Falk, M., … Torn, M. S. (2008). Estimation of net ecosystem carbon exchange for the conterminous United States by combining MODIS and AmeriFlux data. *Agricultural and Forest Meteorology*, *148*(11), 1827–1847. https://doi.org/10.1016/j.agrformet.2008.06.015

Xu, K., Metzger, S., & Desai, A. R. (2017). Upscaling tower-observed turbulent exchange at fine spatio-temporal resolution using environmental response functions. *Agricultural and Forest Meteorology*, *232*, 10–22. https://doi.org/10.1016/j.agrformet.2016.07.019

Xu, L., & Baldocchi, D. D. (2004). Seasonal variation in carbon dioxide exchange over a Mediterranean annual grassland in California. *Agricultural and Forest Meteorology*, *123*(1), 79–96. https://doi.org/10.1016/j.agrformet.2003.10.004

Xu, L., Baldocchi, D. D., & Tang, J. (2004). How soil moisture, rain pulses, and growth alter the response of ecosystem respiration to temperature. *Global Biogeochemical Cycles*, *18*(4). https://doi.org/10.1029/2004GB002281

Yan, L., Chen, S., Xia, J., & Luo, Y. (2014). Precipitation Regime Shift Enhanced the Rain Pulse Effect on Soil Respiration in a Semi-Arid Steppe. *PLOS ONE*, *9*(8), e104217. https://doi.org/10.1371/journal.pone.0104217

Google. Satellite embedding v1, June 2025. URL https://developers.google.com/ earth-engine/datasets/catalog/ GOOGLE_SATELLITE_EMBEDDING_V1_ ANNUAL.

Jaclyn Hatala Matthes, Cove Sturtevant, Patty Oikawa, Samuel D Chamberlain, Daphne Szutu, Ariane Arias-Ortiz, Joseph Verfaillie, Dennis Baldocchi (2026), AmeriFlux FLUXNET-1F US-Myb Mayberry Wetland, Ver. v1.3_r1, AmeriFlux AMP, (Dataset). https://doi.org/10.17190/AMF/1871139

De Meulder, T., Lefevre, L., Roland, M., Segers, J., Van Look, J. (2025). Fluxnet Archive Product from Lochristi, 2019–2022, FLUXNET, https://hdl.handle.net/11676/oc2rvgUbNz-kUIeMsNmvNv8X

Carrara, A., El-Madany, T., Hammer, T., Kolle, O., Lee, S., Migliavacca, M., Reichstein, M. (2026). Fluxnet Product from Majadas del Tietar North, 2013-12-31–2024-12-31, FLUXNET, https://hdl.handle.net/11676/WfJwzjN5ceMJsrP955axTJMA

FLUXNET. (2025). About the FLUXNET network. Retrieved June 15, 2026, from https://fluxnet.org/about/

The Quantitative Ecosystem Dynamics Lab. (2026). The FLUXNET Data Explorer. University of California, Berkeley. Retrieved June 15, 2026, from https://www.keenangroup.info/fluxnet-data-explorer/

2.9. Extended Data

Extended Data Table 2.1. *List of 184 eddy-covariance flux sites and years of data used in this study.*

No.	Site_ID	IGBP	Longitude	Latitude	Start	End	ID/DOI/PID
1	AR-CCa	CRO	-61.3181	-35.621	2017	2020	10.17190/AMF/2571134
2	AR-CCg	GRA	-61.1855	-35.9244	2018	2021	10.17190/AMF/2469434
3	AU-ASM	SAV	133.249	-22.283	2017	2020	https://dx.doi.org/10.25901/azz4-x655
4	AU-Cpr	SAV	140.5891	-34.0021	2017	2024	https://dx.doi.org/10.25901/braj-w973
5	AU-Cum	EBF	150.7236	-33.6152	2017	2024	https://dx.doi.org/10.25901/gjm4-9020
6	AU-DaS	SAV	131.3881	-14.1593	2017	2022	https://dx.doi.org/10.25901/nkbt-pa39
7	AU-Dry	SAV	132.3706	-15.2588	2017	2022	https://dx.doi.org/10.25901/mt7s-d941
8	AU-GWW	SAV	120.6541	-30.1913	2017	2021	https://dx.doi.org/10.25901/683k-7e46
9	AU-Stp	GRA	133.3502	-17.1507	2018	2022	https://dx.doi.org/10.25901/exc5-x691
10	AU-Wom	EBF	144.0944	-37.4222	2017	2020	https://dx.doi.org/10.25901/

							gw8s-7a26
11	BE-Dor	GRA	4.968591	50.31135	2017	2024	geqYNPk-fvkZDGtnJI-sq1Je
12	BE-Lcr	DBF	3.85043	51.11218	2019	2022	oc2rvgUbNz-kUIeMsNmvNv8X
13	BE-Lon	CRO	4.7462	50.5516	2017	2022	1u2xQ5XcQoX0j2wJiZcyDP3M
14	BE-Maa	CSH	5.631851	50.97987	2017	2024	ZG_uAsLMIT7yUsnXnJSB5Ufb
15	BE-Vie	MF	5.9981	50.3049	2017	2024	h7WL05ckcTEzgXiZaFsQDL4r
16	CA-Cbo	DBF	-79.9333	44.3167	2017	2020	10.17190/AMF/1854365
17	CA-DB2	WET	-122.9951	49.119	2020	2024	10.17190/AMF/1881564
18	CA-DBB	WET	-122.9849	49.1293	2018	2021	10.17190/AMF/1881565
19	CA-DSM	WET	-122.8954	49.0887	2022	2024	10.17190/AMF/2571137
20	CA-ER1	CRO	-80.4123	43.6405	2017	2020	10.17190/AMF/1832154
21	CA-Mer	WET	-75.5186	45.4094	2017	2020	10.17190/AMF/2571102
22	CA-TP1	ENF	-80.5595	42.6609	2017	2023	10.17190/AMF/2006962
23	CA-TP3	ENF	-80.3483	42.7068	2017	2023	10.17190/AMF/1881566

24	CA-TPD	DBF	-80.5577	42.6353	2017	2022	10.17190/AMF/1881567
25	CH-Dav	ENF	9.8559	46.8153	2017	2024	eHcoHNvdn-kHLqQoJbyUs0Yq
26	CH-Fru	GRA	8.5378	47.1158	2017	2024	xnRKIWdx6isC5GLqv_pHq5hU
27	CH-Lae	MF	8.3644	47.4783	2017	2024	V_BAvTqbUlgSltmCcoHgP3Vy
28	CZ-BK1	ENF	18.5369	49.5021	2017	2024	KiFUcCsC30gKhoS-4oJf5__f
29	CZ-KrP	CRO	15.078773	49.573257	2017	2023	cqH_ifs_P83CsahNQXGTp3Im
30	CZ-Lnz	MF	16.946416	48.681611	2017	2021	B2BjRQCUXetA0_vGI3x7WFUJ
31	CZ-RAJ	ENF	16.6965125	49.4437236	2017	2024	LImTy3u9548FEMXEW59RiWpY
32	CZ-Stn	DBF	17.9699	49.035975	2017	2024	CM9ZMyBcfqBoKkmLPUDwiyMo
33	CZ-wet	WET	14.7704	49.0247	2017	2024	r4kitQikcZG6sLZsHDmHf8Ks
34	DE-Geb	CRO	10.9146	51.0997	2021	2024	jFkfMT_3ZahqoODz-R82VeUG
35	DE-Gri	GRA	13.5126	50.95	2017	2024	H0WNTp4g4beCHZLD5k_u1

							SJ5
36	DE-Hai	DBF	10.4522	51.0792	2017	2022	M1ET1IeG31p-6n4BFjDb3ZO7
37	DE-HoH	DBF	11.219222	52.085306	2017	2024	-aRYvkkX6D6wd2ijWclesXaK
38	DE-Kli	CRO	13.5224	50.8931	2018	2024	ViYMPdxbY25optpqiQ7OVgXN
39	DE-Obe	ENF	13.7213	50.7867	2017	2024	mk-YBqXT0YwblulI9V726yD2d
40	DE-RuR	GRA	6.3041	50.6219	2017	2024	MoiyY0KjXITz5V_oFs-x9bUj
41	DE-RuS	CRO	6.4471	50.8659	2017	2024	9m1zuO-nvw0zGnEdt0qo3Xzw
42	DK-Sor	DBF	11.6446	55.4859	2017	2024	lwXfRUVQCnuq5Ocle-F6tpib
43	ES-LM1	SAV	-5.778683	39.94269	2017	2024	9c9e--DRFTTyhtl6c0lcA3O6
44	ES-LM2	SAV	-5.775881	39.934592	2017	2024	CgWe1iCQaO3oYYxgSMEe1BSq
45	FI-Hyy	ENF	24.2948	61.8474	2019	2024	pIDsMGxYyXTg31dHecNO55Nq
46	FI-Ken	ENF	24.24301	67.98721	2018	2024	BhlqiN95ECto

							SXoxmf0Q4V35
47	FI-Let	ENF	23.9595	60.6418	2017	2020	DkII-LaynvPoGMvnIbInqLrw
48	FI-Qvd	CRO	22.391607	60.295242	2018	2023	UuvYrldK3v4VzDgfH6nC0ed7
49	FI-Sii	WET	24.1928	61.8327	2018	2024	mkbfyrZKqg3Djz0tW1rRap1c
50	FI-Var	ENF	29.61	67.7549	2017	2024	Ve8588DeHh2Y-t-dtZGWggl6
51	FR-Bil	ENF	-0.956082	44.493672	2017	2024	Qa701KsgkCkpYT4vev--kpOk
52	FR-EM2	CRO	3.02065	49.8721083	2017	2024	jEdjHpIeW8bczJxWBYm_jkpP
53	FR-FBn	MF	5.67865	43.24079	2017	2024	dw5JqZoWiNVw0JQS-QXykPY6
54	FR-Fon	DBF	2.7801	48.4764	2020	2024	vgMluaOupOEt-hzl3RWXI99X
55	FR-Gri	CRO	1.9519	48.8442	2019	2024	_WcCYfVZLDpg4Gz-RlhwVX6Y
56	FR-Lam	CRO	1.237878	43.496437	2021	2024	zwxh7ZEI7AWEJOF5ggdX2bpK

57	FR-Pue	EBF	3.5957	43.7413	2017	2024	5vx0Ks1CqWMCVA8BrWv_lDrV
58	FR-Tou	GRA	1.37474	43.572857	2018	2024	LZSDmUp2MspQPlyTfDwNXYhi
59	IL-Yat	ENF	35.05198851	31.34504459	2017	2024	ddBS_ZLjXuBl8SSQV2cskqda
60	IT-BFt	DBF	10.741966	45.197754	2019	2022	lUOlBlndAhz4kdSgYJUDyq-D
61	IT-Cp2	EBF	12.3573	41.7043	2022	2024	B6lVx5OEcdr4ZS-3ix2K7iPP
62	IT-Lsn	OSH	12.750297	45.740481	2017	2024	wjxZGQl8gUxBPVKPVlu4-g5L
63	IT-MBo	GRA	11.0458	46.0147	2017	2020	E0wSFc1mB8oN23pHXtN2iH3Z
64	IT-Ren	ENF	11.4337	46.5869	2017	2019	MneKjijlv5X9lwsAh_VHcJt6
65	IT-SR^2	ENF	10.2909	43.732	2020	2023	Frhkznd6pBhhJKKaYoAShaV2
66	IT-Tor	GRA	7.5781	45.8444	2017	2024	jpLpilIX0DYcAXQubpEJEEBn
67	KR-CRK	CRO	127.2506	38.2013	2017	2021	H8OP2ngO7ZJkZ087BV4UNehk
68	NL-Loo	ENF	5.7436	52.1666	2020	2024	WewhyVCaeifJzeZN8L6Cdb

							W3
69	RU-Ch2	WET	161.3509	68.6169	2018	2021	3xSmQwrTa-Ufn-rKi86qwxkR
70	RU-Fy2	ENF	32.9019	56.4476	2017	2022	Vh2pWjfw5HPNZJDA6XfQSvcP
71	RU-Fyo	ENF	32.9221	56.4615	2017	2024	GW1i5FQInU-IW_0iisGVDXW3
72	SE-Deg	GRA	19.5565	64.182	2020	2024	IiyJGdmPkDhdItxg1_8IgLFp
73	SE-Htm	ENF	13.41897	56.09763	2018	2024	8hMY0IY7kERIfokXkEpev-03
74	SE-Svb	ENF	19.7745	64.25611	2018	2024	SxJ5MBCJuCmHLPK4C1fgwGCc
75	US-ALQ	WET	-89.6067	46.0308	2019	2023	10.17190/AMF/2006964
76	US-ARM	CRO	-97.4888	36.6058	2017	2024	10.17190/AMF/1854366
77	US-BRG	GRA	-86.5406	39.2167	2017	2019	10.17190/AMF/2006969
78	US-BZB	WET	-148.3208	64.6955	2017	2024	10.17190/AMF/1871134
79	US-BZF	WET	-148.3121	64.7013	2017	2024	10.17190/AMF/1871135
80	US-BZS	ENF	-148.3235	64.6963	2017	2021	10.17190/AMF/2006970
81	US-BZo	WET	-148.33	64.6936	2018	2024	10.17190/AMF/1881569
82	US-Bar	DBF	-71.2881	44.0646	2019	2021	10.17190/AM

							F/1881570
83	US-Bi1	CRO	-121.4993	38.0992	2017	2024	10.17190/AMF/1881571
84	US-Bi2	CRO	-121.5351	38.1091	2018	2021	10.17190/AMF/1881572
85	US-CF1	CRO	-117.0821	46.7815	2018	2021	10.17190/AMF/2469445
86	US-CF2	CRO	-117.0908	46.784	2018	2020	10.17190/AMF/1832158
87	US-CGG	GRA	-121.9761	37.938	2020	2023	10.17190/AMF/1881573
88	US-CdM	WSA	-109.7471	37.5241	2020	2024	10.17190/AMF/2469446
89	US-DFC	CRO	-89.7117	43.3448	2022	2024	10.17190/AMF/2006975
90	US-DS3	CRO	-121.549	38.1235	2022	2024	10.17190/AMF/2469451
91	US-Dmg	WET	-121.6691	38.0015	2022	2024	10.17190/AMF/2229376
92	US-Elm	WET	-80.7826	25.5519	2017	2022	10.17190/AMF/2007169
93	US-Esm	WET	-80.5946	25.4379	2017	2024	10.17190/AMF/2007171
94	US-GLE	ENF	-106.2399	41.3665	2017	2020	10.17190/AMF/1871136
95	US-HB1	WET	-79.1957	33.3455	2019	2022	10.17190/AMF/1871137
96	US-HB3	ENF	-79.2322	33.3482	2019	2022	10.17190/AMF/1832160
97	US-HB4	WET	-79.2975	33.2015	2020	2024	10.17190/AMF/2229378
98	US-Ha1	DBF	-72.1715	42.5378	2017	2020	10.17190/AM

							F/2571130
99	US-Ho1	ENF	-68.7402	45.2041	2017	2021	10.17190/AMF/2469453
100	US-Ho2	ENF	-68.747	45.2091	2020	2023	10.17190/AMF/1881581
101	US-Hsm	WET	-122.0212	38.2368	2022	2024	10.17190/AMF/2571131
102	US-ICh	OSH	-149.2958	68.6068	2018	2024	10.17190/AMF/2007175
103	US-ICs	WET	-149.311	68.6058	2017	2020	10.17190/AMF/1871138
104	US-ICt	OSH	-149.3041	68.6063	2017	2019	10.17190/AMF/1881583
105	US-Jo1	OSH	-106.635	32.582	2018	2020	10.17190/AMF/1902833
106	US-Jo2	OSH	-106.6032	32.5849	2017	2020	10.17190/AMF/1881584
107	US-MMS	DBF	-86.4131	39.3232	2017	2020	10.17190/AMF/1854368
108	US-MOz	DBF	-92.2	38.7441	2017	2021	10.17190/AMF/2204871
109	US-Me2	ENF	-121.5574	44.4523	2018	2021	10.17190/AMF/1854369
110	US-Me6	ENF	-121.6078	44.3233	2017	2024	10.17190/AMF/2229382
111	US-Mo1	CRO	-92.1167	39.2298	2017	2024	10.17190/AMF/2229383
112	US-Mo2	GRA	-91.9945	38.9488	2018	2024	10.17190/AMF/2229384
113	US-Mo3	CRO	-92.1497	39.2311	2017	2021	10.17190/AMF/1854370
114	US-Mpj	WSA	-106.2377	34.4385	2017	2023	10.17190/AM

							F/1832161
115	US-Myb	WET	-121.765	38.0499	2017	2021	10.17190/AMF/1871139
116	US-NC3	ENF	-76.656	35.799	2017	2019	10.17190/AMF/2204872
117	US-Ne1	CRO	-96.4766	41.1651	2017	2024	10.17190/AMF/1871140
118	US-Ne2	CRO	-96.4701	41.1649	2017	2023	10.17190/AMF/2574638
119	US-ONA	GRA	-81.9509	27.3836	2017	2022	10.17190/AMF/1832163
120	US-RGA	CRO	-91.6752	34.4121	2021	2024	10.17190/AMF/2204873
121	US-RGB	CRO	-121.867	39.5771	2021	2023	10.17190/AMF/2204874
122	US-RGo	CRO	-122.0052	39.6769	2022	2024	10.17190/AMF/2204875
123	US-Rls	CSH	-116.7356	43.1439	2017	2023	10.17190/AMF/2229387
124	US-Rms	CSH	-116.7486	43.0645	2017	2023	10.17190/AMF/1881587
125	US-Ro4	GRA	-93.0723	44.6781	2017	2024	10.17190/AMF/1881589
126	US-Ro5	CRO	-93.0576	44.691	2017	2024	10.17190/AMF/1818371
127	US-Ro6	CRO	-93.0578	44.6946	2017	2024	10.17190/AMF/1881590
128	US-Rpf	DBF	-147.429	65.1198	2017	2019	10.17190/AMF/2229388
129	US-Rwf	CSH	-116.7231	43.1207	2017	2023	10.17190/AMF/1881591
130	US-Rws	OSH	-116.7132	43.1675	2017	2023	10.17190/AM

							F/1881592
131	US-SHC	ENF	-120.2398	39.4315	2018	2020	10.17190/AMF/1984572
132	US-SP1	ENF	-82.2188	29.7381	2017	2019	10.17190/AMF/1984573
133	US-SRG	GRA	-110.8277	31.7894	2017	2024	10.17190/AMF/2571110
134	US-SRM	WSA	-110.8661	31.8214	2017	2024	10.17190/AMF/1871144
135	US-SSH	DBF	-77.9041	40.6658	2019	2021	10.17190/AMF/2469470
136	US-Seg	GRA	-106.702	34.3623	2017	2024	10.17190/AMF/2204877
137	US-Ses	OSH	-106.7442	34.3349	2017	2021	10.17190/AMF/2475756
138	US-Sne	GRA	-121.7547	38.0369	2017	2020	10.17190/AMF/2469471
139	US-Syv	MF	-89.3477	46.242	2020	2023	10.17190/AMF/2204879
140	US-Ton	WSA	-120.966	38.4309	2017	2024	10.17190/AMF/2204880
141	US-Tw1	WET	-121.6469	38.1074	2020	2023	10.17190/AMF/1832165
142	US-Tw4	WET	-121.6413	38.1027	2017	2023	10.17190/AMF/2204881
143	US-UC1	CVM	-78.0056	40.7536	2020	2024	10.17190/AMF/2469472
144	US-UC2	CVM	-77.9998	40.7559	2020	2024	10.17190/AMF/2469473
145	US-UMB	DBF	-84.7138	45.5598	2017	2021	10.17190/AMF/2204882
146	US-	DBF	-84.6975	45.5625	2017	2022	10.17190/AM

	UMd						F/1881597
147	US-Var	GRA	-120.9508	38.4133	2017	2021	10.17190/AMF/1993904
148	US-Vcm	ENF	-106.5321	35.8884	2017	2023	10.17190/AMF/2229391
149	US-Vcp	ENF	-106.5967	35.8642	2017	2024	10.17190/AMF/2229392
150	US-Whs	OSH	-110.0522	31.7438	2017	2020	10.17190/AMF/1984574
151	US-Wjs	SAV	-105.8615	34.4255	2017	2024	10.17190/AMF/1871146
152	US-Wkg	GRA	-109.9419	31.7365	2017	2024	10.17190/AMF/1984575
153	US-xAE	GRA	-99.0588	35.4106	2019	2024	10.17190/AMF/1985434
154	US-xBL	DBF	-78.0716	39.0603	2021	2024	10.17190/AMF/2229405
155	US-xBN	ENF	-147.5026	65.154	2019	2024	10.17190/AMF/2229406
156	US-xBR	DBF	-71.2873	44.0639	2019	2023	10.17190/AMF/1881598
157	US-xCL	GRA	-97.57	33.4012	2020	2024	10.17190/AMF/1985435
158	US-xCP	GRA	-104.7456	40.8155	2021	2024	10.17190/AMF/1985436
159	US-xDC	GRA	-99.1066	47.1617	2019	2024	10.17190/AMF/1985437
160	US-xDJ	ENF	-145.7514	63.8811	2020	2024	10.17190/AMF/2229407
161	US-xDL	MF	-87.8039	32.5417	2021	2024	10.17190/AMF/1985438
162	US-xGR	DBF	-83.5019	35.689	2021	2024	10.17190/AM

							F/1985440
163	US-xHA	DBF	-72.1727	42.5369	2021	2024	10.17190/AMF/1985441
164	US-xHE	OSH	-149.2133	63.8757	2021	2024	10.17190/AMF/1985442
165	US-xJE	ENF	-84.4686	31.1948	2020	2022	10.17190/AMF/1985443
166	US-xJR	OSH	-106.8425	32.5907	2019	2024	10.17190/AMF/2229408
167	US-xKA	GRA	-96.6129	39.1104	2021	2024	10.17190/AMF/1985444
168	US-xKZ	GRA	-96.5631	39.1008	2019	2021	10.17190/AMF/1985445
169	US-xMB	OSH	-109.3883	38.2483	2020	2024	10.17190/AMF/1985446
170	US-xNG	GRA	-100.9154	46.7697	2021	2024	10.17190/AMF/1985448
171	US-xRM	ENF	-105.5459	40.2759	2022	2024	10.17190/AMF/1985450
172	US-xRN	DBF	-84.2826	35.9641	2020	2024	10.17190/AMF/2571119
173	US-xSC	DBF	-78.1395	38.8929	2022	2024	10.17190/AMF/2229409
174	US-xSE	DBF	-76.56	38.8901	2020	2024	10.17190/AMF/1985452
175	US-xSJ	SAV	-119.7323	37.1088	2021	2024	10.17190/AMF/2229410
176	US-xSL	CRO	-103.0293	40.4619	2022	2024	10.17190/AMF/2229411
177	US-xSR	OSH	-110.8355	31.9107	2022	2024	10.17190/AMF/1985453
178	US-xST	DBF	-89.5864	45.5089	2022	2024	10.17190/AM

							F/1985454
179	US-xTL	WET	-149.3705	68.6611	2021	2024	10.17190/AMF/2469475
180	US-xTR	DBF	-89.5857	45.4937	2019	2023	10.17190/AMF/1985456
181	US-xUK	DBF	-95.1921	39.0404	2020	2024	10.17190/AMF/1985457
182	US-xUN	MF	-89.5373	46.2339	2019	2024	10.17190/AMF/1985458
183	US-xWD	GRA	-99.2414	47.1282	2020	2024	10.17190/AMF/2229412
184	US-xWR	ENF	-121.9519	45.8205	2019	2024	10.17190/AMF/2571118

Extended Data Table 2.2. *Parameters for XGBoost models used in our study.*

Hyperparameter	**Value**
n_estimators	1500
learning_rate	0.03
max_depth	7
objective	reg:squarederror
subsample	0.8
colsample_bytree	0.8
nthread	-1
lamda	2.0
min_child_weight	10
early_stopping_rounds	30

Extended Data Table 2.3. *Pairwise t-test comparisons (reported in P values) of model performance in terms of R^2 among five model setups for GPP monthly predictions.*

Model setups	*XGB_SWin*	*XGB_Clim*	*XGB_Emb*	*XGB_Emb+SWin*	*XGB_Emb+Clim*
XGB_SWin	NA	$P < 0.05$	$P < 0.001$	$P < 0.001$	$P < 0.001$
XGB_Clim		NA	$P < 0.01$	$P < 0.01$	$P < 0.01$
XGB_Emb			NA	$P = 0.83$	$P = 0.76$
XGB_Emb+ SWin				NA	$P = 0.92$
XGB_Emb+ Clim					NA

Extended Data Table 2.4. *Pairwise t-test comparisons (reported in P values) of model performance in terms of R^2 among five model setups for R_{eco} monthly*

predictions.

Model setups	*XGB_Tair*	*XGB_Clim*	*XGB_Emb*	*XGB_Emb+Tair*	*XGB_Emb+Clim*
XGB_Tair	NA	$P = 0.19$	$P < 0.001$	$P < 0.001$	$P < 0.001$
XGB_Clim		NA	$P = 0.08$	$P < 0.05$	$P < 0.05$
XGB_Emb			NA	$P = 0.76$	$P = 0.69$
XGB_Emb+Tair				NA	$P = 0.93$
XGB_Emb+Clim					NA

Extended Data Table 2.5. *Pairwise t-test comparisons (reported in P values) of model performance in terms of R^2 among five model setups for predicting GPP mean seasonal cycle (MSC).*

Model setups	*XGB_SWin*	*XGB_Clim*	*XGB_Emb*	*XGB_Emb+SWin*	*XGB_Emb+Clim*
XGB_SWin	NA	$P < 0.01$	$P < 0.001$	$P < 0.001$	$P < 0.001$
XGB_Clim		NA	$P < 0.001$	$P < 0.001$	$P < 0.01$
XGB_Emb			NA	$P = 0.86$	$P = 0.99$
XGB_Emb+SWin				NA	$P = 0.88$
XGB_Emb+Clim					NA

Extended Data Table 2.6. *Pairwise t-test comparisons (reported in P values) of model performance in terms of R^2 among five model setups for predicting R_{eco} mean seasonal cycle (MSC).*

Model setups	*XGB_Tair*	*XGB_Clim*	*XGB_Emb*	*XGB_Emb+Tair*	*XGB_Emb+Clim*
XGB_Tair	NA	$P = 0.32$	$P < 0.001$	$P < 0.001$	$P < 0.001$
XGB_Clim		NA	$P < 0.05$	$P < 0.05$	$P < 0.05$
XGB_Emb			NA	$P = 0.84$	$P = 0.91$

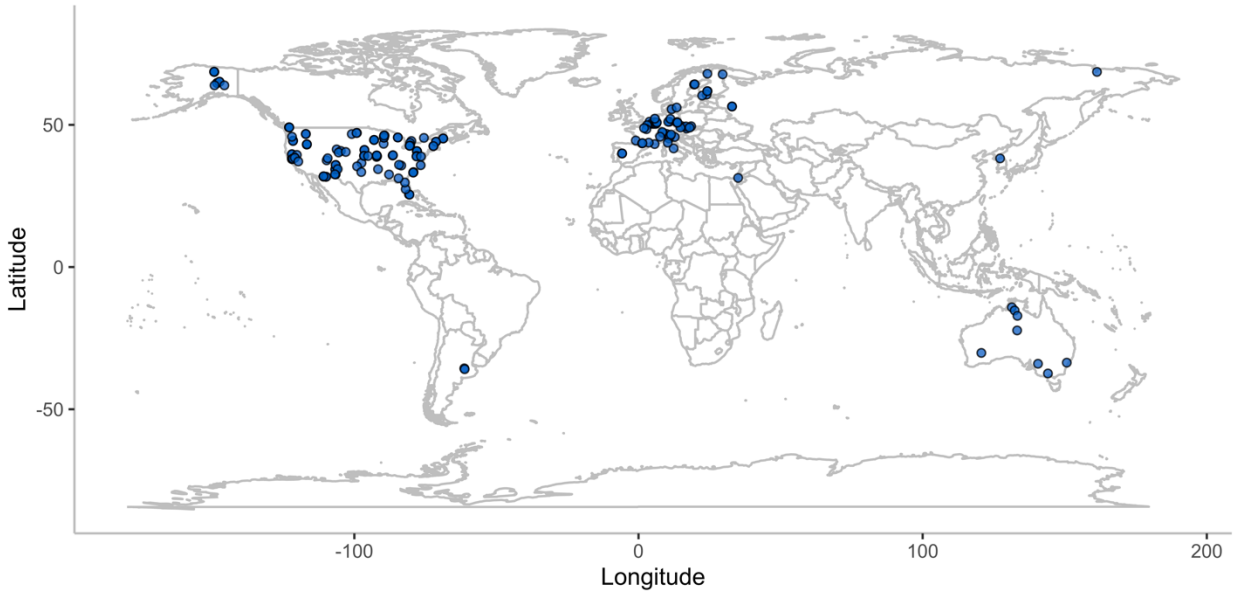
XGB_Emb+Tair				NA	$P = 0.93$
XGB_Emb+Clim					NA

Extended Data Table 2.7. *Pairwise t-test comparisons (reported in P values) of model performance in terms of R^2 among five model setups for predicting GPP monthly anomaly.*

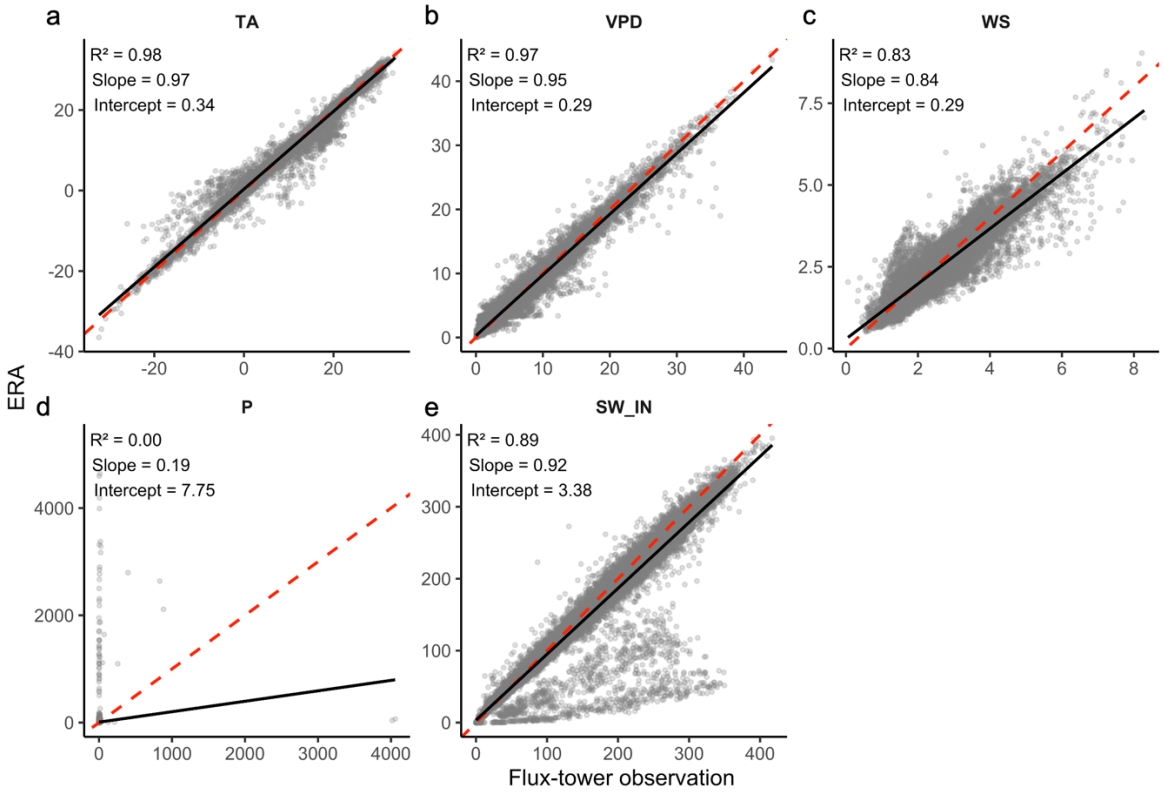
Model setups	*XGB_SWin*	*XGB_Clim*	*XGB_Emb*	*XGB_Emb+SWin*	*XGB_Emb+Clim*
XGB_SWin	NA	$P < 0.001$	$P < 0.001$	$P < 0.001$	$P < 0.001$
XGB_Clim		NA	$P < 0.05$	$P < 0.01$	$P < 0.001$
XGB_Emb			NA	$P = 0.79$	$P = 0.56$
XGB_Emb+SWin				NA	$P = 0.75$
XGB_Emb+Clim					NA

Extended Data Table 2.8. *Pairwise t-test comparisons (reported in P values) of model performance in terms of R^2 among five model setups for predicting R_{eco} monthly anomaly.*

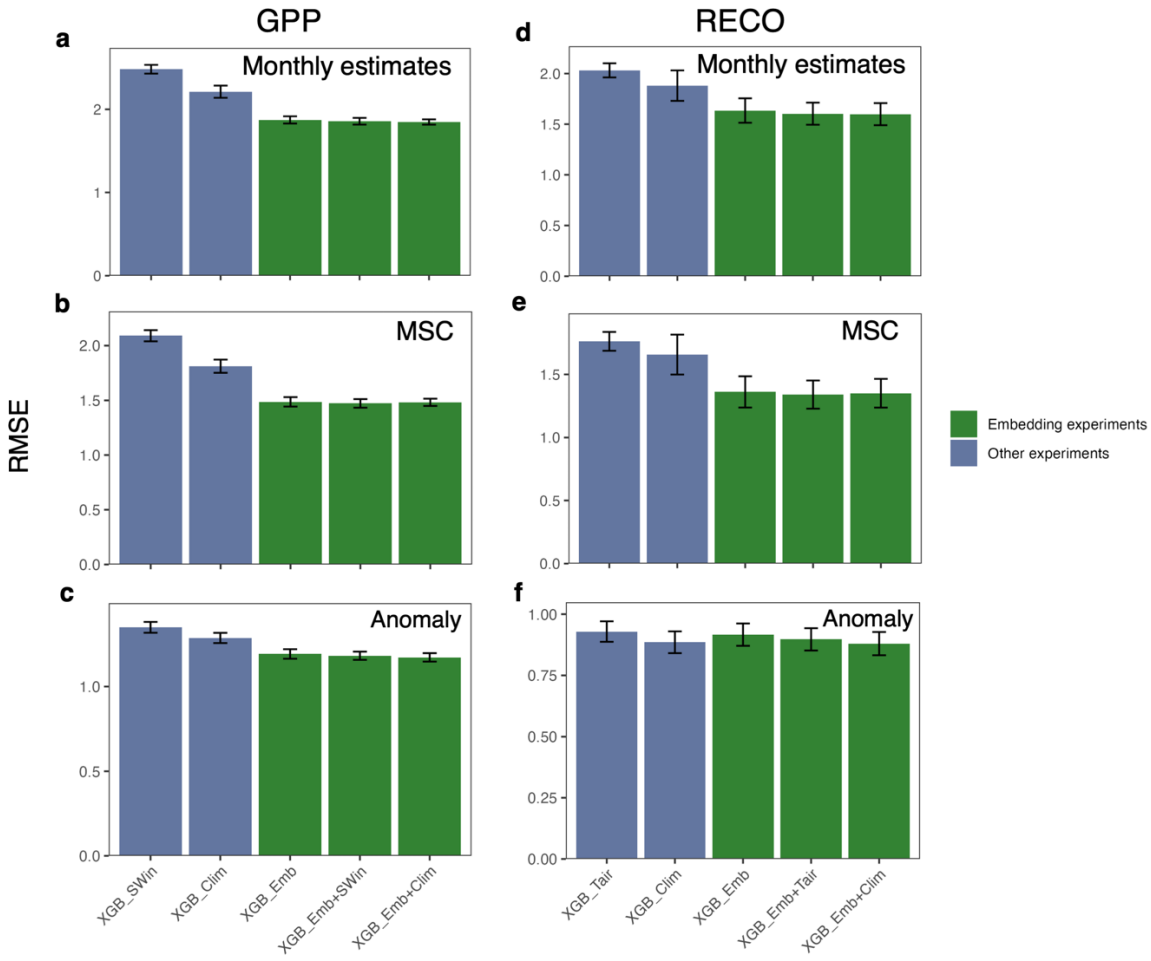
Model setups	*XGB_Tair*	*XGB_Clim*	*XGB_Emb*	*XGB_Emb+Tair*	*XGB_Emb+Clim*
XGB_Tair	NA	$P < 0.001$	$P = 0.45$	$P < 0.05$	$P < 0.001$
XGB_Clim		NA	$P = 0.06$	$P = 0.38$	$P = 0.58$
XGB_Emb			NA	$P = 0.33$	$P < 0.05$
XGB_Emb+Tair				NA	$P = 0.28$
XGB_Emb+Clim					NA



Extended Data Figure 2.1. *Global distribution of 184 eddy-covariance flux sites (blue dots) used in this study.*



Extended Data Figure 2.2. *Comparison between ERA-Interim reanalysis and flux-based meteorological variables (air temperature (TA), Vapor Pressure Deficit (VPD), wind speed (WS), precipitation (P), and incoming shortwave radiation (SW_IN)).*



Extended Data Figure 2.3. Performance of different model setups in terms of RMSE in estimating GPP (a-c) and R_{eco} (d-f) from 115 unseen datasets across runs and temporal scales. *Five model setups are evaluated for each variable and grouped into two categories: models using Google AlphaEarth Foundations (AEF) embedding features (green bars), and models without embedding features (blue bars). Details on the feature sets used in each setup are provided in Table 1. Model performance was evaluated based on RMSE of predicting monthly estimates (a, d), mean season cycles (MSC; b, e), and monthly anomalies (c, f). Bars represent averages across all runs, and error bars indicate standard errors.*

Chapter 3

Long-term biomass growth unimpeded by short-term photosynthetic decoupling

Long-term biomass growth unimpeded by short-term photosynthetic decoupling

Ngoc B. Nguyen[1], Miao Zhang[1,3,4], Trevor F. Keenan[1,2]

[1] *Department of Environmental Science, Policy, and Management, University of California, Berkeley, CA, USA*

[2] *Climate and Ecosystem Sciences Division, Lawrence Berkeley National Laboratory, Berkeley, CA, USA*

[3] *School of Hydrology and Water Resources, Nanjing University of Information Science and Technology, Nanjing, 210044, China*

[4] *Key Laboratory of Hydrometeorological Disaster Mechanism and Warning of Ministry of Water Resources, Nanjing University of Information Science and Technology, Nanjing, 210044, China*

An edited version of this chapter is currently under revision at Nature Plants.

Abstract

Plant carbon uptake depends on the balance between carbon sources (e.g., photosynthesis) and sinks (e.g., respiration, storage, and growth), which together determine how much CO_2 uptake translates into lasting biomass gains. Eddy-covariance and tree-ring analyses have suggested a decoupling between photosynthetic carbon assimilation and growth on interannual timescales, often interpreted as evidence for widespread sink-limitation. Using long-term observations at flux towers and a global vegetation model ensemble, we show that such annual, or short-term, decoupling neither implies sink limitation nor constrains long-term growth. Across observations and more than half of the ensemble, short-term correlations between photosynthesis and woody carbon biomass increment ($r_{\Delta cWood,GPP}$) are weak, confirming previous reported decoupling. Despite the weak correlations, however, woody carbon biomass increases in proportion to photosynthesis between 1951–2020. Notably, there is no relationship between $r_{\Delta cWood,GPP}$ and the long-term sensitivity of biomass to photosynthesis across models. These results caution against inferring source–sink control from observational records and suggest sink limitation is likely less prevalent than previously reported.

3.1. Introduction

Terrestrial ecosystems have sequestered approximately 21% of human-emitted CO_2 over the last decade, acting as a major buffer to climate change (Friedlingstein et al., 2025, 2026). Plants take up CO_2 through photosynthesis and allocate the assimilated carbon to fast-cycling pools (e.g., leaves, fine roots, nonstructural carbohydrates (NSCs), respiratory fluxes), and slow-cycling carbon pools (e.g., woody biomass) (Litton et al., 2007; Richardson et al., 2013; Waring et al., 1998). Ultimately, the rate at which carbon (C) is stored in long-term carbon pools, particularly wood and soil, largely determines the ability of the terrestrial sink to slow atmospheric CO_2 accumulation.

Rising atmospheric CO_2 stimulates global terrestrial photosynthesis (Keenan et al., 2016; Norby, 2025; Walker et al., 2021) and global gross primary production (*GPP*) increased by nearly 13.5% in the last 40 years (Keenan et al., 2023). Whether this additional carbon uptake translates into sustained biomass growth depends on the balance between plant carbon sources and sinks. Leaves function as C source tissues, generating sugars through photosynthesis, while other plant parts act as sinks, consuming or storing these sugars through respiration, growth, storage, and exudation (Green & Keenan, 2022; White et al., 2016). The sensitivity of source and sink activities varies with environmental conditions (Cabon et al., 2020; Hsiao, 1973; Muller et al., 2011). When source activity exceeds sink capacity, plants are considered sink-limited; when sinks could store more carbon than sources provide, they are source-limited. Thus, the amount of carbon ultimately sequestered in plant biomass depends on the interaction between source and sink activities, which are increasingly influenced by rising CO_2 and climate variability.

Although elevated CO_2 has enhanced terrestrial photosynthesis (Keenan et al., 2023), recent studies suggest that additional carbon assimilation does not yield proportional gains in plant growth, due to sink constraints such as nutrient limitation, low temperature, increasing atmospheric aridity, and reduced water availability (Cabon et al., 2022; Fatichi et al., 2014, 2019; Jiang et al., 2020; Kannenberg et al., 2022; Körner, 2022; Rao et al., 2026; Teets et al., 2018; Terrer et al., 2019). For example, (Cabon et al., 2022) reports widespread short-term decoupling between annual *GPP*

and tree-ring width across biomes, interpreted as evidence that sink-limitation is becoming more prevalent, and that current dynamic global vegetation models (DGVMs) might be overly source-biased due to the linear relationship between assimilation and growth within models (Fatichi et al., 2014; Friend et al., 2019). Although such short-term decoupling is widely reported in the literature (Babst et al., 2014; Kannenberg et al., 2025; Litton et al., 2007; Teets et al., 2022), its interpretation as an indicator of sink limitation has been called into question (Gessler & Zweifel, 2024; Green & Keenan, 2022; Trugman & Anderegg, 2025). Previous studies primarily relied on aboveground wood growth, such as tree-ring width, without accounting for assimilated C allocated to other C pools (e.g., roots, leaves, soil organic matter), and major C fluxes such as autotrophic respiration (Green & Keenan, 2022; Trugman & Anderegg, 2025). Importantly, given high short-term climate variability, the relatively small fraction of photosynthesis allocated to wood growth, and the limited length of available datasets, the observed decoupling might not causally indicate long-term sink-limitation.

Direct observations of source-sink dynamics are limited (Green & Keenan, 2022; Jiang et al., 2020; Norby, 2025). Biomass increment can be estimated from tree rings, dendrometers, and related measurement approaches, while whole tree photosynthesis is estimated from eddy-covariance towers or experimental chambers (Baldocchi, 2020; Kannenberg et al., 2025). Together, these datasets provide valuable insights but are often short in duration and restricted in spatial coverage, limiting their ability to capture long-term dynamics. Dynamic global vegetation models (DGVMs) offer a complementary perspective by simulating carbon fluxes and pools from annual to centennial scales. They incorporate the ecosystem processes and feedbacks that shape long-term carbon cycle dynamics and, despite known deficiencies, reproduce broad features of the global terrestrial carbon budget (Friedlingstein et al., 2025; Sitch et al., 2024). Furthermore, DGVMs can be used to examine the potential influence of rising CO_2 concentrations and climate variability on terrestrial carbon budgets through controlled experiments (Sitch et al., 2024). Combining these complementary lines of evidence provides an opportunity to assess the relationship between short-term patterns and long-term source–sink dynamics.

Here we examine estimates of source-sink decoupling and implications for

sink limitation by leveraging eddy-covariance observations and tree-ring width data in combination with simulation experiments from dynamic global vegetation models. Specifically, we use observations of tree-ring width and gross primary production from 31 available long-term eddy-covariance sites, together with simulations from nine DGVMs in the Trends in Net Land–Atmosphere Exchange (TRENDY version 10) project (Friedlingstein et al., 2022). We further demonstrate annual correlations, or lack thereof, between *GPP* and woody C biomass growth bear no relationship to long-term responses across TRENDY models. Finally, we disentangle how assimilated carbon is partitioned among woody, leaf, and root C biomass, as well as respiration, across temporal scales in each model. Combining long-term observational records with model simulations, our study provides a novel perspective on the degree to which short-term source–sink relationships represent a proxy for sink limitation and scale up to long-term ecosystem carbon sequestration.

3.2. Methods

3.2.1. Data sources

In-situ observations. We collected openly available data of site-level Gross Primary Production (*GPP*) from 31 eddy-covariance towers and associated on-site tree-ring width records compiled by (Cabon et al., 2022; Pastorello et al., 2020) (Extended Data Table 3.1; Extended Data Fig. 3.1). These towers have the Mean Annual Temperature (MAT) ranging from −2.7 to 20.5 °C, Mean Annual Precipitation (MAP) from 297 to 1946 mm, and latitudes from 29.7 to 64.9° N. Plant Functional Types (PFTs) examined include Deciduous Broadleaf Forest (n=10), Evergreen Needleleaf Forest (n=18), Mixed Forest (n=2), and Woody Savanna (n=1) (Extended Data Table 3.1).

Global Vegetation models. The carbon fluxes and pools were obtained from the Trends in Net Land–Atmosphere Exchange (TRENDY version 10 – v10) initiative (Friedlingstein et al., 2022) (https://globalcarbonbudgetdata.org/). We analyzed outputs from nine TRENDY models with published woody biomass data: CLM5.0 (Lawrence et al., 2019), ISBA-CTRIP (Delire et al., 2020), CABLE-POP (Haverd et al., 2018), CLASSIC (Melton et al., 2020), CLASSIC-N, ORCHIDEE, ORCHIDEEv3 (Vuichard et al., 2019), LPX-Bern (Lienert & Joos, 2018), and LPJ-GUESS (B. Smith et al., 2014) (see ref. (Friedlingstein et al., 2022) for detailed model descriptions). Both ORCHIDEE and ORCHIDEEv3 were included in the analysis, as ORCHIDEEv3 incorporates key advances such as the nitrogen (N) cycle and C-N interactions (Vuichard et al., 2019). Similarly, both CLASSIC and CLASSIC-N (CLASSIC with nitrogen cycle) were included. Data from all TRENDYv10 models were used through 2020, except for CLM5.0, which was limited to 2019.

3.2.2. Short-term correlation between *GPP* and Δ*cWood*

We computed the short-term correlation between annual *GPP* and woody C biomass increment (Δ*cWood*) for each of nine vegetation models under three scenarios (S0, S1, S2), using the same method as (Cabon et al., 2022) (Eq. 1). Our analyses were restricted to grid cells containing the 31 flux towers with on-site tree-ring width data and to years covered by the eddy-covariance towers used in (Cabon et al., 2022). Cells with missing and zero *GPP* or Δ*cWood* (e.g., coastal land–ocean

overlaps) were excluded. Since models differ in spatial and temporal resolution, not all tower-overlapping cells are represented, and the number of selected cells varies by model.

To remove long-term trends and low-frequency signals, we linearly detrended *GPP* and ΔWood (Cabon et al., 2022) (Equation 1). Note that short-term correlation does not refer to examining the relationship over a short time period, but rather to the detrended relationship over time. The short-term correlation was computed as follows (Eq. 1):

$$r_{\Delta cWood,GPP} = r_{(detrended\ \Delta cWood,\ \ detrended\ GPP)} \quad \text{Equation 1}$$

, in which annual *GPP* unit is kgC m^{-2} s^{-1} and $\Delta cWood$ unit is kgC m^{-2} with $\Delta cWood$ defined as the difference from the previous year. We calculated same-year annual *GPP*-$\Delta cWood$ correlation, with the assumption that they are most correlated on an annual scale (Cabon et al., 2022; Lempereur et al., 2015), despite there could be one-year time lag between *GPP* and $\Delta cWood$ in some sites (Teets et al., 2022).

To obtain observations of $r_{\Delta cWood,GPP}$, we aggregated to annual scale the detrended monthly *GPP* already reported in (Cabon et al., 2022) (with QC > 0.07), which compiled *GPP*_NT_VUT_REF from FLUXNET2015 and AmeriFlux datasets. We then computed the correlation between the obtained detrended annual *GPP*, and detrended annual Ring Width Index (RWI) also compiled by (Cabon et al., 2022). Note that the observational data here is the short-term correlation between annual *GPP* and RWI extracted from (Cabon et al., 2022), with RWI representing community-weighted ring width with removed tree age and size effects. Since the variations in tree-ring width are the closest observational proxy for woody biomass increment and often used as an index for plant growth, we assume that RWI represents $\Delta cWood$ and use it as a benchmark for evaluating TRENDY vegetation models (Fig. 3.1). Note that, consistent with standard approaches (Cabon et al., 2022), we do not use allometric equations to convert tree-ring width to woody biomass increment as this would introduce additional uncertainties (Kannenberg et al., 2025).

3.2.3. Long-term responses of woody biomass to changes in C assimilation

To test whether short-term relationships scale to long-term responses, we analyzed scenario S1 (CO_2-only forcing) for 1951–2020 at tower-overlapping cells, corresponding to the period of rapidest CO_2 increase. We computed (i) the short-term correlation between annual *GPP* and Δ*cWood* ($r_{\Delta cWood,GPP}$), as described above (see section *'Short-term correlation between GPP and ΔcWoods'*), and (ii) the long-term response of the woody biomass stock to assimilated carbon as the *cWood*-to-*GPP* response ratio ($\beta_{cWood,GPP}$) (Eq. 2):

$$\beta_{cWood,GPP} = \frac{\log_e(cWood_{t1}/cWood_{t0})}{\log_e(GPP_{t1}/GPP_{t0})} \quad \text{Equation 2}$$

, in which *cWood* (kg m^{-2}) and *GPP* (kg m^{-2} s^{-1}) were aggregated annually at selected pixels. This log-log formula of response ratio is more robust than the original one proposed in (Bacastow & Keeling, 1973) since it down-weights extreme values (Norby, 2025; Walker et al., 2021). β = 1 indicates proportional scaling between *cWood* and *GPP*. Baseline (t_0) and end-period (t_1) values were taken as fitted values from linear regressions over 1951–2020 to remove year-to-year variations (Keenan et al., 2023).

3.2.4. Allocation and trends in plant carbon fluxes and pools

Across models under scenario S1 (1951–2020) at selected tower-overlapping grid cells, we computed the percent of annual *GPP* allocated to same-year growth of woody, leaf, and root biomasses (Δ*cWood*, Δ*cLeaf*, and Δ*cRoot*), converting these to kg m^{-2} s^{-1} units to align with *GPP* (Fig. 3.3a). Long-term increases of *GPP* and biomass stocks (*cWood*, *cLeaf*, *cRoot*) were summarized as percent change between 1951 and 2020 from linear-fit estimates (Fig. 3.3b). For further analysis of changes in Δ*cWood:GPP* ratio over time (Fig. 3.4), we computed the percent of annual *GPP* allocated to same-year growth of woody biomass from 1901-2020 at selected tower-overlapping grid cells under all scenarios.

3.3. Results and Discussion

3.3.1. *GPP*-Δ*cWood* decoupling does not imply sink limitation

We show that short-term decoupling between *GPP* and woody C biomass increment does not constitute evidence of sink limitation as it also arises in source-biased DGVMs. We found evidence of short-term decoupling between annual *GPP* and woody C biomass increment ($r_{\Delta cWood,GPP}$) across 5/9 of the DGVMs examined (Fig. 3.1a-e), with mean correlations across all scenarios ranging from 0.03 to 0.38 (Extended Data Table 3.2). Such low correlations have previously been interpreted as indicative of sink limitation in observations (Cabon et al., 2022). Note that the short-term correlation was calculated as the correlation between detrended annual *GPP* and detrended annual Δ*cWood* over time to remove long-term trends and low-frequency signals, and thus does not refer to examining the relationship over a short time period (Cabon et al., 2022) (see Methods).

Among five models with low correlations, ISBA-CTRIP, CABLE-POP, LPJ-GUESS, and CLM5.0 exhibit similarly low and no statistically different $r_{\Delta cWood,GPP}$ values when comparing to observations ($P > 0.05$) across all scenarios of constant CO_2 & climate (S0), rising CO_2 (S1), and rising CO_2 & historic climate changes (S2), except for CLM5.0 and LPJ-GUESS under scenario S2 ($P < 0.05$) (Fig. 3.1a-d; Extended Data Table 3.3). Since DGVMs are widely considered to be overly source-limited rather than sink-limited (Fatichi et al., 2014; Friend et al., 2019, 2025), this suggests that the low $r_{\Delta cWood,GPP}$ values are an unreliable proxy of the degree of sink-limitation.

The other DGVMs show $r_{\Delta cWood,GPP}$ values that are statistically higher than those of observations across all scenarios except for LPX-Bern under S1 (Fig. 3.1e-,i). Comparing across three scenarios S0, S1, and S2, however, these models show no significant differences in $r_{\Delta cWood,GPP}$ between scenarios (pairwise t-test, $P > 0.05$ for all pairs of scenarios within each model) (Fig. 3.1; Extended Data Table 3.3). This suggests that changes in source (e.g., CO_2 fertilization, growing season extensions) or sink activity (e.g., warming induced respiration increases) do not affect the short-term or annual correlation between *GPP* and woody C biomass increment. Our results thus indicate that the low observed correlation between *GPP* and wood

growth is not necessarily an indication of sink limitation.

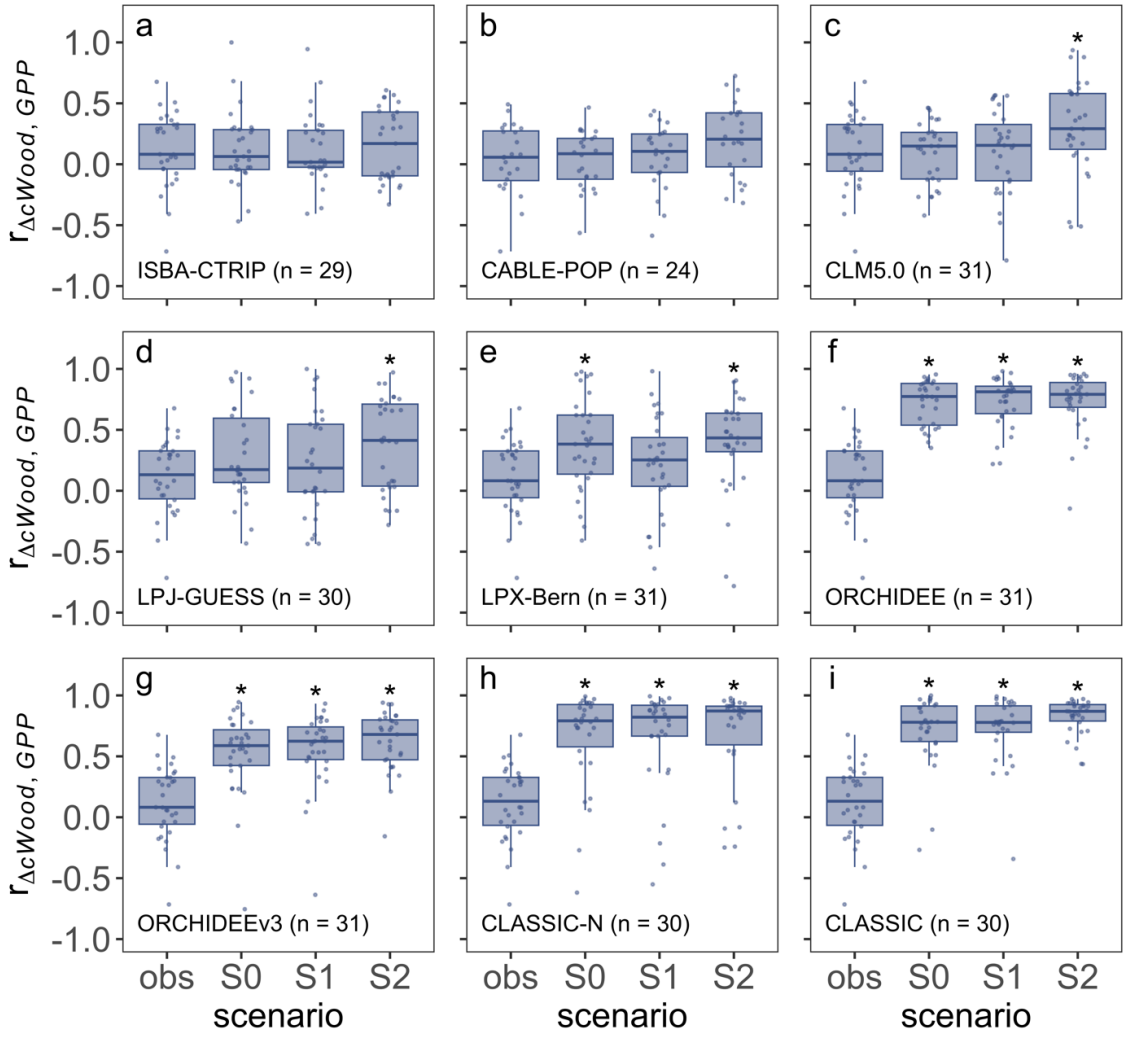


***Figure 3.1. Short-term correlations between annual gross primary production** (GPP**) and annual woody carbon increment (Δ cWood).** Observed (obs) and modelled correlations ($r_{\Delta cWood,GPP}$) from flux towers (n = number of sites with valid pixel data) are shown as boxplots in each panel. Modelled correlations are computed for simulations from nine TRENDYv10 dynamic global vegetation models (panels a–i) at the tower grid cells under three scenarios: preindustrial control (S0), CO_2-only forcing (S1), and combined CO_2 and climate forcing (S2). Asterisks mark model distributions that differ significantly from observations ($P < 0.05$).*

3.3.2. Short- and long-term relationship between *GPP* and *cWood*

Another evidence is that the annual correlation between *GPP* and Δ*cWood* ($r_{\Delta cWood,GPP}$) does not represent their long-term relationship. To assess the long-term growth response to *GPP*, we calculated the response ratio ($\beta_{cWood,GPP}$) as an indicator of *cWood* sensitivity to changing *GPP*. The response ratio (β) is a metric commonly used to quantify how one variable responds to changes in another over time (Keenan et al., 2023; Norby, 2025; Walker et al., 2021). We computed both $\beta_{cWood,GPP}$ and $r_{\Delta cWood,GPP}$ for 1951-2020 at tower-overlapping grid cells under scenario S1, to assess the short-term and long-term responses of plant growth to photosynthesis under rising atmospheric CO_2 (see Methods). If lower $r_{\Delta cWood,GPP}$ indicates stronger sink limitation, higher $r_{\Delta cWood,GPP}$ would suggest stronger source limitation, which therefore would correspond to higher $\beta_{cWood,GPP}$.

If lower $r_{\Delta cWood,GPP}$ is indicative of sink limitation as suggested by previous studies (Cabon et al., 2022), lower $r_{\Delta cWood,GPP}$ should imply a lower $\beta_{cWood,GPP}$. On the other hand, we found no such relationship at the examined flux locations, either across all models (P = 0.64, slope = -0.12) (Fig. 3.2) or individually, except for ORCHIDEE (P < 0.05) and ORCHIDEEv3 (P < 0.01) (Extended Data Fig. 3.2). Notably, LPX-Bern, on average, shows the highest values of $\beta_{cWood,GPP}$ but is among the lowest values for $r_{\Delta cWood,GPP}$. In contrast, CLASSIC, CLASSIC-N, and ORCHIDEE have the highest values of $r_{\Delta cWood,GPP}$ but are among the lowest of $\beta_{cWood,GPP}$, indicating no proportional relationship between the response ratio and the correlation between woody *C* biomass increment and *GPP* across models. These results show that $r_{\Delta cWood,GPP}$ does not capture the response of woody biomass to source activity under increasing CO_2, and that correlation metrics are not a reliable proxy of long-term source-sink dynamics.

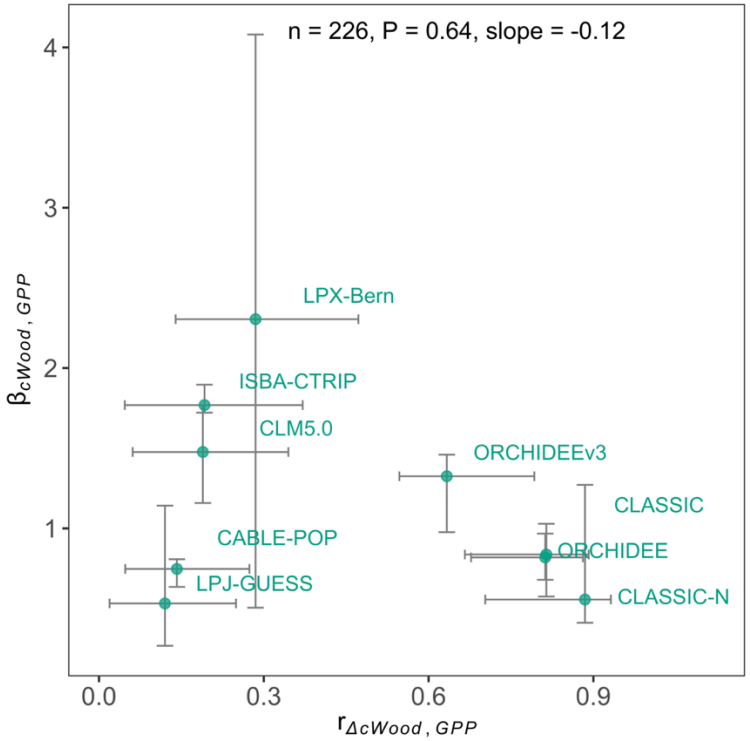


Figure 3.2. Relationship between $\beta_{cWood,GPP}$ and $r_{\Delta cWood,GPP}$. *$\beta_{cWood,GPP}$ and $r_{\Delta cWood,GPP}$ were calculated at flux tower locations across nine TRENDYv10 models under CO_2-only forcing scenario (S1) from 1951-2020. Solid dots indicate median values, while whiskers indicate the 25th-75th percentile range. The response ratio ($\beta_{cWood,GPP}$) was calculated as the log transformed ratio of the percent change in woody C biomass (cWood) relative to the percent change in gross primary production (GPP) from 1951-2020 under CO_2-only forcing scenario (S1; see Methods). P value and slope are from regressions between $r_{\Delta cWood,GPP}$ and $\beta_{cWood,GPP}$ using n data points from all models (n = total number of tower-overlapping grid cells with valid data across models). Nine outliers with beta values outside the range [-5, 10] were removed in the analysis, resulting in a total of 226 (n) valid cells across all models.*

3.3.3. *GPP* minimally allocates to annual wood growth but drives long-term biomass gain

In addition, the low short-term correlation between *GPP* and Δ*cWood* could result from the small fraction of *GPP* allocated to woody biomass growth each year, even though woody biomass increases proportionally with *GPP* over time. We quantified the fraction of annual *GPP* allocated to same-year net biomass growth in tower-overlapping grid cells across eight TRENDY models, excluding LPJ-GUESS as TRENDYv10 does not provide whole-root biomass output for this model, under CO_2-only forcing scenario (S1) from 1952-2020 (Fig. 3.3a). Annually, *GPP* allocation to Δ*cWood*, net of *cWood* losses due to mortality, is 0.86 ± 0.80% (mean ± sd, across models and sites), while allocation to autotrophic respiration (R_a) is 47.57 ± 10.42%. Year-to-year change in leaf and root biomass (Δ*cLeaf* and Δ*cRoot*) is negligible, contributing just 0.03 ± 0.05% and 0.25 ± 0.24% of annual *GPP*, respectively (Fig. 3.3a). The weak short-term correlation between *GPP* and Δ*cWood* therefore likely reflects the small fraction of *GPP* allocated to wood growth and the resulting low signal-to-noise ratio.

Despite the small net annual allocation of *GPP* to Δ*cWood*, woody biomass increases on average 23.83 ± 43.14% from 1951-2020 at flux tower-overlapping grid cells across models, closely tracking the 21.28 ± 17.65% increases in modeled *GPP* (Fig. 3.3b). We found similar long-term increases for other carbon fluxes and pools such as R_a (20.86 ± 20.24%), *cLeaf* (21.22 ± 46.39%), and *cRoot* (19.92 ± 30.34%) (Fig. 3.3b). Thus, while only a small portion of *GPP* is allocated to woody biomass growth each year across models, on a longer time scale plant carbon fluxes and pools converge toward comparable rates of increase. This supports the "a rising tide lifts all boats" hypothesis (Litton et al., 2007). Although TRENDY models simulate proportional increases in *cWood* with *GPP*, the annual *GPP* net allocation to wood growth and their correlation remain low, preventing inference of sink limitation from the correlation alone.

It is worth noting that while these estimates of *GPP* net allocation to woody biomass increment is within the broad range in literature (0-30%) (Chapin et al., 2011), on average, they fall in the lower end of the range of estimates inferred from

allometric and empirical equations applied on tree diameter growth (Babst et al., 2014; Campioli et al., 2015; Kannenberg et al., 2025; Teets et al., 2022; Vicca et al., 2012). This could be due to the fact that allometric equations do not account for biomass losses from plant mortality and branch turnover, whereas DGVMs simulate both losses and gains in woody biomass over years. Branch turnover alone can account for 16% of above ground wood production and reduce stem wood biomass in model simulations by 7 to 17% (Lim et al., 2024). Further studies are needed to quantify the true fraction of *GPP* allocated to annual woody biomass increment at the plot scale.

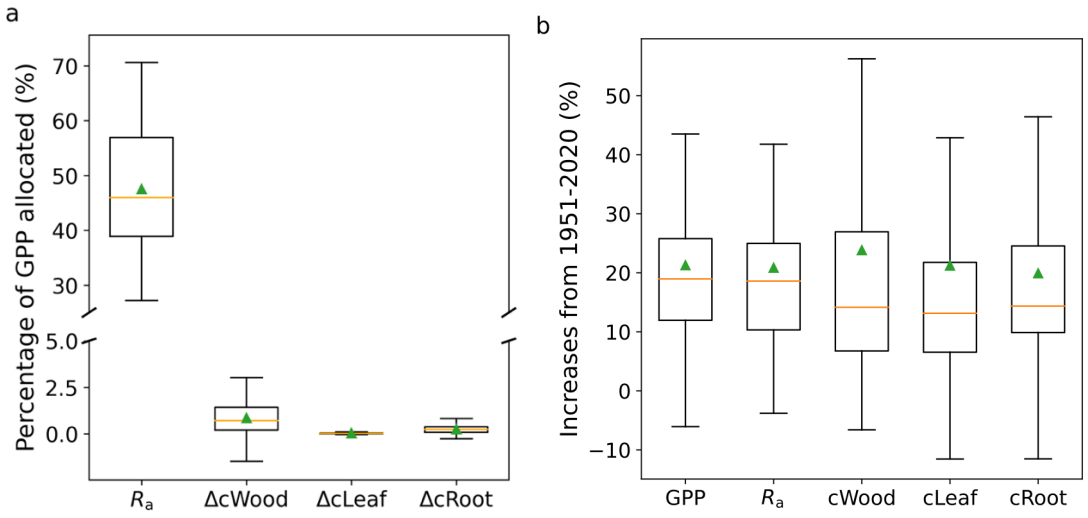


Figure 3.3. Net allocation and trends in plant carbon fluxes and pools. (a) *Percent of annual gross primary production (GPP) allocated to same-year autotrophic respiration (R_a), net growth of woody (ΔcWood), leaf (ΔcLeaf), and root (ΔcRoot) C biomass from 1952-2020 at flux tower-overlapping grid cells from TRENDY models under CO_2-only forcing scenario S1.* ***(b)*** *Percent increase in GPP, Ra, cWood, cLeaf, cRoot from 1951-2020. In both panel (a) and (b), boxes represent the interquartile range (IQR) (25th- 75th percentile) with median values and whiskers extending to 1.5 times the IQR, while green triangles indicate the mean values. In both (a) and (b), a total of 209 grid cells with valid data from eight models (except LPJ-GUESS) were included in the analysis.*

3.3.4. *GPP* increasingly allocates to annual wood growth

Although the proportion of carbon derived from *GPP* that is allocated to woody biomass is small, it is not necessarily constant. We analyzed the temporal changes in the fraction of annual *GPP* allocated to same-year net woody biomass growth (Δ*cWood*/ *GPP*, %) during 1901-2020 across nine TRENDY models at the flux sites (Fig. 3.4). Under the CO_2 & climate forcing scenario (S2), 8/9 models show a significant increase in the Δ*cWood:GPP* ratio from 1901–2020 ($P < 0.01$, slope (α) > 0), except for LPJ-GUESS. Under the CO_2-only scenario (S1), 6/9 models exhibit significant positive trends ($P < 0.05$, $\alpha > 0$) (Fig. 3.4a–f). In contrast, the preindustrial control scenario (S0) shows no significant trend, with slopes near zero across all models. The rate of increase in the Δ*cWood:GPP* ratio is highest under S2, followed by S1, and negligible under S0 (S2 > S1 > S0) (Fig. 3.4).

This increasing Δ*cWood:GPP* ratio under CO_2 & climate forcing scenario suggests that across models, increases in carbon sources and changing environmental conditions lead to a greater proportion of assimilated carbon being allocated to net woody biomass growth over time. Notably, while ISBA-CTRIP and CLM5.0 are among the models with the lowest range of $r_{\Delta cWood,GPP}$ under S1 (Fig. 3.2), they rank among the models with the strongest increases in Δ*cWood:GPP* allocation over time (ISBA-CTRIP: slope = 0.016; CLM5.0: slope = 0.011) (Fig. 3.4a, b). This contradiction confirms that short-term Δ*cWood*- *GPP* correlations do not reflect long-term net allocation patterns to woody biomass and are not indicative of source-sink dynamics. Instead, metrics such as the response ratio and the Δ*cWood:GPP* allocation ratio provide more robust indicators of source-sink relationships.

The consistent increase in the Δ*cWood:GPP* ratio across most model simulations spanning more than a century suggests that greater carbon availability could enhance allocation to wood, indicating that long-term increases in modeled source strength can offset modeled sink constraints. Such shifts may reflect improved carbon-use efficiency, enhanced nutrient recycling, or other long-term adjustments that reduce sink limitations. As most in-situ measurements are not long-term enough to capture this dynamic, longer observations and experiments are needed to test whether the modelled increase in allocation to woody biomass occurs in real world ecosystems.

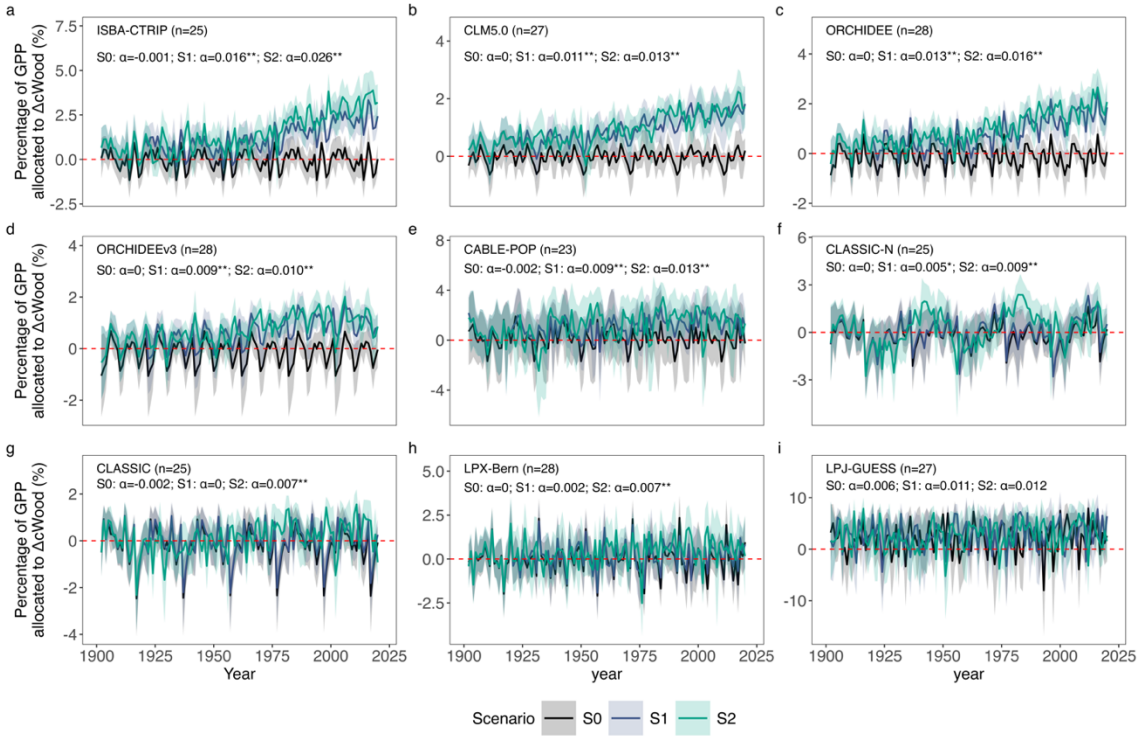


Figure 3.4. Long-term changes in the allocation of gross primary production to net woody C biomass growth. *Each panel shows the percent of gross primary production (GPP) allocated to net woody biomass growth (ΔcWood/GPP, %) simulated by nine TRENDY v10 models under three scenarios from 1901 to 2020: preindustrial control (S0, black), CO_2-only forcing (S1, blue), and combined CO_2 and climate forcing (S2, green). Solid lines show the annual means across selected grid cells, while shaded areas indicate the 95% distribution across grid cells. Data outliers beyond three standard deviations were removed for each scenario. Linear regression was applied to all the solid mean lines, with slope (α) and statistical significance asterisks (*P < 0.05; **P < 0.01) shown at the top of each panel. The number of overlapping-tower grid cells (n), which is a subset of the total available flux towers (31) due to pixel sharing and missing data, is displayed in each panel.*

3.4. Conclusions

Using a combination of long-term observations at flux towers, tree-ring width data, and a global vegetation model ensemble, we demonstrate that the widely reported observed short-term decoupling between *GPP* and woody C biomass increment does not indicate their long-term relationship or prevalent sink limitation. Across observations and 5/9 of examined DGVMs, we show that short-term decoupling correlations between photosynthesis and woody carbon biomass increment ($r_{\Delta cWood,GPP}$) exist across most scenarios. However, $\Delta cWood{:}GPP$ ratio increases consistently over time across most models under the CO_2 & climate forcing scenario (S2) and 6/9 models under scenario S1. Furthermore, woody carbon biomass increases on average 23.83 ± 43.14%, which is in proportion to photosynthesis increases (21.28 ± 17.65%) between 1951–2020 at flux tower-overlapping grid cells across models under the CO_2-only forcing scenario (S1). In addition, we also found that there is no statistically significant relationship between short-term correlation ($r_{\Delta cWood,GPP}$) and long-term responses ($\beta_{cWood,GPP}$) across models. Overall, combining long-term observational records with model simulations, our study provides a novel perspective on the degree to which short-term source–sink relationships represent a proxy for sink limitation and scale up to long-term ecosystem carbon sequestration.

3.5. Acknowledgments

NBN and TFK acknowledge support from the Schmidt Sciences, LLC. TFK acknowledges additional support from the RUBISCO SFA, which is sponsored by the Regional and Global Model Analysis (RGMA) Program in the Climate and Environmental Sciences Division (CESD) of the Office of Biological and Environmental Research (BER) in the U.S. Department of Energy (DOE) Office of Science, and additional support from a DOE Early Career Research Program award #DE-SC0021023, and NASA Awards 80NSSC21K1705 and 80NSSC24K0600. The authors thank the FLUXNET and TRENDY communities for the unique data contributions. Funding for the AmeriFlux data portal was provided by the U.S. Department of Energy Office of Science. MZ was supported by the National Natural Science Foundation of China (42205030) and the State Scholarship Post-Doctoral Fellow from China Scholarship Council.

3.6. Data availability

Eddy-covariance *GPP* and tree-ring width data are obtained from the compilation provided by (Cabon et al., 2022), which compiles eddy-covariance *GPP* from FLUXNET2015 (https://fluxnet.org/data/fluxnet2015-dataset) and AmeriFlux datasets (https://ameriflux.lbl.gov) with on-site Ring Width data observations at 31 sites. TRENDYv10 datasets are obtained from the Global Carbon Budget (https://globalcarbonbudgetdata.org/). All data used in this study is publicly available.

3.7. Bibliography

Abatzoglou, J. T., Dobrowski, S. Z., Parks, S. A., & Hegewisch, K. C. (2018). TerraClimate, a high-resolution global dataset of monthly climate and climatic water balance from 1958–2015. *Scientific Data*, *5*(1), 170191. https://doi.org/10.1038/sdata.2017.191

Ahlström, A., Raupach, M. R., Schurgers, G., Smith, B., Arneth, A., Jung, M., Reichstein, M., Canadell, J. G., Friedlingstein, P., Jain, A. K., Kato, E., Poulter, B., Sitch, S., Stocker, B. D., Viovy, N., Wang, Y. P., Wiltshire, A., Zaehle, S., & Zeng, N. (2015). The dominant role of semi-arid ecosystems in the trend and variability of the land CO2 sink. *Science*, *348*(6237), 895–899. https://doi.org/10.1126/science.aaa1668

Babst, F., Bouriaud, O., Papale, D., Gielen, B., Janssens, I. A., Nikinmaa, E., Ibrom, A., Wu, J., Bernhofer, C., Köstner, B., Grünwald, T., Seufert, G., Ciais, P., & Frank, D. (2014). Above-ground woody carbon sequestration measured from tree rings is coherent with net ecosystem productivity at five eddy-covariance sites. *New Phytologist*, *201*(4), 1289–1303. https://doi.org/10.1111/nph.12589

Bacastow, R., & Keeling, C. K. (1973). Atmospheric carbon dioxide and radiocarbon in the natural carbon cycle: II. Changes from A. D. 1700 to 2070 as deduced from a geochemical model. *Brookhaven Symposia in Biology*, (30), 86–135.

Baldocchi, D. (2014). Measuring fluxes of trace gases and energy between ecosystems and the atmosphere – the state and future of the eddy covariance method. *Global Change Biology*, *20*(12), 3600–3609. https://doi.org/10.1111/gcb.12649

Baldocchi, D. D. (2020). How eddy covariance flux measurements have contributed to our understanding of Global Change Biology. *Global Change Biology*, *26*(1), 242–260. https://doi.org/10.1111/gcb.14807

Baldocchi, D., Falge, E., Gu, L., Olson, R., Hollinger, D., Running, S., null, Anthoni, P., Bernhofer, C., Davis, K., Evans, R., Fuentes, J., Goldstein, A., Katul, G., Law, B., Lee, X., Malhi, Y., Meyers, T., Munger, W., Oechel, W., … Wofsy, S. (2001). FLUXNET: A new tool to study the temporal and spatial variability of ecosystem-scale carbon dioxide, water vapor, and energy flux densities.

Bulletin of the American Meteorological Society, *82*(11), 2415–2434. https://doi.org/10.1175/1520-0477(2001)082%3C2415:FANTTS%3E2.3.CO;2

Barnard, R. L. (2020). Rewetting of soil: Revisiting the origin of soil CO2 emissions. *Soil Biology and Biochemistry*.

Birch, H. F. (1958). The effect of soil drying on humus decomposition and nitrogen availability. *Plant and Soil*, *10*(1), 9–31. https://doi.org/10.1007/BF01343734

Bottner, P. (1985). Response of microbial biomass to alternate moist and dry conditions in a soil incubated with 14C- and 15N-labelled plant material. *Soil Biology and Biochemistry*, *17*(3), 329–337. https://doi.org/10.1016/0038-0717(85)90070-7

Breiman, L., Friedman, J., Olshen, R. A., & Stone, C. J. (2017). *Classification and Regression Trees*. Chapman and Hall/CRC. https://doi.org/10.1201/9781315139470

Broeckx, L. S., Verlinden, M. S., Berhongaray, G., Zona, D., Fichot, R., & Ceulemans, R. (2014). The effect of a dry spring on seasonal carbon allocation and vegetation dynamics in a poplar bioenergy plantation. *GCB Bioenergy*, *6*(5), 473–487. https://doi.org/10.1111/gcbb.12087

Brown, C. F., Kazmierski, M. R., Pasquarella, V. J., Rucklidge, W. J., Samsikova, M., Zhang, C., Shelhamer, E., Lahera, E., Wiles, O., Ilyushchenko, S., Gorelick, N., Zhang, L. L., Alj, S., Schechter, E., Askay, S., Guinan, O., Moore, R., Boukouvalas, A., & Kohli, P. (2025). *AlphaEarth Foundations: An embedding field model for accurate and efficient global mapping from sparse label data* (arXiv:2507.22291). arXiv. https://doi.org/10.48550/arXiv.2507.22291

Bu, J., & Xiao, J. (2025). Upscaling eddy covariance measurements of carbon and water fluxes to the continental scale by incorporating GEDI-derived canopy structural complexity metrics. *Remote Sensing of Environment*, *329*, 114930. https://doi.org/10.1016/j.rse.2025.114930

Burba, G. (2022). *Eddy covariance method for scientific, regulatory, and commercial applications*. LI-COR Biosciences. https://books.google.com/books?hl=en&lr=&id=acKEEAAAQBAJ&oi=fnd&pg=PA1&dq=Eddy+Covariance+Method+for+Scientific,+Regulatory,+and+C

ommercial+Applications&ots=BE9CiHBLZy&sig=OVSnaD2X5VrmAkdIxvT2uuyZDpI

Cabon, A., Kannenberg, S. A., Arain, A., Babst, F., Baldocchi, D., Belmecheri, S., Delpierre, N., Guerrieri, R., Maxwell, J. T., McKenzie, S., Meinzer, F. C., Moore, D. J. P., Pappas, C., Rocha, A. V., Szejner, P., Ueyama, M., Ulrich, D., Vincke, C., Voelker, S. L., … Anderegg, W. R. L. (2022). Cross-biome synthesis of source versus sink limits to tree growth. *Science*, *376*(6594), 758–761. https://doi.org/10.1126/science.abm4875

Cabon, A., Peters, R. L., Fonti, P., Martínez-Vilalta, J., & De Cáceres, M. (2020). Temperature and water potential co-limit stem cambial activity along a steep elevational gradient. *New Phytologist*, *226*(5), 1325–1340. https://doi.org/10.1111/nph.16456

Campioli, M., Vicca, S., Luyssaert, S., Bilcke, J., Ceschia, E., Chapin III, F. S., Ciais, P., Fernández-Martínez, M., Malhi, Y., Obersteiner, M., Olefeldt, D., Papale, D., Piao, S. L., Peñuelas, J., Sullivan, P. F., Wang, X., Zenone, T., & Janssens, I. A. (2015). Biomass production efficiency controlled by management in temperate and boreal ecosystems. *Nature Geoscience*, *8*(11), 843–846. https://doi.org/10.1038/ngeo2553

Chapin, F. S., Matson, P. A., & Vitousek, P. M. (2011). *Principles of Terrestrial Ecosystem Ecology*. Springer. https://doi.org/10.1007/978-1-4419-9504-9

Chen, S., Lin, G., Huang, J., & Jenerette, G. D. (2009). Dependence of carbon sequestration on the differential responses of ecosystem photosynthesis and respiration to rain pulses in a semiarid steppe. *Global Change Biology*, *15*(10), 2450–2461. https://doi.org/10.1111/j.1365-2486.2009.01879.x

Chen, T., & Guestrin, C. (2016). XGBoost: A Scalable Tree Boosting System. *Proceedings of the 22nd ACM SIGKDD International Conference on Knowledge Discovery and Data Mining*, 785–794. https://doi.org/10.1145/2939672.2939785

Chu, H., Baldocchi, D. D., John, R., Wolf, S., & Reichstein, M. (2017). Fluxes all of the time? A primer on the temporal representativeness of FLUXNET. *Journal of Geophysical Research: Biogeosciences*, *122*(2), 289–307. https://doi.org/10.1002/2016JG003576

Chu, H., Luo, X., Ouyang, Z., Chan, W. S., Dengel, S., Biraud, S. C., Torn, M. S., Metzger, S., Kumar, J., Arain, M. A., Arkebauer, T. J., Baldocchi, D., Bernacchi, C., Billesbach, D., Black, T. A., Blanken, P. D., Bohrer, G., Bracho, R., Brown, S., … Zona, D. (2021). Representativeness of Eddy-Covariance flux footprints for areas surrounding AmeriFlux sites. *Agricultural and Forest Meteorology*, *301–302*, 108350. https://doi.org/10.1016/j.agrformet.2021.108350

Chu, H., Metzger, S., Ouyang, Z., Griebel, A., Yi, K., Durden, D., Wolf, S., Kasak, K., Rey-Sanchez, C., Hernandez Rodriguez, L. C., Oikawa, P., Falco, N., Runkle, B. R. K., Ahmadi, A., & Matthes, J. (2026). Flux Footprints: A Critical Link to Bridge Eddy-Covariance Measurements With Models, Remote Sensing, and Other Observations. *Global Change Biology*, *32*(4), e70887. https://doi.org/10.1111/gcb.70887

Cohrs, K.-H., Varando, G., Carvalhais, N., Reichstein, M., & Camps-Valls, G. (2024). Causal hybrid modeling with double machine learning—Applications in carbon flux modeling. *Machine Learning: Science and Technology*. https://doi.org/10.1088/2632-2153/ad5a60

Dacal, M., Bradford, M. A., Plaza, C., Maestre, F. T., & García-Palacios, P. (2019). Soil microbial respiration adapts to ambient temperature in global drylands. *Nature Ecology & Evolution*, *3*(2), 232–238. https://doi.org/10.1038/s41559-018-0770-5

Delire, C., Séférian, R., Decharme, B., Alkama, R., Calvet, J.-C., Carrer, D., Gibelin, A.-L., Joetzjer, E., Morel, X., Rocher, M., & Tzanos, D. (2020). The Global Land Carbon Cycle Simulated With ISBA-CTRIP: Improvements Over the Last Decade. *Journal of Advances in Modeling Earth Systems*, *12*(9), e2019MS001886. https://doi.org/10.1029/2019MS001886

Delwiche, K., Matthes, J. H., Arias-Ortiz, A., Knox, S. H., Oikawa, P., Sturtevant, C., Verfaillie, J., Szutu, D., Keenan, T. F., & Baldocchi, D. (2025). Dynamic methane emissions in a restored wetland: Decadal insights into uncertain climate outcomes and critical science needs. *Agricultural and Forest Meteorology*, *373*, 110735. https://doi.org/10.1016/j.agrformet.2025.110735

Deng, Q., Hui, D., Chu, G., Han, X., & Zhang, Q. (2017). Rain-induced changes in soil CO2 flux and microbial community composition in a tropical forest of China. *Scientific Reports*, *7*(1), 5539. https://doi.org/10.1038/s41598-017-06345-2

El-Madany, T. S., Reichstein, M., Perez-Priego, O., Carrara, A., Moreno, G., Pilar Martín, M., Pacheco-Labrador, J., Wohlfahrt, G., Nieto, H., Weber, U., Kolle, O., Luo, Y.-P., Carvalhais, N., & Migliavacca, M. (2018). Drivers of spatio-temporal variability of carbon dioxide and energy fluxes in a Mediterranean savanna ecosystem. *Agricultural and Forest Meteorology*, *262*, 258–278. https://doi.org/10.1016/j.agrformet.2018.07.010

Fatichi, S., Leuzinger, S., & Körner, C. (2014). Moving beyond photosynthesis: From carbon source to sink-driven vegetation modeling. *New Phytologist*, *201*(4), 1086–1095. https://doi.org/10.1111/nph.12614

Fatichi, S., Pappas, C., Zscheischler, J., & Leuzinger, S. (2019). Modelling carbon sources and sinks in terrestrial vegetation. *New Phytologist*, *221*(2), 652–668. https://doi.org/10.1111/nph.15451

Feldman, A. F., Feng, X., Felton, A. J., Konings, A. G., Knapp, A. K., Biederman, J. A., & Poulter, B. (2024). Plant responses to changing rainfall frequency and intensity. *Nature Reviews Earth & Environment*, *5*(4), 276–294. https://doi.org/10.1038/s43017-024-00534-0

Feldman, A. F., Short Gianotti, D. J., Konings, A. G., McColl, K. A., Akbar, R., Salvucci, G. D., & Entekhabi, D. (2018). Moisture pulse-reserve in the soil-plant continuum observed across biomes. *Nature Plants*, *4*(12), 1026–1033. https://doi.org/10.1038/s41477-018-0304-9

Fierer, N., Grandy, A. S., Six, J., & Paul, E. A. (2009). Searching for unifying principles in soil ecology. *Soil Biology and Biochemistry*, *41*(11), 2249–2256. https://doi.org/10.1016/j.soilbio.2009.06.009

Fierer, N., & Schimel, J. P. (2003). A Proposed Mechanism for the Pulse in Carbon Dioxide Production Commonly Observed Following the Rapid Rewetting of a Dry Soil. *Soil Science Society of America Journal*, *67*(3), 798–805. https://doi.org/10.2136/sssaj2003.7980

Friedlingstein, P., Jones, M. W., O'Sullivan, M., Andrew, R. M., Bakker, D. C. E., Hauck, J., Le Quéré, C., Peters, G. P., Peters, W., Pongratz, J., Sitch, S., Canadell, J. G.,

Ciais, P., Jackson, R. B., Alin, S. R., Anthoni, P., Bates, N. R., Becker, M., Bellouin, N., … Zeng, J. (2022). Global Carbon Budget 2021. *Earth System Science Data*, *14*(4), 1917–2005. https://doi.org/10.5194/essd-14-1917-2022

Friedlingstein, P., Le Quéré, C., O'Sullivan, M., Hauck, J., Landschützer, P., Luijkx, I. T., Li, H., van der Woude, A., Schwingshackl, C., Pongratz, J., Regnier, P., Andrew, R. M., Bakker, D. C. E., Canadell, J. G., Ciais, P., Gasser, T., Jones, M. W., Lan, X., Morgan, E., … Tian, H. (2026). Emerging climate impact on carbon sinks in a consolidated carbon budget. *Nature*, *649*(8095), 98–103. https://doi.org/10.1038/s41586-025-09802-5

Friedlingstein, P., O'Sullivan, M., Jones, M. W., Andrew, R. M., Bakker, D. C. E., Hauck, J., Landschützer, P., Le Quéré, C., Li, H., Luijkx, I. T., Peters, G. P., Peters, W., Pongratz, J., Schwingshackl, C., Sitch, S., Canadell, J. G., Ciais, P., Aas, K., Alin, S. R., … Zeng, J. (2025). *Global Carbon Budget 2025*. ESSD – Anthroposphere/Energy and anthropogenic emissions. https://doi.org/10.5194/essd-2025-659

Friend, A. D., Chen, Y., Eckes-Shephard, A. H., Fonti, P., Hellmann, E., Rademacher, T., Richardson, A. D., & Thomas, P. R. (2025). *Implications of source-sink feedbacks for modelling tree carbon assimilation and growth* (p. 2024.09.27.615358). bioRxiv. https://doi.org/10.1101/2024.09.27.615358

Friend, A. D., Eckes-Shephard, A. H., Fonti, P., Rademacher, T. T., Rathgeber, C. B. K., Richardson, A. D., & Turton, R. H. (2019). On the need to consider wood formation processes in global vegetation models and a suggested approach. *Annals of Forest Science*, *76*(2), Article 2. https://doi.org/10.1007/s13595-019-0819-x

Gaber, M., Kang, Y., Schurgers, G., & Keenan, T. (2024). Using automated machine learning for the upscaling of gross primary productivity. *Biogeosciences*, *21*(10), 2447–2472. https://doi.org/10.5194/bg-21-2447-2024

Gardner, W. R. (1959). Solutions of the Flow Equation for the Drying of Soils and Other Porous Media. *Soil Science Society of America Journal*, *23*(3), 183–187. https://doi.org/10.2136/sssaj1959.03615995002300030010x

Gebler, S. (2015). Actual evapotranspiration and precipitation measured by lysimeters: A comparison with eddy covariance and tipping bucket. *Hydrol. Earth Syst. Sci.*

Gessler, A., & Zweifel, R. (2024). Beyond source and sink control – toward an integrated approach to understand the carbon balance in plants. *New Phytologist*, *242*(3), 858–869. https://doi.org/10.1111/nph.19611

Gherardi, L. A., & Sala, O. E. (2019). Effect of interannual precipitation variability on dryland productivity: A global synthesis. *Global Change Biology*, *25*(1), 269–276. https://doi.org/10.1111/gcb.14480

Green, J. K., & Keenan, T. F. (2022). The limits of forest carbon sequestration. *Science (New York, N.Y.)*, *376*(6594), 692–693. https://doi.org/10.1126/science.abo6547

Grinsztajn, L., Oyallon, E., & Varoquaux, G. (2022). *Why do tree-based models still outperform deep learning on tabular data?* (arXiv:2207.08815). arXiv. http://arxiv.org/abs/2207.08815

Griscom, B. W., Adams, J., Ellis, P. W., Houghton, R. A., Lomax, G., Miteva, D. A., Schlesinger, W. H., Shoch, D., Siikamäki, J. V., Smith, P., Woodbury, P., Zganjar, C., Blackman, A., Campari, J., Conant, R. T., Delgado, C., Elias, P., Gopalakrishna, T., Hamsik, M. R., … Fargione, J. (2017). Natural climate solutions. *Proceedings of the National Academy of Sciences*, *114*(44), 11645–11650. https://doi.org/10.1073/pnas.1710465114

Haverd, V., Smith, B., Nieradzik, L., Briggs, P. R., Woodgate, W., Trudinger, C. M., Canadell, J. G., & Cuntz, M. (2018). A new version of the CABLE land surface model (Subversion revision r4601) incorporating land use and land cover change, woody vegetation demography, and a novel optimisation-based approach to plant coordination of photosynthesis. *Geoscientific Model Development*, *11*(7), 2995–3026. https://doi.org/10.5194/gmd-11-2995-2018

Hsiao, T. C. (1973). Plant Responses to Water Stress. *Annual Review of Plant Biology*, *24*(Volume 24, 1973), 519–570. https://doi.org/10.1146/annurev.pp.24.060173.002511

Huang, B., & Nobel, P. S. (1993). Hydraulic conductivity and anatomy along lateral roots of cacti: Changes with soil water status. *New Phytologist*, *123*(3), 499–507. https://doi.org/10.1111/j.1469-8137.1993.tb03762.x

Huang, J., Yu, H., Guan, X., Wang, G., & Guo, R. (2016). Accelerated dryland expansion under climate change. *Nature Climate Change*, *6*(2), 166–171. https://doi.org/10.1038/nclimate2837

Huxman, T. E., Cable, J. M., Ignace, D. D., Eilts, J. A., English, N. B., Weltzin, J., & Williams, D. G. (2004). Response of net ecosystem gas exchange to a simulated precipitation pulse in a semi-arid grassland: The role of native versus non-native grasses and soil texture. *Oecologia*, *141*(2), 295–305. https://doi.org/10.1007/s00442-003-1389-y

Huxman, T. E., Snyder, K. A., Tissue, D., Leffler, A. J., Ogle, K., Pockman, W. T., Sandquist, D. R., Potts, D. L., & Schwinning, S. (2004). Precipitation pulses and carbon fluxes in semiarid and arid ecosystems. *Oecologia*, *141*(2), 254–268. https://doi.org/10.1007/s00442-004-1682-4

Inglima, I., Alberti, G., Bertolini, T., Vaccari, F. P., Gioli, B., Miglietta, F., Cotrufo, M. F., & Peressotti, A. (2009). Precipitation pulses enhance respiration of Mediterranean ecosystems: The balance between organic and inorganic components of increased soil CO2 efflux. *Global Change Biology*, *15*(5), 1289–1301. https://doi.org/10.1111/j.1365-2486.2008.01793.x

Jarvis, P., Rey, A., Petsikos, C., Wingate, L., Rayment, M., Pereira, J., Banza, J., David, J., Miglietta, F., Borghetti, M., Manca, G., & Valentini, R. (2007). Drying and wetting of Mediterranean soils stimulates decomposition and carbon dioxide emission: The "Birch effect"†. *Tree Physiology*, *27*(7), 929–940. https://doi.org/10.1093/treephys/27.7.929

Jenerette, G. D., Scott, R. L., & Huxman, T. E. (2008). Whole ecosystem metabolic pulses following precipitation events. *Functional Ecology*, *22*(5), 924–930. https://doi.org/10.1111/j.1365-2435.2008.01450.x

Jiang, M., Medlyn, B. E., Drake, J. E., Duursma, R. A., Anderson, I. C., Barton, C. V. M., Boer, M. M., Carrillo, Y., Castañeda-Gómez, L., Collins, L., Crous, K. Y., De Kauwe, M. G., dos Santos, B. M., Emmerson, K. M., Facey, S. L., Gherlenda, A. N., Gimeno, T. E., Hasegawa, S., Johnson, S. N., … Ellsworth, D. S. (2020). The fate of carbon in a mature forest under carbon dioxide enrichment. *Nature*, *580*(7802), 227–231. https://doi.org/10.1038/s41586-020-2128-9

Joiner, J., & Yoshida, Y. (2020). Satellite-based reflectances capture large fraction of variability in global gross primary production (GPP) at weekly time scales. *Agricultural and Forest Meteorology*, *291*, 108092. https://doi.org/10.1016/j.agrformet.2020.108092

Jung, M., Koirala, S., Weber, U., Ichii, K., Gans, F., Camps-Valls, G., Papale, D., Schwalm, C., Tramontana, G., & Reichstein, M. (2019). The FLUXCOM ensemble of global land-atmosphere energy fluxes. *Scientific Data*, *6*(1), 74. https://doi.org/10.1038/s41597-019-0076-8

Jung, M., Nelson, J., Migliavacca, M., El-Madany, T., Papale, D., Reichstein, M., Walther, S., & Wutzler, T. (2024). *Technical note: Flagging inconsistencies in flux tower data*.

Jung, M., Reichstein, M., & Bondeau, A. (2009). Towards global empirical upscaling of FLUXNET eddy covariance observations: Validation of a model tree ensemble approach using a biosphere model. *Biogeosciences*, *6*(10), 2001–2013. https://doi.org/10.5194/bg-6-2001-2009

Jung, M., Reichstein, M., Ciais, P., Seneviratne, S. I., Sheffield, J., Goulden, M. L., Bonan, G., Cescatti, A., Chen, J., de Jeu, R., Dolman, A. J., Eugster, W., Gerten, D., Gianelle, D., Gobron, N., Heinke, J., Kimball, J., Law, B. E., Montagnani, L., … Zhang, K. (2010). Recent decline in the global land evapotranspiration trend due to limited moisture supply. *Nature*, *467*(7318), 951–954. https://doi.org/10.1038/nature09396

Kang, Y., Bassiouni, M., Gaber, M., Lu, X., & Keenan, T. F. (2025). CEDAR-GPP: Spatiotemporally upscaled estimates of gross primary productivity incorporating CO_2 fertilization. *Earth System Science Data*, *17*(6), 3009–3046. https://doi.org/10.5194/essd-17-3009-2025

Kannenberg, S. A., Babst, F., Barnes, M. L., Cabon, A., Dannenberg, M. P., Johnston, M. R., & Anderegg, W. R. L. (2025). Stand density and local climate drive allocation of GPP to aboveground woody biomass. *New Phytologist*, *246*(2), 543–553. https://doi.org/10.1111/nph.20414

Kannenberg, S. A., Barnes, M. L., Bowling, D. R., Driscoll, A. W., Guo, J. S., & Anderegg, W. R. L. (2023). Quantifying the drivers of ecosystem fluxes and water potential across the soil-plant-atmosphere continuum in an arid woodland. *Agricultural*

and Forest Meteorology, *329*, 109269. https://doi.org/10.1016/j.agrformet.2022.109269

Kannenberg, S. A., Cabon, A., Babst, F., Belmecheri, S., Delpierre, N., Guerrieri, R., Maxwell, J. T., Meinzer, F. C., Moore, D. J. P., Pappas, C., Ueyama, M., Ulrich, D. E. M., Voelker, S. L., Woodruff, D. R., & Anderegg, W. R. L. (2022). Drought-induced decoupling between carbon uptake and tree growth impacts forest carbon turnover time. *Agricultural and Forest Meteorology*, *322*, 108996. https://doi.org/10.1016/j.agrformet.2022.108996

Keenan, T. F. (2026). *FLUXNET Data Explorer* [Computer software]. Zenodo. https://doi.org/10.5281/zenodo.20331228

Keenan, T. F., Luo, X., Stocker, B. D., De Kauwe, M. G., Medlyn, B. E., Prentice, I. C., Smith, N. G., Terrer, C., Wang, H., Zhang, Y., & Zhou, S. (2023). A constraint on historic growth in global photosynthesis due to rising CO2. *Nature Climate Change*, *13*(12), 1376–1381. https://doi.org/10.1038/s41558-023-01867-2

Keenan, T. F., Prentice, I. C., Canadell, J. G., Williams, C. A., Wang, H., Raupach, M., & Collatz, G. J. (2016). Recent pause in the growth rate of atmospheric CO2 due to enhanced terrestrial carbon uptake. *Nature Communications*, *7*(1), 13428. https://doi.org/10.1038/ncomms13428

Kim, J., Guo, Q., Baldocchi, D. D., Leclerc, M. Y., Xu, L., & Schmid, H. P. (2006). Upscaling fluxes from tower to landscape: Overlaying flux footprints on high-resolution (IKONOS) images of vegetation cover. *Agricultural and Forest Meteorology, Advances in Surface-Atmosphere Exchange - A Tribute to Marv Wesely*, *136*(3), 132–146. https://doi.org/10.1016/j.agrformet.2004.11.015

Kljun, N., Calanca, P., Rotach, M. W., & Schmid, H. P. (2015). A simple two-dimensional parameterisation for Flux Footprint Prediction (FFP). *Geoscientific Model Development*, *8*(11), 3695–3713. https://doi.org/10.5194/gmd-8-3695-2015

Körner, C. (2022). The forest's nutrient cycle drives its carbon cycle. *Tree Physiology*, *42*(3), 425–427. https://doi.org/10.1093/treephys/tpab170

Lasslop, G., Reichstein, M., Papale, D., Richardson, A. D., Arneth, A., Barr, A., Stoy, P., & Wohlfahrt, G. (2010). Separation of net ecosystem exchange into assimilation and respiration using a light response curve approach: Critical

issues and global evaluation. *Global Change Biology*, *16*(1), 187–208. https://doi.org/10.1111/j.1365-2486.2009.02041.x

Lauber, C. L., Hamady, M., Knight, R., & Fierer, N. (2009). Pyrosequencing-Based Assessment of Soil pH as a Predictor of Soil Bacterial Community Structure at the Continental Scale. *Applied and Environmental Microbiology*, *75*(15), 5111–5120. https://doi.org/10.1128/AEM.00335-09

Lawrence, D. M., Fisher, R. A., Koven, C. D., Oleson, K. W., Swenson, S. C., Bonan, G., Collier, N., Ghimire, B., van Kampenhout, L., Kennedy, D., Kluzek, E., Lawrence, P. J., Li, F., Li, H., Lombardozzi, D., Riley, W. J., Sacks, W. J., Shi, M., Vertenstein, M., … Zeng, X. (2019). The Community Land Model Version 5: Description of New Features, Benchmarking, and Impact of Forcing Uncertainty. *Journal of Advances in Modeling Earth Systems*, *11*(12), 4245–4287. https://doi.org/10.1029/2018MS001583

Lee, X., Wu, H.-J., Sigler, J., Oishi, C., & Siccama, T. (2004). Rapid and transient response of soil respiration to rain. *Global Change Biology*, *10*(6), 1017–1026. https://doi.org/10.1111/j.1529-8817.2003.00787.x

Legates, D. R., & DeLiberty, T. L. (1993). Precipitation Measurement Biases in the United States. *JAWRA Journal of the American Water Resources Association*, *29*(5), 855–861. https://doi.org/10.1111/j.1752-1688.1993.tb03245.x

Lempereur, M., Martin-StPaul, N. K., Damesin, C., Joffre, R., Ourcival, J.-M., Rocheteau, A., & Rambal, S. (2015). Growth duration is a better predictor of stem increment than carbon supply in a Mediterranean oak forest: Implications for assessing forest productivity under climate change. *New Phytologist*, *207*(3), 579–590. https://doi.org/10.1111/nph.13400

Lienert, S., & Joos, F. (2018). A Bayesian ensemble data assimilation to constrain model parameters and land-use carbon emissions. *Biogeosciences*, *15*(9), 2909–2930. https://doi.org/10.5194/bg-15-2909-2018

Lim, H., Medvigy, D., Mäkelä, A., Kim, D., Albaugh, T. J., Knier, A., Blaško, R., C Campoe, O., Deshar, R., Franklin, O., Henriksson, N., Littke, K., Lutter, R., Maier, C. A., Palmroth, S., Rosenvald, K., Slesak, R. A., Tullus, A., & Oren, R. (2024). Overlooked branch turnover creates a widespread bias in forest carbon accounting. *Proceedings of the National Academy of Sciences of the United*

States of America, *121*(42), e2401035121. https://doi.org/10.1073/pnas.2401035121

Lindeman, R. H., Merenda, P. F., & Gold, R. Z. (1980). *Introduction to bivariate and multivariate analysis* (Vol. 4). Scott, Foresman Glenview, IL. https://library.wur.nl/WebQuery/titel/1714678

Litton, C. M., Raich, J. W., & Ryan, M. G. (2007). Carbon allocation in forest ecosystems. *Global Change Biology*, *13*(10), 2089–2109. https://doi.org/10.1111/j.1365-2486.2007.01420.x

Liu, X., Wan, S., Su, B., Hui, D., & Luo, Y. (2002). Response of soil CO2 efflux to water manipulation in a tallgrass prairie ecosystem. *Plant and Soil*, *240*(2), 213–223. https://doi.org/10.1023/A:1015744126533

Lloyd, J., & Taylor, J. A. (1994). On the Temperature Dependence of Soil Respiration. *Functional Ecology*, *8*(3), 315–323. https://doi.org/10.2307/2389824

Luo, Y., El-Madany, T. S., Filippa, G., Ma, X., Ahrens, B., Carrara, A., Gonzalez-Cascon, R., Cremonese, E., Galvagno, M., Hammer, T. W., Pacheco-Labrador, J., Martín, M. P., Moreno, G., Perez-Priego, O., Reichstein, M., Richardson, A. D., Römermann, C., & Migliavacca, M. (2018). Using Near-Infrared-Enabled Digital Repeat Photography to Track Structural and Physiological Phenology in Mediterranean Tree–Grass Ecosystems. *Remote Sensing*, *10*(8), 1293. https://doi.org/10.3390/rs10081293

MacBean, N., Scott, R. L., Biederman, J. A., Peylin, P., Kolb, T., Litvak, M. E., Krishnan, P., Meyers, T. P., Arora, V. K., Bastrikov, V., Goll, D., Lombardozzi, D. L., Nabel, J. E. M. S., Pongratz, J., Sitch, S., Walker, A. P., Zaehle, S., & Moore, D. J. P. (2021). Dynamic global vegetation models underestimate net CO2 flux mean and inter-annual variability in dryland ecosystems. *Environmental Research Letters*, *16*(9), 094023. https://doi.org/10.1088/1748-9326/ac1a38

Maier, M., Schack-Kirchner, H., Hildebrand, E. E., & Holst, J. (2010). Pore-space CO2 dynamics in a deep, well-aerated soil. *European Journal of Soil Science*, *61*(6), 877–887. https://doi.org/10.1111/j.1365-2389.2010.01287.x

Mcshane, E. J. (1937). *JENSEN'S INEQUALITY*.

Melton, J. R., Arora, V. K., Wisernig-Cojoc, E., Seiler, C., Fortier, M., Chan, E., & Teckentrup, L. (2020). CLASSIC v1.0: The open-source community successor

to the Canadian Land Surface Scheme (CLASS) and the Canadian Terrestrial Ecosystem Model (CTEM) – Part 1: Model framework and site-level performance. *Geoscientific Model Development*, *13*(6), 2825–2850. https://doi.org/10.5194/gmd-13-2825-2020

Metz, E.-M., Vardag, S. N., Basu, S., Jung, M., Ahrens, B., El-Madany, T., Sitch, S., Arora, V. K., Briggs, P. R., Friedlingstein, P., Goll, D. S., Jain, A. K., Kato, E., Lombardozzi, D., Nabel, J. E. M. S., Poulter, B., Séférian, R., Tian, H., Wiltshire, A., … Butz, A. (2023). Soil respiration–driven CO2 pulses dominate Australia's flux variability. *Science*, *379*(6639), 1332–1335. https://doi.org/10.1126/science.add7833

Metzger, S., Junkermann, W., Mauder, M., Butterbach-Bahl, K., Trancón y Widemann, B., Neidl, F., Schäfer, K., Wieneke, S., Zheng, X. H., Schmid, H. P., & Foken, T. (2013). Spatially explicit regionalization of airborne flux measurements using environmental response functions. *Biogeosciences*, *10*(4), 2193–2217. https://doi.org/10.5194/bg-10-2193-2013

Migliavacca, M., Reichstein, M., Richardson, A. D., Colombo, R., Sutton, M. A., Lasslop, G., Tomelleri, E., Wohlfahrt, G., Carvalhais, N., Cescatti, A., Mahecha, M. D., Montagnani, L., Papale, D., Zaehle, S., Arain, A., Arneth, A., Black, T. A., Carrara, A., Dore, S., … Van Der MOLEN, M. K. (2011). Semiempirical modeling of abiotic and biotic factors controlling ecosystem respiration across eddy covariance sites. *Global Change Biology*, *17*(1), 390–409. https://doi.org/10.1111/j.1365-2486.2010.02243.x

Muller, B., Pantin, F., Génard, M., Turc, O., Freixes, S., Piques, M., & Gibon, Y. (2011). Water deficits uncouple growth from photosynthesis, increase C content, and modify the relationships between C and growth in sink organs. *Journal of Experimental Botany*, *62*(6), 1715–1729. https://doi.org/10.1093/jxb/erq438

Nelson, J. A., Walther, S., Gans, F., Kraft, B., Weber, U., Novick, K., Buchmann, N., Migliavacca, M., Wohlfahrt, G., Šigut, L., Ibrom, A., Papale, D., Göckede, M., Duveiller, G., Knohl, A., Hörtnagl, L., Scott, R. L., Dušek, J., Zhang, W., … Jung, M. (2024). X-BASE: The first terrestrial carbon and water flux products from an extended data-driven scaling framework, FLUXCOM-X. *Biogeosciences*, *21*(22), 5079–5115. https://doi.org/10.5194/bg-21-5079-2024

Nguyen, N. B., Migliavacca, M., Bassiouni, M., Baldocchi, D. D., Gherardi, L. A., Green, J. K., Papale, D., Reichstein, M., Cohrs, K.-H., Cescatti, A., Nguyen, T. D., Nguyen, H. H., Nguyen, Q. M., & Keenan, T. F. (2025). Widespread underestimation of rain-induced soil carbon emissions from global drylands. *Nature Geoscience*, 1–8. https://doi.org/10.1038/s41561-025-01754-9

Norby, R. J. (2025). Forest productivity response to elevated CO2 in free-air CO2 enrichment experiments: The 23 percent solution, revisited. *New Phytologist*, *246*(5), 1952–1959. https://doi.org/10.1111/nph.70162

Novick, K. A., Metzger, S., Anderegg, W. R. L., Barnes, M., Cala, D. S., Guan, K., Hemes, K. S., Hollinger, D. Y., Kumar, J., Litvak, M., Lombardozzi, D., Normile, C. P., Oikawa, P., Runkle, B. R. K., Torn, M., & Wiesner, S. (2022). Informing Nature-based Climate Solutions for the United States with the best-available science. *Global Change Biology*, *28*(12), 3778–3794. https://doi.org/10.1111/gcb.16156

Noy-Meir, I. (1973). Desert Ecosystems: Environment and Producers. *Annual Review of Ecology and Systematics*, 25–51. http://www.jstor.org/stable/2096803

Oikawa, P. Y., Jenerette, G. D., Knox, S. H., Sturtevant, C., Verfaillie, J., Dronova, I., Poindexter, C. M., Eichelmann, E., & Baldocchi, D. D. (2017). Evaluation of a hierarchy of models reveals importance of substrate limitation for predicting carbon dioxide and methane exchange in restored wetlands. *Journal of Geophysical Research: Biogeosciences*, *122*(1), 145–167. https://doi.org/10.1002/2016JG003438

Orchard, V. A., & Cook, F. J. (1983). Relationship between soil respiration and soil moisture. *Soil Biology and Biochemistry*, *15*(4), 447–453. https://doi.org/10.1016/0038-0717(83)90010-X

Papale, D., & Valentini, R. (2003). A new assessment of European forests carbon exchanges by eddy fluxes and artificial neural network spatialization. *Global Change Biology*, *9*(4), 525–535. https://doi.org/10.1046/j.1365-2486.2003.00609.x

Pastorello, G., Trotta, C., Canfora, E., Chu, H., Christianson, D., Cheah, Y.-W., Poindexter, C., Chen, J., Elbashandy, A., Humphrey, M., Isaac, P., Polidori, D., Reichstein, M., Ribeca, A., van Ingen, C., Vuichard, N., Zhang, L., Amiro, B.,

Ammann, C., ⋯ Papale, D. (2020). The FLUXNET2015 dataset and the ONEFlux processing pipeline for eddy covariance data. *Scientific Data*, *7*(1), 225. https://doi.org/10.1038/s41597-020-0534-3

Placella, S. A., Brodie, E. L., & Firestone, M. K. (2012). Rainfall-induced carbon dioxide pulses result from sequential resuscitation of phylogenetically clustered microbial groups. *Proceedings of the National Academy of Sciences*, *109*(27), 10931–10936. https://doi.org/10.1073/pnas.1204306109

Poggio, L., de Sousa, L. M., Batjes, N. H., Heuvelink, G. B. M., Kempen, B., Ribeiro, E., & Rossiter, D. (2021). SoilGrids 2.0: Producing soil information for the globe with quantified spatial uncertainty. *SOIL*, *7*(1), 217–240. https://doi.org/10.5194/soil-7-217-2021

Poulter, B., Frank, D., Ciais, P., Myneni, R. B., Andela, N., Bi, J., Broquet, G., Canadell, J. G., Chevallier, F., Liu, Y. Y., Running, S. W., Sitch, S., & van der Werf, G. R. (2014). Contribution of semi-arid ecosystems to interannual variability of the global carbon cycle. *Nature*, *509*(7502), 600–603. https://doi.org/10.1038/nature13376

Rahman, M. (2026). Physically interpretable AlphaEarth foundation model embeddings enable LLM-based land surface intelligence. *Remote Sensing Applications: Society and Environment*, *42*, 102045. https://doi.org/10.1016/j.rsase.2026.102045

Raich, J. W., & Potter, C. S. (1995). Global patterns of carbon dioxide emissions from soils. *Global Biogeochemical Cycles*, *9*(1), 23–36. https://doi.org/10.1029/94GB02723

Rao, M. P., Pacheco-Solana, A., Li, R., Oryan, B., Jensen, J. E., Rodriguez-Caton, M., Klinek, L., Pierrat, Z. A., Ruehr, S., Oelkers, R., Boeschoten, L. E., Griffin, K. L., McCormack, M. L., Yang, X., Verfaillie, J., Baldocchi, D., Hise, J., Turner, A. J., Scanlon, T. M., ⋯ Magney, T. S. (2026). Decoupled carbon assimilation and growth responses to aridity in temperate deciduous oaks. *Science Advances*, *12*(24), eady7139. https://doi.org/10.1126/sciadv.ady7139

Reichstein, M., Falge, E., Baldocchi, D., Papale, D., Aubinet, M., Berbigier, P., Bernhofer, C., Buchmann, N., Gilmanov, T., Granier, A., Grünwald, T., Havránková, K., Ilvesniemi, H., Janous, D., Knohl, A., Laurila, T., Lohila, A., Loustau, D., Matteucci,

G., ⋯ Valentini, R. (2005). On the separation of net ecosystem exchange into assimilation and ecosystem respiration: Review and improved algorithm. *Global Change Biology*, *11*(9), 1424–1439. https://doi.org/10.1111/j.1365-2486.2005.001002.x

Reichstein, M., Rey, A., Freibauer, A., Tenhunen, J., Valentini, R., Banza, J., Casals, P., Cheng, Y., Grünzweig, J. M., Irvine, J., Joffre, R., Law, B. E., Loustau, D., Miglietta, F., Oechel, W., Ourcival, J.-M., Pereira, J. S., Peressotti, A., Ponti, F., ⋯ Yakir, D. (2003). Modeling temporal and large-scale spatial variability of soil respiration from soil water availability, temperature and vegetation productivity indices. *Global Biogeochemical Cycles*, *17*(4). https://doi.org/10.1029/2003GB002035

Reynolds, J. F., Smith, D. M. S., Lambin, E. F., Turner, B. L., Mortimore, M., Batterbury, S. P. J., Downing, T. E., Dowlatabadi, H., Fernández, R. J., Herrick, J. E., Huber-Sannwald, E., Jiang, H., Leemans, R., Lynam, T., Maestre, F. T., Ayarza, M., & Walker, B. (2007). Global Desertification: Building a Science for Dryland Development. *Science*, *316*(5826), 847–851. https://doi.org/10.1126/science.1131634

Richardson, A. D., Carbone, M. S., Keenan, T. F., Czimczik, C. I., Hollinger, D. Y., Murakami, P., Schaberg, P. G., & Xu, X. (2013). Seasonal dynamics and age of stemwood nonstructural carbohydrates in temperate forest trees. *The New Phytologist*, *197*(3), 850–861. https://www.jstor.org/stable/newphytologist.197.3.850

Roby, M. C., Scott, R. L., & Moore, D. J. P. (2020). High Vapor Pressure Deficit Decreases the Productivity and Water Use Efficiency of Rain-Induced Pulses in Semiarid Ecosystems. *Journal of Geophysical Research: Biogeosciences*, *125*(10), e2020JG005665. https://doi.org/10.1029/2020JG005665

Romero, E., Rey-Sanchez, C., Gerlein-Safdi, C., Baldocchi, D. D., Lee, P., & Dronova, I. (2026). Photosynthesis, heat, and structure: An evident hierarchy of environmental conditions driving wetland carbon assimilation. *Remote Sensing of Environment*, *338*, 115339. https://doi.org/10.1016/j.rse.2026.115339

Rousk, J., & C. Brangarí, A. (2022). Do the respiration pulses induced by drying–rewetting matter for the soil–atmosphere carbon balance? *Global Change Biology*, *28*(11), 3486–3488. https://doi.org/10.1111/gcb.16163

Rutledge, S., Campbell, D. I., Baldocchi, D., & Schipper, L. A. (2010). Photodegradation leads to increased carbon dioxide losses from terrestrial organic matter. *Global Change Biology*, *16*(11), 3065–3074. https://doi.org/10.1111/j.1365-2486.2009.02149.x

Sala, O. E., Gherardi, L. A., Reichmann, L., Jobbágy, E., & Peters, D. (2012). Legacies of precipitation fluctuations on primary production: Theory and data synthesis. *Philosophical Transactions of the Royal Society B: Biological Sciences*, *367*(1606), 3135–3144. https://doi.org/10.1098/rstb.2011.0347

Schimel, J. P. (2018). *Life in Dry Soils: Effects of Drought on Soil Microbial Communities and Processes*.

Schmid, H. P., & Lloyd, C. R. (1999). Spatial representativeness and the location bias of flux footprints over inhomogeneous areas. *Agricultural and Forest Meteorology*, *93*(3), 195–209. https://doi.org/10.1016/S0168-1923(98)00119-1

Schneider, T., Keiblinger, K. M., Schmid, E., Sterflinger-Gleixner, K., Ellersdorfer, G., Roschitzki, B., Richter, A., Eberl, L., Zechmeister-Boltenstern, S., & Riedel, K. (2012). Who is who in litter decomposition? Metaproteomics reveals major microbial players and their biogeochemical functions. *The ISME Journal*, *6*(9), 1749–1762. https://doi.org/10.1038/ismej.2012.11

Serrano-Ortiz, P., Roland, M., Sanchez-Moral, S., Janssens, I. A., Domingo, F., Goddéris, Y., & Kowalski, A. S. (2010). Hidden, abiotic CO2 flows and gaseous reservoirs in the terrestrial carbon cycle: Review and perspectives. *Agricultural and Forest Meteorology*, *150*(3), 321–329. https://doi.org/10.1016/j.agrformet.2010.01.002

Shuttleworth, J., Gurney R, J., Hsu A., Y., & Ormsby J., P. (1989). FIFE: The variation in energy partition at surface flux sites. *IAHS Publication (International Association of Hydrological Sciences)*, (186), 67–74. https://jglobal.jst.go.jp/en/detail?JGLOBAL_ID=200902011991788720

Singh, S. (2023). How the Birch effect differs in mechanisms and magnitudes due to soil texture. *Soil Biology and Biochemistry*.

Sinsabaugh, R. L., Lauber, C. L., Weintraub, M. N., Ahmed, B., Allison, S. D., Crenshaw, C., Contosta, A. R., Cusack, D., Frey, S., Gallo, M. E., Gartner, T. B., Hobbie, S. E., Holland, K., Keeler, B. L., Powers, J. S., Stursova, M., Takacs-Vesbach, C., Waldrop, M. P., Wallenstein, M. D., … Zeglin, L. H. (2008). Stoichiometry of soil enzyme activity at global scale. *Ecology Letters*, *11*(11), 1252–1264. https://doi.org/10.1111/j.1461-0248.2008.01245.x

Sitch, S., O'Sullivan, M., Robertson, E., Friedlingstein, P., Albergel, C., Anthoni, P., Arneth, A., Arora, V. K., Bastos, A., Bastrikov, V., Bellouin, N., Canadell, J. G., Chini, L., Ciais, P., Falk, S., Harris, I., Hurtt, G., Ito, A., Jain, A. K., … Zaehle, S. (2024). Trends and Drivers of Terrestrial Sources and Sinks of Carbon Dioxide: An Overview of the TRENDY Project. *Global Biogeochemical Cycles*, *38*(7), e2024GB008102. https://doi.org/10.1029/2024GB008102

Smith, B., Wårlind, D., Arneth, A., Hickler, T., Leadley, P., Siltberg, J., & Zaehle, S. (2014). Implications of incorporating N cycling and N limitations on primary production in an individual-based dynamic vegetation model. *Biogeosciences*, *11*(7), 2027–2054. https://doi.org/10.5194/bg-11-2027-2014

Smith, W. K., Dannenberg, M. P., Yan, D., Herrmann, S., Barnes, M. L., Barron-Gafford, G. A., Biederman, J. A., Ferrenberg, S., Fox, A. M., Hudson, A., Knowles, J. F., MacBean, N., Moore, D. J. P., Nagler, P. L., Reed, S. C., Rutherford, W. A., Scott, R. L., Wang, X., & Yang, J. (2019). Remote sensing of dryland ecosystem structure and function: Progress, challenges, and opportunities. *Remote Sensing of Environment*, *233*, 111401. https://doi.org/10.1016/j.rse.2019.111401

Tang, J., Baldocchi, D. D., & Xu, L. (2005). Tree photosynthesis modulates soil respiration on a diurnal time scale. *Global Change Biology*, *11*(8), 1298–1304. https://doi.org/10.1111/j.1365-2486.2005.00978.x

Teets, A., Fraver, S., Hollinger, D. Y., Weiskittel, A. R., Seymour, R. S., & Richardson, A. D. (2018). Linking annual tree growth with eddy-flux measures of net ecosystem productivity across twenty years of observation in a mixed conifer

forest. *Agricultural and Forest Meteorology*, *249*, 479–487. https://doi.org/10.1016/j.agrformet.2017.08.007

Teets, A., Moore, D. J. P., Alexander, M. R., Blanken, P. D., Bohrer, G., Burns, S. P., Carbone, M. S., Ducey, M. J., Fraver, S., Gough, C. M., Hollinger, D. Y., Koch, G., Kolb, T., Munger, J. W., Novick, K. A., Ollinger, S. V., Ouimette, A. P., Pederson, N., Ricciuto, D. M., … Richardson, A. D. (2022). Coupling of Tree Growth and Photosynthetic Carbon Uptake Across Six North American Forests. *Journal of Geophysical Research: Biogeosciences*, *127*(4), e2021JG006690. https://doi.org/10.1029/2021JG006690

Terrer, C., Jackson, R. B., Prentice, I. C., Keenan, T. F., Kaiser, C., Vicca, S., Fisher, J. B., Reich, P. B., Stocker, B. D., Hungate, B. A., Peñuelas, J., McCallum, I., Soudzilovskaia, N. A., Cernusak, L. A., Talhelm, A. F., Van Sundert, K., Piao, S., Newton, P. C. D., Hovenden, M. J., … Franklin, O. (2019). Nitrogen and phosphorus constrain the CO2 fertilization of global plant biomass. *Nature Climate Change*, *9*(9), 684–689. https://doi.org/10.1038/s41558-019-0545-2

Tramontana, G., Ichii, K., Camps-Valls, G., Tomelleri, E., & Papale, D. (2015). Uncertainty analysis of gross primary production upscaling using Random Forests, remote sensing and eddy covariance data. *Remote Sensing of Environment*, *168*, 360–373. https://doi.org/10.1016/j.rse.2015.07.015

Tramontana, G., Migliavacca, M., Jung, M., Reichstein, M., Keenan, T. F., Camps-Valls, G., Ogee, J., Verrelst, J., & Papale, D. (2020). Partitioning net carbon dioxide fluxes into photosynthesis and respiration using neural networks. *Global Change Biology*, *26*(9), 5235–5253. https://doi.org/10.1111/gcb.15203

Tripathi, B. M., Stegen, J. C., Kim, M., Dong, K., Adams, J. M., & Lee, Y. K. (2018). Soil pH mediates the balance between stochastic and deterministic assembly of bacteria. *The ISME Journal*, *12*(4), 1072–1083. https://doi.org/10.1038/s41396-018-0082-4

Trugman, A. T., & Anderegg, L. D. L. (2025). Source vs sink limitations on tree growth: From physiological mechanisms to evolutionary constraints and terrestrial carbon cycle implications. *New Phytologist*, *245*(3), 966–981. https://doi.org/10.1111/nph.20294

Vicca, S., Luyssaert, S., Peñuelas, J., Campioli, M., Chapin III, F. S., Ciais, P., Heinemeyer, A., Högberg, P., Kutsch, W. L., Law, B. E., Malhi, Y., Papale, D., Piao, S. L., Reichstein, M., Schulze, E. D., & Janssens, I. A. (2012). Fertile forests produce biomass more efficiently. *Ecology Letters*, *15*(6), 520–526. https://doi.org/10.1111/j.1461-0248.2012.01775.x

Vuichard, N., Messina, P., Luyssaert, S., Guenet, B., Zaehle, S., Ghattas, J., Bastrikov, V., & Peylin, P. (2019). Accounting for carbon and nitrogen interactions in the global terrestrial ecosystem model ORCHIDEE (trunk version, rev 4999): Multi-scale evaluation of gross primary production. *Geoscientific Model Development*, *12*(11), 4751–4779. https://doi.org/10.5194/gmd-12-4751-2019

Vuichard, N., & Papale, D. (2015). Filling the gaps in meteorological continuous data measured at FLUXNET sites with ERA-Interim reanalysis. *Earth System Science Data*, *7*(2), 157–171. https://doi.org/10.5194/essd-7-157-2015

Walker, A. P., De Kauwe, M. G., Bastos, A., Belmecheri, S., Georgiou, K., Keeling, R. F., McMahon, S. M., Medlyn, B. E., Moore, D. J. P., Norby, R. J., Zaehle, S., Anderson-Teixeira, K. J., Battipaglia, G., Brienen, R. J. W., Cabugao, K. G., Cailleret, M., Campbell, E., Canadell, J. G., Ciais, P., … Zuidema, P. A. (2021). Integrating the evidence for a terrestrial carbon sink caused by increasing atmospheric CO2. *New Phytologist*, *229*(5), 2413–2445. https://doi.org/10.1111/nph.16866

Waring, R. H., Landsberg, J. J., & Williams, M. (1998). Net primary production of forests: A constant fraction of gross primary production? *Tree Physiology*, *18*(2), 129–134. https://doi.org/10.1093/treephys/18.2.129

Warm Winter 2020 Team, & ICOS Ecosystem Thematic Centre. (2022). *Warm Winter 2020 ecosystem eddy covariance flux product for 73 stations in FLUXNET-Archive format—Release 2022-1 (Version 1.0).* https://doi.org/10.18160/2G60-ZHAK

White, A. C., Rogers, A., Rees, M., & Osborne, C. P. (2016). How can we make plants grow faster? A source-sink perspective on growth rate. *Journal of Experimental Botany*, *67*(1), 31–45. https://doi.org/10.1093/jxb/erv447

Whitford, W. G., & Duval, B. D. (2020). Chapter 3—Characterization of Desert Climates. In W. G. Whitford & B. D. Duval (Eds.), *Ecology of Desert Systems (Second Edition)* (pp. 47–72). Academic Press. https://doi.org/10.1016/B978-0-12-815055-9.00003-5

Xiao, J., Baldocchi, D., Ichii, K., Li, F., & Papale, D. (2025). Insights into terrestrial carbon and water cycling from the global eddy covariance network. *Nature Reviews Earth & Environment*, 1–20. https://doi.org/10.1038/s43017-025-00743-1

Xiao, J., Ollinger, S. V., Frolking, S., Hurtt, G. C., Hollinger, D. Y., Davis, K. J., Pan, Y., Zhang, X., Deng, F., Chen, J., Baldocchi, D. D., Law, B. E., Arain, M. A., Desai, A. R., Richardson, A. D., Sun, G., Amiro, B., Margolis, H., Gu, L., … Suyker, A. E. (2014). Data-driven diagnostics of terrestrial carbon dynamics over North America. *Agricultural and Forest Meteorology*, *197*, 142–157. https://doi.org/10.1016/j.agrformet.2014.06.013

Xiao, J., Zhuang, Q., Baldocchi, D. D., Law, B. E., Richardson, A. D., Chen, J., Oren, R., Starr, G., Noormets, A., Ma, S., Verma, S. B., Wharton, S., Wofsy, S. C., Bolstad, P. V., Burns, S. P., Cook, D. R., Curtis, P. S., Drake, B. G., Falk, M., … Torn, M. S. (2008). Estimation of net ecosystem carbon exchange for the conterminous United States by combining MODIS and AmeriFlux data. *Agricultural and Forest Meteorology*, *148*(11), 1827–1847. https://doi.org/10.1016/j.agrformet.2008.06.015

Xu, K., Metzger, S., & Desai, A. R. (2017). Upscaling tower-observed turbulent exchange at fine spatio-temporal resolution using environmental response functions. *Agricultural and Forest Meteorology*, *232*, 10–22. https://doi.org/10.1016/j.agrformet.2016.07.019

Xu, L., & Baldocchi, D. D. (2004). Seasonal variation in carbon dioxide exchange over a Mediterranean annual grassland in California. *Agricultural and Forest Meteorology*, *123*(1), 79–96. https://doi.org/10.1016/j.agrformet.2003.10.004

Xu, L., Baldocchi, D. D., & Tang, J. (2004). How soil moisture, rain pulses, and growth alter the response of ecosystem respiration to temperature. *Global Biogeochemical Cycles*, *18*(4). https://doi.org/10.1029/2004GB002281

Yan, L., Chen, S., Xia, J., & Luo, Y. (2014). Precipitation Regime Shift Enhanced the Rain Pulse Effect on Soil Respiration in a Semi-Arid Steppe. *PLOS ONE*, *9*(8), e104217. https://doi.org/10.1371/journal.pone.0104217

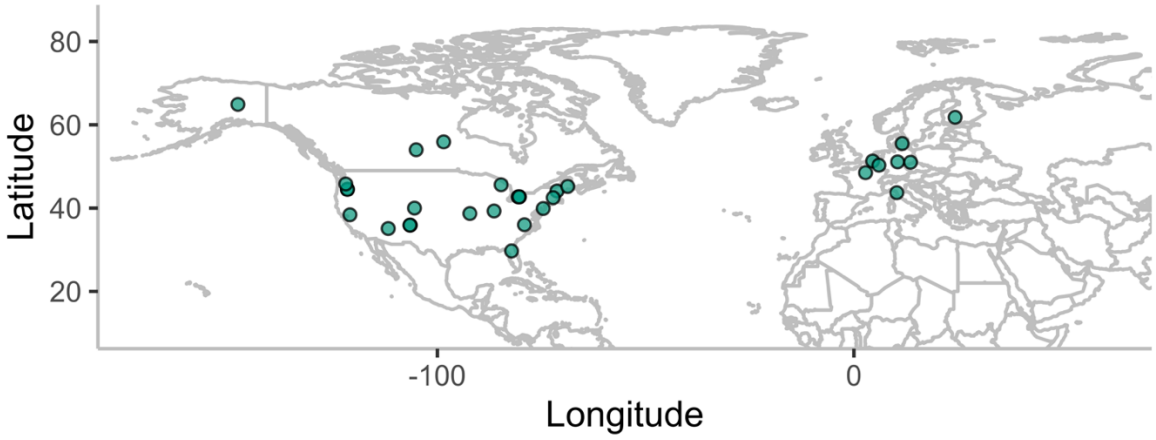
3.8. Extended Data

Extended Data Table 3.1. List of eddy-covariance flux towers used in this study that have onsite ring width measurements (Cabon et al., 2022; Pastorello et al., 2020).

	Site	DOI	Lon	Lat	Elev	IGBP	MAT	MAP	Start	End
1	BE-Bra	10.18140/FLX/1440128	4.5	51.3	16	MF	10.8	841	1996	2014
2	BE-Vie	10.18140/FLX/1440130	6	50.3	493	MF	8.3	1134	1996	2014
3	CA-Man	10.18140/FLX/1440035	-98.5	55.9	259	ENF	-2.7	508	1994	2008
4	CA-Obs	10.18140/FLX/1440044	-105.1	54	629	ENF	0.1	488	1997	2010
5	CA-TP1	10.18140/FLX/1440050	-80.6	42.7	265	ENF	8.6	1002	2002	2014
6	CA-TP3	10.18140/FLX/1440052	-80.3	42.7	184	ENF	8.7	982	2002	2014
7	CA-TP4	10.18140/FLX/1440053	-80.4	42.7	184	ENF	8.5	988	2002	2014
8	DE-Hai	10.18140/FLX/1440148	10.5	51.1	430	DBF	8.2	899	2000	2012
9	DE-Tha	10.18140/FLX/1440152	13.6	51	385	ENF	8.6	766	1996	2014
10	DK-Sor	10.18140/FLX/1440155	11.6	55.5	40	DBF	8.9	648	1996	2014
11	FI-Hyy	10.18140/FLX/1440158	24.3	61.8	181	ENF	3.6	679	1996	2014
12	FR-Fon	10.18140/FLX/1440161	2.8	48.5	103	DBF	11.1	626	2005	2014
13	IT-SRo	10.18140/FL	10.3	43.7	6	ENF	15.3	868	199	201

		X/1440176							9	2
14	US-Bar	10.17190/AMF/1246030	-71.3	44.1	272	DBF	6.2	1272	2004	2020
15	US-Dk2	10.17190/AMF/1246047	-79.1	36	168	DBF	15.1	1165	2001	2008
16	US-Fuf	10.17190/AMF/1246051	-111.8	35.1	2180	ENF	7.7	567	2006	2010
17	US-Ha1	10.18140/FLX/1440071	-72.2	42.5	340	DBF	7.4	1118	1991	2012
18	US-Ho1	10.17190/AMF/1246061	-68.7	45.2	60	ENF	6.1	1101	1996	2020
19	US-Me2	10.18140/FLX/1440079	-121.6	44.5	1253	ENF	7	808	2002	2014
20	US-Me4	10.18140/FLX/1440081	-121.6	44.5	922	ENF	6.8	1008	1996	2000
21	US-MMS	10.18140/FLX/1440083	-86.4	39.3	275	DBF	11.5	1143	1999	2014
22	US-MOz	10.17190/AMF/1246081	-92.2	38.7	219	DBF	12.9	1060	2004	2020
23	US-NR1	10.18140/FLX/1440087	-105.5	40	3050	ENF	2.1	577	1998	2014
24	US-Slt	10.17190/AMF/1246096	-74.6	39.9	30	DBF	12.3	1179	2005	2014
25	US-SP1	10.17190/AMF/1246100	-82.2	29.7	50	ENF	20.5	1313	2000	2011
26	US-Ton	10.17190/AMF/1245971	-121	38.4	177	WSA	16.5	605	2001	2020
27	US-Uaf	10.17190/AMF/1480322	-147.9	64.9	155	ENF	-2.2	297	2002	2020
28	US-UMB	10.18140/FLX/1440093	-84.7	45.6	234	DBF	6.6	816	2000	2014
29	US-	10.17190/A	-	35.9	30	ENF	4.4	692	200	202

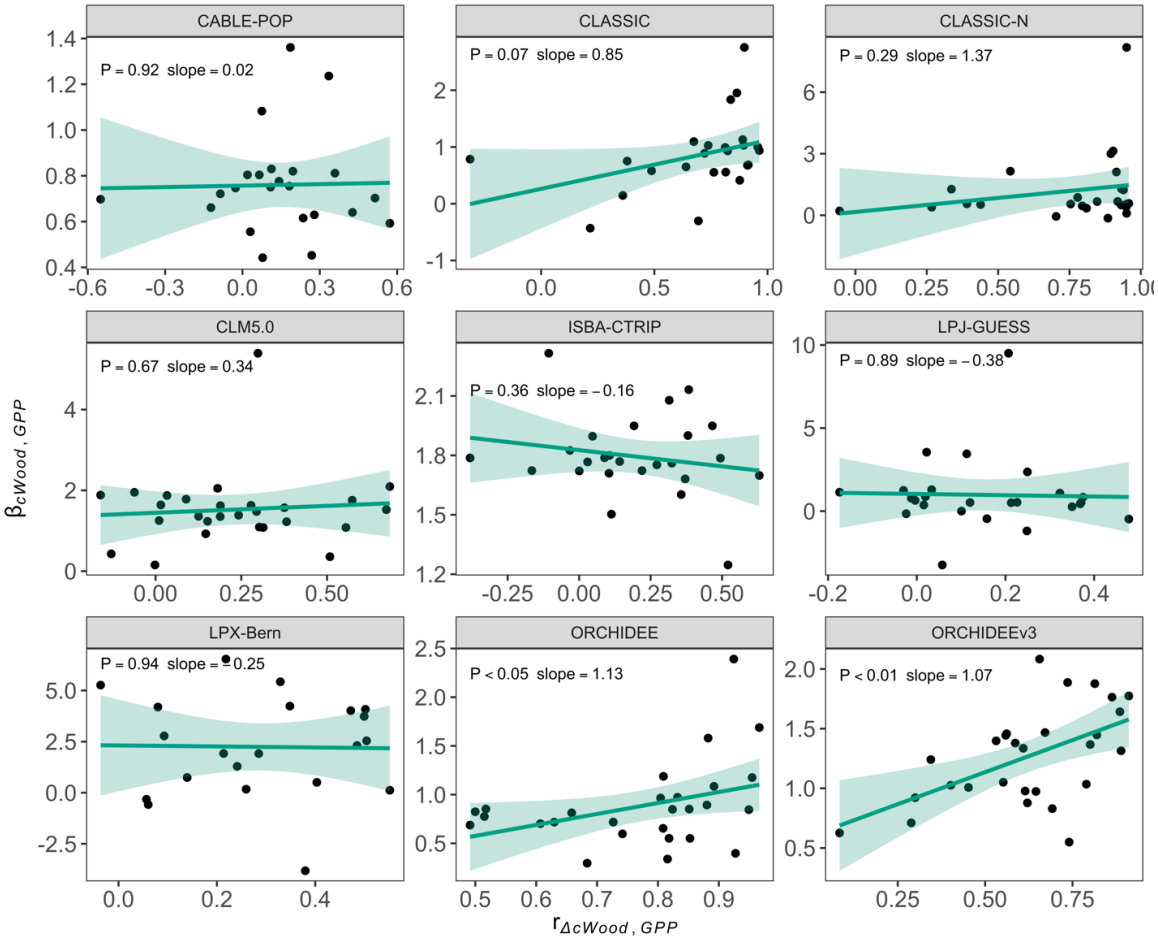
	Vcm	MF/1246121	106.5		30				7	0
30	US-Vcp	10.17190/AMF/1246122	-106.6	35.9	2500	ENF	6.3	588	2007	2020
31	US-Wrc	10.17190/AMF/1246114	-122	45.8	371	ENF	9.4	1946	1998	2015



Extended Data Figure 3.1. *Global maps of 31 eddy-covariance sites with on-site tree-ring data used in this research.*

Extended Data Table 3.2. *Mean* $r_{\Delta cWood,GPP}$ *across all tower-overlapping grid cells for each model and scenario presented in Figure 3.1.*

Model	Scenario	Mean $r_{\Delta cWood,GPP}$
CABLE-POP	S0	0.03
CABLE-POP	S1	0.07
CABLE-POP	S2	0.2
CLASSIC	S0	0.71
CLASSIC	S1	0.72
CLASSIC	S2	0.82
CLASSIC-N	S0	0.65
CLASSIC-N	S1	0.65
CLASSIC-N	S2	0.68
CLM5.0	S0	0.1
CLM5.0	S1	0.11
CLM5.0	S2	0.31
ISBA-CTRIP	S0	0.12
ISBA-CTRIP	S1	0.12
ISBA-CTRIP	S2	0.15
LPJ-GUESS	S0	0.29
LPJ-GUESS	S1	0.23
LPJ-GUESS	S2	0.38
LPX-Bern	S0	0.38
LPX-Bern	S1	0.22
LPX-Bern	S2	0.38
ORCHIDEE	S0	0.72
ORCHIDEE	S1	0.73
ORCHIDEE	S2	0.73
ORCHIDEEv3	S0	0.52
ORCHIDEEv3	S1	0.56
ORCHIDEEv3	S2	0.62



Extended Data Figure 3.2. Relationship between $\beta_{cWood,GPP}$ and $r_{\Delta cWood,GPP}$ within individual models. *$\beta_{cWood,GPP}$ and $r_{\Delta cWood,GPP}$ were calculated at flux tower locations in each TRENDYv10 model under CO_2-only forcing scenario (S1) from 1951-2020. The response ratio ($\beta_{cWood,GPP}$) was calculated as the log transformed ratio of the percent change in woody biomass (cWood) relative to the percent change in GPP from 1951-2020 under CO_2-only forcing scenario (S1; see Methods). Linear fits between $r_{\Delta cWood,GPP}$ and $\beta_{cWood,GPP}$ for each model were displayed (green lines, 95% CI shaded), with P-values and slopes.*

Extended Data Table 3.3. *Pair t-test p-values for mean distribution differences of* $r_{\Delta cWood,GPP}$ *between observations (obs) and scenarios (S0, S1, S2).*

Model	obs-S0	obs-S1	obs-S2	S0-S1	S0-S2	S1-S2
ISBA-CTRIP	0.992	0.92	0.756	0.928	0.745	0.674
CLM5.0	0.778	0.902	P <0.05	0.898	P <0.05	P <0.05
ORCHIDEE	P < 0.001	P < 0.001	P < 0.001	0.917	0.903	0.979
ORCHIDEEv3	P < 0.001	P < 0.001	P < 0.001	0.684	0.196	0.367
CABLE-POP	0.913	0.747	0.06	0.641	P <0.05	0.098
CLASSIC-N	P < 0.001	P < 0.001	P < 0.001	0.934	0.766	0.71
CLASSIC	P < 0.001	P < 0.001	P < 0.001	0.89	0.067	0.077
LPX-Bern	P < 0.01	0.256	P < 0.01	0.099	0.965	0.118
LPJ-GUESS	0.06	0.27	P < 0.01	0.55	0.34	0.14